FACULTAD DE CIENCIAS

Departamento de Química Inorgánica

PROGRAMA OFICIAL DE DOCTORADO EN QUÍMICA

TESIS DOCTORAL

NANOESTRUCTURAS HÍBRIDAS BIOINORGÁNICAS. APLICACIONES EN NANOMEDICINA

Rocío Jurado Palomares

Granada, Octubre de 2017

Editor: Universidad de Granada. Tesis Doctorales
Autor: Rocío Jurado Palomares
ISBN: 978-84-1306-123-8
URI: http://hdl.handle.net/10481/54942

NANOESTRUCTURA HÍBRIDAS BIOINORGÁNICAS. APLICACIONES EN NANOMEDICINA

Memoria de Tesis Doctoral presentada por
Rocío Jurado Palomares
para aspirar al título de Doctor por la
Universidad de Granada

Fdo. Rocío Jurado Palomares

LOS DIRECTORES DE LA TESIS DOCTORAL:

Natividad Gálvez Rodríguez
Profesora titular del Departamento de Química Inorgánica.
Universidad de Granada
y
José Juan Calvino Gámez
Catedrático del Departamento de Ciencia de los Materiales e Ingeniería Metalúrgica y Química Inorgánica.
Universidad de Cádiz

La doctorando Rocío Jurado Palomares y los directores de la Tesis Natividad Gálvez Rodríguez y José Juan Calvino Gámez garantizamos, al firmar esta Tesis Doctoral, que el trabajo ha sido realizado por la doctorando bajo la dirección de los directores de Tesis y hasta donde nuestro conocimiento alcanza, en la realización del trabajo, se han respetado los derechos de otros autores a ser citados, cuando se han utilizado sus resultados o publicaciones.

Granada, Octubre de 2017

La Doctorando

Fdo.: Rocío Jurado Palomares

Los Directores de la Tesis

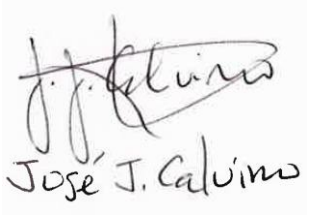

Fdo.: Natividad Gálvez Rodríguez y José Juan Calvino Gámez

Los resultados del trabajo de investigación realizado durante el desarrollo de esta Tesis Doctoral han dado lugar a la publicación de artículos cuyos indicios de calidad son:

- Rocío Jurado, Paulina Frączek, Mélissa Droetto, Purificación Sánchez, Elsa Valero, José M. Domínguez-Vera and Natividad Gálvez (2016) Apomaghemite as a doxorubicin carrier for anticancer drug delivery. **Journal of Inorganic Biochemistry**, 157, 46-51.

  INDICIOS DE CALIDAD:

  Datos del Journal Citation Reports

  - Impact Factor: 3.205
  - Categorías (incluyendo Nº de revistas y posición revistas): CHEMISTRY, INORGANIC & NUCLEAR, 46 revistas, posición 11
  - Cuartil: Primer cuartil

RESUMEN Y ESTRUCTURA DE LA TESIS DOCTORAL

La presente Tesis Doctoral se enmarca en el estudio del potencial que presenta el uso de proteínas para la creación de nanoestructuras híbridas bioinorgánicas con propiedades y aplicaciones fascinantes en el campo biomédico.

Los resultados experimentales obtenidos y la discusión de los mismos se presentan en esta Memoria divididos en 6 capítulos.

En el **primer capítulo, la introducción,** se revisan los conceptos básicos del tema de investigación en el que se ha trabajado en la Tesis Doctoral y la motivación del mismo en el contexto actual. Inicialmente, se expone una idea general de la relación existente entre la Nanotecnología, la Química y la Medicina. Posteriormente, se lleva a cabo una presentación de las aplicaciones que presenta la Nanotecnología a la Medicina, incluyendo conceptos claves como el diagnóstico por imagen, la liberación controlada de fármacos, la hipertermia o la Medicina regenerativa. A continuación, también se exponen otros conceptos básicos de esta Tesis Doctoral, como la definición de biomateriales, de agentes teranósticos o el uso de proteínas para la preparación de materiales híbridos bioinorgánicos. Además, se presenta de manera general las propiedades más características de la apoferritina (una de las proteínas en la que se centra este trabajo) así como de las fibras de tipo amiloide. Finalmente, se concluye el capítulo con los objetivos que se han pretendido alcanzar en esta Tesis Doctoral.

En el **segundo capítulo**, se ha puesto de manifiesto un nuevo nanotransportador teranóstico usando las ventajas que presenta la estructura única de la proteína apoferritina. Esta proteína es efectiva para la encapsulación de nanopartículas de maghemita así como del fármaco doxorrubicina. El uso simultáneo de nanopartículas de maghemita y doxorrubicina se han conseguido mediante co-encapsulación y unión superficial. Las nanopartículas de maghemita recubiertas con la proteína apoferritina son una manera efectiva de conseguir imágenes de contraste

MRI de larga duración en hígado. Además, se ha puesto de manifiesto que pueden servir como un sistema de liberación de fármacos anticancerígenos. En concreto, se muestra que la apoferritina conteniendo la maghemita puede liberar la doxorrubicina durante un período de 10 a 25 días dependiendo de las condiciones ambientales. Por lo tanto, este nanotransportador doxo-Apomaghemita podría encontrar aplicaciones en el campo de la "medicina teranóstica", combinando simultáneamente dos componentes de diagnosis y terapia en una único vector.

En el **tercer capítulo**, hemos demostrado por primera vez la formación de fibras de tipo amiloide para la proteína apoferritina. La morfología, el tamaño y la rigidez de estas estructuras unidimensionales son comparables a las de las fibras de β-lactoglobulina, una proteína que se ha usado frecuentemente como modelo en el estudio de las proteínas fibrilares de tipo amiloide. La apoferritina globular tiene un tamaño nanométrico y es capaz de auto-ensamblarse para formar estructuras 1D de tamaño micrométrico después de ser expuesta a un proceso adecuado de desnaturalización. Dependiendo de las condiciones experimentales, se obtienen fibras de diferentes tamaños y formas.

Además, hemos identificado y caracterizado las diferentes estructuras implicadas en el proceso de formación de las fibras de apoferritina, desde pequeños agregados u oligómeros hasta las fibras maduras. El empleo de diversas técnicas (AFM, SDS-PAGE, CD y FLIM-PIE) proporcionan evidencias convincentes de que el desensamblaje de la proteína así como su hidrólisis completa son esenciales para la formación de las fibras y que fragmentos de péptidos pequeños (<5KDa) participan en la formación de las mismas. El estudio por TEM y las medidas de DLS también fueron capaces de resolver e identificar diferentes estados indiividuales del proceso de formación de las fibras. Además, la técnica

novedosa FLIM-PIE proporciona información muy valiosa a nivel molecular que permite la identificación de los diferentes tipos de oligómeros.

En el **cuarto capítulo**, hemos demostrado cómo las subunidades H y L (con una secuencia peptídica que coincide al 54-57%) que presenta la apoferritina, son capaces de controlar la quiralidad final de las fibras de apoferritina. De esta manera, hemos comparado las fibras formadas en dos casos diferentes: partiendo de Apoferritina recombinante humana 100% H y partiendo de apoferritina recombinante humana 100% L. La quiralidad que se observó fue de casi un 100% dextrógira en el caso de la apoferritina L y casi un 100% levóriga en el caso de la apoferritina H.

Además, hemos sido capaces de estudiar su estructura mediante la combinación de diferentes técnicas. Parámetros morfológicos como la longitud, la altura media o la periodicidad se han evaluado mediante un análisis estadístico por AFM. El estudio mediante TEM ha permitido confirmar que las fibras se han formado correctamente. La tomografía electrónica ha proporcionado resultados muy novedosos tales como que las fibras de apoferritina presentan un patrón común con una subestructura compuesta por dos filamentos con una disposición helicoidal. Además, se han extraído la distancia que hay entre estas dos fibras así como la anchura total de las fibras. También se ha obtenido el valor de la periodicidad que concuerda con el valor obtenido mediante el análisis estadístico por AFM. Por otro lado, las medidas de CD, FTIR y WAXS proporcionaron información acerca de la estructura secundaria de las diferentes iso-apoferritinas.

Estos resultados ofrecen la posibilidad de usar el control de la quiralidad para acceder a nuevas formas de proteínas o nanoestructuras peptídicas y muestran cómo la secuencia peptídica de estas estructuras puede controlar la morfología final de las fibras. Todos estos mecanismos podrían tener grandes implicaciones en el campo de las nanoestructuras 1D.

En el **quinto capítulo,** hemos preparado nanofibras fluorescentes 1D usando tanto la proteína apoferritina como la β-lactoglobulina. La estructura proteica con forma fibrilar es rica en grupos funcionales que permiten una funcionalización química con diversos quantum dots (QD), así como con diferentes marcadores de tipo Alexa fluor (AF), lo cual conduce a la formación de fibras híbridas fluorescentes con diferentes longitudes de onda de emisión, del verde al infrarrojo cercano, dependiendo del QD y AF que se acopla. Además, en las fibras que contienen el par AF488 y AF647, se puede observar una transferencia de energía eficiente (FRET) por parte del donor covalentemente enlazado (AF488) hacia el aceptor (AF647).

Por otro lado, también obtenemos información complementaria de las estructuras y las propiedades luminiscentes de estos nanomateriales híbridos mediante la combinación de AFM y microscopía de fluorescencia con súper-resolución. Mientras que la imagen tomográfica permite determinar la estructura de la fibra, la imagen de súper-resolución (en uno o dos colores) permite la identificación de QDs emisivos y no emisivos.

Por lo tanto, se pone de manifiesto que estos nanomateriales y en concreto las fibras de apoferritina son una nueva plantilla muy prometedora para la síntesis de materiales híbridos multifuncionales.

En el **sexto capítulo**, hemos preparado nanofibras metálicas usando tanto la proteína apoferritina como la β-lactoglobulina. Hemos demostrado por primera vez que las fibras de apoferritina presentan la habilidad de ensamblar diferentes nanopartículas metálicas, así como la β-lactoglobulina. De esta manera se han preparado nanofibras metálicas 1D con diferentes propiedades ópticas y magnéticas mediante la unión de diferentes nanopartículas de oro y de maghemita a las fibras de apoferritina y β-lactoglobulina. Estos nanomateriales híbridos podrían encontrar aplicaciones muy atractivas como sensores o como agentes de contraste y podrían ser muy útiles también para la hipertermia.

Este estudio también se ha comprobado con nanopartículas de oro, plata y paladio producidas mediante reducción química en presencia de las fibras amiloides. Por lo tanto, también hemos reportado por primera vez cómo las fibras de apoferritina pueden servir como nanoreactores para la preparación de nanopartículas metálicas con diversas aplicaciones en Biomedicina y Nanotecnología.

Por último, en las **conclusiones** hacemos un resumen del trabajo desarrollado durante esta Tesis Doctoral y extraemos y comentamos los resultados más significativos.


UNIVERSITATIS·GRANATENSIS
CAROLVS·RO·IMP·SEMPER·AVG·
HISPAN·REX·FUNDATOR·

SUMMARY

This Thesis is part of the study of the potential of using proteins for the creation of hybrid bioinorganic nanostructures with fascinating properties and applications in the biomedical field.

The experimental results obtained and the discussion of them is presented in this report divided into 6 chapters.

In **chapter one**, the **introduction**, we review the basic concepts of the research topic in which we have worked on the Thesis and the motivation of them in the current context. Initially, a general idea of the relation between Nanotechnology, Chemistry and Medicine is presented. Subsequently, we describe the applications presented by Nanotechnology to Medicine, including key concepts such as diagnostic imaging, controlled drug delivey, hypethermia or regenerative medicine. Other basic concepts such as biomaterials definition, teranostic agent or the use of proteins for the preparation of hybrid bioinorganic materials are also presented. In addition, the most characteristic properties of apoferritin (one of the proteins on which this work is centered) as well as the amyloid-type fibers are generally presented. Finally, the chapter concludes with the objectives that have been sought to achieve in this Thesis.

In **second chapter**, a new theranostic nanocarrier is proposed using the advantages presented by the unique structure of apoferritin protein. This protein is effective for the encapsulation of maghemite nanoparticles as well as a significant dose of doxorubicin drug. The simultaneous use of maghemite nanoparticles and doxrubicin has been achieved by co-encapsulation or surface binding. Maghemite nanoparticles coated with apoferritin protein are an effective way of achieving long-term MRI liver contrast imaging. In addition, it has been shown that they can serve as a system for delivering anticancer drugs. Specifically, it is shown that apoferritin containing maghemite can release doxorubicin over a period of 10 to 25 days depending on environmental conditions. Therefore, this

doxo-Apomaghemite nanotransporter is very useful in the field of "theranostic medicine", combining diagnosis and therapy components into a single nanoparticle.

In **third chapter**, we have shown for the first time the formation of apoferritin amyloid-like protein fibers. The morphology, size and stiffness of these one-dimensional structures are comparable to those of β-lactoglobulin fibers, a protein that has been frequently used as a model in the study of amyloid-like fibrillar proteins. The globular apoferritin has a nanometric size and is capable of self-assembling to form 1D micrometer-sized structures after being exposed to a detanuration process. Depending on the experimental conditions, fibers with different sizes and morphologies are obtained.

Moreover, we have identified and characterized different stages involved in the formation of apoferritin fibers, from small aggregates or oligomers to mature fibers. Using different techniques (AFM , SDS-PAGE, CD and FLIM-PIE) all provide convincing evidence that protein unfolding and complete hydrolysis are essential for the formation of large laminated aggregates and that small peptides fragments (<5 kDa) participate in the formation of these fibrils. TEM study and DLS measurements were able to resolve and identify different individual stages of the fibrillation process as well. Moreover, the novel technique FLIM-PIE provided single-molecule information that allowed precise identification of different types of oligomers.

In **fourth chapter**, we have demonstrated how H or L apoferritins subunits (with a peptide sequence coincidence of only 54-57%) can direct the final chirality of apoferritin fibers. In this way, we have compared the apoferritin fibers formed in two different cases: starting from pure Human apoferritin H (H APO) and from pure Human apoferritin L (L APO). The

observed chirality was nearly a 100% of right-handeness for L APO and nearly a 100% of left-handeness for H APO.

Moreover, we have been able to study their structure by combining different techniques. Morphological parameters such as total contour length, average height, or pitch size were evaluated from the AFM statistical analysis. TEM allowed confirming the optimal formation of the fibers. Electron tomography provided novel appealing results such as APO fibers have a common building block comprising paired strands with a double helical substructure. Additionally, the gap with between each strand and the strand width were extracted by the intensity profiles. The pitch value was as well measured and it was in perfect agreement with the AFM statistical analysis. On the other hand, CD, FTIR and WAXS measurements provided information about the secondary structure of the different iso-apoferritins.

These results open up the possibility of using the control of chirality to access new forms of protein and peptide nanostructures and show how the peptide sequence of such structures can control their final morphology. Insights into these mechanisms can have significant implications into the growing field of 1D nanostructures.

In **fifth chapter**, we have prepared 1D fluorescent nanofibers either using apoferritin or β-lactoglobulin proteins as templates. The fibrillar-like protein structure is rich in functional groups that allow chemical functionalization with different quantum dots (QD), as well as with different Alexa fluor (AF) dyes, leading to the formation of hybrid fluorescent fibers with variable emission wavelengths, from green to near infrared, depending on the QD and AF that is coupled. In addition, for fibers containing the pair AF488 and AF647, an efficient energy transfer (FRET) can be observed from the covalently coupled donor (AF488) to the acceptor (AF647).

On the other hand, valuable complementary information about the structure and properties of luminescent hybrid nanomaterials was provided by hybrid nanoscopy combining AFM and super-resolution imaging. While the topography image allowed determining the fiber structure, the super-resolution image (in one or two colors) allowed the identification of emissive and nonemissive QDs.

Therefore, it is shown that these nanomaterials and in particular apoferritin fibers are a very promising new template for the synthesis of multifunctional hybrid materials.

In **sixth chapter**, we have prepared 1D hybrid metallic nanofibers either using apoferritin or β-lactoglobulin proteins as templates. We have shown for the first time that apoferritin fibers have the ability to assembly different metallic nanoparticles, as well as the β-lactoglobulin. Thus, 1D metallic nanofibers with different optical and magnetic properties were prepared by coupling different AuNPs and maghemite NPs to apoferritin and β-lactoglobulin fibers. These hybrid nanomaterials could find very appealing applications as sensors or as imaging contrast agents and they could be very useful for hyperthermia as well.

These findings have been validated as well with synthetic gold, silver and palladium nanoparticles produced by chemical reduction in the presence of the amyloid fibrils. Therefore, we have reported for the first time how amyloid apoferritin protein fibrils can serve as nanoreactors for the preparation of metallic NPs with several applications in biomedicine and nanotechnology.

Finally, in the **conclusions**, it is made a summary of all the results obtained in this doctoral thesis and the most significant results are analyzed.

ÍNDICE

CAPÍTULO 1. INTRODUCCIÓN……23

1. Nanotecnología, química y medicina……25
2. Aplicaciones de la nanotecnología a la medicina……27
   - 2.1. Métodos de diagnóstico……27
     - 2.1.1. Diagnóstico por imagen……28
   - 2.2. Métodos terapéuticos: liberación de fármacos e hipertermia……29
   - 2.3. Sistemas terapéuticos y de diagnóstico: agentes teranósticos……35
   - 2.4. Medicina regenerativa……36
3. Nanomateriales híbridos bioinorgánicos: el uso de biomoléculas como plantillas para la síntesis de nanomateriales……40
4. Apoferritina como proteína para dirigir la síntesis de materiales híbridos bioinorgánicos……42
5. Uso de fibras de tipo amiloide para la síntesis de materiales híbridos bioinorgánicos……47
6. Objetivos……53
7. Bibliografía……58

CHAPTER 2. APOMAGHEMITE AS A DOXORUBICIN CARRIER FOR ANTICANCER DRUG DELIVERY……67

1. Introduction……69
2. Incorporation of DOX into Apoferritin protein……76
   - 2.1. Co-encapsulation……76
   - 2.2. Surface-binding……77
   - 2.3. Encapsulation efficiency……77
3. Apomaghemite TEM study……78

4. DLS measurements.....79
5. Co-encapsulation and surface-binding release comparison.....80
5.1. pH and temperature influence.....82
6. Gel electrophoresis.....84
7. Cell toxicity test.....85
8. Conclusions.....87
9. References.....88

CHAPTER 3. APOFERRITIN PROTEIN: UNDERSTANDING THE FORMATION OF AMYLOID-LIKE FIBRILS.....91

1. Introduction 93
2. Formation of APO and Blg fibers.....96
2.1. Influence of temperature.....98
2.2. Influence of pH.....99
2.3. Influence of incubation time.....101
2.4. Influence of protein concentration.....103
2.5. Influence of stirring.....104
3. APO aggregation kinetics.....106
3.1. APO fibers AFM study.....107
3.2. APO fibers TEM study.....111
3.3. DLS measurements.....113
3.4. Gel electrophoresis.....115
3.5. ThT analysis.....116
3.6. CD measurements.....116
3.7. FLIM measurements.....118
4. Conclusions.....123
5. References.....125

CHPATER 4. HUMAN RECOMBINANT LIGHT AND HEAVY APOFERRITIN SUBUNITS DIRECT CHIRALITY IN APOFERRITIN FIBERS……127

1. Introduction ……129
2. Formation of human L and H APO fibers……132
3. TEM study……137
4. Electron tomography analysis……138
5. CD and FTIR measurements……144
6. WAXS measurements……148
7. Gel electrophoresis……150
8. Conclusions……151
9. References……153

CHAPTER 5. APOFERRITIN FIBERS: A NEW TEMPLATE FOR 1D FLUORESCENT HYBRID NANOSTRUCTURES……155

1. Introduction ……157
2. Dye-labelled fibrils proteins……162
3. Fluorescence lifetime imaging microscopy with pulsed interleaved excitation (FLIM-PIE) measurements ……166
4. Fluorescent 1D hybrid QD-fibers ……171
5. Conclusions……181
6. References……183

CHAPTER 6. 1D HYBRID METALLIC PROTEIN NANOFIBER…187

1. Introduction……189
2. Decorating APO and Blg fibrils with different nanoparticles…….190
   2.1. Decorating APO and Blg fibrils with gold nanoparticles ……191
      2.1.1. Assembly of gold spherical nanoparticles……192
      2.1.2. Assembly of gold nanorods ……194

2.2. Decorating Apo and Blg fibrils with iron oxide nanoparticles……195
3. Metal-binding APO fibers as templates for the preparation of hybrid nanostructures ……200
3.1. Fabrication of gold nanoparticle nanowires……201
3.2. Fabrication of silver nanoparticle nanowires……202
3.3. Fabrication of palladium nanoparticle nanowires……204
4. Conclusions……205
5. References……207

CONCLUSIONS……211

MATERIALS AND METHODS……217

1. Materials and methods from Chapter 2……219
2. Materials and methods from Chapter 3……223
3. Materials and methods from Chapter 4……228
4. Materials and methods from Chapter 5……231
5. Materials and methods from Chapter 6……234
6. Techniques……237
6.1. Fluorescence Lifetime Imaging Microscopy with Pulsed Interleaved Excitation (FLIM-PIE)…… ……237
6.2. Transmission Electron Microscopy (TEM)……239
6.3. Atomic force microscopy (AFM)……242
6.4. Electron tomography (ET)……244
6.5. Dynamic light scattering (DLS)……246
6.6. Polyacrylamide gel electrophoresis (PAGE)……247
6.7. Circular dichroism (CD)……248
6.8. Wide Angle X-ray Scattering (WAXS)……250
6.9. Fourier-transform infrared spectroscopy (FTIR)……251
6.10. Magnetism……253

CAPÍTULO 1. INTRODUCCIÓN

1. Nanotecnología, química y medicina

La rama de la Química Fundamental dedicada a la preparación de especies químicas que puedan tener aplicaciones en Medicina vive un momento de grandes retos, promovidos en parte por un mayor nivel de exigencia de los nuevos fármacos. Diagnóstico precoz, alta especificidad, no toxicidad o multifuncionalidad son términos que marcan la ruta de la Química orientada hacia la Medicina y representan los retos en un futuro a corto-medio plazo en esta área.

En el famoso discurso de Richard Feynman (*"There is plenty of room at the bottom",* Pasadena 1959), se exponía una idea revolucionaria: la manipulación directa de átomos para la creación de nuevos materiales con nuevas propiedades. Desde entonces, la ciencia ha desarrollado primero y usado después esta moderna tecnología en una amplia variedad de aplicaciones, desde la producción de aparatos extremadamente pequeños hasta el desarrollo de una nueva generación de herramientas para identificar células diana infectadas.[1] Para muchos autores este discurso marca el comienzo de una nueva disciplina científica conocida como Nanotecnología.

Posteriormente, se produciría un importante paso adelante en esta nueva disciplina cuando Gerd Binnig y Heinrich Rohrer (Premio Nobel de Física en 1986) desarrollaron el microscopio de efecto túnel, que fue el precursor de todas las otras formas de microscopía de sonda de barrido. Y es que no es suficiente con ser capaces de fabricar materiales en la escala nanométrica sino que también debemos poder caracterizarlos. Más tarde durante los años 90, surgieron novedosos métodos físicos y químicos para la producción de materiales mediante manipulación a nivel atómico. Estos nuevos métodos son conocidos como tecnología "nano". Hoy en día se

pueden sintetizar, mediante diferentes rutas, nanomateriales con una gran precisión en su morfología, tamaño y propiedades físico-químicas.

El trabajo en las áreas de la Nanociencia y la Nanotecnología ha sido y es multidisciplinar, así como ambicioso en sus metas. De esta manera la ciencia de los nanomateriales coincidió con la Química y la Medicina dando lugar a la Nanomedicina, una ciencia traslacional que tiene el objetivo de suministrar métodos más novedosos y mejorados de terapia y diagnosis usando el mundo en expansión de la Nanotecnología (Figura 1). Para alcanzar este objetivo, el uso de nanopartículas en Medicina en lugar de compuestos químicos discretos tradicionales es una alternativa que ofrece numerosas ventajas que están siendo exploradas dentro de esta área. En este contexto, la nanopartícula puede ser visualizada como una plataforma donde pueden combinarse distintas especies activas para diferentes fines o bien para llevar a cabo una acción sinérgica en pro de abordar un único problema. Asimismo, la incorporación de algunas especies activas en una nanoestructura puede alterar de forma favorable su mecanismo de actuación, pudiendo incrementarse su acumulación o especificidad en un tejido, ralentizar su metabolización, etc.[2]

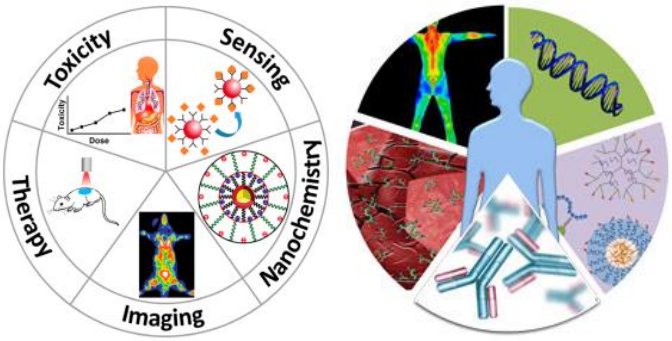

Fig. 1. Nanomedicina y Nanotecnología.[3] Imágenes tomadas de: G. Chen, I. Roy, C. Yang, P.N. Prasad, *Chem. Rev.* **2016**, *116*, 2826 (izquierda); https://nano.tau.ac.il/fta/ (derecha).

2. Aplicaciones de la Nanotecnología a la Medicina.

Entre todas las aplicaciones que ofrece la Nanotecnología, es especialmente en el campo biomédico donde ya ha dado más frutos y donde parece tener un mayor potencial de aplicaciones. Y es que la posibilidad de introducir en el cuerpo humano nanopartículas o nanoestructuras ofrece enormes posibilidades en Medicina.

Dentro de las aplicaciones biomédicas que han sido desarrolladas gracias a la Nanotecnología, se pueden distinguir tres grupos generales: métodos de **diagnóstico**, métodos **terapéuticos** mediante la liberación controlada de fármacos y/o hipertermia, y el desarrollo de nanoestructuras capaces de regenerar tejidos (**Medicina regenerativa**).

De esta manera, se pueden diseñar y preparar nanomateriales con aplicaciones terapéuticas y de diagnosis variadas como por ejemplo: nanopartículas magnéticas como agentes de bioimagen mediante Resonancia Magnética (MRI), nanosistemas para la liberación controlada de fármacos o especies activas (*Drug Delivery Systems*), nanopartículas magnéticas para el tratamiento del cáncer por hipertermia local, nanosistemas para la regeneración de tejidos, etc.[3]

2.1. Métodos de diagnóstico

Los métodos de diagnóstico desempeñan un papel clave en Medicina ya que gracias a ellos se puede garantizar el éxito de la prevención y el tratamiento eficaz de numerosas enfermedades. La ventaja que presentan los métodos de diagnóstico basados en nanoestructuras reside en su sensibilidad y selectividad potencialmente mayores en comparación con los métodos tradicionales, además de desarrollar procesos cada vez más rápidos y sencillos. Por lo tanto, el objetivo fundamental de estos sistemas es ofrecer un diagnóstico precoz eficaz.[4]

Las herramientas de diagnóstico se pueden agrupar a su vez dentro de dos grandes categorías: los dispositivos de diagnóstico *in vitro*, dentro de los cuales se incluyen los biosensores, los *nanoarrays* de genes, proteínas o células y los dispositivos *lab-on-a-chip* (laboratorio en un chip); y el diagnóstico por imagen.[4]

2.1.1. Diagnóstico por imagen

La Nanotecnología ha impulsado un nuevo avance en las técnicas de diagnóstico por imagen, ya sea desarrollando nuevos métodos o aumentando la resolución y sensibilidad de técnicas ya existentes. Este método ha ido ganando importancia a través de los años y hoy en día es una herramienta indispensable para el diagnóstico eficaz de numerosas enfermedades como el cáncer o las enfermedades neurodegenerativas.[3]

En paralelo al desarrollo de las técnicas de imagen, se están desarrollando agentes de contraste nuevos entre los que se incluyen las **nanopartículas magnéticas y superparamagnéticas** (como por ejemplo las nanopartículas de óxido de hierro) para ser utilizadas en **MRI**[5] y las **nanopartículas fluorescentes** de tipo *Quantum Dots* (QD, puntos cuánticos) para la toma de **imágenes ópticas**, esta última aún en las primeras fases de desarrollo, ya que sólo ha sido probada en ratones.[6] Estas nanoestructuras ofrecen una serie de ventajas frente a los agentes de contraste tradicionales ya que las propiedades físicas, mecánicas y eléctricas cambian según nos acercamos a la escala nanométrica. De esta manera, son capaces de aumentar sustancialmente la resolución, la especificidad y la sensibilidad mientras que permiten un diagnóstico más temprano de la enfermedad.

La técnica de mayor relevancia destinada al uso potencial de estos agentes de contraste es la Resonancia Magnética por Imagen (*Magnetic*

Resonance Imaging, MRI). Esta técnica se basa en la resonancia magnética de los protones de los tejidos del cuerpo (agua, membranas, lípidos, proteínas, etc.) y es actualmente uno de los métodos más potentes de diagnosis. Cabe destacar la existencia de otras técnicas de imagen relevantes como la técnica de toma de Imágenes Ópticas (*Optical Imaging*, OI), o las Técnicas por Imagen Nuclear, entre las que se incluyen la Tomografía por emisión de Positrones (*Positron Emission Tomography*, PET) y la Tomografía Computarizada por Emisión de Fotón Único (*Single Photon Emission Computed Tomography*, SPECT) (Figura 2).

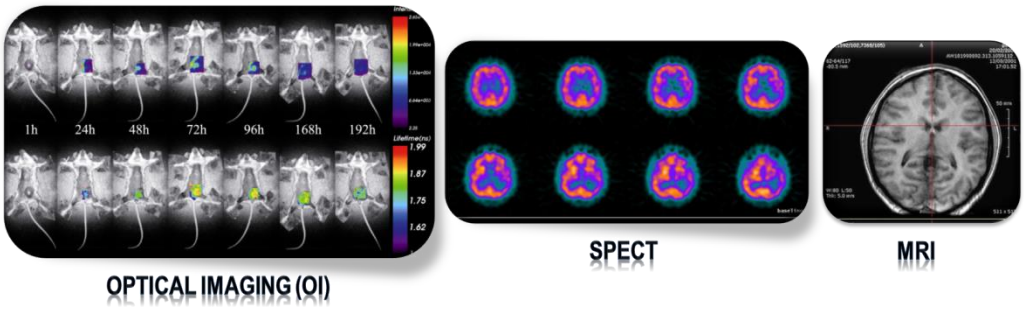

Fig. 2. Diferentes técnicas de imagen usadas en diagnosis.

2.2. Métodos terapéuticos: liberación de fármacos e hipertermia

La falta de selectividad por parte de los fármacos actuales además del uso prolongado de sistemas convencionales de administración conduce al daño de células sanas. Los sistemas de **liberación controlada de fármacos** basados en Nanotecnología presentan un impacto significativo en la medicina actual ya que son capaces de dirigir el fármaco de manera selectiva y controlada a su sitio de acción, disminuyendo así la toxicidad asociada al fármaco en las células sanas.[7]

Estos nanosistemas también presentan otras ventajas ya que son capaces de evitar problemas relacionados con la solubilidad del fármaco y

además presentan un tiempo de circulación elevado, lo cual garantiza su efectividad. De esta manera, estos sistemas proporcionan alternativas a las vías de administración tradicionales, mucho más invasivas.

Algunos ejemplos de nanomateriales liberadores de fármacos recientes incluyen nanopartículas poliméricas,[8] liposomas,[9] micelas,[10] nanocarcasas, nanotubos de carbono,[11] cápsulas, dendrímeros,[12] nanoconstrucciones basadas en ácidos nucleicos, **nanoestructuras basadas en proteínas**[13] y diversas nanopartículas metálicas, entre otros.[14,15,16,17] (Figura 3).

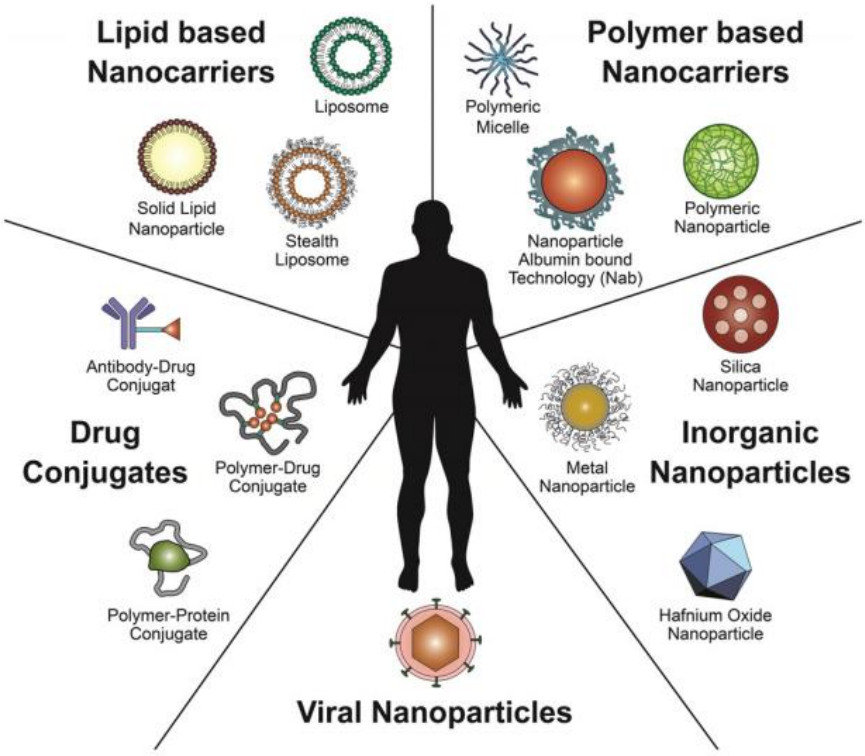

Fig. 3. Representación esquemática de diversas nanoplataformas terapéuticas.[2] Imagen tomada de: A. Wicki, D. Witzigmannb, V. Balasubramanianc, J. Huwylerb, *J. Control. Release,* **2015,** *200*, 138.

Muchos de estos sistemas de liberación son ya realidades en el mercado biomédico mientras que otros se encuentran en la última etapa del

ensayo clínico.[18] Por ejemplo, Doxil (liposomas con doxorrubicina), usados para el tratamiento del SIDA asociado al Sarcoma de Kaposi, el cáncer de mama, el ovárico y otros tumores sólidos, fue el primer sistema de liberación basado en liposomas en recibir aprobación en 1999 por parte de la FDA (United States Food and Drug Administration)[19] y Abraxane, una albúmina de 130 nm con paclitaxel, recibió la aprobación de la FDA para su tratamiento en pacientes con cáncer de mama en 2007.[20]

Otras nanoestructuras, como Dauno-Xome (liposomas con daunorrubicina), Ambisome (liposomas con anfotericina B), Genexol-PM (partículas de PEG-PLGA-Paclitaxel) y DE-310 (Dextrano-Camptotecina), son algunos ejemplos más.[21]

La **hipertermia** es otro método de terapia ampliamente utilizado en el campo de la Nanomedicina. La hipertermia es un tratamiento específico y efectivo contra el cáncer que consiste en la destrucción del tumor mediante sobre-calentamiento local del tejido (de hasta 44°C). Esta alta temperatura puede dañar y destruir las células cancerosas, pero generalmente causa lesiones mínimas en los tejidos sanos.

Cuando la técnica se lleva a cabo mediante el uso de nanopartículas magnéticas, la hipertermia se desarrolla exponiendo las nanopartículas a un campo magnético alterno (Figura 4) y se denomina hipertermia magnética.[22] La acumulación específica se debe a un efecto llamado *enhanced permeability and retention* (EPR).[23]

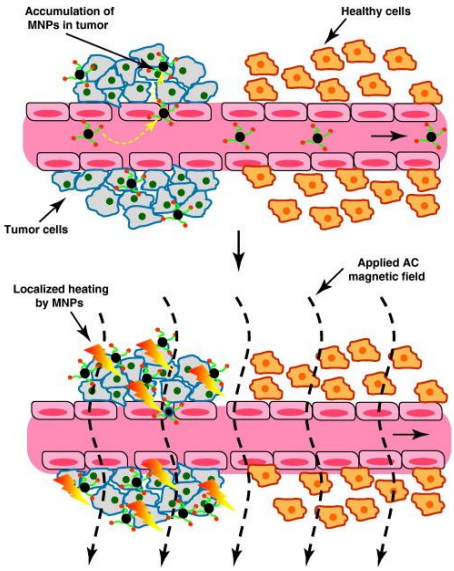

Fig. 4. Principio de la hipertermia magnética.[22] Imagen tomada de: A. J. Cole, V. C. Yang, A.E. David, *Trends in Biotechnology*, **2011**, *29*, 7.

Este fenómeno de EPR ocurre debido a la angiogénesis (formación de nuevos vasos sanguíneos) inducida cuando las células tumorales se multiplican, agregan y alcanzan un tamaño de 2-3mm, ya que se necesitan satisfacer las necesidades cada vez mayores de nutrición y oxígeno del tumor en crecimiento. Estos vasos tumorales presentan una morfología irregular y las células endoteliales se encuentran desalineadas o desorganizadas y presentan fenestraciones anchas (Figura 5).[23] Además, las células perivasculares y la membrana basal o la capa muscular lisa, con frecuencia están ausentes o anormales en la pared vascular. Por otro lado, los vasos tumorales presentan un lumen amplio, mientras que los tejidos tumorales tienen un drenaje linfático deficiente. Todas estas anomalías anatómicas, junto con otras anomalías funcionales, permiten una extensa difusión de los componentes del plasma sanguíneo (tales como macromoléculas, nanopartículas o partículas lipídicas) hacia el tejido tumoral. Por otra parte, el lento retorno venoso en el tejido tumoral y el mal drenaje linfático permite que las macromoléculas se mantengan en el

tumor, mientras que la extravasación hacia el intersticio tumoral continúa. Curiosamente, el efecto EPR no se aplica a los fármacos de bajo peso molecular debido a su rápida difusión en sangre.

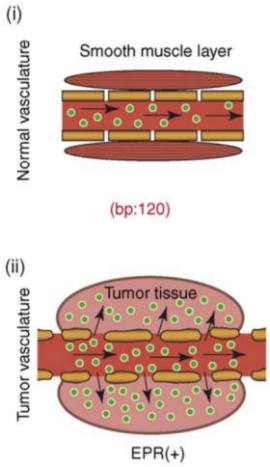

Fig. 5. Efecto EPR.[23] Imagen tomada de: A. K. Iyer, G. Khaled, J. Fang, H. Maeda, *Drug Discovery Today*, **2006,** *11*, 17.

Por lo tanto, estas técnicas presentan numerosos beneficios frente a los métodos de terapia clásicos que dan lugar a que el tejido sano que rodea al tumor también se destruya. Estos beneficios se pueden resumir en mínima invasividad, accesibilidad a tumores ocultos y muy pocos efectos secundarios.

Otra manera de conseguir que la acumulación en el tejido canceroso sea específica es el empleo de sistemas de liberación con marcadores (***Targeted Drug Delivery Systems***).[2] En este caso, un ligando con alta afinidad se une a la superficie del nanotransportador. Este ligando es capaz de unirse selectivamente a un receptor en la célula diana (Figura 6), por lo tanto, el ligando debe elegirse de manera que permita la unión a las células diana mientras minimiza la unión a las células sanas. La entrega dirigida se garantiza gracias a la elevada especificidad que presenta el ligando hacia su

receptor. Para ello, han sido empleados diversos ligandos, entre los que se incluyen pequeñas moléculas como el ácido fólico [24] o los carbohidratos, [25] pero también macromoléculas tales como péptidos, proteínas, anticuerpos, aptámeros y oligonucleótidos.[26,27,28] Un ejemplo del que se están desarrollando ensayos clínicos son los inmunoliposomas cargados con doxorrubicina dirigidos contra el receptor del factor de crecimiento epidérmico (EGFR) (Figura 7).[29]

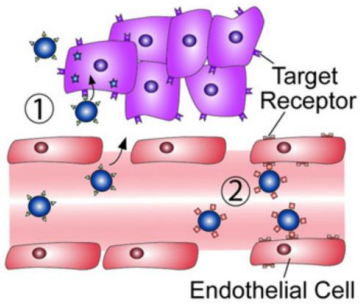

Fig. 6. Marcaje activo de las células cancerosas (1) o del tumor endotelial (2) mediante nanotransportadores con ligandos modificados. Imagen tomada de: A. Wicki, D. Witzigmannb, V. Balasubramanianc, J. Huwylerb, *J. Control. Release,* **2015,** *200*, 138.

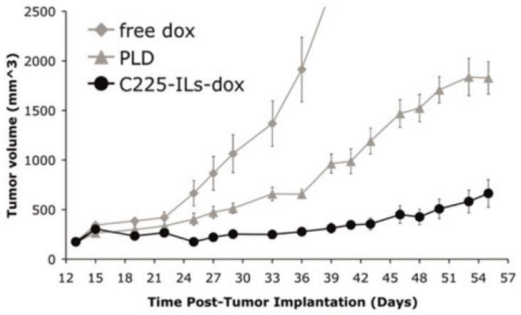

Fig. 7. Marcaje activo específico de las células cancerosas utilizando immunoliposomas contra EGFR (anti-EGFR-ILs). Comparación del efecto terapéutico de anti-EGFR-ILs (C225-ILs-dox) frente a doxorrubicina libre (free dox) o liposomas pegilados (PLD). Imagen tomada de: A. Wicki, D. Witzigmannb, V. Balasubramanianc, J. Huwylerb, *J. Control. Release,* **2015,** *200*, 138.

2.3. Sistemas terapéuticos y de diagnóstico: agentes teranósticos.

Tal y como se ha comentado anteriormente, la investigación en el campo de la Nanomedicina es extremadamente multidisciplinar por lo que existe una estrecha relación entre el área de diagnosis y terapia. En contraste con el desarrollo y el uso de materiales separados para la diagnosis y la terapia, los **agentes teranósticos** combinan estos dos objetivos en una única estructura (Figura 8).[30]

Un ejemplo de agente teranóstico puede ser un sistema que incluya un agente de contraste para su seguimiento mediante MRI a la vez que un fármaco terapéutico para el tratamiento de una enfermedad, como por ejemplo, el cáncer.

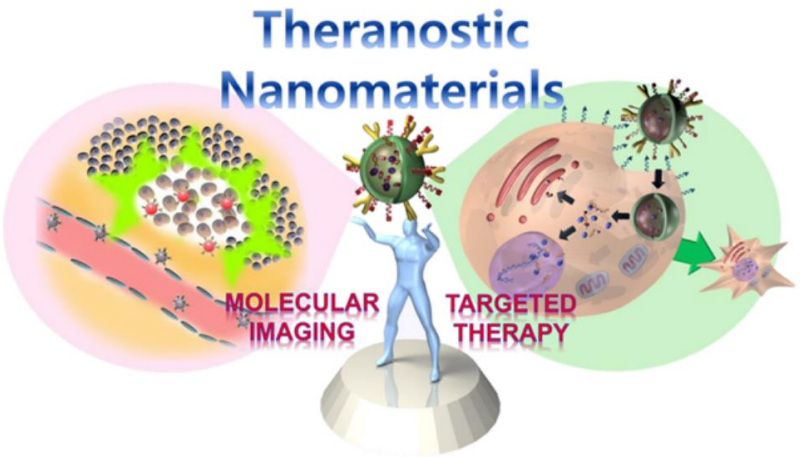

Fig. 8. Agentes nanoteranósticos.[30] Imagen tomada de: K. Lee, T. Kim, S. Paik, S. Haam, Y. Huh, K. Lee, *Chem. Rev*., **2015**, *115*, 327.

En este contexto, han sido desarrollados diversos agentes teranósticos. Por ejemplo, Wu and Chen *et al.* emplearon nanorods de oro encapsulados en sílice mesoporosa (Au@SiO_2) cargados con moléculas de doxorrubicina (Figura 9);[31] Feng *et al.* encapsularon un QD comercial junto

con el fármaco doctaxel en el copolímero PLGA-D-α-TPGS–COOH;[32] Sokolov and Johnston *et al.* desarrollaron nanoclusters de óxido de hierro/oro conjugados con un anticuerpo marcador de EGFR para su uso específico en imagen y terapia;[33] entre muchos otros.

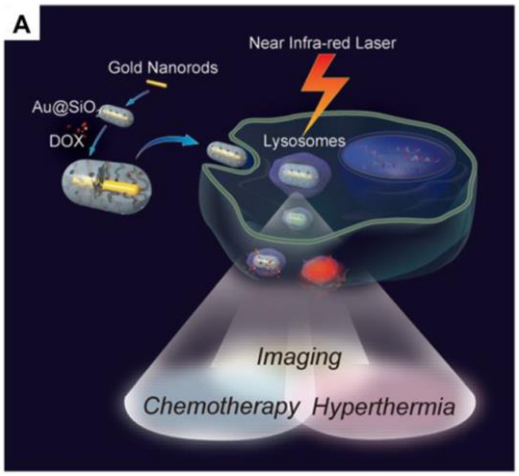

Fig. 9. Nanorods de oro recubiertos con sílice mesoporosa ($Au@SiO_2$) como agentes teranósticos.[31] Imagen tomada de: Z. Zhang, L. Wang, J. Wang, X. Jiang, X. Li, Z. Hu, Y. Ji, X. Wu, C. Chen, *Adv. Mater.,* **2012**, *24*, 1418.

A pesar de estas ventajas, los sistemas de liberación e imagen desarrollados también presentan algunas desventajas, por ejemplo, una limpieza rápida por parte del sistema inmune o una baja eficiencia en el marcaje específico.[34] Debido a ello, también se han propuesto numerosas soluciones modificando las propiedades físicas (como el tamaño, la forma o las propiedades mecánicas) y químicas (por ejemplo, modificando químicamente la superficie) de las partículas para mejorar su eficacia.[35,36]

2.4. Medicina regenerativa

Algunas de las aplicaciones más espectaculares de la Nanotecnología se han desarrollado en el campo de la Medicina regenerativa, una disciplina

cuyo fin consiste en el mantenimiento, la mejora o la restauración de la función de las células, tejidos y órganos.[37]

En la investigación clínica, la Medicina regenerativa abarca la manipulación de células madre mediante nanopartículas y superficies nanoestructuradas, así como la ingeniería tisular para tratar órganos dañados por enfermedades o traumatismos. Esto incluye, por ejemplo, la sustitución de la piel después de una quemadura, la reversión de una parálisis o la ceguera a través de la regeneración de la médula espinal o la retina, la regeneración del corazón después de un infarto y la minimización de la disfunción de un ictus mediante la reparación neuronal.[38]

De esta manera, los recientes avances en Nanotecnología suponen un impulso en la ingeniería de tejidos, ya que facilitan nuevos materiales y nuevas técnicas, que permiten una integración de los tejidos de manera más eficiente.

Dentro de las aportaciones de la Nanotecnología a la Medicina regenerativa se incluye el desarrollo de nuevos materiales y sistemas de soporte, dando lugar a los denominados **bionanomateriales**.

La síntesis de bionanomateriales surgió en la década de los 60 y desde entonces la investigación en este campo ha ido avanzando de manera progresiva. En los últimos años ha surgido una generación de biomateriales que se caracteriza por producir respuestas celulares específicas a escala molecular, los cuales son capaces de estimular a determinados genes cuya acción está relacionada con la regeneración tisular. [39]

La principal ventaja que presentan estos bionanomateriales en el campo de la Medicina regenerativa es que son bioactivos y biodegradables simultáneamente, lo cual supone un gran avance ya que por una parte son

capaces de estimular la regeneración del tejido y al mismo tiempo disminuyen las necesidades de cirugía. De esta forma los nuevos biomateriales constituyen un auténtico soporte, idéntico al que presentan de forma natural las células, sobre el que podrán crecer las células progenitoras para posteriormente insertar este implante en el paciente y así reparar o sustituir el órgano dañado. Como además se trata de soportes reabsorbibles, con el tiempo el soporte es reemplazado por el propio tejido.[39]

Otra forma de afrontar la regeneración del tejido es la denominada regeneración de tejidos *in situ,* en la que estos materiales bioactivos liberan compuestos tales como factores de crecimiento u otras moléculas activas que estimulan la reparación local del tejido.[40]

En la actualidad existen diferentes tipos de bionanomateriales, los cuales se resumen en la Tabla 1. Dentro de ellos, un tipo que presenta un amplio interés en el campo biomédico son las **nanofibras y los soportes nanofibrosos**.

Tipo de bionanomaterial	Aplicaciones	Ventajas	Inconvenientes
Nanofibras	Problemas cardiovasculares	Baja toxicidad	Necesidad de controlar la estructura del material a escala nanométrica
Soportes porosos y nanofibrosos	Epidermis, cartílago, óseos	Bioactivos y biocompatibles	Toxicidad cuestionable
Nanoesferas	Alzheimer	Capacidad de responder frente a cambios externos	Problemas regulatorios
Nanocomposites	Enfermedades Neurodegenerativas	Vida de los implantes no reabsorbibles extendida	
Nanotubos de carbono	Diabetes		
	Cáncer		

Tabla 1. Diferentes tipos de bionanomateriales.

Un ejemplo de estos bionanomateriales aplicados a la Medicina regenerativa fue propuesto por Stupp y colaboradores,[41] los cuales han indicado que la regeneración dentro del sistema nervioso central puede ser alcanzada aplicando nanofibras auto-organizadas. Para este propósito utilizaron un péptido anfifílico (IKVAV) que se auto-ensambla en un nanotubo y reconoce la integrina $\alpha_3\beta_1$ (Figura 10). La señalización inducida parece estimular el crecimiento de los axones y promueve el desarrollo de las neuronas.[42,43]

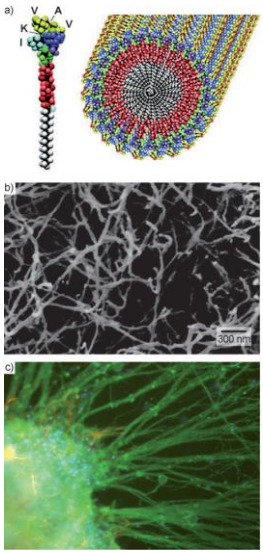

Fig. 10. Nanopartículas funcionalizadas para regeneración nerviosa: a) representación esquemática de un péptido anfifílico que contiene IKVAV; b) Imagen SEM de una red auto-ensamblada de anfifilos IKVAV; c) apoyado por una red de nanofibras, células progenitoras diferenciadas a neuronas funcionales en lugar del astrocito formador de cicatrices.[41] Imagen tomada de: G. A. Silva, C. Czeisler, K. L. Niece, E. Beniash, D. A.Harrington, J. A. Kessler, S. I. Stupp, *Science,* **2004**, *303*, 1352.

En resumen, todas estas aplicaciones y funciones ofrecidas por la Nanomedicina hacen que sea, sin ninguna duda, un campo de investigación muy prometedor que ha experimentado un crecimiento exponencial en los últimos tiempos.

3. Nanomateriales híbridos bioinorgánicos: el uso de biomoléculas como plantillas para la síntesis de nanomateriales.

En la frontera entre el mundo biológico y el inorgánico se encuentran los **materiales híbridos bioinorgánicos**, una rama dentro del campo de los biomateriales que despierta especial interés en el campo de la investigación debido a sus propiedades químicas y aplicaciones únicas.[44]

Los materiales híbridos producidos en la naturaleza tanto por plantas como por animales tienen en común que son compuestos fuertes formados a partir de componentes inorgánicos y orgánicos muy débiles como las proteínas o el carbonato cálcico. Las condiciones de síntesis en las que se forman estos materiales son condiciones de química suave tales como: temperatura ambiente, ambiente acuoso, pH neutro y además son procesos que consumen poca energía.[44] Todo esto hace que estos materiales sean muy atractivos desde el punto de vista de la síntesis química. Inspirarnos en la naturaleza imitando estos procesos de formación es, por tanto, una alternativa muy interesante para la preparación de materiales híbridos multifuncionales.

Los sistemas biológicos además presentan propiedades muy ventajosas que los hacen muy atractivos dentro del campo de la Nanotecnología. La popularidad de estos materiales se puede atribuir a la selectividad, la biocompatibilidad y la versatilidad que presentan a la hora de poder controlar su estructura.[39]

Por otro lado, los métodos de síntesis convencionales presentan en numerosas ocasiones una serie de inconvenientes, especialmente cuando se trata de escalar hasta producción industrial, como son el uso de compuestos tóxicos, la necesidad de condiciones de reacción agresivas y la generación de subproductos dañinos para el medio ambiente[45,46,47,48,49,50]. Por todo ello, lo más deseado sería poder producir estos nanomateriales

mediante métodos limpios, no tóxicos, biocompatibles y "*eco-friendly*". De esta manera, el interés en crear métodos de síntesis verde (*Green Chemistry*), respetuosos con el medio ambiente para la síntesis de nanomateriales, ha hecho que los investigadores también acudan a procesos y sistemas biológicos como fuente de inspiración.

Algunas biomoléculas como el ADN, los péptidos y las proteínas han sido y son usadas extensamente para la síntesis de nanomateriales bioinorgánicos.[51,52,53] Estos nanomateriales híbridos presentan un amplio abanico de aplicaciones en Biomedicina, ya sea como sistemas liberadores de fármacos y/o de biomagen, o como plantillas para su uso en Medicina regenerativa. Algunos ejemplos de estos biomateriales y sus aplicaciones se encuentran resumidos en la Tabla 2.

Material inorgánico	Biomolécula	Aplicaciones
Oro	ADN	Diagnóstico[54]
Oro	Proteína/enzima	Bioelectrónica
Paladio	Proteína	Biocatálisis[55]
Plata	Ligando antiamiloide	Detección Alzheimer[56]
Óxido de hierro	Proteína/péptido	MRI, terapia[57]
QD semiconductor	ADN/proteína/péptido	Sensor, liberador de fármaco[58]
Óxido de níquel	Proteína	Biocatálisis[59]
Nanotubo de carbono	ADN/proteína	Bioelectrónica y bioanálisis[60]
Nanotubo de carbono	Proteína/enzima	Liberador de fármaco[61]
QD semiconductor/óxido de hierro	Anticuerpo	MRI multimodal, imagen de fluorescencia[62]

Tabla 2. Aplicaciones de materiales híbridos bioinorgánicos.[63] Tabla tomada de: K. E. Sapsford, W. R. Algar, L. Berti, K. B. Gemmill, B. J. Casey, E. Oh, M. H. Stewart, I. L. Medintz, *Chem. Rev.* **2013**, *113*, 1904.

Aunque el desarrollo de esta Tesis se ha centrado principalmente en las posibles aplicaciones biomédicas, cabe destacar que estos materiales también poseen interés en otras áreas, pudiendo ser empleados, por ejemplo, en la conversión de energía solar, en biocatálisis, como sensores, como materiales bioelectrónicos o como materiales fotoluminiscentes, entre otros.[63]

La combinación de diferentes materiales se ha desarrollado por tanto para beneficiarse de sus diversas ventajas mientras se abordan sus propias limitaciones. Por ejemplo, las nanopartículas inorgánicas poseen propiedades ópticas y magnéticas únicas, pero carecen de propiedades mecánicas favorables y de características para la manipulación de su superficie. Por el contrario, las biomoléculas ofrecen flexibilidad con respecto a la manipulación de la química superficial y presentan propiedades mecánicas favorables.

4. Apoferritina como proteína para dirigir la síntesis de materiales híbridos bioinorgánicos

El uso de proteínas y péptidos para dirigir la síntesis de materiales inorgánicos *in vitro* es por lo tanto una consecuencia lógica de observar los procesos que ocurren en la naturaleza y en los procesos de biomineralización. Es además muy interesante por varias razones. La primera de ellas es la producción de materiales bajo condiciones de reacción que son mucho más suaves que las utilizadas en las síntesis tradicionales de materiales. La segunda ventaja es el exquisito control que las proteínas y péptidos pueden imponer en el tamaño, la forma, la química y la estructura cristalina del producto inorgánico resultante. Esto es significativo porque a menudo estas características determinan las propiedades del material sintetizado. Por otro lado, estas biomoléculas

tienen el potencial para producir materiales con funciones altamente específicas o múltiples.[64]

Un ejemplo de una proteína ampliamente empleada como plantilla para la preparación de materiales bioinorgánicos es la **ferritina**.[65] La no toxicidad, estabilidad y las importantes funciones biológicas que presenta esta proteína la convierten en un biosistema de liberación e imagen muy útil y versátil. Por otro lado, esta proteína puede ser funcionalizada mediante los residuos lisina que se encuentran en su capa externa introduciendo así una nueva propiedad física (óptica, fluorescente, etc.).[66] Como consecuencia, se pueden obtener gracias a ella una amplia librería de materiales híbridos bioinorgánicos con un amplio abanico de aplicaciones.[67]

La ferritina es la principal proteína de almacén del hierro en la mayor parte de los organismos vivos en los reinos animal, vegetal y microbiano. Su localización es básicamente intracelular y su estructura, altamente conservada, consiste en una envoltura proteica hueca de 12nm, la apoferritina, con un peso molecular aproximado de 450 kDa compuesta por 24 subunidades ensambladas en una simetría cúbica que rodea una cavidad de 8 nm de diámetro, capaz de acomodar hasta 4000 átomos de hierro como un mineral de Fe (III) tradicionalmente descrito como ferrihidrita [$Fe^{III}_{10}O_{14}(OH)_2$] (Figura 11).[65] Una vez almacenado, este hierro ferritínico sigue estando biodisponible para ser movilizado cuando la célula lo necesite.

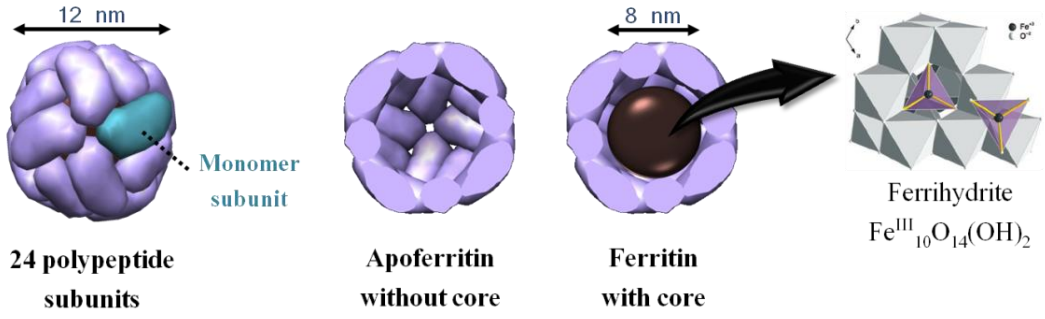

Fig . 11. Estructura de la ferritina.

Por otro lado, las 24 cadenas polipeptídicas de la envoltura proteica pueden ser clasificadas en dos tipos: las subunidades H (*heavy* o cadenas pesadas) de 183 aminoácidos y 21 kDa, y las subunidades L (*light* o ligeras) con 175 aminoácidos y 20 kDa de peso. Ambos tipos de subunidades están estrechamente relacionadas en términos de estructura primaria (54-57% de identidad en la secuencia proteica) y terciaria.[68,69] Sin embargo, estas subunidades tienen diferente funcionalidad. Las subunidades H juegan un papel crucial en la rápida detoxificación del hierro debido a que contienen el centro catalítico ferroxidasa para la rápida oxidación del Fe(II), en cambio, las subunidades L están asociadas con la nucleación, mineralización y almacén del hierro en la cavidad de la ferritina.[70]

Con el fin de explotar la ferritina como un sistema de liberación de fármacos y bioimagen, la cavidad interior ha de estar libre para acomodar el cargo. Por lo tanto, el hierro ha de ser extraído de su cavidad, dando lugar a la **apoferritina**, la cual mantiene las mismas características que la ferritina en cuanto a términos de estructura externa e interna.

La apoferritina ha sido propuesta ampliamente como un sistema liberador de fármacos para su uso en terapia.[67] Entre las moléculas que se han encapsulado en su interior se incluyen la doxorrubicina (Figura 12),[71] el cisplatino [72] o el carboplatino [73] con aplicaciones anticancerígenas.

Además, la apoferritina puede actuar como una herramienta teranóstica con doble funcionalidad que permita el uso de su cavidad para albergar diferentes moléculas terapéuticas a la vez que diversos agentes de contraste en MRI.[74] De esta manera, se han encapsulado en el interior de la proteína metales como el gadolinio,[75] el manganeso[74] o el hierro.[76] Algunas aplicaciones de la apoferritina se encuentran resumidas en la Tabla 3.

Material /fármaco	Apoferritina	Aplicaciones
Gefitinib	Recombinante	Liberador de fármaco, cáncer[77]
Doxorrubicina	H Humana Recombinante	Liberador de fármaco, cáncer[78, 71]
Daunomicina	No indicada	Liberador de fármaco, cáncer pulmón[79]
Cisplatino	H Humana Recombinante	Liberador de fármaco, melanoma[72]
Gd	Bazo de caballo	Diagnosis, MRI[75]
Óxido de Fe	H Humana Recombinante	Diagnosis, cáncer[76]
Mn	No indicada	Diagnosis, MRI, melanoma[74]
Doxorrubicina, Au	Bazo de caballo	Teranosis, cáncer próstata[80]
Glucosa oxidasa	No indicada	Diagnosis[81]

Tabla 3. Resumen de fármacos o nanopartículas inorgánicas empleadas con la apoferritina y sus aplicaciones.[67] Tabla tomada de: D. Belletti, F. Pederzoli, F. Forni, M. Vandelli, G. Tosi, B. Ruozi, *Expert. Opin. Drug Deliv.,* **2016,** *21,* 1.

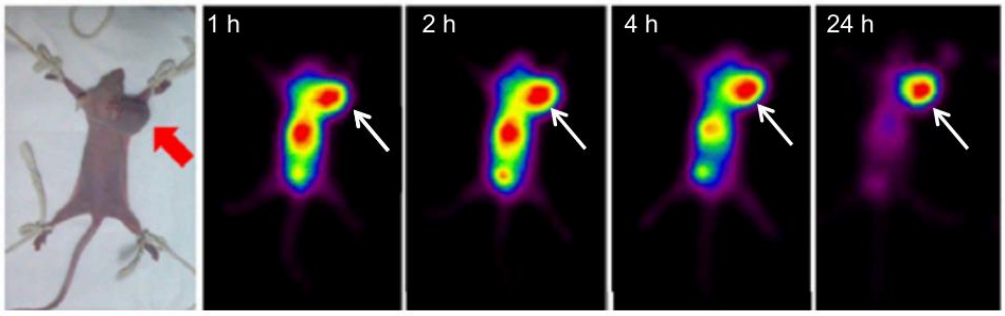

Fig. 12. La ferritina H cargada con doxorrubicina es capaz de marcar específicamente tumores *in vivo* e *in vitro.*[71] Imagen tomada de: M. Liang, K. Fan, M. Zhou, D. Duan, J. Zheng, D. Yang, J. Feng, X. Yan, *Proc. Natl. Acad. Sci. U S A*, **2014**, *111,* 4900.

Además, existen desórdenes en las funciones de la ferritina que han sido asociados con enfermedades típicamente relacionadas con el hierro, como la hemocromatosis o la anemia, pero la ferritina está también siendo cada vez más reconocida como una molécula crucial en algunas patologías neurológicas, como la enfermedad de Parkinson o el Alzheimer.[82]

Por otro lado, existen cada vez más evidencias de que los niveles de ferritina aumentan en presencia de ciertos trastornos como la inflamación, la angiogénesis o los tumores y, por lo tanto, ha generado una especial atención como biomarcador tumoral.[83] Esto se debe a que la subunidad H de la proteína es capaz de unirse específicamente al receptor de transferrina (TtR1), el cual se encuentra sobreexpresado en muchas células cancerosas (alrededor de 100 veces más con respecto a los tejidos normales).[84,85] Este hecho garantiza por tanto una unión específica de la ferritina hacia el tumor. Algunos estudios ya se han llevado a cabo usando la ferritina como un biomarcador tumoral. Por ejemplo, Matzner *et al.*[86] reportaron un aumento considerable del nivel de ferritina de suero en casos de leucemia aguda. En todos los casos, la remisión se asoció con la normalización de los niveles de ferritina. Szymendera *et al.* [87] y Volpino *et al.* [88] demostraron que la medida de los niveles de ferritina en suero es un indicador clínico muy útil en pacientes con tumores testiculares y con cáncer de pulmón, respectivamente.

Todas estas características, junto con sus propiedades únicas estructurales, convierten a la ferritina en un sistema teranóstico muy prometedor. En el transcurso de esta Tesis se ha utilizado esta proteína como biomolécula para la preparación de un agente teranóstico soluble en agua con interés en el campo biomédico.

5. Uso de fibras de tipo amiloide para la síntesis de materiales híbridos bioinorgánicos.

Tal y como se ha comentado anteriormente, el uso de biomoléculas como plantilla es un excelente método para la síntesis de materiales híbridos bioinorgánicos multifuncionales. Dentro del campo de los bionanomateriales, un ejemplo que presenta amplio interés en el ámbito biomédico son las **nanofibras**. Además del ADN, otras biomacromoléculas fibrosas lineales son candidatas excelentes para la producción de materiales híbridos bioinorgánicos unidimensionales (1D). Por ejemplo, Dujardin *et al*.[89] y Mann *et al*.[90] utilizaron el virus del mosaico del tabaco, que tiene la forma de un tubo lineal, para el montaje de diversos tipos de nanopartículas (NPs) dentro y fuera de esos tubos. Belcher *et al*.[91] emplearon un bacteriófago para obtener nanohilos orientados de CdS, ZnS y FePt. También se han obtenido nanohilos de Ag y Au mediante la deposición de soluciones de Au^{3+} y Ag^{+} sobre la superficie de levadura. Kunitake *et al.*[92, 93] prepararon diferentes tipos de estructuras 1D de metales y óxidos metálicos a partir de NPs utilizando papel de celulosa natural como plantilla.

Numerosas proteínas naturales como la tubulina, la actina, la fibrina o el colágeno se encuentran como nanoestructuras fibrosas en los organismos biológicos, cuyas propiedades únicas se relacionan con sus funciones biológicas específicas.[94] A pesar de su aparente simplicidad, estas estructuras poseen funciones muy variadas en la naturaleza, incluyendo: "andamios" para catalizadores,[95, 96, 97] medios de almacenamiento de información epigenética,[98, 99, 100, 101, 102] y como recubrimientos funcionales.[103,104]

Este tipo de auto-ensamblaje de proteína también ha conseguido desarrollar materiales proteicos artificiales con una gran variedad de

aplicaciones, que van desde la liberación lenta de péptidos terapéuticos,[105] componentes en compuestos activos,[106] sensores**¡Error! Marcador no definido.** y materiales biomiméticos funcionales.[107,108,109] Por ejemplo, Fu *et al.*[110] obtuvieron matrices dobles helicoidales mediante el ensamblaje de nanopartículas de Au y Pd en nanofibras peptídicas en diferentes condiciones de pH. La tubulina heterodimérica fue usada como una plantilla para ensamblar NPs de Pd.[111] Matsui y colaboradores[112] ensamblaron NPs de Au sobre la superficie de nanotubos de polipéptidos controlando su posición gracias a la afinidad específica de dichas secuencias.

Dentro de este contexto, las **fibras de tipo amiloide**, ya sean naturales o sintéticas, son plantillas perfectas para la producción de nanoestructuras inorgánicas 1D.[113,114,115,116] Estas formaciones monodimensionales son de relevancia ya que probablemente desempeñan un papel fundamental en la mejora de la eficiencia de diversos dispositivos electrónicos, optoelectrónicos y/o magnéticos.[117,118] Además, pueden ayudar de manera significativa en la comprensión de un número de procesos biológicos y de la mecánica cuántica fundamentales de los sistemas a escala nanométrica.[119,120]

Algunas características de estas estructuras 1D es que son estructuras rígidas con una alta fuerza mecánica, presentan una rigidez comparable a la seda de araña y al acero, su preparación a partir de proteínas disponibles es muy sencilla y se puede controlar su crecimiento con el fin de obtener una gran variedad de estructuras con diferentes propiedades físicas.[121,122,123] Una de las características más importantes es que las fibras amiloides rígidas poseen una gran variedad de grupos funcionales en su superficie que pueden ser funcionalizados fácilmente con nanoprecisión. Una última ventaja es que su diámetro es homogéneo, reproducible y fácilmente modificable.[124]

La agregación de proteínas, y en particular la formación de fibras amiloides, tiene por lo tanto un gran interés en el campo de la investigación de proteínas, ya que existe cada vez más evidencia de que las estructuras *β-sheet* (estructura en hoja beta plegada) presentes en numerosas proteínas globulares, impulsan la formación de estos agregados en forma de nanohilos o nanofibras y probablemente tienen un papel decisivo en el desarrollo de enfermedades neurodegenerativas como el Alzheimer, el Parkinson, la enfermedad de Creutzfeldt-Jakob o la enfermedad de Huntington.[125]

Estas fibras amiloides presentan además un amplio abanico de aplicaciones biomédicas relacionadas con la Medicina regenerativa, tal y como se ha explicado anteriormente. Por otro lado, también se han usado como sistemas de diagnosis y/o liberadores de fármacos.[126,127] Cabe destacar además que los materiales amiloides funcionales presentan aplicaciones en otras áreas, por ejemplo, en la conversión de energía solar o como materiales activos y de detección.[128] La Figura 13 resume algunas de las características y funciones de las fibras amiloides como materiales funcionales naturales y artificiales.

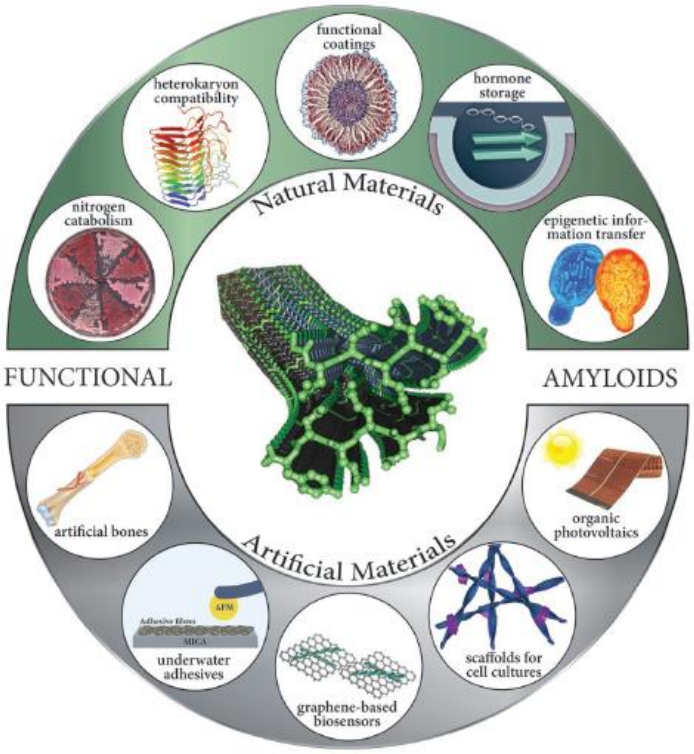

Fig. 13. Mapa de las diversas funciones de los materiales basados en fibras amiloides.[129] Imagen tomada de: T. P. J. Knowles, R. Mezzenga, *Adv. Mater.* **2016**, *28,* 6546.

Un ejemplo de fibras de tipo amiloide, utilizadas como *template* para la obtención de estrucutras 1D, es el caso de las formadas a partir de la proteína globular **β-lactoglobulina**.[130] Mezzenga *et al.* han mostrado cómo las fibras obtenidas a partir de esta proteína (Figura 14) actúan como plantillas perfectas para conducir la síntesis de diferentes materiales inorgánicos (nanotubos de carbono,[131] nanopartículas de TiO_2,[128] magnetita,[132] oro[133]) y obtener así "nanoclables" híbridos orgánicos-inorgánicos. Estas fibras de β-lactoglobulina también se han empleado como sistemas de diagnosis y terapia, ya que han servido para transportar nanopartículas metálicas en células vivas.[126]

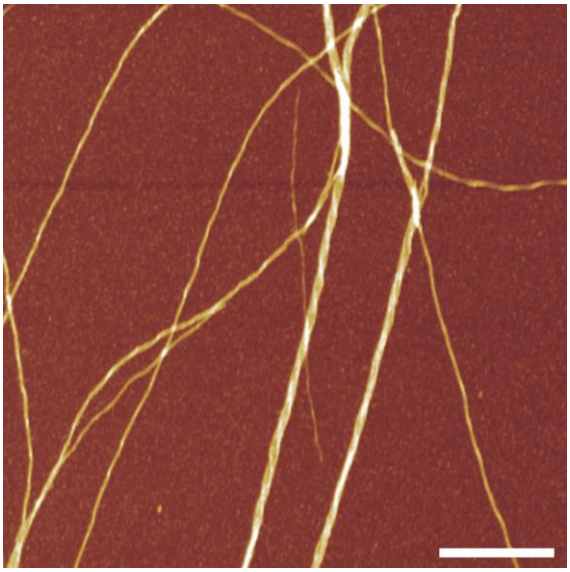

Fig. 14. Imagen AFM de fibras amiloides de β-lactoglobulina.[134] Imagen tomada de: J. Adamcik, J. Jung, J. Flakowski, P. De Los Rios, G. Dietler, R. Mezzenga, *Nat. Nanotech.*, **2010**, *5*, 423.

La β-lactoglobulina (Blg) es una proteína globular que forma parte de uno de los principales componentes del suero de leche de vaca. Se compone de 162 aminoácidos con un peso molecular de 18,4 kDa. Aunque su función hasta ahora es desconocida, la Blg tiene la capacidad de interactuar con moléculas hidrofóbicas y se cree que funciona como una proteína portadora de ácidos grasos.[130]

La proteína asume una estructura dimérica a pH neutro, pero se disocia en sus monómeros a pH ácido (Figure 15). La conformación de la proteína a pH neutro y a pH ácido ha sido determinada mediante cristalografía de Rayos X y espectroscopía RMN.[135] Las estructuras a diferentes pHs poseen la misma topología básica, teniendo nueve hojas β antiparalelas y una α-hélice corta y otra larga en la terminación carboxílica (Figura 16).[136]

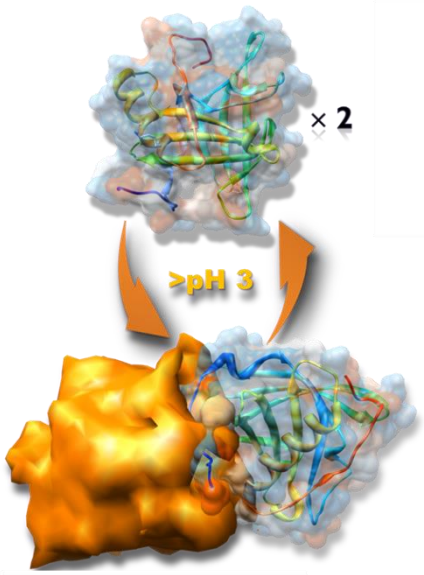

Fig. 15. Estructura de la β-lactoglobulina y su asociación/disociación en función del pH.

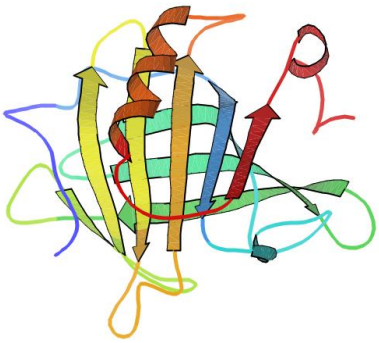

Fig. 16. Estructura de la β-lactoglobulina. Imagen de: http://www.pdb.org, entry 3BLG.

Estas fibras amiloides se han usado como modelo de proteínas fibrilares, ya que la β-lactoglobulina es una proteína robusta y se puede aislar fácilmente. Además, debido a su tendencia a formar geles bajo ciertas condiciones experimentales, es muy atractiva para su uso en la mejora de la calidad de ciertos productos alimenticios.[134]

En el trascurso de esta Tesis se utilizarán las proteínas globulares apoferritina y β-lactoglobulina para la formación de nanoestructuras fibrilares bioinorgánicas con propiedades fluorescentes, magnéticas y/u ópticas.

6. Objetivos.

El objetivo general de esta Tesis Doctoral es preparar y caracterizar un conjunto de nanomateriales híbridos bioinorgánicos multifuncionales basados en proteínas. De forma más concreta, los aspectos que pretendemos abordar son los siguientes:

1. Preparación de un nanomaterial teranóstico con aplicaciones anticancerígenas basado en nanopartículas de maghemita recubiertas por apoferritina y conteniendo doxorrubicina.

El proceso de recubrimiento de nanopartículas con péptidos/proteínas puede llevarse a cabo en presencia de una molécula terapeútica de manera que quede encapsulada junto a la nanopartícula y al recubrimiento peptídico. Este proceso ha sido demostrado por otros grupos para moléculas como doxorrubicina, heparina, Pd-porfirina, cis-platino, taxol y por el nuestro para la incorporación de deferoxamina B (DFO). Se pretende utilizar el mismo método para incorporar nanopartículas de maghemita (γ–Fe_2O_3), así como cargar una dosis significativa de doxorrubicina (DOXO, fármaco anticancerígeno ampliamente utilizado) a la proteína apoferritina. Pretendemos con este método obtener nanopartículas teranósticas (diagnosis MRI + terapia DOXO) en las que la presencia del componente magnético (maghemita) se suma a la presencia del componente DOXO, lo cual permite efectos sinérgicos terapéuticos.

2. Preparación de proteínas fibrilares de β-lactoglobulina y apoferritina.

El segundo objetivo consiste en preparar nanofibras a partir de las proteínas globulares apoferritina y β-lactoglobulina como modelos de la formación de estructuras fibrilares de tipo beta-amiloide. La motivación en estudiar la formación de fibras amiloides de apoferritina es doble: por un lado, la fibrilación de apoferritina, una proteína que juega un papel central en un contexto neuronal, podría tener un impacto en el entendimiento de las enfermedades neuronales relacionadas con la formación de estructuras amiloides. Por otro lado, su interés también se enfoca en la posibilidad de diseñar e integrar diferentes propiedades físicas en las fibras, proporcionando la oportunidad de crear materiales funcionales con propiedades nuevas y/o mejoradas.

Se pretende formar y emplear las fibras amiloides de β-lactoglobulina como modelo de proteínas fibrilares, ya que es una proteína ampliamente estudiada en la literatura.

3. Optimización y estudio de la cinética de formación de proteínas fibrilares de apoferritina y caracterización estructural de las mismas.

Se pretende optimizar el método químico de formación de nanofibras de apoferritina así como estudiar el proceso de formación de estas estructuras fibrilares comparándolo con el proceso de formación de fibras de tipo amiloide.

Se estudiará cómo diferentes parámetros experimentales de síntesis como la concentración, el pH, la temperatura o el tiempo de incubación pueden afectar a la formación y estructura final de las fibras.

Para la caracterización estructural se pretende llevar a cabo un estudio de la cinética de formación de las fibras a diferentes tiempos

durante su proceso de formación. Para ello se estudiarán las diferentes alícuotas recogidas mediante diferentes técnicas: Microscopía de Fuerza Atómica (AFM), Microscopía Electrónica de Transmisión (TEM), Dispersión Dinámica de Luz (DLS), Dicroísmo Circular (CD) o electroforesis SDS-PAGE, entre otras. De esta manera se pretende resolver e identificar los diferentes estadíos individuales del proceso de fibrilación, incluyendo la formación de protofilamentos, su agregación en fibras maduras y el desarrollo de un giro periódico a lo largo de su contorno longitudinal.

4. Preparación de proteínas fibrilares a partir de apoferritina formada por subunidades H y apoferritina formada por subunidades L y estudio de su quiralidad.

En células eucariotas la apoferritina está compuesta por 24 subunidades ensambladas que se clasifican en dos tipos: las subunidades H y las subunidades L. El ensamblaje de estas subunidades puede producir diversas ferritinas (isoferritinas) cuyo radio H:L está genéticamente controlado dependiendo del tejido. Cualquier modificación en este radio H:L o cualquier mutación en la subunidad H o L está de hecho relacionado con el origen de una patología. Por ejemplo, se ha reportado que los niveles de ferritina y de Fe(III) almacenado se ven alterados en enfermedades como el Parkinson, el Alzheimer o el síndrome de inmunodeficiencia adquirida (SIDA). Se pretende preparar fibras a partir de las proteínas recombinantes humanas de apoferritina L y H (que contienen 100% subunidades L y 100% subunidades H, respectivamente) y compararlas con las fibras formadas a partir de ferritina de bazo de caballo (ferritina usualmente utilizada como modelo). Una vez formadas, el siguiente objetivo será caracterizar química y estructuralmente ambos tipos de fibras.

5. Preparación de proteínas fibrilares fluorescentes de β-lactoglobulina y apoferritina para obtener nanoestructuras multifuncionales.

Se pretende preparar nanofibras fluorescentes unidimensionales (1D) usando tanto la proteína β-lactoglobulina como la apoferritina como plantillas para la creación de materiales híbridos bioinorgánicos. Además, nuestro objetivo es comprobar si la proteína apoferritina en su forma fibrilar es capaz de mantener su capacidad para ser funcionalizada.

De esta manera se pretenden preparar nanofibras fluorescentes 1D con diversas emisiones fluorescentes mediante la incorporación de diferentes fluoróforos de tipo *Alexa fluor* (AF), ATTOS o *quantum dots* (QDs).

Por otro lado se pretende estudiar estudiar el fenómeno de transferencia de energía fluorescente conocido como FRET (*fluorescence resonance energy transfer*). La eficiencia de dicho proceso de FRET para estas estructuras se estudiará mediante la técnica FLIM-PIE (*Fluorescence lifetime imaging microscopy with pulsed interleaved excitation*), muy utilizada en el estudio y caracterización estructural de proteínas. Dicha funcionalización nos permitirá, por tanto, una mejor comprensión del proceso de formación de estructuras tipo amiloide.

Se llevará a cabo un análisis exhaustivo de estas estructuras mediante el sistema dual AFM + microscopía de fluorescencia de súper-resolución, así como mediante diferentes técnicas como TEM, AFM, HAADF-STEM (*High-angle annular dark-field - scanning transmission electron microscopy*) o EDX (*Energy Dispersive X-Ray Analysis)*, entre otras.

6. Preparación de proteínas fibrilares de β-lactoglobulina y apoferritina que incorporen nanopartículas metálicas.

Por último, se propone incorporar diferentes nanopartículas inorgánicas metálicas a las fibras amiloides que confieran diferentes propiedades y aplicaciones al material final resultante. En concreto, se pretenden incorporar nanopartículas magnéticas de tipo maghemita, así como nanopartículas de oro de diferentes formas y tamaños. Estas nanopartículas serán formadas previamente mediante métodos de síntesis conocidos.

Por otro lado, también se pretende estudiar la capacidad de estas fibras para producir nanopartículas metálicas mediante la reducción de diferentes sales de paladio, plata y oro.

En general, con este objetivo tratamos de mostrar la naturaleza versátil que presentan estas plantillas proteicas unidimensionales y su gran potencial para desarrollar materiales híbridos multifuncionales.

7. Referencias

[1] K. Eric Drexler at <http://edrexler.com/d/06/00/EOC/EOC_Table_of_Contents.html>

[2] A. Wicki, D. Witzigmannb, V. Balasubramanianc, J. Huwylerb, *J. Control. Release,* **2015**, *200*, 138.

[3] G. Chen, I. Roy, C. Yang and P. N. Prasad, *Chem. Rev.,* **2016**, *116*, 2826.

[4] K. Riehemann, S. W. Schneider, T. A. Luger, B. Godin, M. Ferrari, H. Fuchs, *Angew. Chem. Int. Ed.,* **2009**, *48*, 872.

[5] R. Weissleder, G. Elizondo, J. Wittenberg, C.A. Rabito, H.H. Bengele, L. Josephson, *Radiology,* **1990**, *175*, 489.

[6] H. Kobayashi, Y. Hama, Y. Koyama, T. Barrett, C.A.S. Regino, Y. Urano, P.L. Choyke, *Nano Lett.,* **2007**, *7*, 1711.

[7] L. Yan , Y. Yang , W. Zhang , X. Chen, *Adv. Mater.,* **2014**, *26*, 5533.

[8] S.R. Deka, A. Quarta, R.D. Corato, A. Riedinger, R. Cingolani, T. Pellegrino, *Nanoscale*, **2011**, *3*, 619.

[9] C. Yang, W. Guo, L. Cui, N. An, T. Zhang, H. Lin, F. Qu, *Langmuir,* **2014**, *30,* 9819.

[10] D. Kim, E.S. Lee, K.T. Oh, Z.G. Gao, Y.H. Bae, *Small*, **2008**, *4*, 2043.

[11] L.A. Guzman, V. Labhasetwar, C. Song, Y. Jang, A.M. Lincoff, R. Levy, E.J. Topol, *Circulation,* **1996**, *94*, 1441.

[12] C.C. Lee, E.R. Gillies, M.E. Fox, S.J. Guillaudeu, J.M.J. Fréchet, E.E. Dy, F.C. Szoka, *PNAS,* **2006**, *103*, 16649

[13] Y. Tian, X. Jiang, X. Chen, Z. Shao, W. Yang, *Adv. Mater.,* **2014**, *26,* 7393.

[14] O. Farokhzad, R. Langer, *Adv. Drug Delivery Rev*., **2006**, 58, 1456.

[15] N. A. Peppas, *Smart Polym*. *Appl. Biotechnol. Biomed.,* **2007**, 331.

[16] M. E. Davis, *Nat. Rev. Drug Discovery,* **2008**, 7, 771.

[17] G. Wang, H. Uludag, *Expert Opin. Drug Delivery,* **2008**, 5, 499.

[18] C. Li, S. Wallace, *Adv. Drug Delivery Rev,.* **2008**, 60, 886.

[19] D. W. Northfelt, B. J. Dezube, J. A. Thommes, B. J. Miller, M. A. Fischl, A. Friedman-Kien, L. D. Kaplan, C. Du Mond, R. D. Mamelok, D. H. Henry, *J. Clin. Oncol*., **1998**, 16, 2445.

[20] M. R. Green, G. M. Manikhas, S. Orlov, B. Afanasyev, A. M. Makhson, P. Bhar, M. J. Hawkins, *Ann. Oncol.*, **2006**, 17, 1263.

[21] Y. Min, J. M. Caster, M. J. Eblan, A. Z. Wang, *Chem. Rev.,* **2015***, 115*, 11147.

[22] A. J. Cole, V. C. Yang, A.E. David, *Trends in Biotechnology*, **2011**, *29*, 7.

[23] A. K. Iyer, G. Khaled, J. Fang, H. Maeda, *Drug Discovery Today*, **2006,** *11*, 1718.

[24] A. Sulistio, J. Lowenthal, A. Blencowe, M. N. Bongiovanni, L. Ong, S. L. Gras, X. Zhang, G. G. Qiao, *Biomacromolecules,* **2011***, 12*, 3469.

[25] S.R. Popielarski, S.H. Pun, M.E. Davis, *Bioconjug. Chem*., **2015**, *16*, 1063.

[26] X. Wu, J. Chen, M. Wu, J. X. Zhao, *Theranostics*, **2015**, *5*, 322.

[27] X. Huang, X. Peng, Y. Wang, Y. Wang, D. M. Shin, M. A. El-Sayed, S. Nie, *ACS Nano.,* **2010***, 4*, 5887.

[28] X. Montet, M. Funovics, K. Montet-Abou, R. Weissleder, L. Josephson, *J. Med. Chem.,* **2006,** *49*, 6087.

[29] C. Mamot, R. Ritschard, A. Wicki, W. Küng, J. Schuller, R. Herrmann, C. Rochlitz , *J. Drug Target.,* 2012, *20,* 422.

[30] K. Lee, T. Kim, S. Paik, S. Haam, Y. Huh, K. Lee, *Chem. Rev.,* **2015**, *115,* 327.

[31] Z. Zhang, L. Wang, J. Wang, X. Jiang, X. Li, Z. Hu, Y. Ji, X. Wu, C. Chen, *Adv. Mater.,* **2012**, *24*, 1418.

[32] J. Pan, Y. Liu, S.S. Feng, *Nanomedicine*, **2010**, *5*, 347.

[33] L.L. Ma, J.O. Tam, B.W. Willsey, D. Rigdon, R. Ramesh, K. Sokolov, K.P. Johnston, *Langmuir,* **2011***, 27*, 7681.

[34] M. Dobrovolskaia, S. McNeil. *Nat. Nanotechnol.,* **2007**, 2, 469.

[35] S. Mitragotri, J. Lahann, *Nat. Mater.,* **2009**, 8, 15.

[36] S. M. Moghimi, A. C. Hunter, J. C. Murray, *Pharmacol. Rev.*, **2001**, 53, 283.

[37] S. Pina, J.M. Oliveira, R.L. Reis, *Adv. Mater.,* **2015**, *27,* 1143.

[38] P. Bajaj, R. M. Schweller, A. Khademhosseini, J. L. West, R. Bashir, *Annual Review of Biomedical Engineering*, **2014**, *16,* 247.

[39] L.L. Hench, J.M. Polar, *Science*, 2002, *295*, 1014.

[40] M. H.Murdock, S. F.Badylak, *Curr. Op. Biomed. Eng.,* **2017**, *1,* 4.

[41] G. A. Silva, C. Czeisler, K. L. Niece, E. Beniash, D. A.Harrington, J. A. Kessler, S. I. Stupp, *Science,* **2004**, *303*, 1352.

[42] V. M. Tysseling-Mattiace, V. Sahni, K. L. Niece, D. Birch, C. Czeisler, M. G. Fehlings, S. I. Stupp, J. A. Kessler, *J. Neurosci*., **2008**, *28*, 3814.

[43] K. Rajangam, H. A. Behanna, M. J. Hui, X. Han, J. F. Hulvat, J. W. Lomasney, S. I. Stupp, *Nano Lett.,* **2006**, *6*, 2086.

[44] M. Darder, P. Aranda, E. Ruiz-Hitzky, *Adv. Mat.,***2007**, *19,* 1309.

[45] V. Bansal, R. Ramanathan, S.K. Bhargava, *Aust. J. Chem.,* **2011**, *64,* 279.

[46] R.Y. Parikh et al., *PLoS One,* **2011,** *6***,** e21401.

[47] R.Y. Parikh, S. Singh, B. L. V. Prasad, M. S. Patole, M. Sastry, Y. S. Shouche, *Chem. Bio. Chem.,* **2008**, 9, 1415.

[48] R. Ramanathan, J.L. Campbell, S.K. Soni, S. K. Bhargava, V. Bansal, *PLoS One,* **2011,** 6.

[49] C.M. Niemeyer, C.A. Mirkin, (eds) (**2004**) Front Matter, in Nanobiotechnology: Concepts, Applications and Perspectives, Wiley-VCH Verlag GmbH & Co. KGaA, Weinheim, FRG. doi: 10.1002/3527602453.fmatter

[50] R. Ramanathan, A.P. O'Mullane, R.Y. Parikh, P.M. Smooker, S.K. Bhargava, V. Bansal, *Langmuir,* **2011**, 27**,** 714.

[51] M.G. Warner, J.E. Hutchison, *Nature Materials,* **2003**, *2*, 272.

[52] E. Gazit, *Chem. Soc. Rev.,* **2007**, *36*, 1263.

[53] L.C. Palmer, S.I. Stupp, *Acc. Chem. Res.,* **2008**, *41*, 1674.

[54] E. Katz, I. Willner, *Angew. Chem., Int. Ed.* **2004***, 43*, 6042.

[55] T. Ueno, M. Suzuki, T. Goto, T. Matsumoto, K. Nagayama, Y. Watanabe, *Angew. Chem., Int. Ed.,* **2004***, 43*, 2527.

[56] V. Biju, T. Itoh, A. Anas, A. Sujith, M. Ishikawa, *Anal. Bioanal. Chem.,* **2008***, 391,* 2469.

[57] J.W. Seo, H. Chung, M.Y. Kim, J. Lee, I.H. Choi, J. Cheon, *Small,* **2007***, 3*, 850.

[58] I. Medintz, H. Uyeda, E. Goldman, H. Mattoussi, *Nat. Mater.,* **2005***, 4*, 435.

[59] A.B. Moghaddam, M.R. Ganjali, R. Dinarvand, S. Ahadi, A.A. Saboury, *Biophys. Chem.,* **2008***, 134*, 25.

[60] S.N. Kim, J.F. Rusling, F. Papadimitrakopoulos, *Adv. Mater.,* **2007***, 19*, 3214.

[61] P. Asuri, S.S. Bale, R.C. Pangule, D.A. Shah, R.S. Kane, J.S. Dordick, *Langmuir* **2007***, 23,* 12318.

[62] W.J.M. Mulder, G.J. Strijkers, K.C. Briley-Saboe, J.C. Frias, J.G.S. Aguinaldo, E. Vucic, V. Amirbekian, C. Tang, P.T.K. Chin, K. Nicolay, Z.A. Fayad, *Magn. Reson. Med.,* **2007***,* 58, 1164.

[63] K. E. Sapsford, W. R. Algar, L. Berti, K. B. Gemmill, B. J. Casey, E. Oh, M. H. Stewart and I. L. Medintz, *Chem. Rev.,* **2013**, *113*, 1904.

[64] A. MaHam, Z. Tang, H. Wu, J. Wang, Y.Lin*, Small,* **2009***, 5*, 1706.

[65] N. D. Chasteen, P. M. Harrison, *J. Struct. Biol.*, **1999**, *126*, 182.

[66] B. Fernandez, N. Galvez, R. Cuesta, A.B. Hungrıa, J.J. Calvino J.M. Domınguez-Vera., *Adv. Funct. Mater.,* **2008**, *18*, 3931.

[67] D. Belletti, F. Pederzoli, F. Forni, M. Vandelli, G. Tosi and B. Ruozi, *Expert. Opin. Drug. Deliv.,* **2016,** *21,* 1.

[68] S. Levi, S.J. Yewdall, P.M. Harrison, P. Santambrogio, A. Cozzi, E. Rovida, A. Albertini, P. Arosio, *Biochem. J.,* **1992***, 288*, 591.

[69] P.D. Hempstead, S.J. Yewdall, A.R. Fernie, D.M. Lawson, P.J. Artymiuk, D.W. Rice, G.C. Ford, P.M. Harrison, *J. Mol. Biol*., **1997**, *268*, 424.

[70] E. C. Theil, *Curr. Opin. Struct. Biol*., **2011**, *15*, 304.

[71] M. Liang, K. Fan, M. Zhou, D. Duan, J. Zheng, D. Yang, J. Feng, X. Yan, *Proc. Natl. Acad. Sci. U S A*, **2014**, *111,* 4900.

[72] E. Falvo, E. Tremante, R. Fraioli, C. Leonetti, C. Zamparelli, A. Boffi, V. Morea, P. Ceci, P. Giacomini, *Nanoscale*, **2013**, *5*, 12278.

[73] Y. Yang, X. Wang, H. Diao H, J. Zhang, H. Li, H. Sun, Z. Guo, *Chem. Commun.,* **2007**, *7*, 3453.

[74] I. Szabó, S.G. Crich, D. Alberti, F. K. Kálmán, S. Aime, *Chem. Commun.,* **2012**, *48*, 2436.

[75] P. Sánchez, E. Valero, N. Gálvez, J.M. Domínguez-Vera, M. Marinone, G. Poletti, M. Corti, A. Lascialfari, *Dalton Trans*., **2009**, *7*, 800.

[76] X. Li, L.H. Qiu, P. Zhu, X. Tao, T. Imanaka, J. Zhao, Y. Huang, Y. Tu, X. Cao, *Small.* **2012**, *8*, 2505.

[77] A.I. Kuruppu, L. Zhang, H. Collins, L. Turyanska, N.R. Thomas, T.D. Bradshaw, *Adv. Healthc. Mater*., **2015**, *4*, 2816.

[78] L. Zhang, L. Li, A. Di Penta, U. Carmona, F. Yang, R. Schöps, M. Brandsch, J.L. Zugaza, M. Knez, *Adv. Healthc. Mater.,* **2015**, *4*, 1305.

[79] Y. Luo, X. Wang, D. Du, *Biomater Sci.,* **2015**, *3*, 1386.

[80] S. Dostalova, T. Cerna, D. Hynek, Z. Koudelkova, T. Vaculovic, P.Kopel, J. Hrabeta, Z. Heger, M. Vaculovicova, T. Eckschlager, M. StiborovA, V. Adam, *ACS Appl. Mater. Interfaces*, **2016**, *8*, 14430.

[81] L. Zhang, L. Li, A. Di Penta, U. Carmona, F. Yang, R. Schöps, M. Brandsch, J.L. Zugaza, M. Knez, *Adv. Healthc. Mater.,* **2015**, *4*, 1305.

[82] D. Berg, G. Beceker, P. Riederer, O. Rieb., *Neurotox. Res*., **2002**, *4*, 637.

[83] K. Fan, L. Gao, X. Yan, *Wiley Interdiscip. Rev. Nanomed. Nanobiotechnol.,* **2013**, *5,* 287.

[84] T.R. Daniels, T. Delgado J.A. Rodriguez, G. Helguera, M.L. Penichet, *Clin. Immunol.,* **2006**, *121,* 144.

[85] M.S. Bretscher, J.N. Thomson, *Embo J.,* **1983**, *2*, 599.

[86] Y. Matzner, A.M. Konijn, C. Hershko, *Am. J. Hematol.,* **1980**, *9*, 13.

[87] J.J. Szymendera, I. Kozlowiczgudzinska, G. Madej, L. Sikorowa, J.A. Kaminska, M. Kowalska, *Oncology,* **1985**, *42,* 253.

[88] P. Volpino, V. Cangemi, V. Caputo, E. Mazzarino, G. Galati, *J. Nucl. Med. Allied. Sci.*, **1984**, *28*, 27.

[89] E. Dujardin, C. Peet, G. Stubbs, J. N. Culver, S. Mann., *Nano Lett.,* **2003**, *3*, 13.

[90] C. E. Fowler, W. Shenton, G. Stubbs, S. Mann., *Adv. Mater.*, **2001**, *13*, 1266.

[91] C. Mao, C. E. Flynn, A. Hayhurst, R. Sweeney, J. Qi, G. Georgious B. Iverson, A. M. Belcher, *Proc. Natl. Acad. Sci. USA,* **2003**, *100*, 6946.

[92] J. He, T. Kunitake, A. Nakao, *Chem. Mater.,* **2003**, *15*, 4401.

[93] J. Huang, T. Kunitake, S. Y. Onoue, *Chem. Commu.,* **2004**, 1008.

[94] H.Y. Kueh, T.J. Mitchison, *Science,* **2009**, *325*, 960.

[95] D. M. Fowler, A. V. Koulov, W. E. Balch, J. W. Kelly, *Trends Biochem. Sci.,* **2007**, *32*, 217.

[96] J. W. Kelly, W. E. Balch, *J. Cell Biol.,* **2003**, *161*, 461.

[97] D. M. Fowler, A. V. Koulov, C. Alory-Jost, M. S. Marks, W. E. Balch, J. W. Kelly, *PLoS Biol.,* **2006**, *4*, e6.

[98] R. Krishnan, S. L. Lindquist, *Nature,* **2005**, *435*, 765.

[99] S. L. Lindquist, S. Henikoff, *Proc. Natl. Acad. Sci. USA,* **2002**, *99*Suppl 4, 16377.

[100] J. Shorter, S. Lindquist, *Nat. Rev. Genet.,* **2005**, *6*, 435.

[101] M. Tanaka, S. R. Collins, B. H. Toyama, J. S. Weissman, *Nature,* **2006**, *442*, 585.

[102] A. H. DePace, J. S. Weissman, *Nat. Struct. Biol.,* **2002**, *9*, 389.

[103] M. R. Chapman, L. S. Robinson, J. S. Pinkner, R. Roth, J. Heuser, M. Hammar, S. Normark, S. J. Hultgren, *Science,* **2002**, *295*, 851.

[104] D. Otzen, P. H. Nielsen, *Cell. Mol. Life Sci.,* **2008**, *65*, 910.

[105] S. K. Maji, D. Schubert, C. Rivier, S. Lee, J. E. Rivier, R. Riek, *PLoS Biol.,* **2008**, *6*, e17.

[106] C. X. Li, J. Adamcik, R. Mezzenga, *Nat. Nanotechnol.,* **2012**, *7*, 421.

[107] S. L. Gras, A. K. Tickler, A. M. Squires, G. L. Devlin, M. A. Horton, C. M. Dobson, C. E. MacPhee, *Biomaterials,* **2008**, *29*, 1553.

[108] C. X. Li, A. K. Born, T. Schweizer, M. Zenobi-Wong, M. Cerruti, R. Mezzenga, *Adv. Mater.,* **2014**, *26*, 3207.

[109] R. S. Jacob, D. Ghosh, P. K. Singh, S. K. Basu, N. N. Jha, S. Das, P. K. Sukul, S. Patil, S. Sathaye, A. Kumar, A. Chowdhury, S. Malik, S. Sen, S. K. Maji, *Biomaterials,* **2015**, *54*, 97.

[110] X. Fu, Y. Wang, L. Huang, Y. Sha, L. Gui, L. Lai, Y. Tang, *Adv. Mater.,* **2003**, *15*, 902.

[111] S. Behrens, K. Rahn, W. Habicht, K. J. Bohm, H. Rosner, E. Dinjus, E. Unger, *Adv. Mater.,* **2002**, *14*, 1621.

[112] I. A. Banerjee, L. Yu, H. Matsui, *Nano Lett.,* **2003**, *3*, 283.

[113] X. Zan, S. Feng, E. Balizan, Y. Lin and Q. Wang, *ACS Nano,* **2013***, 7*, 8385.

[114] A. K. Nair, A. Gautieri, S. W. Chang and M. J. Buehler, *Nat. Commun.,* **2013***, 4*, 1724.

[115] A. Seidel, O. Liivak, S. Calve, J. Adaska, G. Ji, Z. Yang, D. Grubb, D. B. Zax and L. W. Jelinski, *Macromolecules,* **2000***, 33*, 775.

[116] S. Keten, Z. Xu, B. Ihle and M. J. Buehler, *Nat. Mater.,* **2010***, 9*, 359.

[117] S.A. Maier, M.L. Brongersma, P.G. Kik, S. Meltzer, A.A.G. Requicha, H.A. Atwater, *Adv. Mater.,* **2001**, *13*, 1501.

[118] S.A. Maier, P.G. Kik, H.A. Atwater, S. Meltzer, E. Harel, B.E. Koel, A.A.G. Requicha, *Nat. Mater.,* **2003**, *2*, 229.

[119] M.M. Walker, T.E. Dennis, J.L. Kirschvink, *Curr. Opin. Neurobiol.,* **2002**, *12*, 735.

[120] P. Alivisatos, *Nat. Biotechnol.,* **2004**, *22*, 47.

[121] Z. Xu, R. Paparcone, M. J. Buehler, *Biophys. J.,* **2010***, 98*, 2053.

[122] C. Li, A. K. Born, T. Schweizer, M. Zenobi-Wong, M. Cerruti ,R. Mezzenga, *Adv. Mater.,* **2014,** *26*, 3207.

[123] S. J. Eichhorn, A. Dufresne, M. Aranguren, N. E. Marcovich, J. R. Capadona, S. J. Rowan, C. Weder, W. Thielemans, M. Roman, S. Renneckar, W. Gindl, S. Veigel, J. Keckes, H. Yano, K. Abe, M. Nogi, A. N. Nakagaito, A. Mangalam,
J. Simonsen, A. S. Benight, A. Bismarck, L. A. Berglund, T. Peijs*, J. Mater. Sci.,* **2010***, 45*, 1.

[124] T. Nicolai, D. Durand, *Curr. Opin. Colloid Interface Sci.,* **2013***, 18*, 249.

[125] C.A. Ross, M.A. Poirier, *Nat Med.,* **2004***, 10*, S10.

[126] S. Bolisetty, C. S. Boddupalli, S. Handschin, K. Chaitanya, J. Adamcik, Y. Saito, M. G. Manz, R. Mezzenga, *Biomacromolecules,* **2014***, 15,* 2793.

[127] S.K. Maji, D. Schubert, C. Rivier, S. Lee, J.E. Rivier, R. Riek, *PLoS Biol6,* **2008,** 2, e17.

[128] S. Bolisetty, J. Adamcik, J. Heier, R. Mezzenga, *Adv. Funct. Mater*., **2012**, *22*, 3424.

[129] T.P.J. Knowles, R. Mezzenga, *Adv. Mater.,* **2016**, *28,* 6546.

[130] D. Hamada, C.M. Dobson, *Protein Sci.,* **2002**, *11*, 2417.

[131] C.Li, R. Mezzenga, *Nanoscale*, **2013**, *5*, 6207.

[132] S. Bolisetty, J.J. Vallooran, J. Adamcik, R. Mezzenga, *ACS Nano,* **2013**, *7*, 6146.

[133] S. Bolisetty, J.J. Vallooran, J. Adamcik, S. Handschin, F. Gramm, R. Mezzenga, *J. Colloid Interface Sci.,* **2011**, *361*, 90.

[134] J.Adamcik, J. Jung, J. Flakowski, P. De Los Rios, G. Dietler, R. Mezzenga, *Nat. Nanotech.*, **2010**, *5*, 423.

[135] S. Uhrinova, M. H. Smith, G. B. Jameson, D. Uhrin, L. Sawyer, P. N. Barlow, *Biochemistry,* **2000**, *39*, 3565.

[136] http://www.pdb.org, entry 3BLG.

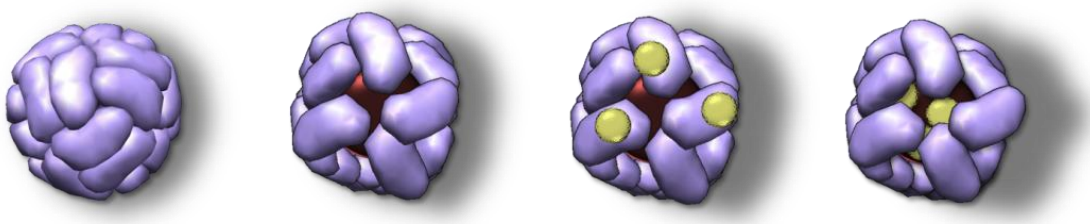

CHAPTER 2. APOMAGHEMITE AS A DOXORUBICIN CARRIER FOR ANTICANCER DRUG DELIVERY

1. Introduction.

Cancer is one of the leading causes of mortality worldwide. For this reason, tremendous efforts in biomedical research have been devoted to clinical therapy and anticancer drug new formulations.[1,2] Nevertheless, most chemotherapeutics have in common nonspecific tissue biodistribution and drug resistance, so that high doses are needed to increase selectivity. To get over these problems, nanoparticle-mediated drug delivery has emerged as a promising therapeutic methodology for the treatment of cancer.[1,2,3,4] In this regard, multifunctional nanoparticles, including nanocomposite,[5] liposomes,[6] dendrimers,[7] polymers,[8] micelles,[9] ceramics,[10] viruses[11] and protein capsids,[12] have been employed as nanocarriers for drug delivery (Figure 1). These nanoplatforms could allow decreasing the dose to the patient (high drug loadings in a small container) and control release, so that succeeding the problems of drug selectivity.[13]

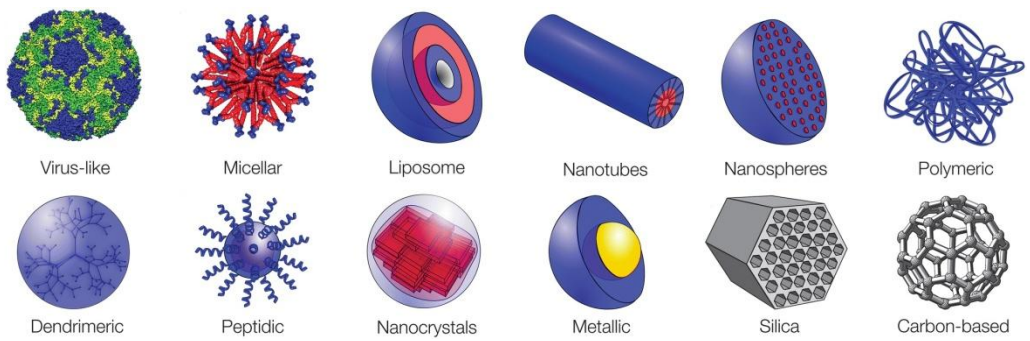

Fig. 1. Schematic representation of different types of nanoparticles employed as nanocarriers for drug deliver.[14] Image from: Braddock, M. (Ed.). (**2016**). *Nanomedicines: Design, Delivery and Detection*. Royal Society of Chemistry.

Doxorubicin (DOX) (Figure 2) is a well-known anthracycline antibiotic which has shown great efficacy against a range of tumors such as breast cancer, Kaposi sarcoma and ovarian cancer. However, this widely used anti-tumor drug is also associated with several common drawbacks,

such as poor selectivity and high cardiotoxicities, a fact that limits its therapeutic applications. Therefore, it is crucial to develop novel DOX-targeted and delivery systems to optimize efficiency and minimize toxicity.11[11]

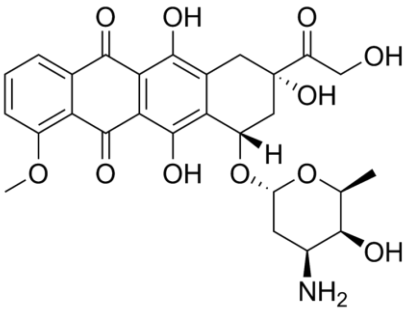

Fig. 2. Doxorubicin molecule.

Theranostic Nanomedicine is emerging as a promising therapeutic strategy. It takes advantage of the high capacity of nanoplatforms to carry cargo and loads onto them both imaging and therapeutic agents. The resulting nanosystems, capable of simultaneous diagnosis and drug delivery are expected to play a significant role in the era of personalized Medicine.[15]

In contrast to the development and use of separate materials for diagnosis and therapy, theranostics combine these two objectives into one "probe", which has the potential to overcome undesirable differences in biodistribution and selectivity that currently exist between distinct imaging and therapeutic agents.[15]

Even though a wide variety of nanostructures has been shown efficient to host, carry and release drugs in vitro, an in vivo evaluation of biodistribution of these nanocarriers is necessary, which can be performed by a non-invasive technique as magnetic resonance imaging (MRI). This technique is based on the magnetic resonance of body tissue protons

(water, membranes, lipids, proteins, etc.) and is currently one of the most powerful methods of diagnosis as the basic technique is already well-introduced and can be applied repeatedly as it does not use ionizing radiation.

Nanoparticles can be used within the human body as contrast agents in magnetic resonance imaging. These particles enhance the resolution and sensitivity dramatically while enabling earlier diagnosis. MRI imaging agents can be separated into two classes, paramagnetic molecular complexes derived from, for example Gd (III), or superparamagnetic iron oxide nanoparticles as Fe_3O_4.

On account of this, Superparamagnetic Iron Oxide (SPIOs) and USPIOs (Ultrasmall Superparamagnetic Iron Oxide) coated with different biocompatible polymers have been extensively studied as MRI contrast agents. They are specifically uptake by the monocyte–macrophage system, and therefore they are good candidates to be MRI probes for tissues with high macrophage phagocytic activity, such as liver or spleen. [16,17,18] In this sense, design and preparation of MRI diagnostic agents capable of exhibiting long-term activity is a very important step in expansion of their applications in Medicine. These long-term agents could overcome two crucial issues: the difficulty of conducting time-dependent imaging studies, due to the rapid clearance from intravascular and interstitial space,[19,20,21] and the administration of high and repeated doses. Development of long-term MRI probes could allow first the diagnosis of a pathology and then the monitoring of therapeutic efficiency without an additional injection. In this way, magnetite and/or maghemite (Fe_3O_4/γ–Fe_2O_3) nanoparticles have been extensively used as a paradigmatic magnetic material for MRI in the biomedical field.

Maghemite is a reddish-brown mixed oxide of Fe(II) and Fe(III) and it is the oxidized form of magnetite. Magnetite has an inverse spinel structure with oxygen forming a face-centered cubic (FCC) unit cell slightly distorted. In magnetite, octahedral sites (B) are occupied by Fe (II) and the half of Fe(III) and tetrahedral sites (A) are occupied by the other half of Fe(III). Only half of the octahedral sites and 1/8 of the tetrahedral sites are occupied. The unit cell contains 8 units $(Fe^{III})_A$ $(Fe^{III}Fe^{II})_BO_4$. The symmetry group is Fd3m. Maghemite differs from magnetite in that all or most of the iron is in the trivalent state (Fe(III)) and by the presence of cation vacancies in the octahedral sites $(Fe^{III})_A(Fe^{III}_{5/3}\square_{1/3})_BO_4$, where □ represents a vacancy (Figure 3). As a consequence, maghemite has a slightly smaller cubic unit cell due to the smaller size of Fe(III) cations. Therefore, maghemite density is slightly lighter (ρ=4870kg/m^3) than magnetite (ρ=5180kg/m^3).

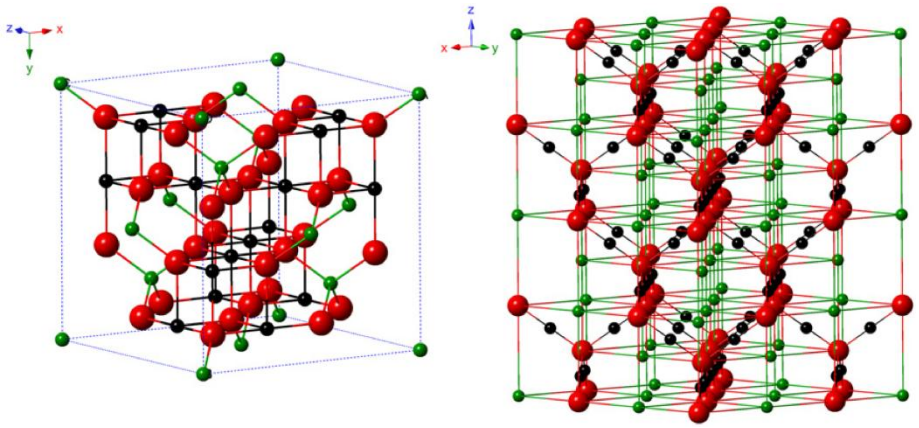

Fig. 3. Magnetite (left) and maghemite (right) structures.[22] Image from: W. Wu, Z. Wu, T. Yu, C. Jiang, W. Kim, *Sci. Technol. Adv. Mater.,* **2015**, *16*, 023501.

This first generation of SPIO/USPIOs may contain, in addition to the magnetic core, a second active specie: either for a second type of diagnosis or in therapy, giving bimodal and theranostic nanoparticles, respectively. One strategy to address this issue involves the simultaneous incorporation

of magnetic nanoparticles and the drug in the same nanocarrier, so obtaining the so-called theranostic agent. [23,24,25,26,27]

As described previously, ferritin is a spherical protein shell composed of 24 subunits surrounding an aqueous cavity with a diameter of about 8 nm, which is filled with a ferric oxohydroxy core. Aiming to exploit ferritin as a theranostic agent, the inner cavity should be free and able to accommodate the cargo, thus the resident iron has to be removed from the cavity producing apoferritin, which maintains the same features of ferritin in terms of inner and outer structure. This hollow protein can be loaded with different metallic and non-metallic species, as reported by our group and many others [28,29,30,31]. Therefore apoferritin protein is a good candidate as a theranostic platform due to its small size, stability, biocompatibility and nonimmunogenic behavior.[32,33,34]

In this context, our group has previously reported that 4 and 6 nm maghemite nanoparticles can be coated with apoferritin protein[35] (Scheme 1). Subsequently, it was reported the successful preparation of long-circulating maghemite nanoparticles coated with apoferritin protein capsids, which are effective for MR imaging of the liver for 45 days.[36] These parameters are even better than the ones presented in ENDOREM®, a drug for MRI diagnosis of hepatic pathologies which has been traditionally regarded as a comparative reference (Figure 4).

These so-called apomaghemites (Apomag) represent a new generation of long-term MRI contrast agents that could allow both an initial diagnosis and also provide information in real time of the progress and efficiency of a medical treatment.

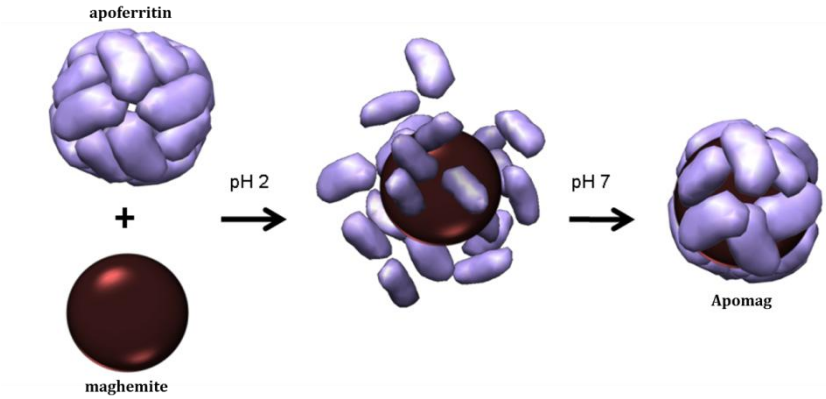

Scheme 1. Schematic encapsulation of maghemite nanoparticles thanks to the pH-driven disassembly-assembly process exhibited in apoferritin.

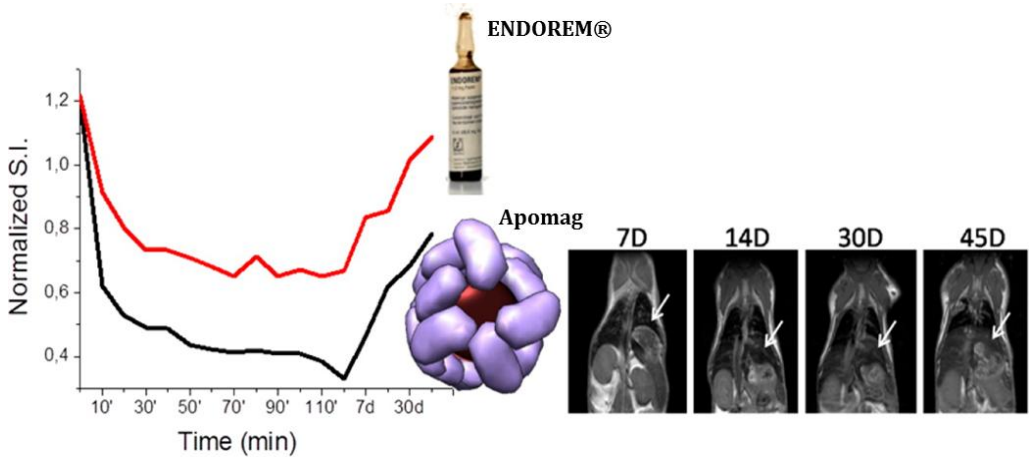

Fig. 4. Long-circulating maghemite nanoparticles coated with apoferritin protein capsids, which are effective for MR imaging of the liver for 45 days. Comparison with ENDOREM®.[36]

Another popular application of iron nanoparticles in Medicine is hyperthermia, which is the destruction of tumors by locally over-heating the tissue. Hyperthermia is an effective and specific anticancer treatment, since an increased temperature of the treated tissue up to 44°C is less well tolerated by cancer cells than by healthy cells. Hyperthermia treatment by iron oxide nanoparticles is induced by exposure of the particles to an

alternating magnetic field (Figure 5). A local accumulation of nanoparticles allows for tissue-specific hyperthermia that preferentially addresses the tumor tissue. This fact is due to the enhanced permeability and retention (EPR) effect which is the property by which molecules or nanoparticles of appropriate size tend to accumulate in tumor tissue much more than they do in normal tissues. The benefits over classical cancer therapies are minimal invasiveness, accessibility of hidden tumors, and very few side effects. Conventional heating of a tissue (microwaves, laser light etc.) results in the healthy tissue surrounding the tumor also being destroyed. However, paramagnetic particles provide a powerful tool for highly localized energy absorption and heating of mainly the cancerous cells.

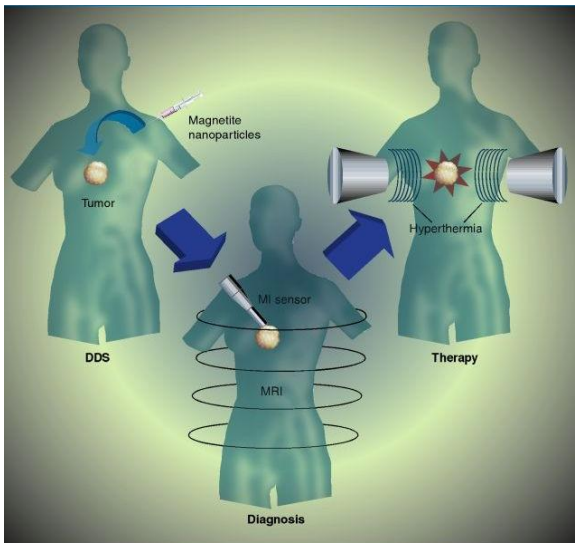

Fig. 5. Magnetic nanoparticles for diagnosis (MRI) and hyperthermia.

All these features prompted us to investigate the possibility of incorporating maghemite nanoparticles as well as loading a significant dose of doxorubicin (DOX) to apoferritin protein with the aim of obtaining a MRI agent capable of delivering a therapeutic drug.

2. Incorporation of DOX into Apoferritin protein.

Two different approaches have been used to incorporate DOX into apoferritin. In the first approach, DOX was co-encapsulated with maghemite using the well-known process based on the pH-driven disassembly/assembly of apoferritin,[35] whereas in the second approach apoferritin was loaded with the drug after maghemite encapsulation (surface binding).

2.1. Co- encapsulation.

In the co-encapsulation approach (**DOX-Apomag**), an acidic colloid of 6 nm maghemite nanoparticles and a solution of DOX were incubated with disassembled apoferritin at pH 2 and then the protein was reassembled by increasing the pH to 7.4, thereby simultaneously entrapping the magnetic nanoparticles and DOX inside the protein cavity (Scheme 2). At pH 2 apoferritin is dissociated into its 24 polypeptide subunits, whereas an increase in pH to 7.4 results in re-assembly of the subunits in an almost intact manner.[37,38] Using this approach, molecules such as Gd-DO3A, cisplatin, desferrioxamine B, DOX and DOX-Cu (II) were previously encapsulated into apoferritin, as previously reported.[39,40,41,42,43,44]

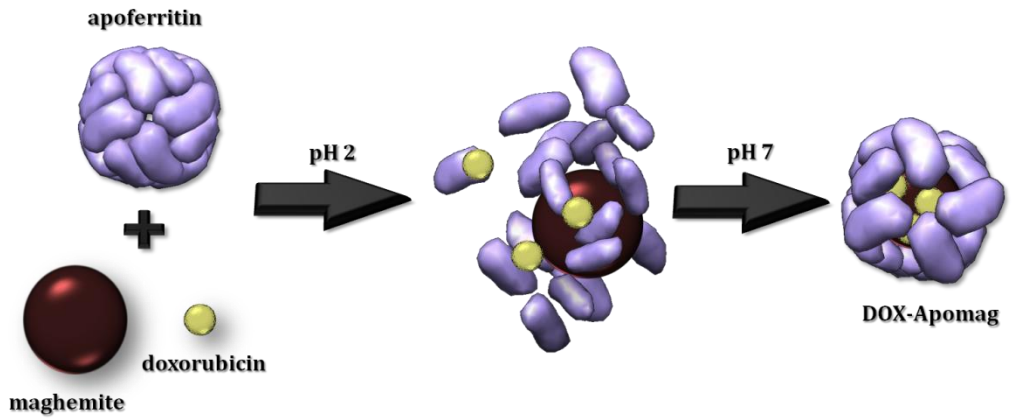

Scheme 2. DOX-co-encapsulation with maghemite within the apoferritin.

2.2. Surface-binding method.

In the surface-binding method (**DOX-Apomag sb**), Apomag was incubated with a solution of DOX (Scheme 3). At physiological conditions, DOX is known to have a high affinity for binding to DNA and RNA by electrostatic interaction due to the presence of negative phosphate groups in these biomolecules.[11] In the same way, DOX is postulated to form non-covalent conjugates with apoferritin through electrostatic attraction, since at this pH, apoferritin has negative residues at its surface.

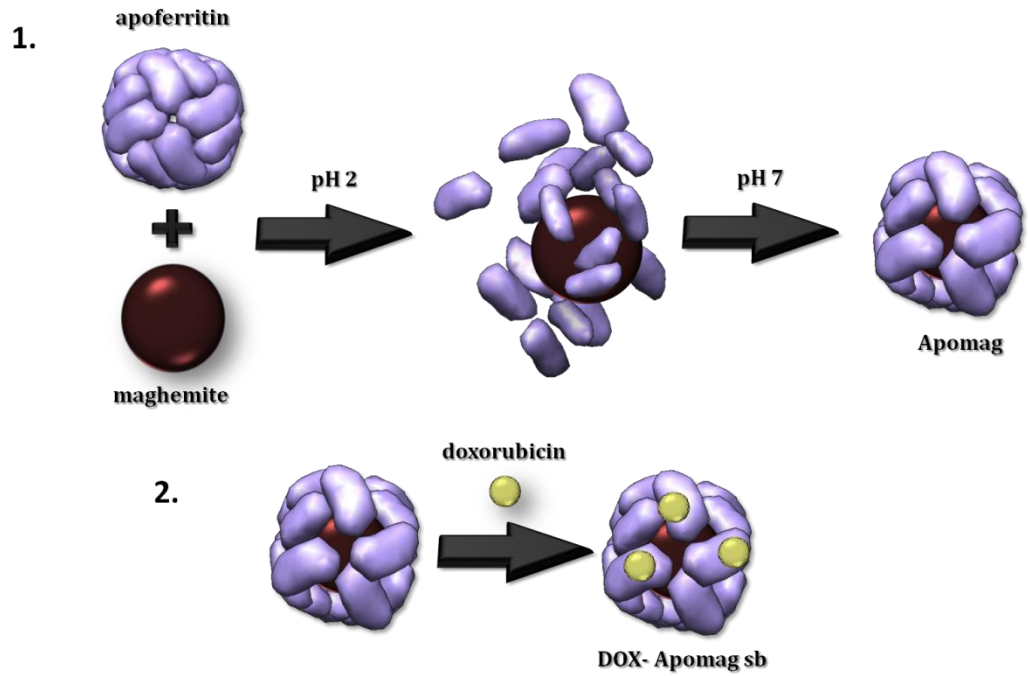

Scheme 3. DOX-surface binding after previous maghemite encapsulation.

2.3. Encapsulation efficiency.

Encapsulation efficiency for both methods was evaluated by using the following formula:

$$EE = \frac{DOX\ encapsulated}{Total\ DOX} * 100$$

A value of 10.75% was obtained for co-encapsulation (pH 7.4) and 8.5% for surface binding, which represent 19 and 6 DOX molecules/protein, respectively. These measurements support the hypothesis that DOX is weakly bound to the protein surface for the surface-binding approach.

DOX-loaded ferritin has been reported to exhibit an excellent biocompatibility profile, thereby reducing healthy organ drug exposure and improving the maximum tolerated dose when compared with free DOX. Besides DOX-loaded ferritin displayed a significantly longer median survival time, as well as lower toxicity compared with the clinically approved Doxil, demonstrating a substantial antitumor activity of DOX-loaded ferritin.[32,33,34]

3. Apomaghemite TEM study.

A transmission electron microscopy (TEM) study was performed for both loading strategies to evaluate sample size and structural conformation after dual loading. DOX-loaded apomaghemite samples showed typical irregular spherical shape (Figure 6a), with no size change being observed after maghemite + DOX loading. The protein shell was visualized by negative staining with uranyl acetate and a mean size of 12 nm was obtained, thus confirming that the nanoparticles had readily been encapsulated within the apoferritin shell (Figure 6b). The co-encapsulation strategy (DOX-Apomag) gave a protein yield of 57% and the surface-binding approach (DOX Apomag sb) a yield of 67%.

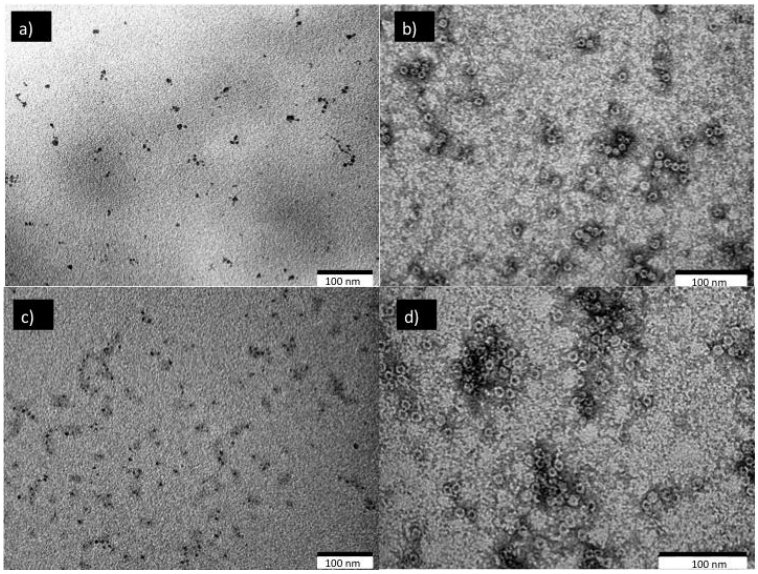

Fig. 6. (a) TEM image of a co-encapsulation sample; (b) uranyl negative stained image of (a). (c) and (d) similar images for the surface-binding sample.

4. DLS measurements.

Dynamic light scattering (DLS) measurements (Figure 7) pointed out the existence of some aggregation, probably through the protein capsids, as it occurs in native ferritin.

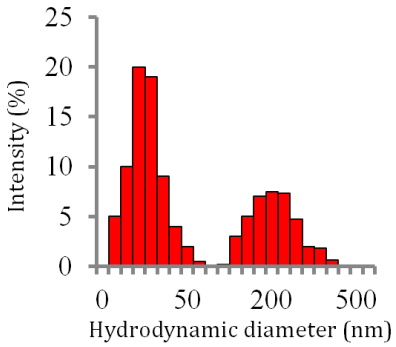

Fig. 7. DLS experiments showing the size distribution in Apomagh-DOX sample (the data analysis was performed via CONTIN methods). Two main populations are observed.

5. Co-encapsulation and surface binding release comparison.

One of the reasons why DOX is used as a model anticancer drug is that it can be followed easily by either UV–vis or fluorescence spectroscopy. As such, its UV–vis band at 481 nm was used to determine the kinetics of DOX release from apomaghemite.

For both strategies, and after dual-loading in DOX and maghemite nanoparticles, an extensive dialysis against TRIS buffer (pH 7.4) was carried out until complete removal of unbound drug.

The release patterns were then compared of both strategies (co-encapsulation and surface binding; Figure 8). Unlike DOX-Apomag surface binding, in which the DOX release was quite fast, co-encapsulated DOX-Apomag was found to be very slow, with approximately 26% of DOX being released during the first 24 h and the remaining drug being released over the next 10–25 days. A substantial burst release effect in the early period was found probably due to interactions of DOX with the hydrophobic and hydrophilic channels of the protein molecule, which impeded the diffusion release of DOX. When using the DOX-Apomag surface binding protocol, release of the drug from apomaghemite is markedly higher (60% after 24 h). This opposite kinetic behavior suggests that when using the surface-binding method, the drug is mostly bonded to the protein surface, probably by electrostatic interactions, rather than being loaded into the protein cavity. This idea is supported by zeta potential measurements. The zeta potential (Figure 9) value increases from −15.1 mV for the co-encapsulated sample to −5.5 mV for the surface-binding sample. The slightly positively charged DOX molecules bound to the surface of apoferritin are responsible for this behavior.

Bearing in mind that an ideal theranostic agent should dissociate slowly from its delivery carrier to maintain a high concentration in the

tumor region for a long period of time, the co-encapsulation strategy seems to be more appropriate.

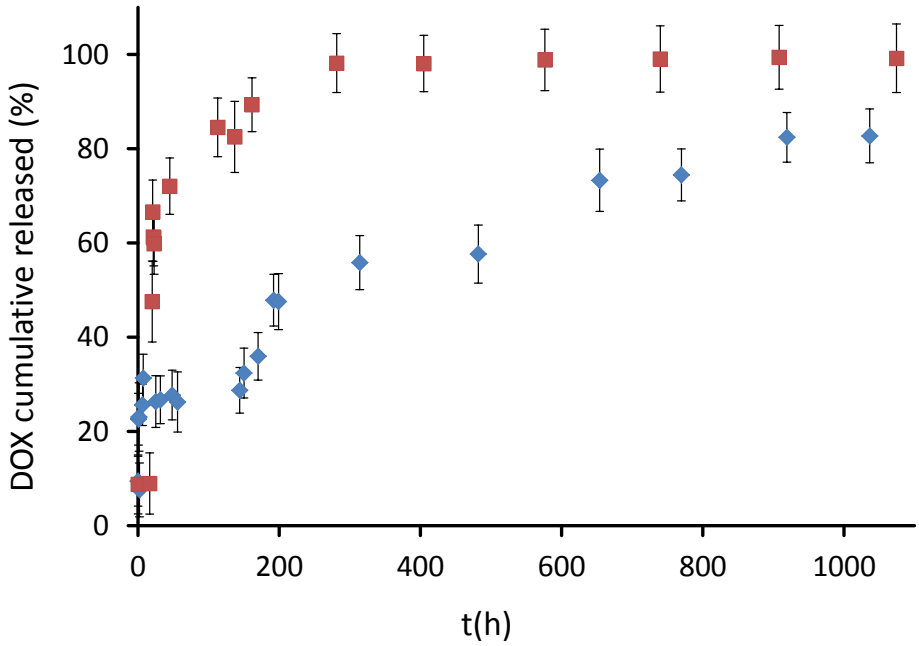

Fig. 8. Kinetics of DOX release from apomaghemite. Blue closed diamonds: co-encapsulation strategy (**DOX-Apomag**); red closed squares: surface-binding protocol (**DOX-Apomag sb**).

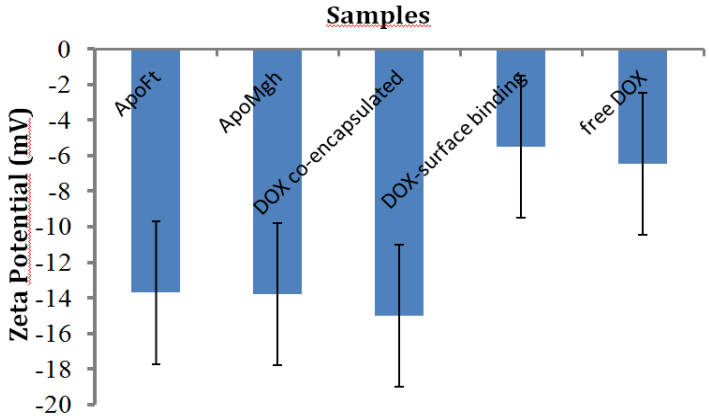

Fig. 9. Zeta potentials of co-encapsulated DOX-Apomag pH 7.4 (DOX 20 μg mL^{-1}), surface binding DOX-Apomag pH 7.4 (DOX 12 μg mL^{-1}), Apomag and apoferritin samples. Error bars indicate the width of the zeta potential distribution of the particles.

5.1. pH and temperature influence.

To gain more insight into the capabilities of Apomag as a drug-delivery system, and using the co-encapsulation method, the same kinetic study was performed but heating at 50 °C (DOX-Apomag 7.4 50 °C) (roughly the temperature obtained in magnetic hyperthermia with superparamagnetic iron oxide nanoparticles; Figure 10). Finally, the DOX release kinetics was studied when the protein is reassembled at acidic pH (pH 5.2 instead of 7.4; Figure 10) as different pH values can be found at different body sites and it is known that the extracellular pH of tumor tissues is acidic.

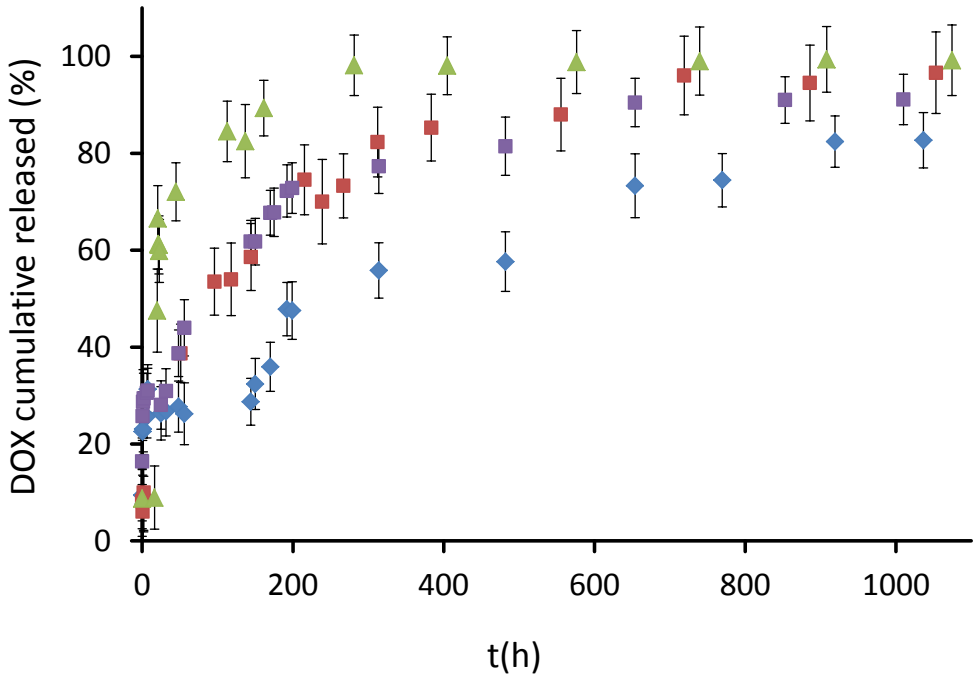

Fig. 10. Kinetics of DOX release from apomaghemite. Blue closed diamonds: co-encapsulation strategy, pH 7.4 (**DOX-Apomag 7.4**); green closed triangles: surface binding protocol, pH 7.4 (**DOX-Apomag 7.4 sb**); red closed squares: co-encapsulation, 50 °C, pH 7.4 (**DOX-Apomag 7.4 50 °C**); pink line closed squared: co-encapsulation, pH 5.2 (**DOX-Apomag 5.2**).

The DOX release profiles from DOX-Apomag obtained by co-encapsulation protocol are very similar during the first 24 h, even under different experimental condition (pH 7.4, pH 5.2 and 50°C/pH 7.4). However, the differences between the various experimental conditions are particularly noticeable after a period of 60–100 h, with an acidic pH (mimicking the microenvironment in endosomes and lysosomes) and temperature accelerating DOX release (Table 1). DOX release increases between 100 and 400 h, with samples approaching a plateau depending on the experimental conditions. This is not the case when the surface-binding protocol was used (Table 1), with 82% of the drug having been released after 100 h.

% (μM)DOX t(h)	**pH 7.4 c_i= 37 μM**	**pH 5.2 c_i= 34 μM**	**50ºC c_i= 35 μM**	**Surface binding c_i= 12 μM**
24	26 (9.6)	28 (9.5)	25 (8.7)	60 (7.2)
100	28 (10.4)	53 (18.0)	54 (18.9)	82 (9.8)
400	57 (21.1)	80 (27.2)	86 (30.1)	98 (11.8)

Table 1. % doxorubicin released with time from DOX-Apomag samples under different experimental conditions. The numbers in parentheses are total amount of DOX bound or co-encapsulated in the different approaches expressed in μM, related to their corresponding initial DOX concentration (c_i).

In the case of the DOX-Apomag sb sample, the electrostatic attraction between positively charged DOX (pKa = 8.4) and the negatively charged protein (pI = 4.5) coat at neutral or weakly alkaline pH must be the driving force for drug loading. The fact that this electrostatic adsorption force is weak explains the faster drug release for this sample, which reaches a final value of 98%.

The DOX co-encapsulation method is better suited for sustained drug release over time, as stated above. Temperature has a strong influence on the kinetics as well as on the amount of drug released. The DOX-Apomag 7.4 50°C sample, heated at 50°C, reaches a maximum value of 86% DOX release compared with 57% for the non-heated sample. A higher drug release from nanocarrier systems with increasing temperature has been reported previously. The possibility of controlling drug release by radio-frequency magnetic hyperthermia has been demonstrated in the case of DOX molecules encapsulated in polymersomes. In this work the authors showed plateau values at 5°C, 20°C, 37°C and 45°C equal to 5%, 30%, 60% and 85% respectively of the initial DOX load in the vesicles.[23]

Notably, the Apomag delivery system exhibits obvious pH dependent release properties at different solution pH values, as shown by the different release profiles for the pH 7.4 and 5.2 co-encapsulated samples. This may be explained by the fact that the potential of the protein inner surface becomes more positive upon decreasing the pH from 7.4 to 5.2, thus weakening the electrostatic adsorption force with positively charged DOX molecules. Another factor accounting for this behavior may be the likely poor protein reassembly at pH 5.2, thus leading to faster drug release.

6. Gel electrophoresis

Native-PAGE was used in order to verify if the protein retained its native structure despite the process of reassembling at different acidic pHs. Figure 11 shows that the native structure is not modified.

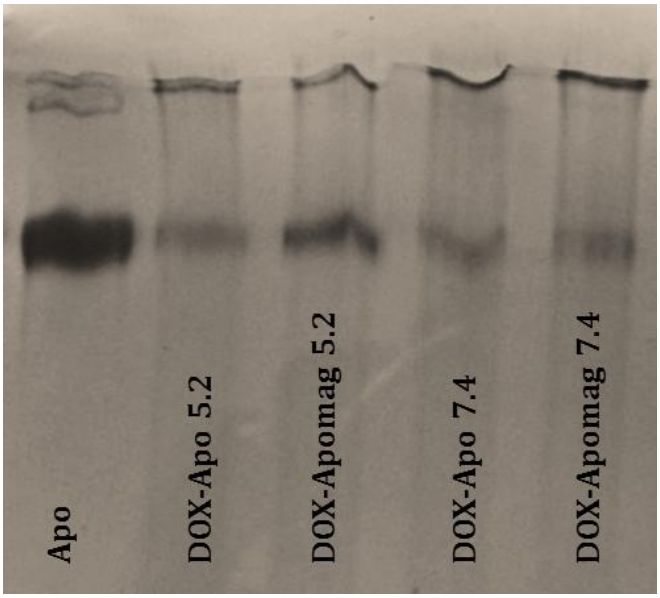

Fig. 11. Native-PAGE of: Apo; DOX-Apo 5.2; DOX-Apomag 5.2; DOX-Apo 7.4; DOX-Apomag 7.4.

7. Cell toxicity test.

The effect of co-encapsulated samples (pH 7.4 and 5.2) on cellular viability of cancer breast (MCF-7) and normal breast (MCF10A) cell lines was assessed by the MTS standard assay. The Apomag sample did not show any cytotoxic effect on the cells and was used as negative control in the MTS assay. Cytotoxicity on MCF7 and MCF10A of DOX-Apomag 7.4, DOX-Apomag 5.2 and ApoDOX was compared at equal amount of encapsulated DOX. Samples inhibited viability in a dose-dependent manner (Figure 12): at low concentrations (less than 10μg/mL DOX), all samples did not cause a significant detrimental effect on cell viability for both cell lines. At concentration of 20μg/mL DOX, samples showed some toxic effect on MCF7 and a less pronounced effect on MCF10A. The co-encapsulated sample at pH 5.2 showed more toxicity especially on MCF7, whereas the free DOX was much more toxic for both cell lines. Interestingly, the encapsulation of

doxorubicin in apoferritin protein led to increased IC50 factor beyond 30 µg g/mL against both cell lines (Table 2).

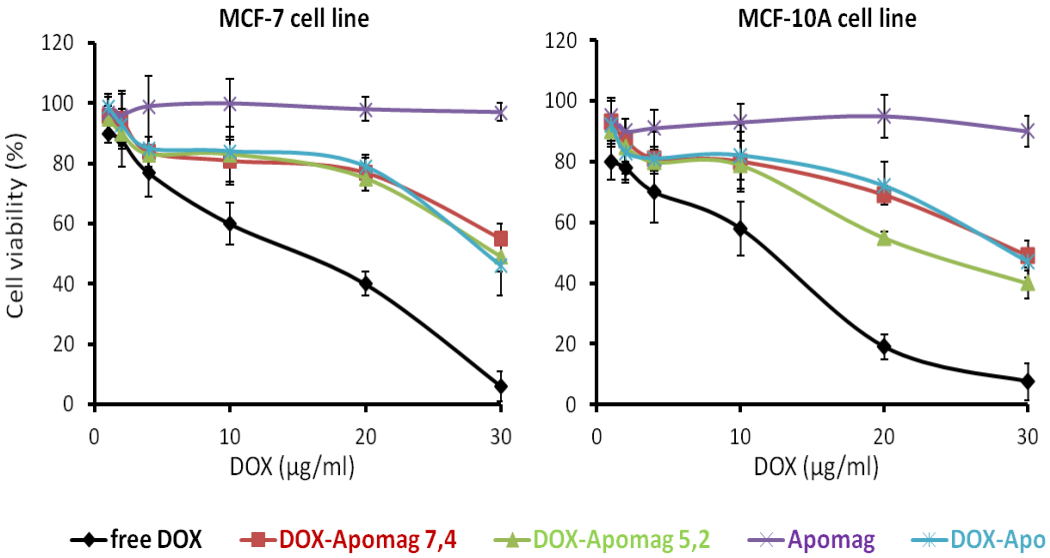

Fig. 12. Effect of co-encapsulated samples on cell viability. Each cell line was also treated with Apo-DOX and free DOX samples. Cell viability was estimated by the MTS assay in three replicate 96-wells. Results are normalized to the growth of cells treated with free medium.

Samples	IC50(µg/mL) MCF-7	IC50(µg/mL) MCF-10A
Apomaghemite-DOX pH 5.2	24.32 ± 2.11	31.66 ± 3.47
Apomaghemite-DOX pH 7.4	30.10 ± 2.98	35.01 ± 4.01
Free-DOX	14.05 ± 1.25	15.65 ± 2.16

Table 2. IC50 values for co-encapsulated samples tested on 2 distinct cell lines.

For all DOX concentrations tested in these experiments, co-encapsulated samples showed less cytotoxicity than free DOX. Therefore, this system show promise as a carrier for drug delivery.

8. Conclusions

The ultimate goal of theranostics is to gain the ability to image and monitor the diseased tissue, and drug efficacy with the long-term hope of tuning the therapy and dose in a control manner.

The simultaneous loading into apoferritin protein of maghemite nanoparticles and DOX has been achieved using co-encapsulation and surface-binding methods. The DOX co-encapsulation method is better suited for sustained drug release over time. The resulting magnetic hybrid displays good MRI contrast properties, as reported by our group previously. Now in this thesis it was shown that this system can provide sustained DOX release during around 25 days. These properties of Apomag system could allow in principle both, an initial diagnosis and information regarding the progress of a medical treatment over time.

This dual DOX-Apomag nanocarrier may prove useful in the field of "theranostic nanomedicines", combining diagnostic and therapeutic components in a single nanoparticle.

9. References

[1] T.M. Allen, *Nat. Rev. Cancer,* **2000**, *22*. 750.

[2] J. Xie, S. Lee, X. Chen, *Adv. Drug Deliv. Rev.,* **2010**, *62*, 1064.

[3] M. Arruebo, R. Fernández-Pacheco, R. Ibarra, J. Santamaría, *Nanotoday*, **2007**, *2*, 22.

[4] U.O. Häfeli, M. Chastellain, in: V.P. Torchilin (Ed.), Nanoparticles as Drug Carriers, *18,* Imperial College Press, London **2006**, 397.

[5] L.A. Guzman, V. Labhasetwar, C. Song, Y. Jang, A.M. Lincoff, R. Levy, E.J. Topol, *Circulation,* **1996**, *94*, 1441.

[6] C. Yang, W. Guo, L. Cui, N. An, T. Zhang, H. Lin, F. Qu, *Langmuir,* **2014**, *30,* 9819.

[7] C.C. Lee, E.R. Gillies, M.E. Fox, S.J. Guillaudeu, J.M.J. Fréchet, E.E. Dy, F.C. Szoka, *PNAS,* **2006**, *103*, 16649.

[8] S.R. Deka, A. Quarta, R.D. Corato, A. Riedinger, R. Cingolani, T. Pellegrino, *Nanoscale*, **2011**, *3*, 619.

[9] D. Kim, E.S. Lee, K.T. Oh, Z.G. Gao, Y.H. Bae, *Small*, **2008**, *4*, 2043.

[10] G. Yang, R. Lv, S. Gai, Y. Dai, F. He, P. Yang, *Inorg. Chem.*, **2014**, *53*, 10917.

[11] Q. Zeng, H. Wen, Q. Wen, X. Chen, Y. Wang, W. Xuan, J. Liang, S. Wan, *Biomaterials,* **2013**, *34*, 4632.

[12] Y. Tian, X. Jiang, X. Chen, Z. Shao, W. Yang, *Adv. Mater.,* **2014**, *26,* 7393.

[13] J. Li, P. Cai, A. Shalviri, J.T. Henderson, C. He,W.D. Foltz, P. Prasad, P.M. Brodersen, Y. Chen, R. DaCosta, A.M. Rauth, X.Y. Wu, *ACS Nano,* **2014**, *8*, 9925.

[14] Braddock, M. (Ed.). (**2016**). Nanomedicines: Design, Delivery and Detection. Royal Society of Chemistry.

[15] S.S. Kelkar, T.M. Reineke, *Bioconjug. Chem.,* **2011**, *22*, 1879.

[16] H.B. Na, I.C. Song, T. Hyeon, *Adv. Mater.,* **2009**, *21*, 2133.

[17] R. Qiao, C. Yang, M. Gao, *J. Mater.Chem.,* **2009***, 19*, 6274.

[18] C. Corot, P. Robert, J.M. Idée, M. Port, *Adv. Drug Delivery Rev.,* **2006***, 58*, 1471.

[19] J.I. Kim, C.J. Chun, B. Kim, J.M. Hong, J.K. Cho, S.H. Lee, S.C. Song, *Biomaterials,* **2012***, 33*, 218.

[20] J.I. Kim, B.S. Lee, C.J. Chun, J.K. Cho, S.Y. Kim, S.C. Song, *Biomaterials,* **2012***, 33*, 2251.

[21] M. Levy, C. Wilhelm, N. Luciani, V. Deveaux, F. Gendron, A. Luciani, M. Devaud, F. Gazeau, *Nanoscale,* **2011***, 10*, 4402.

[22] W. Wu, Z. Wu, T. Yu, C. Jiang and W. Kim, *Sci. Technol. Adv. Mater.,* **2015**, *16*, 023501.

[23] C. Sanson, O. Diou, J. Thévenot, E. Ibarboure, A. Soum, A. Brûlet, S. Miraux, E. Thiaudière, S. Tan, A. Brisson, V. Dupuis, O. Sandre, S. Lecommandoux, *ACS Nano,* **2011**, *5,* 1122.

[24] S. Mornet, S. Vasseur, F. Grasset, E. Duguet, *J. Mater. Chem.,* **2004**, *14,* 2161.

[25] T. Neuberger, B. Schopf, H. Hofmann, M. Hofmann, B. von Rechenberg, *J. Magn. Magn. Mater.,* **2005**, *293*, 483.

[26] S. Laurent, D. Forge, M. Port, A. Roch, C. Robic, L. Vander Elst, R.N. Muller, *Chem. Rev.,* **2008**, *108*, 2064.

[27] C. Sun, J.S.H. Lee, M. Zhang, *Adv. Drug Deliv. Rev.,* **2008**, *60*, 1252.

[28] F.C. Meldrum, T. Douglas, S. Levi, P. Arosio, S. Mann, *JBIC,* **1995**, *58,* 59.

[29] K.K.W. Wong, S. Mann, *Adv. Mater.,* **1996**, *8*, 928.

[30] N. Gálvez, P. Sánchez, J.M. Domínguez-Vera, *Dalton Trans.,* **2005**, 2492.

[31] N. Gálvez, E. Valero, M. Ceolin, S. Trasobares, M. López-Haro, J.J. Calvino, J.M.Domínguez-Vera, *Inorg. Chem.,* **2010**, *49*, 1705.

[32] M. Liang, K. Fan, M. Zhou, D. Duan, J. Zheng, D. Yang, J. Feng, X. Yan, *PNAS*, **2014**, *111*, 14900.

[33] K. Fan, C. Cao, Y. Pan, D. Lu, D. Yang, J. Feng, L. Song, M. Liang, X. Yan, *Nat. Nanotechnology,* **2012**, *7*, 459.

[34] K. Li, Z.P. Zhang, M. Luo, X. Yu, Y. Han, H.P. Wei, Z.Q. Cui, X.E. Zhang, *Nanoscale,* **2012**, *4*, 188.

[35] E. Valero, S. Tambalo, P. Marzola, M. Ortega-Muñoz, F.J. López-Jaramillo, F. Santoyo-González, J. López, J.J. Delgado, J.J. Calvino, R. Cuesta, J.M. Domínguez-Vera, N. Gálvez, *J. Am. Chem. Soc.,* **2011,** *133*, 4889.

[36] E. Valero, S. Fiorini, S. Tambalo, H. Busquier, J. Callejas-Fernández, P. Marzola, N. Gálvez, J.M. Domínguez-Vera, *J. Med. Chem.,* **2014**, *57*, 5686.

[37] Z. Zhen, W. Tang, H. Chen, X. Lin, T. Todd, G. Wang, T. Cowger, X. Chen, J. Xie, *ACS Nano*, **2013**, *7*, 4830.

[38] X. Lin, J. Xie, G. Niu, F. Zhang, H. Gao, M. Yang, Q. Quan, M.A. Aronova, G. Zhang, S. Lee, *Nano Lett.,* **2011**, *11*, 814.

[39] S. Geninatti Crich, B. Bussolati, L. Tei, C. Grange, G. Esposito, S. Lanzardo, G. Camussi, S. Aime, Probe. Cancer. Res. 66 (2006) 9196–9201.

[40] Z. Yang, X.Wang, H. Diao, J. Zhang, H. Li, H. Sun, Z. Guo, *Chem. Commun.*, **2007**, *33,* 3453.

[41] J.M. Dominguez-Vera, *J. Inorg. Biochem.,* **2004**, *98,* 469.

[42]] E. Simsek, M.A. Kilic, *J. Magn. Magn. Mater.,* **2005**, *293*, 509.

[43] M.A. Kilic, E. Ozlu, S. Calis, *J. Biomed. Nanotechnol., 8*, **2012**, 508.

[44] J. Gumulec, M. Fojtu, M. Raudenska, M. Sztalmachova, A. Skotakova, J. Vlachova, S. Skalickova, L. Nejdl, P. Kopel, L. Knopfova, A. Vojtech, R. Kizek, M. Stiborova, P. Babula, M. Masarik, *Int. J. Mol. Sci.,* 2014, *15,* 22960.

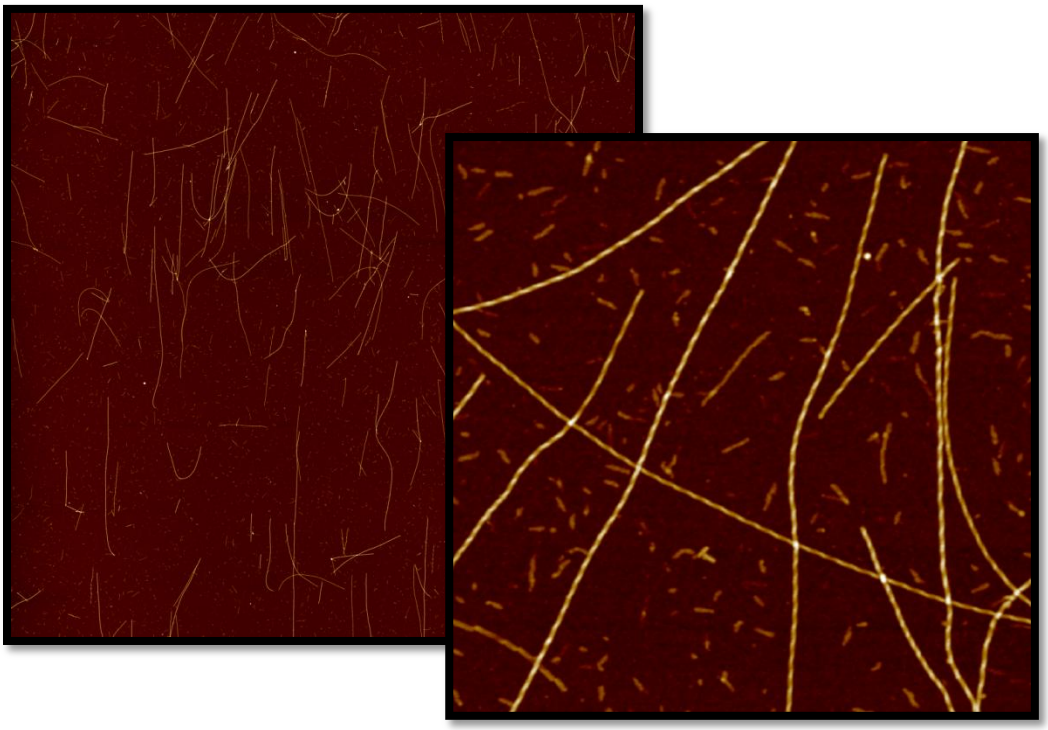

CHAPTER 3. APOFERRITIN PROTEIN: UNDERSTANDING THE FORMATION OF AMYLOID-LIKE FIBRILS

1. Introduction

The structuring of bioinorganic hybrid materials has great interest in basic and applied research because they provide a direct link between the inorganic and biological worlds. Biological systems have great flexibility, hence the interest in them for Nanotechnology. Biomolecules such as DNA, peptides or proteins have been widely used for the synthesis of bioinorganic materials.[1,2,3,4,5] These hybrid nanomaterials find broad applications in Biomedicine, such as tissue engineering, drug delivery, bioimaging or biosensors, and in Nanotechnology, as templates for the fabrication of metal nanowires and functional polymer nanotubes due to their unique anisotropic properties.[6,7]

Within the area of biomaterials, protein-based systems are desirable because of their biocompability and biodegradability and offer several advantages over other traditional methods.[8]

Another important aspect is protein self-assembly which is a wide-ranging phenomenon and is of great importance in many areas of science. The reversible formation of fibrils from globular proteins is a phenomenon that occurs naturally, *in vivo*, for proteins such as actin, tubulin, fibrin or collagen. Other well-known examples of protein fibrillation include the irreversible amyloid fiber formation of several proteins involved in neurological disorders such as Alzheimer's, Parkinson's, Creutzfeldt-Jakob or Huntington's disease.

Amyloid-like fibers, either natural or synthetic, and self-assembling peptides are excellent templates for the production of 1D inorganic hybrid nanostructures.[9,10,11,12] Some strengths of these 1D structures are: rigid structures with high mechanical strength, comparable in specific stiffness to spider silk and steel,[13,14,15] easy preparation from available proteins, and control over growth to obtain a variety of structures and physical properties. Another strong and important point is that rigid amyloid fibers

have rich and diverse surface functional groups on which other components with desirable functionalities can easily be built with nanoprecision.[30] A last but not least advantage of protein fibers is that size diameters are homogeneous, reproducible and easily tuned. Therefore, these 1D structures can significantly help in the understanding of numerous biological processes.[16,17] The simplicity of superstructure assemblies, their multifunctionality, and structural versatility represent interesting directions for future research in nanostructures.[18]

An example of a fibril formation from globular proteins is provided by various globular proteins such as ovalbumin, bovine serum albumin[19] and β-lactoglobulin. As commented in the introductory chapter, β-lactoglobulin has been particularly well studied, because it represents both a relevant model system and a major whey protein of interest to the food industry. Mezzenga and colleagues have several reports on the structural characterization of β-lactoglobulin protein fibrils formed at pH 2 and 90°C. In this way, they have been able to demonstrate their morphology and they have established that multistranded left-handed helical aggregates of β -lactoglobulin occur under equilibrium conditions by performing a statistical analysis on single-molecule AFM images.[20] The atomic force microscopy analysis, supported by theoretical arguments, revealed that the fibrils have a multistranded helical shape with twisted ribbon-like structures. They proposed a possible general model for amyloid fibril assembly and illustrate the potential of this approach for investigating fibrillar systems (Figure 1).

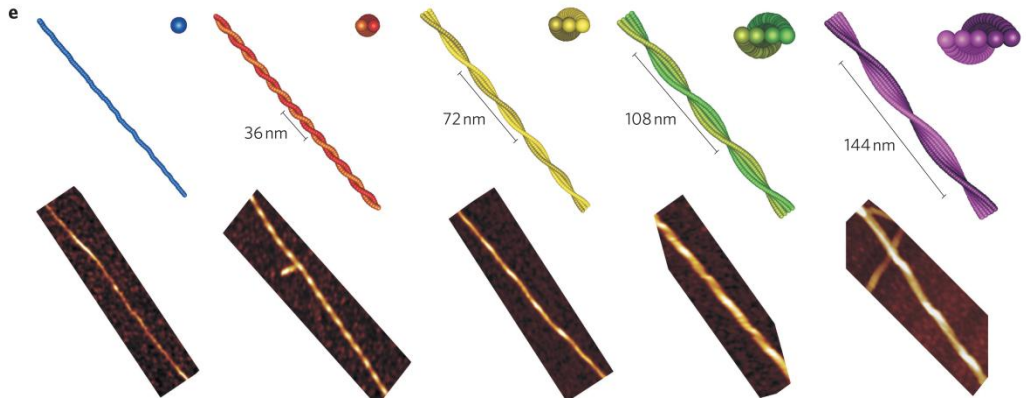

Fig. 1. AFM images and corresponding coarse-grain molecular dynamics reconstructions of left-handed helical fibril formation from the twisting of multistranded ribbons, with the number of filaments ranging between 1 and 5.[20] Image from: J. Adamcik, J. Jung, J. Flakowski, P. De los Rios, G. Dietler, R. Mezzenga, *Nat. Nanotechnol*., **2010**, *5*, 423.

Most globular native proteins in solution, under normal environmental conditions, are in equilibrium with their partially unfolded state, which is not probably the case of the robust apoferritin protein. It is generally accepted that the process of fibrils formation starts from a nucleation site or seed formed of partially unfolded proteins. Globular proteins in their native as opposite to smaller, pathological peptides (Aβ(1-40) peptide), possess a compact rigid structure, and therefore their fibrillation process requires the destabilization of their native rigid structure into partially unfolded conformations via robust changes of environmental conditions, which are usually extremely denaturing (mainly temperature and pH).

In this chapter, it will be first shown how a robust protein as apoferritin is able to form amyloid-like fibers, in similarity to β-lactoglobulin, and latterly, the experimental conditions necessary to optimize the fibrillization process will be studied. The motivation of studying apoferritin fiber formation is double: disorders in ferritin

functions have been related with typical iron-related diseases, such as hemochromatosis or anemia, but ferritin is also increasingly being recognized as a crucial molecule in some neurological pathologies, as Parkinson or Alzheimer's diseases.[21] On the other hand, its interest also lies in the possibility to engineer and integrate diverse properties into fibers, enabling the creation of functional materials with new or improved properties.

2. Formation of APO and Blg fibers

Apoferritin (APO), the empty ferritin protein resulting from iron oxide removal, is a globular protein composed of 24 polypeptide subunits (Mr 450 kDa) with a hollow aqueous cavity 8 nm in diameter where it can accommodate an iron oxide nanoparticle. Ferritin is the primary Fe storing protein in most living organisms.[22] It is remarkably stable to temperature and pH changes, as demonstrated by its stability up to 70 °C and over extreme pH values of 3–10.

TEM contrasted images of the two globular APO and Blg proteins are shown in Figure 2. Native APO is a hollow protein shell with cubic symmetry. At neutral pH and room temperature (RT), APO shows the typical spherical morphology with an average diameter of 12 nm (Figure 2a). Under the same conditions of pH and temperature Blg forms dimers and a heat treatment at 85°C and pH 5.0 is necessary for obtaining globular structures, in particular spherical aggregates with a size distribution centered at about 50–100 nm (Figure 2b).[23] Blg is known to form well-structured fibrils when the temperature is increased above 70 °C under very acidic conditions (pH 2). Figure 2c (APO) and 2d (Blg) show TEM images after heat treatment at 90 °C and pH 2 for 24 h. For the Blg protein, wire-like structures with an average diameter of 10 nm and several microns in length were observed, in agreement with previous reports.[23] Similar to Blg, the APO protein forms quite rigid (segments of 200–1000

nm, straight segments), rod-like fibers with diameters of 10 ± 2 nm. More flexible fibers were formed when the ferritin protein was subjected to the same heat treatment (Figure 3). To optimize the synthesis of these APO protein nanowires it was performed an exhaustive study varying the experimental conditions, which was followed by TEM and AFM.

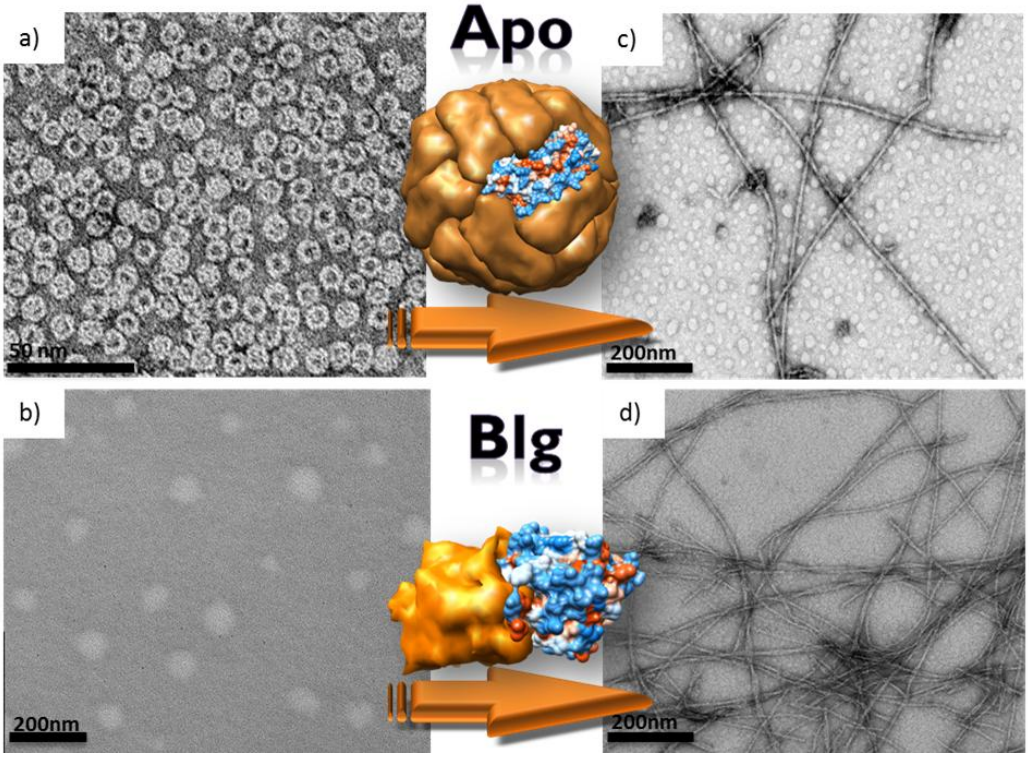

Fig. 2. TEM contrasted images of (a) the globular native APO protein at pH 7.4 and RT, (b) the globular Blg protein at pH 5 and 85°C, (c) amyloid like fibrillar APO at 90 °C, pH 2 and 24 h, (d) same as (c) for Blg.

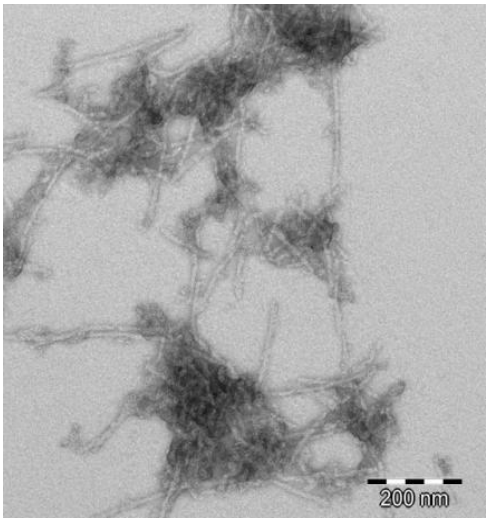

Fig. 3. TEM image of ferritin protein after heat treatment at 90ºC and pH 2 for 24h.

2.1. Influence of temperature

The temperature dramatically influences the final 1D structure obtained (Figure 4). More flexible and aggregated fibers, with bigger diameters of 20–30 nm, were formed when the temperature is decreased from 90 (Figure 4a) to 50 °C (Figure 4b). It should be pointed out that the Blg protein did not form fibers at 50 °C, but temperatures higher than 70 °C must be applied, as previously reported.[25]

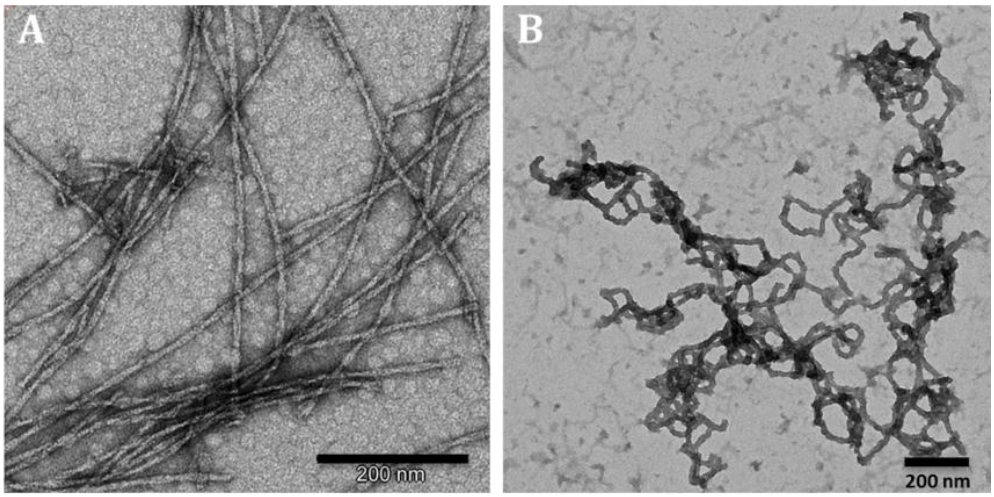

Fig. 4. TEM images of APO (a) heated at 90 °C and (b) 50 °C (pH 2 and 24 h of incubation time in both experiments).

2.2. Influence of pH

The influence of pH on the APO fiber formation is shown in Figure 5. Four different stages of the APO amyloid-like fibril formation can be distinguished after a heat treatment at 50 °C in a weak acidic medium (pH 5). In Figure 5a, it can be observed how the native APO protein forms aggregates while maintaining its globular structure. In Figure 5b APO cages stick together and the process of fiber formation begins and accordingly, thick fibers of APO cages with diameters of 80–100 nm are observed. At this stage the globular native structure of APO, and even its inner cavity (a dark spot at the middle of the cage) can still be perfectly distinguished. In Figure 5c, after a heat treatment of 40 min, the globular structure is barely observed since the fibrillar process goes on. In fact after 24 h of incubation time, Figure 5d, fibers of 20–50 nm in diameter were formed. They were more aggregated, disordered and thicker than fibers formed at pH 2 and 50 °C (Figure 4b). The native globular structure was lost in the final stage. Briefly, during the heating process at 50 °C and pH 5 the globular APO protein cages stick together and they arrange forming thick, aggregated and flexible fibers of around 20–50 nm. Under these experimental conditions (pH 5, 50 °C) the process of fiber formation occurs slowly, compared to that at 90 °C, which allowed us to monitor the system at 4 different stages of the fiber formation process.

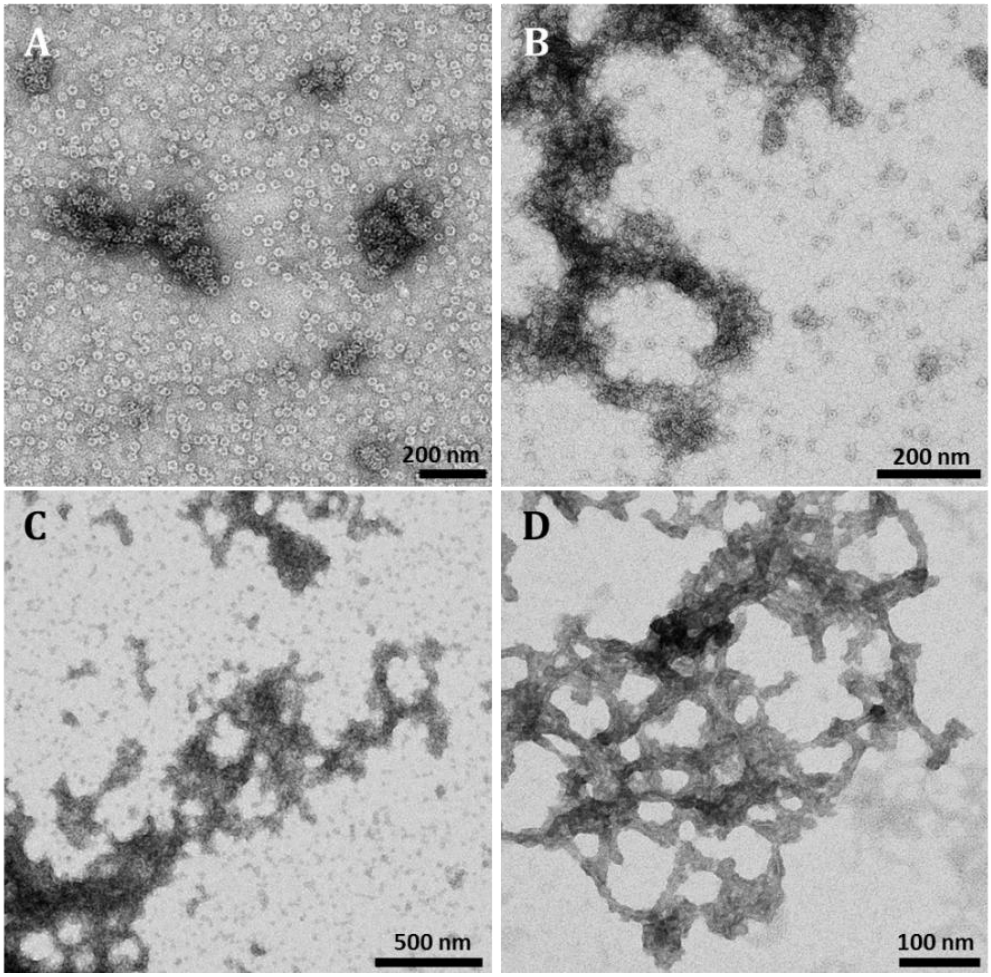

Fig. 5. TEM images of the APO protein heated at 50 °C and pH 5 for different incubation times. (a) 5 min, (b) 20 min, (c) 40 min and (d) 24 h.

After 18 days of incubation at the same experimental conditions (50°C and pH 5), thinner fibers, but still flexible, were observed (Figure 6), similar to the ones obtained at pH 2 and 90 °C after 24 h (Figure 2c).

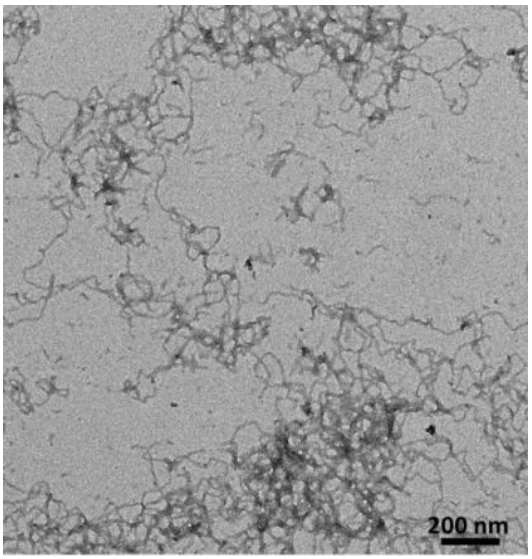

Fig. 6. TEM image of APO protein after heat treatment at 50ºC and pH 5 for 18 days.

Whereas Blg protein only forms fibers under very acidic conditions (pH 2) and high temperatures (90 °C), APO fibers can be obtained at lower temperatures (50 °C) and higher pH values (5).

2.3. Influence of incubation time

It was also observed that the incubation time is another key factor affecting the morphology of the fibers. In a first step, it was studied the evolution with time of APO and Blg fibers while heating at 90 °C and pH 2 (Figure 7). Large protein aggregates were formed after 1 h of treatment. Protein fibers were formed after 12 h of incubation time, remained until 48 h and then started to break down. After 5 days of heat treatment amyloid-like fibers were broken and only smaller protein aggregates could be observed.

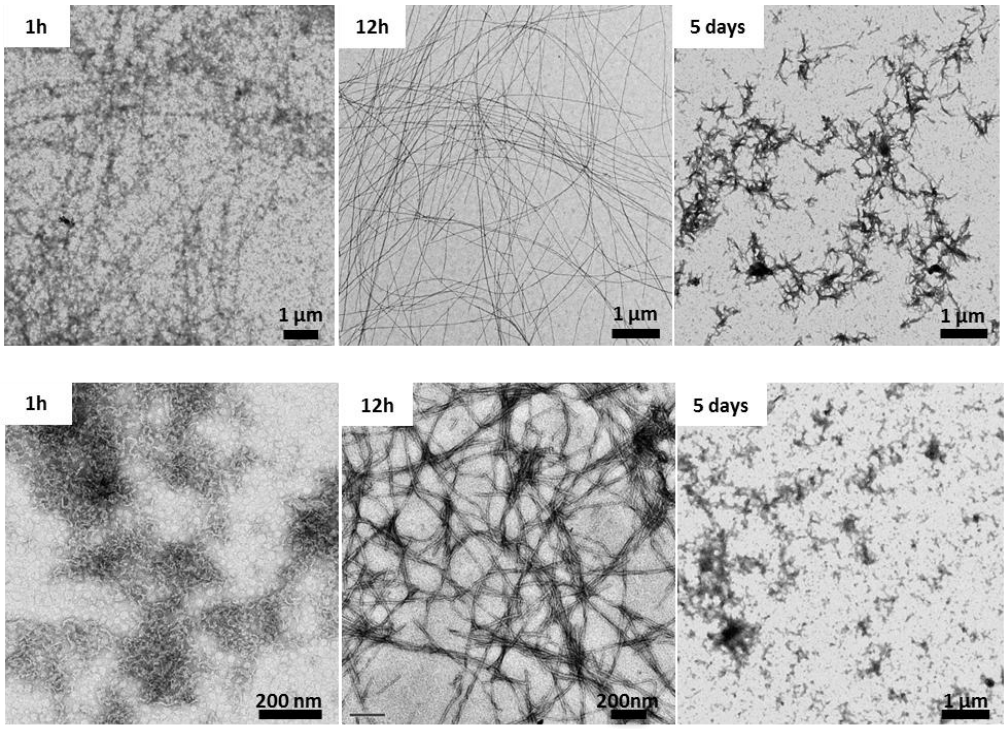

Fig. 7. TEM images of Blg (up) and APO (down) heated at 90 °C and pH 2 for different incubation times. Protein concentration was 0.2% wt for APO and Blg.

The influence of the incubation time on APO fibers was also followed by AFM. By performing a statistical analysis on AFM images it was possible to determine precisely the contour length of APO fibers. Shorter and more aggregated protein fibers were formed after 24h of treatment (length=1185nm) in comparison of those formed after 9h (length=1745nm) in the same conditions (Figure 8).

Taking together TEM and AFM analysis, a range of 9-12h was the optimal incubation time for obtaining rigid, long, non-aggregated APO fibers.

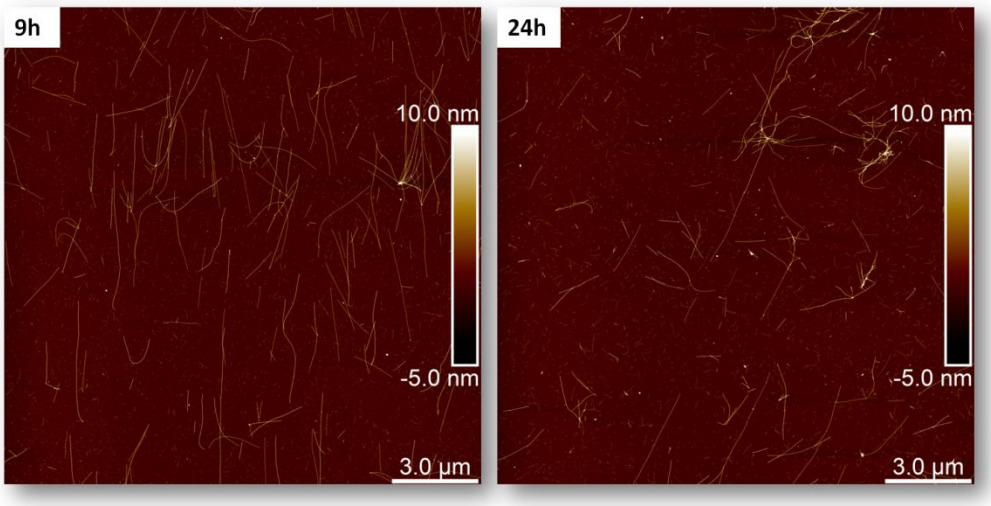

Fig. 8. AFM images of APO heated at 90 °C and pH 2 for (left) 9 h, (right) 24 h. It can be observed that fibers formed at 24 hours are significantly shorter.

2.4. Influence of protein concentration

The influence of protein concentration is shown in Figure 9. Concentrations ranging from 0.05 to 0.2 wt% do not significantly affect the fiber morphology. However, a higher concentration as 0.4 wt% resulted in a greater amount of aggregated flexible fibers.

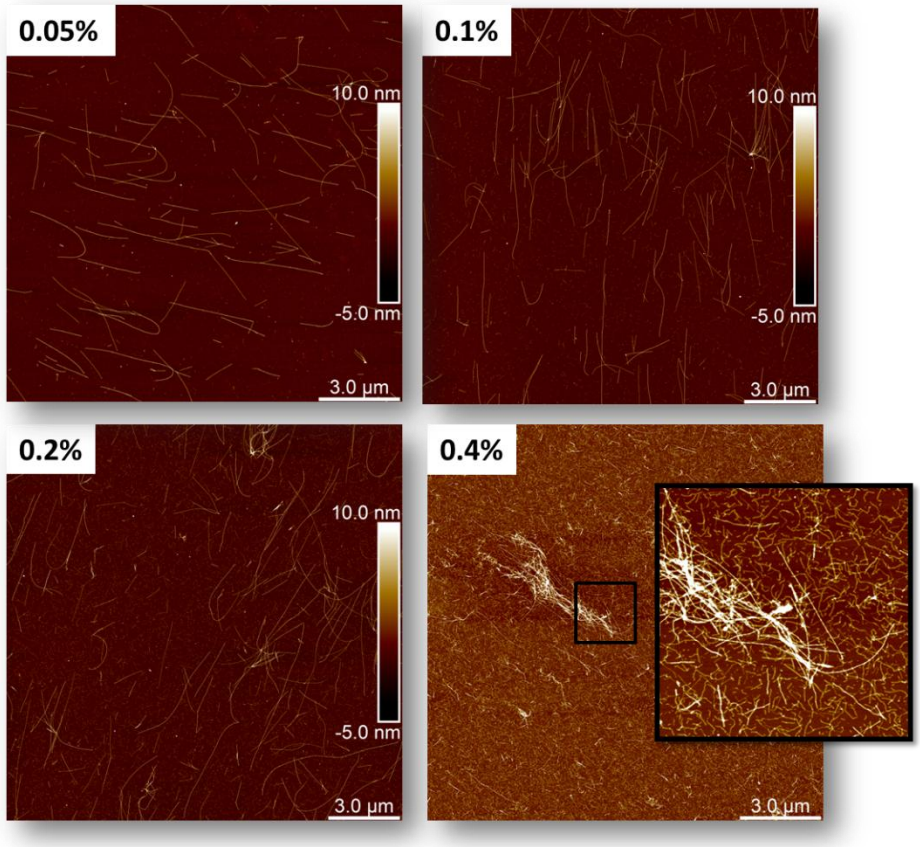

Fig. 9. AFM images of APO at different concentrations heated at 90 °C and pH 2.

2.5. Influence of stirring

The stirring notably affects to the final fiber contour length obtained. Fibers formed using a high speed stirring resulted in a breakage and, therefore, a decrease in their length. In this way, their contour length was determined by a statistical analysis on AFM images. Shorter and more aggregated protein fibers were formed by a stirring speed of 220rpm (length=1085nm) in comparison of those formed at 90rpm (length=1745nm) in the same experimental conditions (Figure 10).

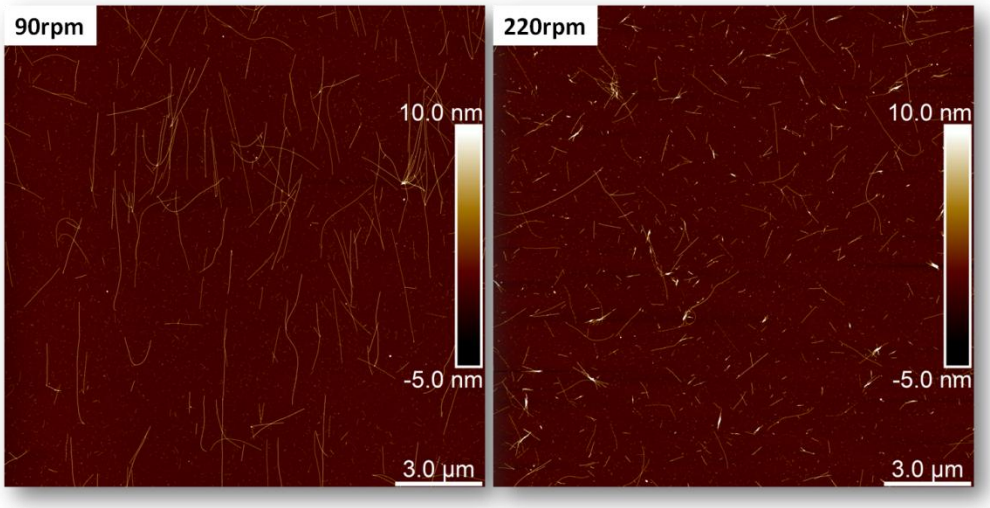

Fig. 10. AFM images of APO heated at 90 °C and pH 2 at 90rpm(left), 220rpm(right). It can be observed that fibers formed at 220rpm are significantly shorter.

Understanding the effect of small chemical changes on amyloid structures thus appears to be essential when studying amyloid formation. Therefore, fibers formation depends on a number of experimental synthesis conditions, but primarily on temperature, heating incubation time and protein concentration. The stirring and the pH also influence the final fibers structure. These results are in agreement with previous protein fibers studies.[24,25]

After globally considering the influence of temperature, pH, incubation time, protein concentration and stirring, we conclude that **pH 2**, **90°C**, an incubation period of **9h**, a protein concentration between **0.05-0.2wt%** and an agitation at **90rpm** are the optimal synthetic conditions to form well-structured, wire-like fibers for APO proteins with long persistence lengths.

3. APO aggregation kinetics

The aim of this Thesis is to assist the understanding of the genesis and development of apoferritin amyloid fibrils by investigating the structural time-evolution taking advantage of diverse techniques. The combination of them will reveal for the very first time new structural details of these systems during their entire process of formation.

To pursue this task, we will focus on the entire time frame of the kinetics of self-assembly from the initial globular protein to the final mature fibrils. For this purpose, the structural time evolution of apoferritin protein fibrils formed at the optimal experimental conditions, that is: pH 2, 90°C and 0.2wt% concentration, was investigated by combining several techniques. In addition, atomic force microscopy (AFM) and fluorescence lifetime imaging microscopy (FLIM) will allow the resolution of some structural details of the fibrils at the molecular length. Therefore, it will be possible to resolve and identify different individual stages of the fibrillation process.

Time-dependent intermediates of the evolving fibrils were collected by quenching at room temperature aliquots of the samples at specific heating times (0, 5 min, 15 min, 30 min, 45 min, 1 h, 3 h, 5 h, 9 h and 24 h). In this chapter, it will be shown which is the kinetics of amyloid-like apoferritin fibrils formation process, and if it involves critical steps driven by nucleation and growth of individual protofilaments, like occurs with β-lactoglobulin. These results allowed the elaboration of a new scenario in which it could be understood the formation of the final amyloid-like apoferritin fibrils.

3.1. APO fibers AFM study

The APO fibers morphology was characterized in detail using super resolution AFM revealing details of the structure at the single fibre length scale. Figure 11 shows the real space height images of apoferritin fibrils solution acquired after different heating times. The presence of very long filaments starts being observed after 3 hours of incubation time. It is also observed the increase with the heating time in the average contour length of filaments. However, 24h fibers are shorter and more aggregated than 9h, as previously reported due to incubation time's influence.

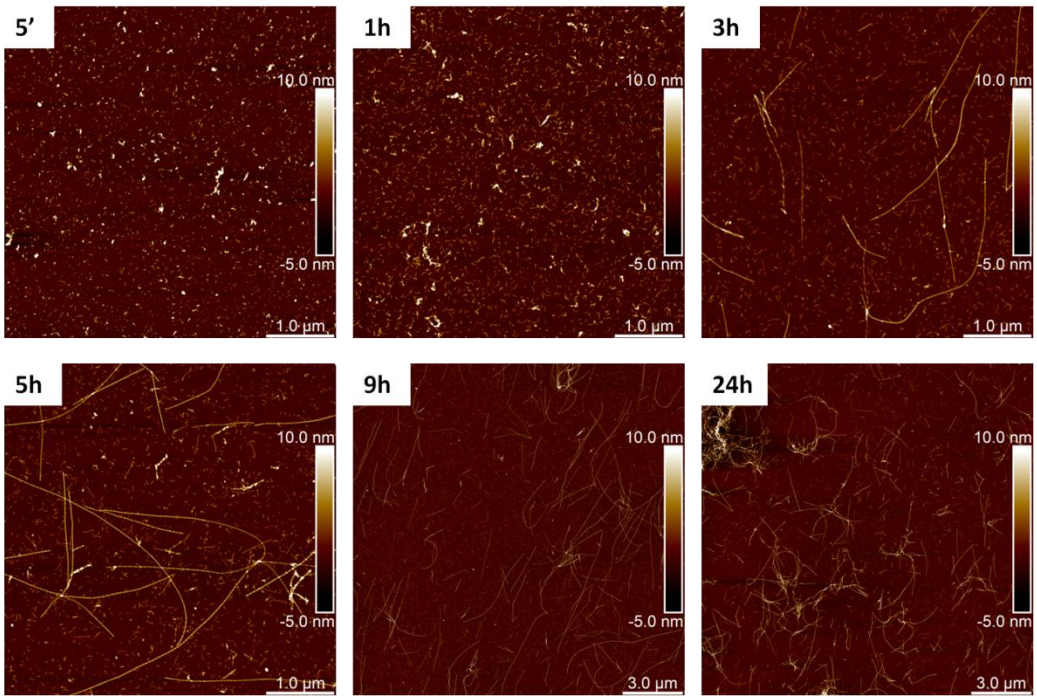

Fig. 11. Real space height AFM images of the apoferritin fibrils acquired after different heating times.

Statistical analysis of AFM images was reported using processing and tracking FibberApp software, an in-house-developed software at Professor's Mezzenga group.[26] Thus, morphological parameters such as total contour length, average height, or pitch size were evaluated accurately from a systematic statistical analysis. Moreover, larger length scale

structural information such as persistence length which gives a measurement of fiber flexibility was also determined.

During the first hour, it could be observed the increase with the heating time in the average contour length of the protein small aggregates called as "oligomers" (Figure 12). After one hour, no presence of long filaments/fibers could be observed.

Time (min)	Length (nm)	Height (nm)
5	48,90	4,09
45	55,70	4,39
60	78,03	4,25

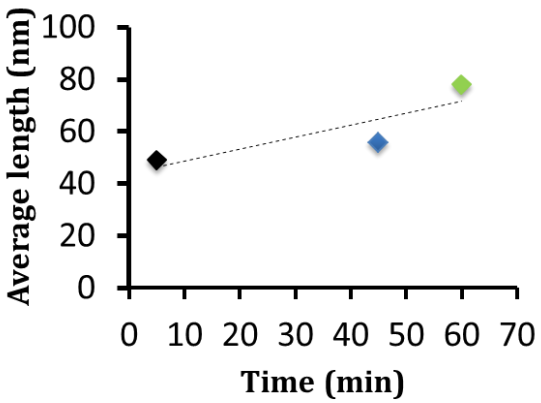

Fig. 12. Comparison between 5, 45 and 60min oligomers.

Long filaments were observed after 3 hours of incubation time. Together with these long rigid fibers, medium size-fibers and small aggregates/oligomers coexist (Figure 13). The same three different populations were also observed for 5, 9 and 24hours.

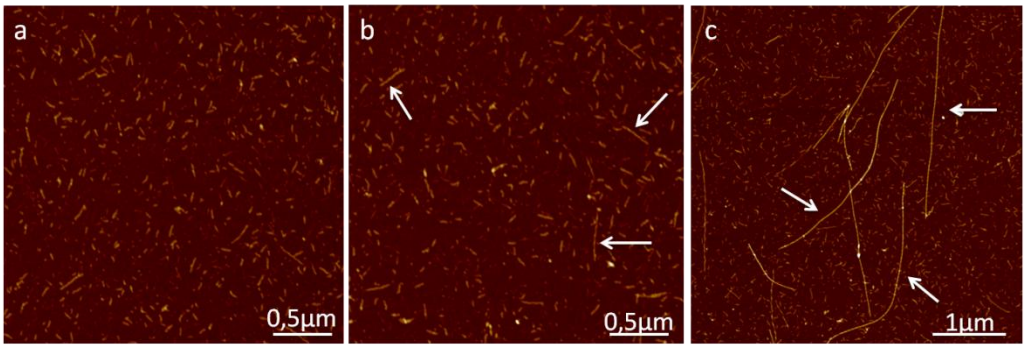

Small aggregates		Medium fibers		Long fibers		
Height	Length	Height	Length	Height	Length	Pitch
2.75 ±0.88	72.05 ±24.2	3.03 ±1.1	226.38 ±53.28	5.28 ±1.29	1631.4 ±1216.8	53.70

Fig. 13. AFM images showing the main three populations of APO at an incubation time of 3 hours: a) small aggregates, b) medium fibers and c) long fibers. The table below shows the statistical analysis of these three populations.

These results taken together demonstrate that the transitions from apoferritin oligomers into medium fibers firstly and finally to mature fibrils is carried out through some critical transient steps.

The statistical analysis of AFM images is summarized in Table 1.

	Small aggregates			Medium fibers			Long fibers				
Time	N	Height	Length	N	Height	Length	N	Height	Length	Pitch	L_p
3h	500	2.75 ±0.88	72.05 ±24.2	116	3.03 ±1.1	226.38 ±53.28	57	5.28 ±1.29	1631.4 ±1216.8	53.7	6708.07 ±57.27
5h	500	3.49 ±0.88	68.45 ±19.8	356	4.29 ±1.5	243.76 ±79.08	92	6.89 ±1.34	1573.83 ±1174.14	52.1	4717.01 ±26.68
9h	500	3.80 ±0.98	49.48 ±15.2	701	4.18 ±1.2	241.51 ±151.2	257	6.92 ±1.24	1888.33 ±1346.17	47.8	3816.25 ±58.18
24h	500	3.06 ±1.04	67.54 ±28.9	765	3.51 ±1.1	237.06 ±145.4	628	6.57 ±1.6	1013.23 ±756.9	47.8	2009.45 ±50.03

Table 1. Basic structural information about small aggregates, medium fibers and longer fibers. N=number of filaments tracked. All measurements are expressed in nanometers.

From this analysis we conclude that long fibers length grows between 3 and 9 hours but they are shorter at 24hours, as previously reported. These results are in concordance with an increase in fibers aggregation as previously mentioned in point 2.3, and in agreement with the behavior of other globular proteins.[27,28] For long fibers a periodic height fluctuation along the contour of the fibrils is observed. The system evolves to a ~50nm periodicity/pitch along the fiber. The AFM images and analysis reveal that the fibrils have a helical morphology with ribbon-like structures. In this case, there is no relation between periodicity and height, as reported for β-lactoglobulin and other protein fibers.[20]

Long APO rigid fibers show an average maximum height centered at 6.6 ± 1.1 nm with contour length varying between 1-3 μm. In contrast, short aggregates have a height of ~3nm and medium fibers ~4nm.

The persistence length (Lp) of the fibers was extracted from the statistical analysis. Lp is the length above which thermal fluctuations can buckle a rod-like polymer, and it is therefore a measure of the elastic properties of a molecule.[20]As shown in Table 1, the Lp decreases within the incubation time. This is because more aggregated fibers are formed through time, as it has been shown previously.

According to Mezzenga and colleagues[29] (J. Adamcik, R. Mezzenga, *Macromolecules,* **2012**, *45*, 1137) there are three different fibers shape: twisted, helical and tube-like. Looking at the fiber height profile of apoferritin fibers, they mostly have a twisted-helical shape (Figure 14), but some tube-like shapes could also be observed.

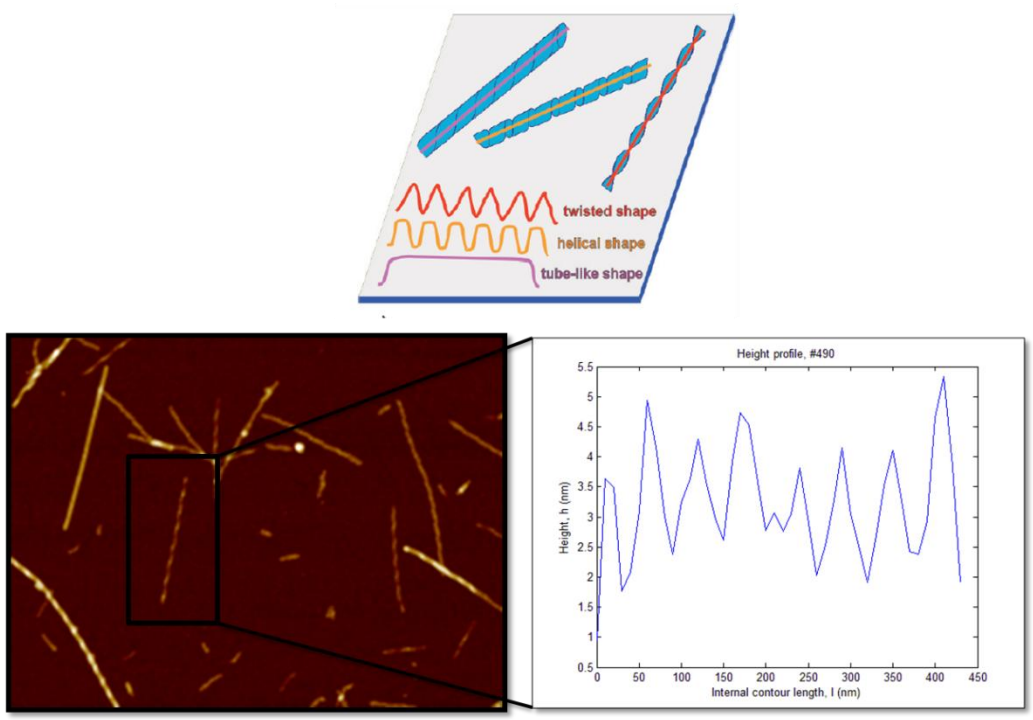

Fig. 14. Scheme showing different fibers shapes (up). AFM image showing twisted-helical shape of one apoferritin fiber and its height profile (down).

3.2. APO fibers TEM study

We investigated the topology and morphology of growing fibrils by TEM analysis. Figure 15 shows the images of APO fibrils solution acquired after different heating times. In agreement with the previous AFM study (Figure 11), only large protein aggregates were formed after 1 h of treatment and long filaments were observed after 3h of incubation time. The first notable trend is the increase with the heating time in the average contour length of filaments.

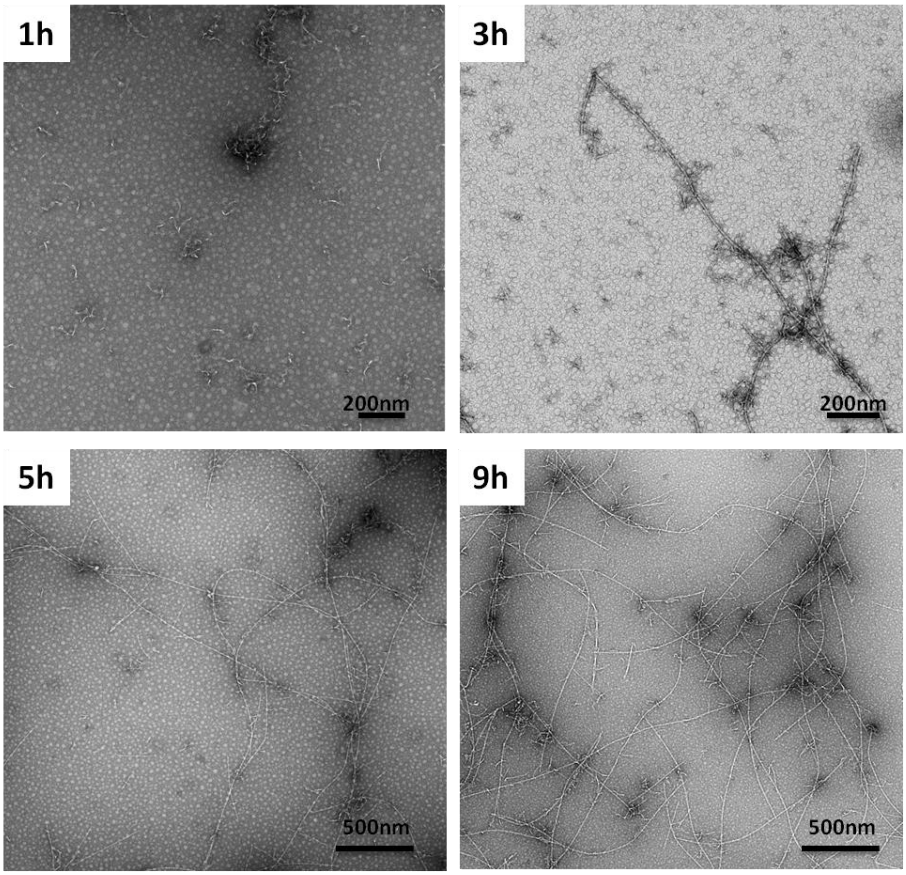

Fig. 15. TEM stained images of APO heated at 90 °C and pH 2 for different incubation times.

TEM images confirmed that fibrils do have a regular twist, leading to a well defined pitch corresponding to ~50nm, as shown in Figure 16, but these images do not contain information about the handedness of the fiber helices. The periodicity is defined here as twice the distance between two consecutive maximum along the contour length to indicate a full twist.

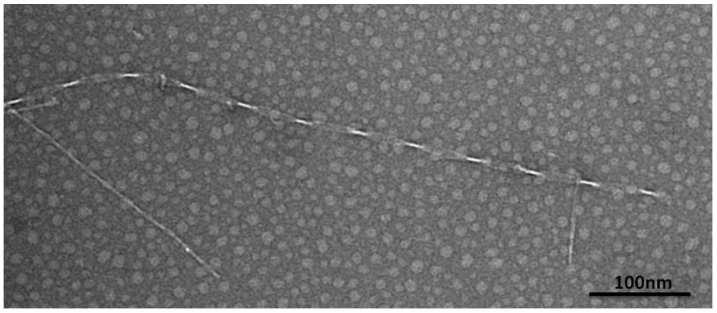

Fig. 16. TEM image of a single APO fiber showing the development of a periodic pitch along its contour length.

This pitch could be as well observed by scanning electron microscopy (SEM) as it is shown in Figure 17 corresponding to ~50nm.

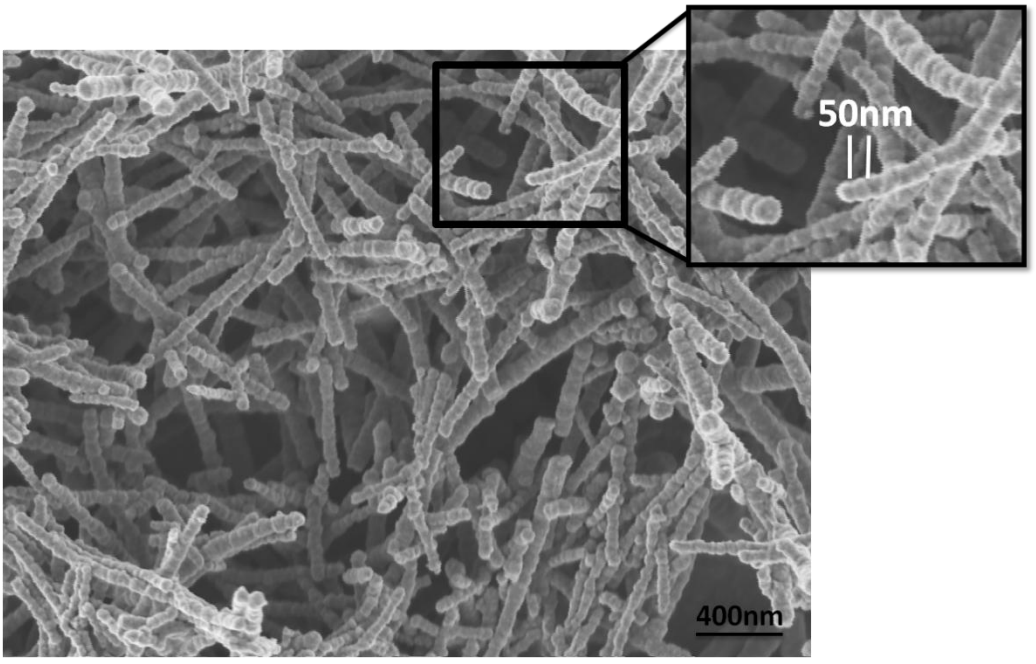

Fig. 17. SEM image of APO fibers showing the development of a periodic pitch along their contour length.

3.3. DLS measurements

Figure 18 shows the results of the CONTIN analysis of DLS data on the different time-aliquots of the developing apoferritin fibrils. With

increasing heating time, different populations of larger size aggregates develop. At 5 minutes heating time, two different populations can be identified. One is centred between 3-60nm, in agreement with the initials oligomers/aggregates observed with AFM (Figure 11). The second peak is very broad suggesting that the aggregates are polydisperse in size. A higher particle size distribution is found after 3 hours in agreement with the first long fibers appearance. As the heating time increases, the population of protein oligomers decreases and the population associated with fibrils increases. At 9 hours three different signals can be observed which correspond with three different populations observed at AFM: short oligomers, medium fibers and long fibers. At 24h a bigger particle size is found, corresponding with more aggregated fibers as shown by AFM. In this analysis, it has been demonstrated the conversion of the protein-monomers into larger aggregates, anticipating that these are of fibrillar type.

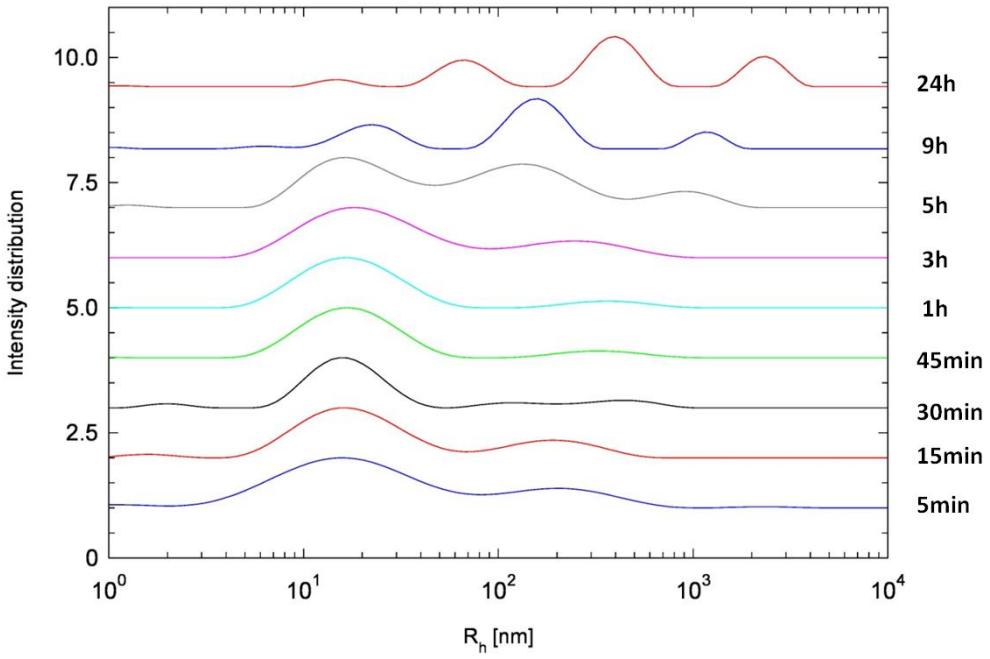

Fig. 18. Particle size distribution (hydrodynamic radius) at different heating times as extracted by CONTIN analysis of DLS data.

3.4. Gel electrophoresis

To explore further whether peptide fragments could be responsible for the formation of the amyloid aggregates observed in the present case, we searched for their presence at different incubation times using SDS-PAGE, as shown in Figure 19. The original apoferritin monomer protein band at 20 KDa is still visible after 1h of incubation, although its amount is already considerably decreased compared with the initial conditions. Appearance of the 11-13 kDa bands in these early stages of incubation is consistent with the partial hydrolysis. In this case, one band around 5kDa can also be found, indicating that hydrolysis is taking place at a much faster kinetics of fragmentation. At 3h, the native protein band at 20KDa has disappeared in concordance with the formation of rigid long fibers. At 24h of incubation the native apoferritin protein is completely hydrolyzed and only low-molecular-weight peptide fragments (<5KDa) are present in the system. These results confirm the decisive role of protein hydrolysis in the formation of amyloid fibrils.

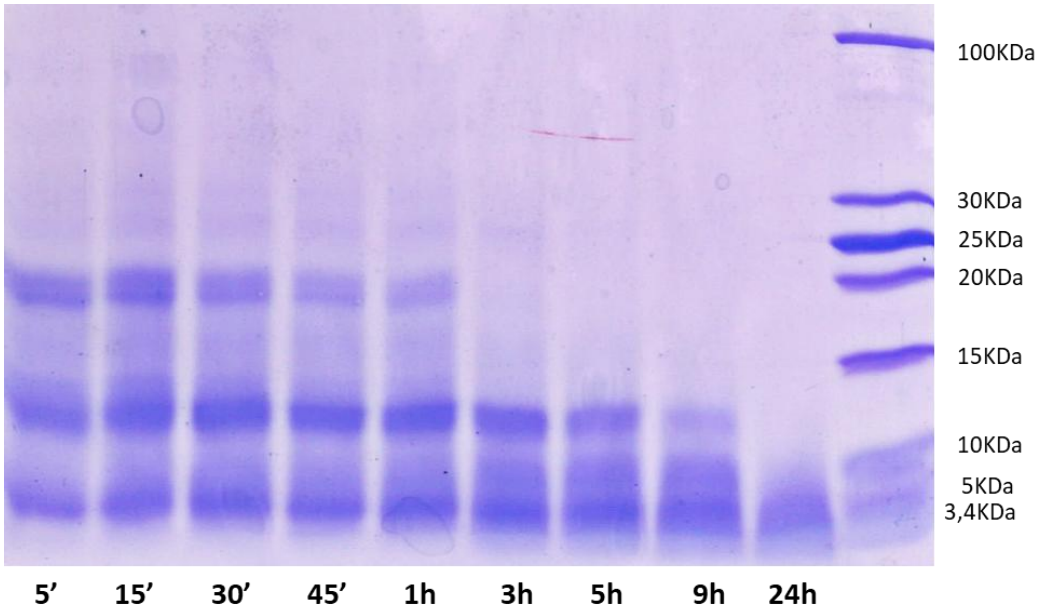

Fig. 19. SDS-PAGE of protein after different incubation times at pH 2 and 90°C.

3.5. ThT analysis

The kinetics of APO aggregation was investigated by Thioflavin-T (ThT) fluorescence assays. Formation of amyloid aggregates was detected as enhancement of the ThT fluorescence intensity, with a characteristic band centered at ~482nm. Figure 20 shows the increase in ThT intensity fluorescence upon binding to amyloid fibrils. In the early stages of aggregation fluorescence intensity increases, corresponding to small aggregates formation. During this first hour there is a short lag phase, in which the fluorescence remained low. At incubation times above 3 h, when the first fibers are formed, the ThT fluorescence intensity increases and reaches a maximum level at 24 h, when mature fibrils are predominantly formed.

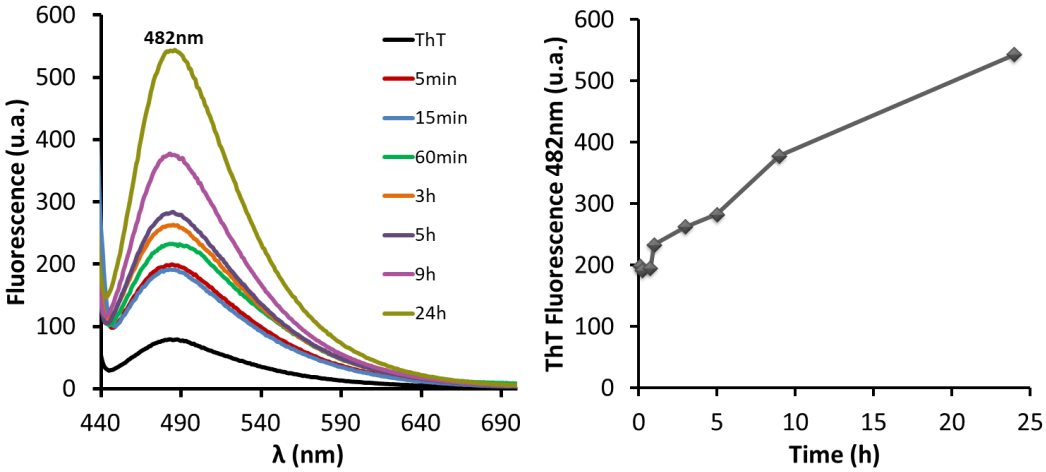

Fig. 20. Fibrillation kinetics of APO fibers formation, monitored by ThT fluorescence.

3.6. CD measurements

The changes in the secondary structure with incubation time have also been followed by circular dichroism (CD, Figure 21). The native globular APO protein incubated for 5 min shows a regular structure with a peak at 210 nm and a diffuse bump in the 220-230 nm region, characteristic

of the α-helical content of the folded native protein. A structural change already occurs between 5min and 1h of incubation at pH 2, and at 3h a pronounced reduction in helical content, relative to the initial spectrum, is evident based on the decrease in ellipticity over a wide range of wavelengths, consistent with the ThT observations. Between 3 and 24h, a shoulder observed around 217 nm suggests the presence of β-sheet structures, as expected for the observed well-ordered amyloid aggregates.

The α-helix and β-sheet content for the different apoferritins determined by CDPRO software is compiled in Table 2. Upon time, the apoferritin protein loses α-helix content and gains β-sheet structure, supporting a pathway towards amyloid fibril formation.

Therefore, APO fibrillation process is revealed by time-resolved CD, in which the overall of its secondary structure evolves following a remarkably pathway from the α-helical to the β-sheet secondary structure.

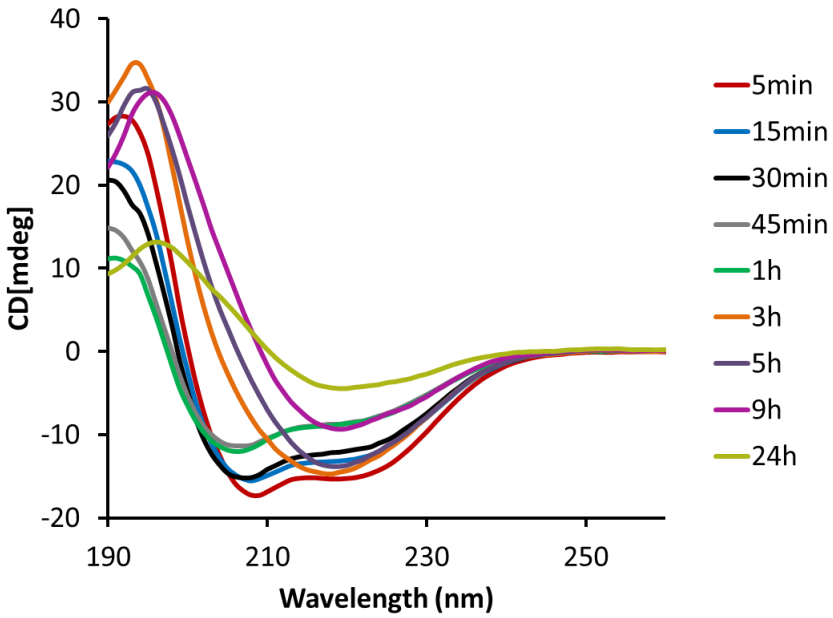

Fig. 21. Far-UV circular dichroism of APO after different incubation times at pH 2 and 90°C.

Time	α-helix	Strand	turns	others
5min	15.4	31.9	21.4	31.2
15min	8.5	37.7	21.1	32.7
30min	7.8	40	20.8	31.4
45min	6	42.6	21.4	30
1h	6	42.2	21.4	32.1
3h	5.7	39.3	22.4	32.6
5h	4.6	40.6	22.2	32.6
9h	3.7	41.9	21.8	32.4
24h	3.6	41.7	21.4	33.3

Table 2. Estimation of protein secondary structure of APO after different incubation times at pH 2 and 90°C. The content is expressed in %.

3.7. FLIM-PIE measurements

To obtain additional information on the nature of the oligomers formed in the apoferritin fibrilization process and their time evolution, we explored the use of single-molecule resolution fluorescence microscopy, as a powerful tool to monitor assembly processes.[30,31,32] We employed an advanced fluorescence lifetime imaging microscopy with pulsed interleaved excitation scheme (FLIM-PIE, see Materials and Methods). The FLIM microscopy presents many advantages compared to conventional fluorescence microscopy, specially for quantitative measurements.[33,34] FLIM-PIE is an imaging technique with single-molecule resolution that allows precise identification of different types of oligomers by focusing on the intra-oligomer energy transfer (FRET) from monomers labelled with donor and acceptor fluorophores. The oligomers are unequivocally detected through the simultaneous reconstruction of the donor, FRET, and directly excited acceptor images and the intra-oligomer FRET efficiency, *E*, is estimated through the donor fluorescence lifetime (τ_{A488}).[35,36] Using this technique, we studied the kinetics of APO aggregation at different

incubation times (Figures 22a and 23). We labelled the apoferritin subunits with a dye pair capable of undergoing FRET when in close proximity. We employed ATTO 488 (A488, as the donor) and ATTO 647 (A647, as the acceptor). The Förster distance, R_0, for this pair of fluorophores is 51 Å, which allowed us to detect the formation of aggregates at the single-molecule level based on the FRET efficiency, E, when the labelled monomers interacted with each other.

The incubation of equimolar mixtures of the donor- and acceptor-labelled APO subunits under fiber formation conditions for several hours resulted in the effective co-aggregation and formation of mature fibrils. The presence of the dye molecules does not alter the fundamental features of the aggregation reaction or the appearance of the resulting fibrillar aggregates as shown by TEM (Figure 24) and SDS-electrophoresis (Figure 25). The distribution of FRET values appears to vary with the size of the oligomers (Figure 22b), revealing three dominant populations, a low-FRET population with $\tau_{488} > 3$ ns ($E < 0.27$); a mid-FRET population with $\tau_{488} = 2.2$ ns ($E = 0.46$); and a high-FRET population with $\tau_{488} = 1.1$ ns ($E = 0.73$). The mid-FRET population appeared after 1 hour of incubation, whereas the high-FRET aggregates arose after 9 hours of incubation time. These results are in perfect consonance with those previous presented by TEM, AFM and DLS, when three main populations could be distinguished: small aggregates, medium fibers and long rigid fibers. Of particular importance in this study has been the identification of a slow conversion from the initially formed and readily degradable oligomers to compact and highly structured oligomers in concordance with an increase in the amyloid-like β sheet structures.

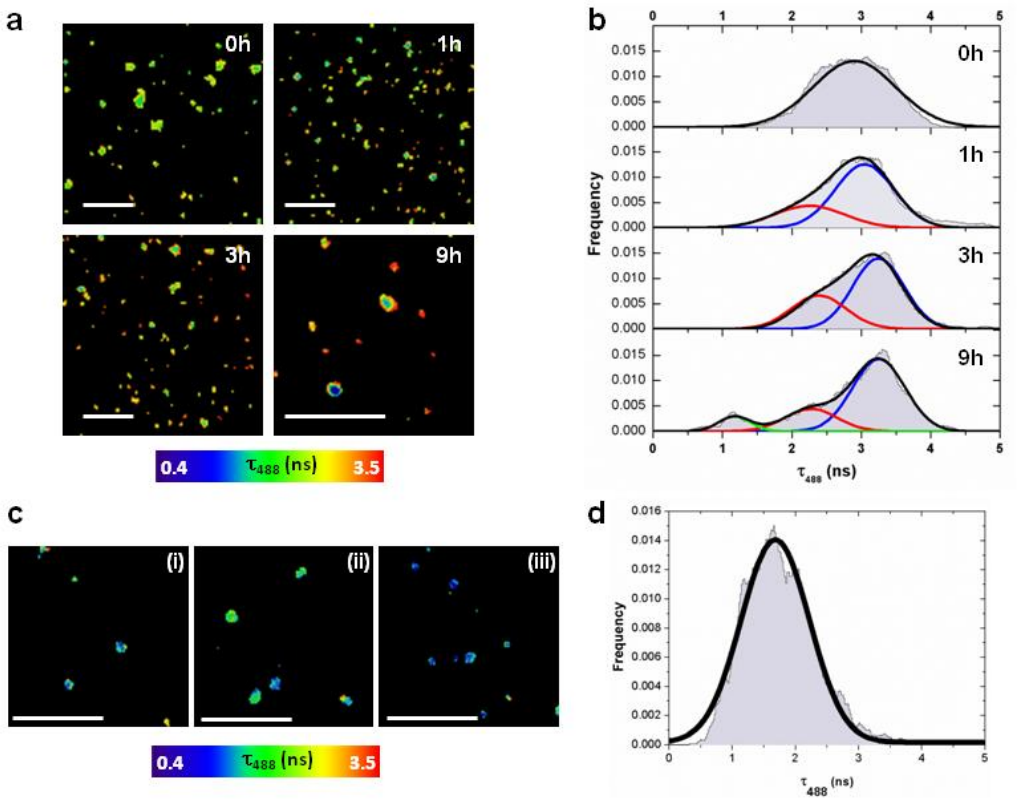

Fig. 22. a) Representative donor (A488) FLIM images of APO aggregates after different incubation times. b) Frequency histograms of τ_{A488} values in APO aggregates, averaged for at least 10 different images. c) Representative donor FLIM images of insoluble aggregates found in filtered samples of APO incubated for 9 h. d) The corresponding frequency histogram of τ_{A488} values in insoluble APO aggregates described in c), averaged over 10 different images. Scalebars represent 5 μm.

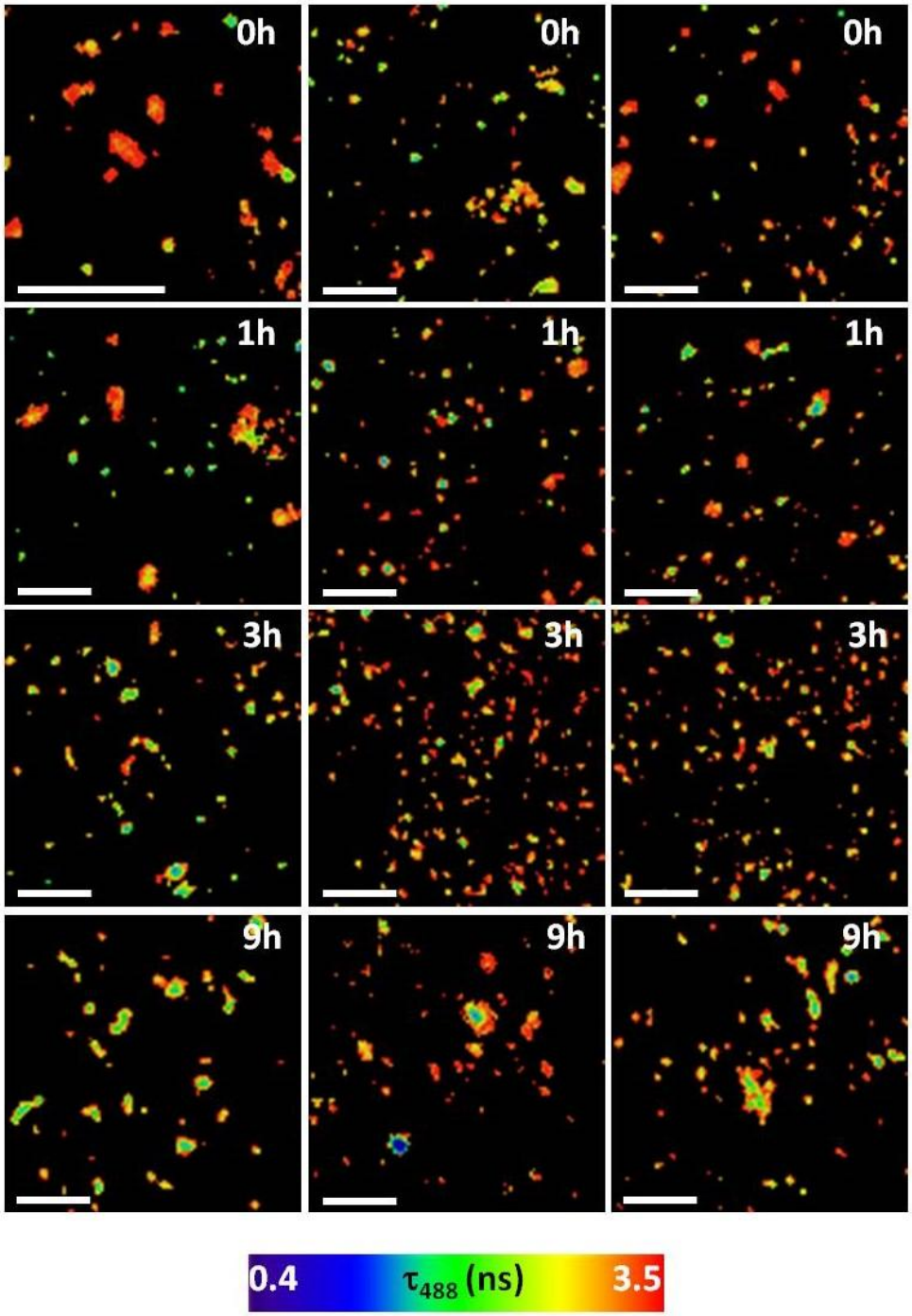

Fig. 23. Examples of donor (A488) FLIM images of APO aggregates after different incubation times. Scalebars represent 5μm.

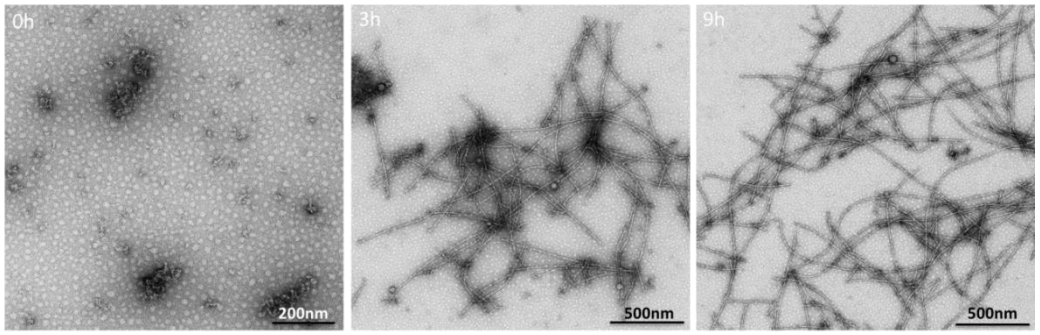

Fig. 24. TEM images of functionalized ATTOS-APO incubated at different times.

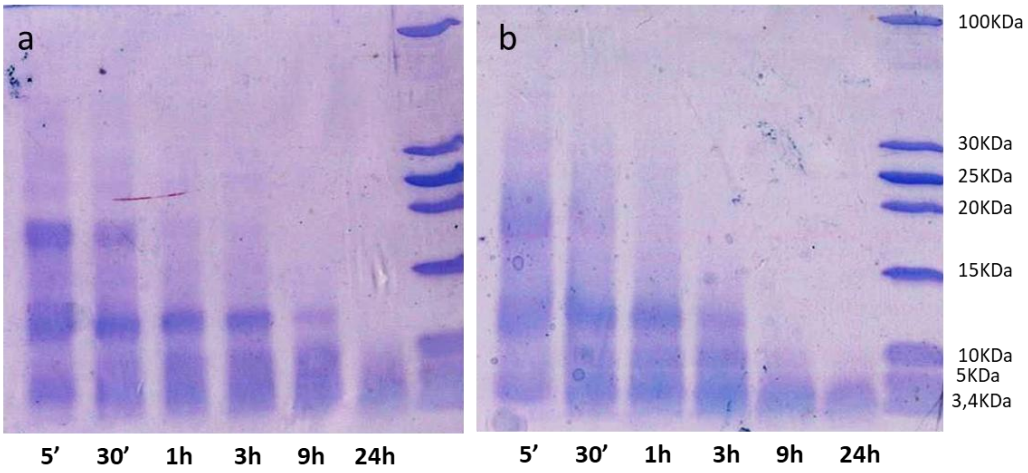

Fig. 25. SDS-PAGE electrophoresis of a) APO and b) ATTOS-APO incubated at different times.

Interestingly, when the 9 h-incubated solution was filtered, and the remaining insoluble aggregates were imaged the single remaining population was that of high-FRET (Figure 22c), exhibiting an average τ_{A488} = 1.6 ns (E = 0.61, Figure 22d). This result confirms that the low-FRET and most of the mid-FRET aggregates are still soluble. However, the detected population likely contains certain contribution of mid-FRET aggregates, so that the average distribution is broader and shifted to slightly larger τ_{A488} values. The presence of aggregates with different compactness, and therefore FRET efficiency, is in line with the heterogeneous nature of the

amyloid fibrillization and the formation of fibrils with polymorphism in the final structures.

4. Conclusions

1D nanofibers have been prepared either using apoferritin or β-lactoglobulin proteins. This is the first time that a wire-like, micrometer-sized structure with persistence length of several microns formed by the heat treatment of apoferritin is described. Optimizing and controlling the experimental conditions such as temperature, pH, incubation time, protein concentration and stirring, the morphology and diameter size can be varied. An incubation time of 9 h, pH of 2, 90 °C, a protein concentration between 0.05-0.2wt% and an agitation at 90rpm are the optimal conditions for the formation of wire-like fibers.

In a second step, we have been able to demonstrate by combining different techniques that the formation of apoferritin amyloid-like fibers starts from short oligomers aggregates. AFM statistical analysis, SDS-PAGE and CD all provide convincing evidence that protein unfolding and complete hydrolysis are essential for the formation of large laminated aggregates and that small peptides fragments (<5 kDa) participate in the formation of these fibrils. AFM, TEM and DLS measurements were able to resolve and identify different individual stages of the fibrillation process. Moreover, the novel technique FLIM-PIE provided single-molecule information about the apoferritin kinetics process that allowed precise identification of different types of oligomers with time. All these results open a new perspective in the understanding of apoferritin fibrillation.

Protein fibrils resulting from the assembly of proteins or peptides into long, highly ordered fibrillar structures are emerging as one of the fastest growing scientific areas, because of their functional versatility and broad applications in Biology (amyloid-like fibers are associated with

numerous neurodegenerative diseases) and in Nanotechnology (as templates for the fabrication of metal nanowires and functional polymer nanotubes). In that sense apoferritin fibers could find similar applications.

5. References

[1] M. G. Warner, J. E. Hutchison, *Nat. Mater.*, **2003**, *2*, 272.

[2] M. Masetti, H. Xie, Ž. Krpetić, M. Recanatini, R. a. Alvarez- Puebla, L. Guerrini, *J. Am. Chem. Soc.*, **2015**, *14*, 469.

[3] J. Pate, F. Zamora, S. M. D. Watson, N. G. Wright, B. R. Horrocks, A. Houlton, *J. Mater. Chem. C.*, **2014**, *2*, 9265.

[4] X. B. Zhao, F. Pan, H. Xu, M. Yaseen, H. H. Shan, C. A. E. Hauser, S. G. Zhang, J. R. Lu, *Chem. Soc. Rev.*, **2010**, *39*, 3480.

[5] G. Fichman, L. Adler-Abramovich, S. Manohar, I. Mironi-Harpaz, T. Guterman, T. Seliktar, P. Messersmith, E. Gazit, *ACS Nano*, **2014**, *8*, 7220.

[6] I. Cherny, E. Gazit, *Angew. Chem., Int. Ed.*, **2008**, *47*, 4062.

[7] T. Scheibel, R. Parthasarathy, G. Sawicki, X. M. Lin, H. Jaeger, S. L. Lindquist, *Proc. Natl. Acad. Sci. U. S. A.*, **2003**, *100*, 4527.

[8] A. MaHam, Z.W. Tang, H. Wu, J. Wang, Y.H. Lin, *Small,* **2009**, *5*, 1706.

[9] X. Zan, S. Feng, E. Balizan, Y. Lin, Q. Wang, *ACS Nano*, **2013**, *7*, 8385.

[10] A.K. Nair, A. Gautieri, S.W. Chang, M.J. Buehler, *Nat. Commun.*, **2013**, *4*, 1724.

[11] A. Seidel, O. Liivak, S. Calve, J. Adaska, G. Ji, Z. Yang, D. Grubb, D.B. Zax, L.W. Jelinski, *Macromolecules*, **2000**, *33*, 775.

[12] S. Keten, Z. Xu, B. Ihle, M. J. Buehler, *Nat. Mater.*, **2010**, *9*, 359.

[13] Z. Xu, R. Paparcone, M. J. Buehler, *Biophys. J.*, **2010**, *98*, 2053.

[14] C. Li, A. K. Born, T. Schweizer, M. Zenobi-Wong, M. Cerruti, R. Mezzenga, *Adv. Mater.*, **2014**, *26*, 3207.

[15] S. J. Eichhorn, A. Dufresne, M. Aranguren, N. E. Marcovich, J. R. Capadona, S. J. Rowan, C. Weder, W. Thielemans, M. Roman, S. Renneckar, W. Gindl, S. Veigel, J. Keckes, H. Yano, K. Abe, M. Nogi, A. N. Nakagaito, A. Mangalam, J. Simonsen, A. S. Benight, A. Bismarck, L. A. Berglund, T. Peijs, *J. Mater. Sci.*, **2010**, *45*, 1.

[16] M. M. Walker, T. E. Dennis, J. L. Kirschvink, *Curr. Opin. Neurobiol.*, **2002**, *12*, 735.

[17] P. Alivisatos, *Nat. Biotechnol.*, **2004**, *22*, 47.

[18] B. Pelaz, S. Jaber, D.J. de Aberasturi, V. Wulf, T. Aida, J.M. de la Fuente, J. Feldmann, H.E. Gaub, L. Josephson, C.R. Kagan, N.A. Kotov, L.M. Liz-Marzán, H.

Mattoussi, P. Mulvaney, C.B. Murray, A.L. Rogach, P.S. Weiss, I. Willner, W.J. Parak, *ACS Nano*, **2012**, *6*, 8468.

[19] F.G. Pearce, S.H. Mackintosh, J.A. Gerrard, *J. Agric. Food Chem.,* **2007**, *55,* 318.

[20] J. Adamcik, J. Jung, J. Flakowski, P. De los Rios, G. Dietler, R. Mezzenga, *Nat. Nanotechnol*., **2010**, *5*, 423.

[21] D. Berg, G. Becker, P. Riederer, O. Rieß, *Neurotoxicity Res*., **2002**, *4*, 637.

[22] F. Carmona, O. Palacios, N. Galvez, R. Cuesta, S. Atrian, M. Capdevila, J.M. Domınguez-Vera, *Coord. Chem. Rev*., **2013**, *257*, 2752.

[23] J.M. Jung, G. Savin, M. Pouzot, C. Schmitt, R. Mezzenga, *Biomacromolecules,* **2008**, *9*, 2477.

[24] E.H.C. Bromley, M.R.H. Krebs, A.M. Donald, *Faraday Discuss*., **2005**, *128*, 13.

[25] W. S. Gosal, A. H. Clark and S. B. Ross-Murphy, *Biomacromolecules*, **2004**, *5*, 2408.

[26] I. Usov, R. Mezzenga, *Macromolecules*, **2015**, *48*, 1269.

[27] C. Lara, S. Gourdin-Bertin, J. Adamcik, S. Bolisetty, R. Mezzenga, *Biomacromolecules,* **2012***, 13*, 4213.

[28] C. Lara, J. Adamcik, S. Jordens, R. Mezzenga, *Biomacromolecules,* **2011***, 12,* 1868.

[29] J. Adamcik, R. Mezzenga, *Macromolecules,* **2012**, *45*, 1137

[30] S. Onogi, H. Shigemitsu, T. Yoshii, T. Tanida, M. Ikeda, R. Kubota I. Hamachi, *Nat. Chem.,* **2016**, *8,* 743.

[31] A. Aliprandi, M. Mauro, L. De Cola, *Nat. Chem.,* **2015**, *8,* 10.

[32] P. Bondia, R. Jurado, S. Casado, J. M. Domínguez-Vera, N. Gálvez, C. Flor, *Small,* **2017**, *13,* 1.

[33] A. Orte, J.M. Alvarez-Pez, M.J. Ruedas-Rama, *ACS Nano,* **2013**, *7,* 6387.

[34] M. K. Kuimova, S. W. Botchway, A.W. Parker, M. Balaz, H. A. Collins, H. L. Anderson, K. Suhling, P. R. Ogilby, *Nat. Chem.,* **2009**, *1,* 69.

[35] R. Jurado, F. Castello, P.Bondia, S. Casado, C. Flors, R. Cuesta, J.M. Domínguez-Vera, A. Orte, N. Gálvez, *Nanoscale,* **2016**, *8,* 9648.

[36] F. Castello, J. M. Paredes, M. J. Ruedas-Rama, M. Martin, M. Roldan, S. Casares, A. Orte, *Sci. Rep.*, **2017**, *7***,** 40065.

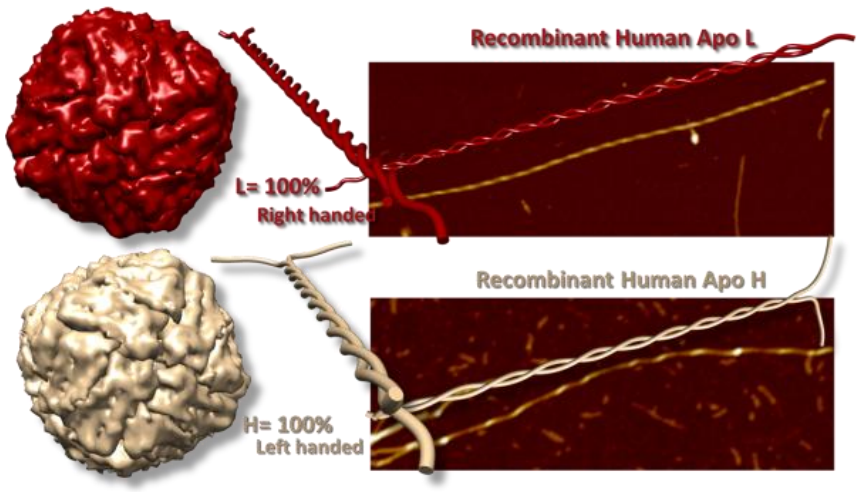

CHAPTER 4. RECOMBINANT HUMAN LIGHT AND HEAVY APOFERRITIN SUBUNITS DIRECT CHIRALITY IN APOFERRITIN FIBERS

1. Introduction

As reported previously, amyloids represent a class of biological one-dimensional nanostructure, which appears to be ubiquitous in Nature and shows promising potential for the area of artificial functional biomaterials.[1,2] They are usually related to human diseases, including numerous neurodegenerative disorders such as Parkinson's, Alzheimer's, Creutzfeldt–Jakob disease, and type II diabetes.[3,4] At the same time, amyloid forms of proteins also carry out useful functions in various biological systems such as algae adhesives, bacteria biofilm formation, and in humans, functional amyloid plays a vital role in physiological processes such as hemostasis and melanin synthesis.[5,6,7]

The hallmark of amyloid assemblies is a conformational transition of the constituent monomeric proteins into a β-sheet rich fibril. Morphological hetereogeneity in amyloid fibrils, such as tapes, twisted ribbons, helical fibers, or nanotubes-like fibers are increasingly emerging as a general feature of the self-assembly of proteins into fibrillar structures.[8] However, to date, the exact reason for protein folding or misfolding is often still unclear.

Amyloid heterogeneity is also demonstrated in their suprastructure. For example, it has been previously demonstrated the spontaneous inversion of chirality.[9,10] Understanding the 3D structure and chirality of polypeptide fibril suprastructures is a key issue because they are linked to its biochemical activity and associated toxicity,[11,12] and because once controlled it could be tuned to access novel synthetic protein-based nanomaterials. For example, Addadi *et al*.[12] studied the correlation among the suprastructural chirality, molecular structure, and molecular chirality of different (all-S) serum amyloid A (SAA) truncated peptides. They found that SAA_{2-9} amyloids have mostly helical morphology. Moreover, these helical fibers show both right-handed and left-handed helicity (Figure 1).

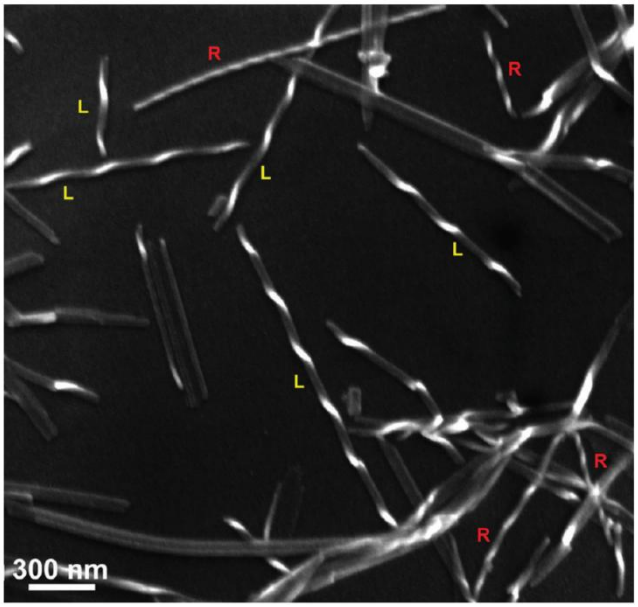

Fig. 1. SEM micrograph of SAA_{2-9} amyloid fibers demonstrating the existence of both left-handed (L) and right-handed (R) SAA_{2-9} amyloids.[12] Image from: N. Rubin, E. Perugia, S.G. Wolf, E. Klein, F. Mátl, L. Addadi, *J. Am. Chem. Soc.,* **2010**, *132*, 4242.

Apoferritin (APO) structure was described in the introductory chapter. Briefly, APO, the iron-free ferritin molecule, is a hollow globular protein composed of 24 poly-peptide subunits (~Mr 480 kDa) where Fe(III) is accommodated as a 5 nm-iron oxyhydroxide nanoparticle. In eukaryotes apoferritin organic shell is the product of the self-assembly of mainly two primary peptide subunits or chains: L "light" (~20 kDa), and H "heavy" (~21 kDa). Each subunit has been assigned a specific role: H chains display ferroxidase activity able to catalyze the oxidation of Fe(II) to Fe(III), while L chains have nucleation sites for iron oxyhydroxides nucleation.[13,14,15] The assembly of the H and L subunits into the 24-mer apoferritin capsid produces a variety of different ferritin molecules (isoferritins) whose H:L ratio is genetically controlled in each tissue (Figure 2).[14] Thus, tissues with iron storage function (liver and spleen) contain L-rich (up to 90 % of L subunits, $L_{21}H_3$) ferritins that may accommodate high iron amounts,

whereas in detox activity tissues (heart and brain) the number of H subunits increases (up to 50% of H subunits, $L_{12}H_{12}$), with the aim to catalytically oxidize Fe(II) to Fe(III), thus avoiding the formation of reactive-oxygen species.

Any disruption of the ferritin H/L ratio or a mutation in the H or L subunit is related in fact, to the origin of a pathology. [16,17] As an example, ferritin expression level and amount of Fe(III) stored have been reported to be altered in diseases such as Parkinson's, Alzheimer's[18] or acquired immunodeficiency syndrome (AIDS).[19,20] In addition, it has been latterly reported the prevalence of iron homeostasis in breast cancer stem cells, pointing towards iron and iron-mediated processes as potential targets against these cells.[21]

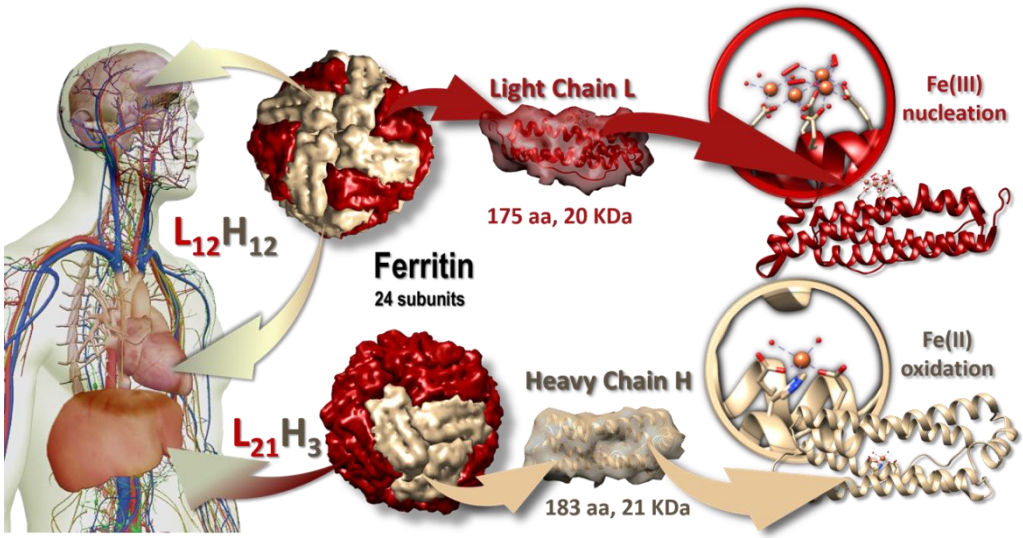

Fig. 2. Subunit composition for different human isoferritins. Human L-subunits are represented in red and human H-chains in grey. The average subunit composition for liver ($L_{21}H_3$) and brain ($L_{12}H_{12}$) ferritins are shown. The ferroxidase center buried inside the α-helix bundle of the ferritin H chain as well as the nucleation center for ferritin L chain are also displayed.

In chapter 3, it has been reported that the globular Horse Spleen Apoferritin, hereafter L-rich APO protein (up to 90% L subunits) can

undergo a fibrillation process, similar to other globular proteins, to form amyloid-like fibers under appropriated experimental conditions. Herein, we present how H or L apoferritin primary subunits, with a peptide sequence coincidence of only 54-57%[13] can drive the final chirality and polymorphism of apoferritin amyloid-like fibers. We therefore compare the apoferritin fibers formed in two different cases: starting from pure Recombinant Human Apoferritin H (H APO) and from pure Recombinant Human Apoferritin L (L APO) with those formed by Horse Spleen Apoferritin (L-rich APO), considered as the model of mammalian ferritin.

2. Formation of human L and H APO fibers

We have reported previously that L-rich APO protein forms fibrillar structures similar to β-lactoglobulin and other globular proteins when submitted to appropriate treatment. The L-rich APO fibers morphology was characterized in detail using super resolution AFM revealing details of the structure at the single fiber length scale.

The more striking feature after AFM observation is the protein fibers helicity. Usually, amyloid-like fibrils obtained by different aggregation mechanisms and starting from globular and non-globular proteins do show evidence of helical structures with a left-handed chirality.[8,22] However, for L-rich APO the observed fibers chirality is right-handed for the 90% of analyzed fibers (Figure 3), with a remaining 10% of left-handed fibers and tube like fibers (Figure 4). To our knowledge, this right-handed fiber chirality shown by apoferritin protein, since the very first steps of its fibrillization process, has not been previously observed for native globular proteins. Inversion on handedness from left- to right- with processing conditions or with incubation time has been reported for insulin and albumin but right-handed amyloid fibrils have only been described for amyloid-forming small peptides.[9,10,12,23]

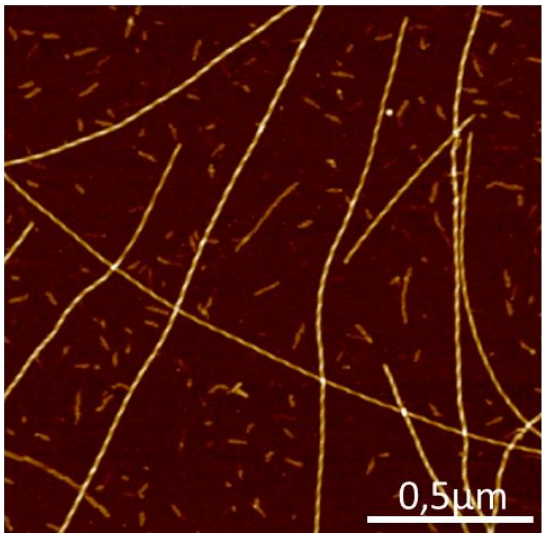

Fig. 3. AFM height images of Horse Spleen Apoferritin (L-rich APO) amyloid fibrils.

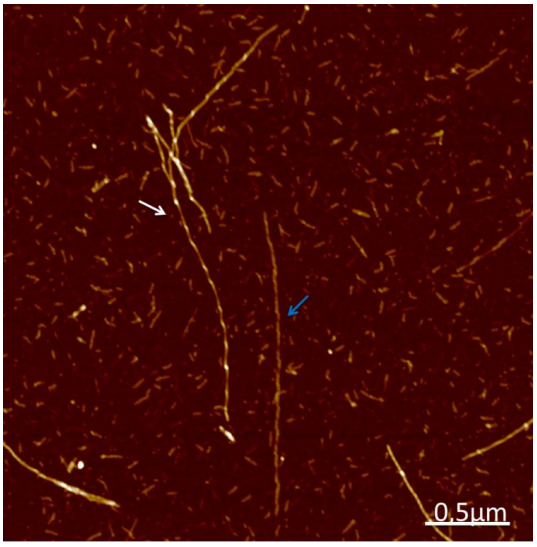

Fig. 4. AFM image showing different morphologies of long fibers: left-handed fibers (white narrow) and tube-like fibers (blue narrow).

Taking into account the L:H composition (light:heavy chains) for L-rich APO, one can expect that subunit peptide sequence may be at the origin of the observed different chirality. Thus, using the same experimental conditions (see Materials and Methods), we prepared fibers starting from both, pure human L APO and human H APO. Interestingly, the observed

fiber chirality was nearly a 100% of right-handed for the L APO sample and mostly left-handed for the H APO one (Figures 5 and 6).

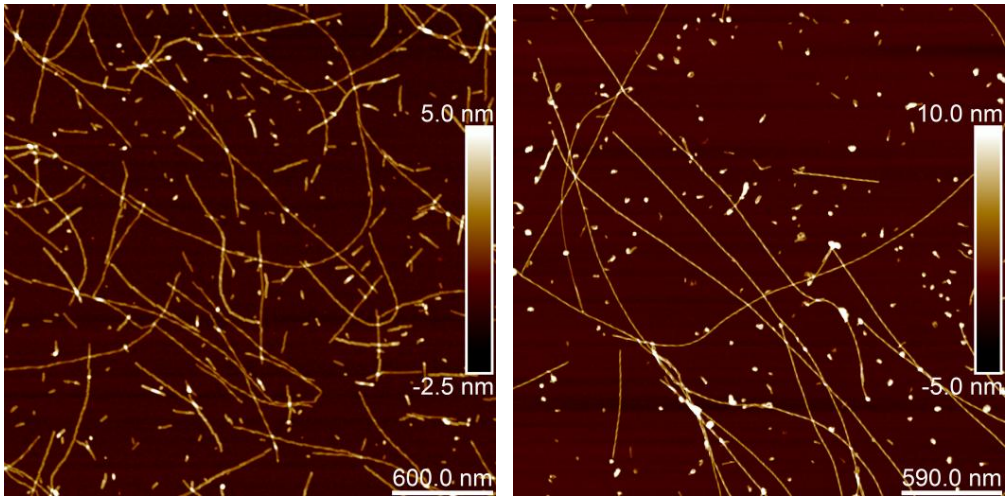

Fig. 5. AFM height images of pure Recombinant Human Apoferritin H (left) amyloid fibrils and pure Recombinant Human Apoferritin L (right) amyloid fibrils.

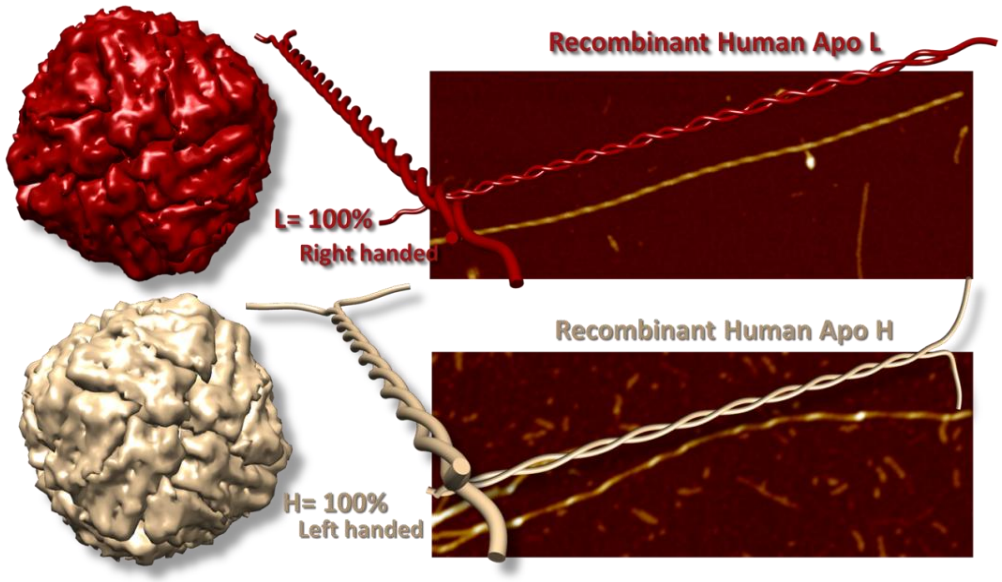

Fig. 6. Scheme showing fibers handeness.

In the case of H APO fibers, morphologies other than left-handed fibers were observed: multistrand tape (rarely) and nanotube-like polymorphs (Figure 7).

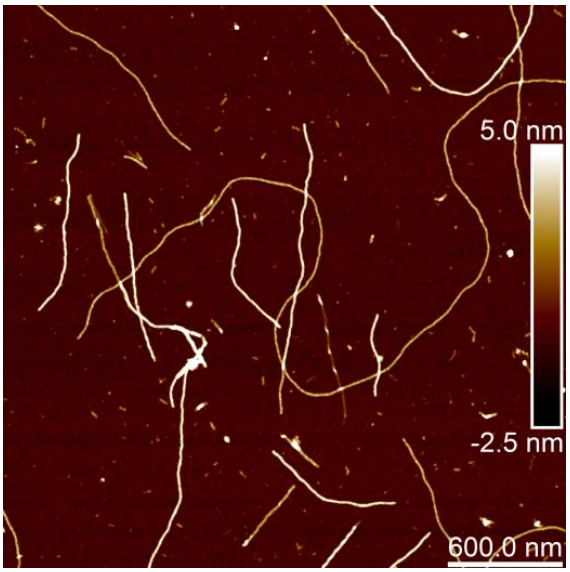

Fig. 7. AFM height images of Recombinant Human Apoferritin H amyloid fibrils showing nanotube-like polymorphs.

Statistical analysis of AFM images are reported in Table 1 using the in-house-developed processing and tracking software "FiberApp". Thus, morphological parameters such as total contour length, average height, or pitch size were evaluated, in analogy with previous work from Chapter 3 and with other classes of amyloids studies.[24]

		H APO	L APO	L-rich APO
Right-handed fibers	N	1	77	158
	Height	4.1 ± 1.2	6.4 ± 1.8	6.6 ± 1.1
	Length	1760	2369.1 ± 1156.5	1738.9 ± 1064.3
	Pitch	73.31	47.91	47.89
	Lp	-	2649.4 ± 45.3	3816.25 ± 58.18
Left-handed fibers	N	171	-	8
	Height	3.4 ± 0.7	-	5.2 ± 1.4
	Length	2189.1 ± 1526.8	-	665 ± 283.7
	Pitch	101.8 - 92.5	-	127.54 - 92.76
	Lp	2732.9 ± 31.42	-	-
Tube-like fibers	N	12	4	15
	Height	4.7 ± 0.8	8.1 ± 2.4	5.1 ± 1.3
	Length	3265 ± 2723	702.9 ± 322.2	816 ± 378.8
	Lp	1335.7 ± 24.5	7566.4 ± 30.1	7486.5 ± 118.9

Table 1. Basic structural information about H APO, L APO and L-rich APO fibers. N=number of filaments tracked. All measurements are expressed in nanometers.

Right-handed and left-handed fibers differ significantly in terms of their average height: 3.4 ± 0.7nm for H APO and 6.4 ± 1.8nm for L APO. Pitch size estimation with height periodicity for the 2 types of chiral fibers was performed by fast Fourier transform (FFT) analysis[22] of the height profiles. Left-handed H APO fibers present a significantly higher helical periodicity (92 – 102 nm, Figure 8) compared to right-handed L APO and L-rich APO fibers (~ 48 nm). Left-handed H APO fibers can be therefore easily distinguished as they exhibit shorter height and longer pitch. On the contrary, fibers contour length does not seem to be a key factor when distinguishing fibers, since its value varies between 1 and 3 μm for all cases. It is important to highlight that the big errors associated to the contour length are due to the fibers length heterogeneity.

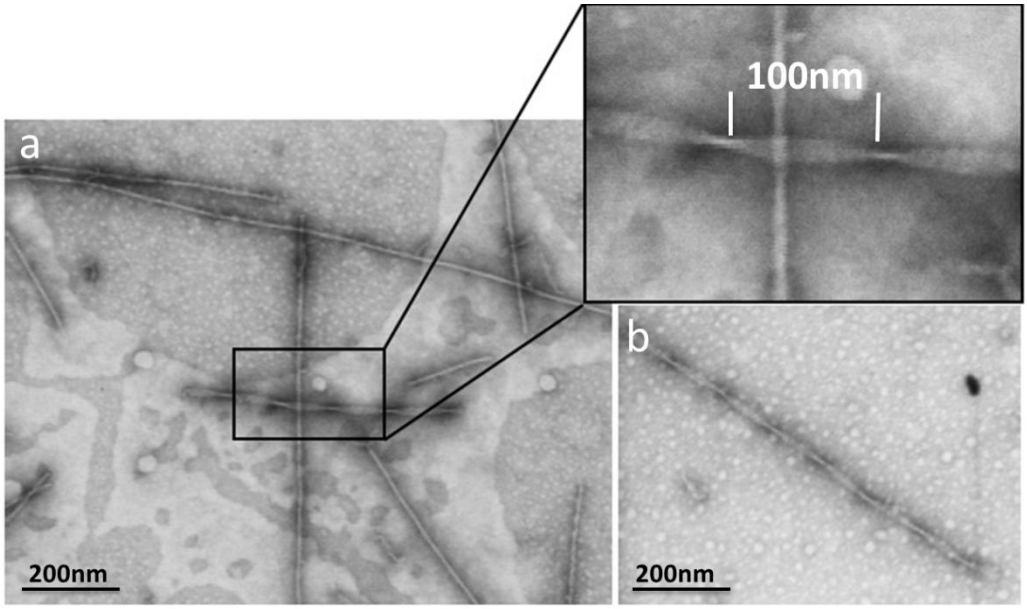

Fig. 8. SEM images showing the pitch in left-handed H APO fibers.

The persistence length (Lp) of the fibers was extracted from the statistical analysis. Lp was described in chapter 3 as the length above which thermal fluctuations can buckle a rod-like polymer, and it is therefore a measure of the elastic properties of a molecule. Rigid fibrils with higher Lp values have a conformation of right-handed helicates for L APO, while H APO fibers can be described as slightly more flexible left-handed fibers.

3. TEM study

We investigated the topology and morphology of L-rich APO, H APO and L APO fibrils formed at the same conditions by high resolution TEM analysis. Figure 9 shows that no morphological differences could be observed by this kind of microscopy. Although the helical structure of the fibers can be intuited, this technique does not allow a deeper study of fibers morphology or in determining if they are left or right-handed. However, this technique allowed confirming the optimal formation of fibers.

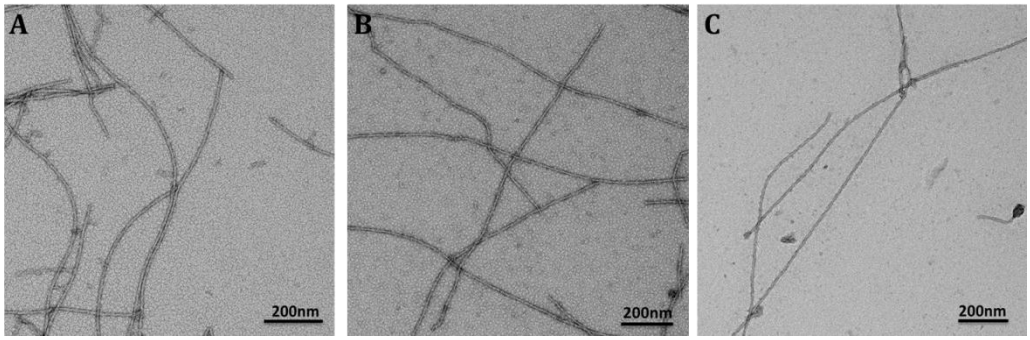

Fig. 9. TEM images of L-rich APO (a), H APO (b) and L APO (c) fibrils.

4. Electron tomography analysis

To further investigate the morphology and to unveil the three-dimensional (3D) organization at nanometric scale of apoferritin fibers, high resolution electron tomography (ET) experiments were performed. Like for discrete molecules, no single technique is sufficient to completely characterize the helical structure both in solution and in the dried state.

Electron tomography has proven to be a powerful tool for obtaining detailed 3D structures and therefore for the characterization of macro-molecular assemblies and different nanostructures at very high resolution.[25,26,27,28,29] Electron tomography is an extension of traditional transmission electron microscopy and uses a transmission electron microscope to collect the data. In the process, a beam of electrons is passed through the sample at incremental degrees of rotation around the center of the target sample. This information is collected and used to assemble a three-dimensional image of the target (see Materials and Methods). For biological applications, the typical resolution of ET systems is in the 5–20 nm range, suitable for examining supra-molecular multi-protein structures.[30] With this technique, measurements such as width, height or length can be extracted with sufficient accuracy from the reconstructions. Therefore, we used electron tomography to examine the 3D structure of L-rich APO fibers and to further investigate the chirality of pure H APO and pure L APO fibers.

In a first step, electron tomography analysis was performed in the high angle annular dark field scanning transmission electron microscopy (HAADF-STEM) for the Horse Spleen Apoferritin (L-rich APO) fibers. HAADF-STEM electron tomography series were performed on the same stained samples by acquiring images from −70° to 70° each 5°.

Orthoslice (XY plane, Figure 10b) extracted from the reconstructed volume of an isolated L-rich APO fiber (Figure 10a) clearly shows its helical structure. Interestingly, this fiber contains a pair of two, intercrossed strands, each with a helical repeating substructure. Analyses of two horizontal planes are shown in Figures 10c and 10d. The images show 2 dots corresponding to 2 strands separated by a gap and 1 dot when going through an intercrossed point.

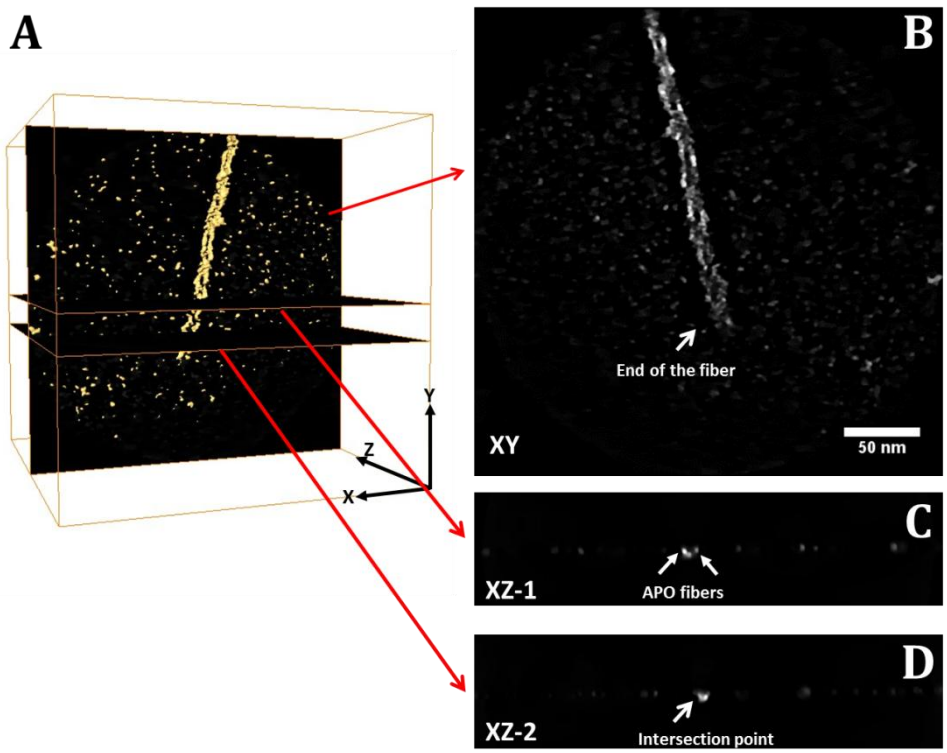

Fig. 10. Electron tomography 3D reconstruction of a single L-rich APO fiber (a) and XY (b) and XZ planes (c, d) extracted from the reconstructed volume.

Lateral dimensions of these two strands are in concordance with the TEM images, i.e., thickness of 10-15 nm and a gap of around 7nm (Figure 11b). The intensity profile in Figure Xb shows actually the double stranded nature of the fibers. In order to determine the periodicity of these intersection points (which correspond to the fiber pitch and where only 1 dot was observed), XZ planes along the fiber (Figures 11c) were extracted from different fibers. As an example, Figure 11c shows the pitch value and the XZ planes extracted from a single fiber. These image displays a L-rich APO fiber in which it can be distinguished the intersection points corresponding to the turns of the helical fiber with a pitch value around 50nm (Figure 11b, down). This pitch value is in total concordance with the previously described in Chapter 3.

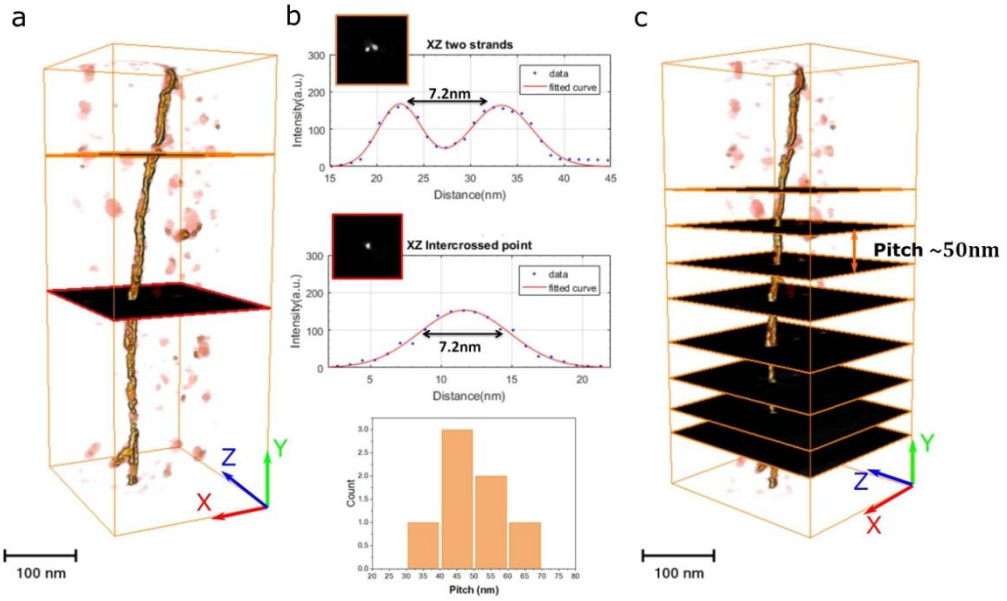

Fig. 11. Electron tomography 3D reconstruction of a single L-rich APO fiber (a) XZ planes intensity profiles of two strands and an intercrossed point (b), average value of pitches measured (b, down) and XZ planes on the 3D reconstruction of a L-rich APO fiber showing its pitch (c).

The nanometric-level detailed structure of these helical fibers is difficult to discern by TEM images, which are two-dimensional density projections, although they could be rarely observed as shown in Figure 12. However, the double stranded helical structure as well as the twisted nature of the paired fibrils, are definitely revealed when the assembly is resolved by 3D tomography.

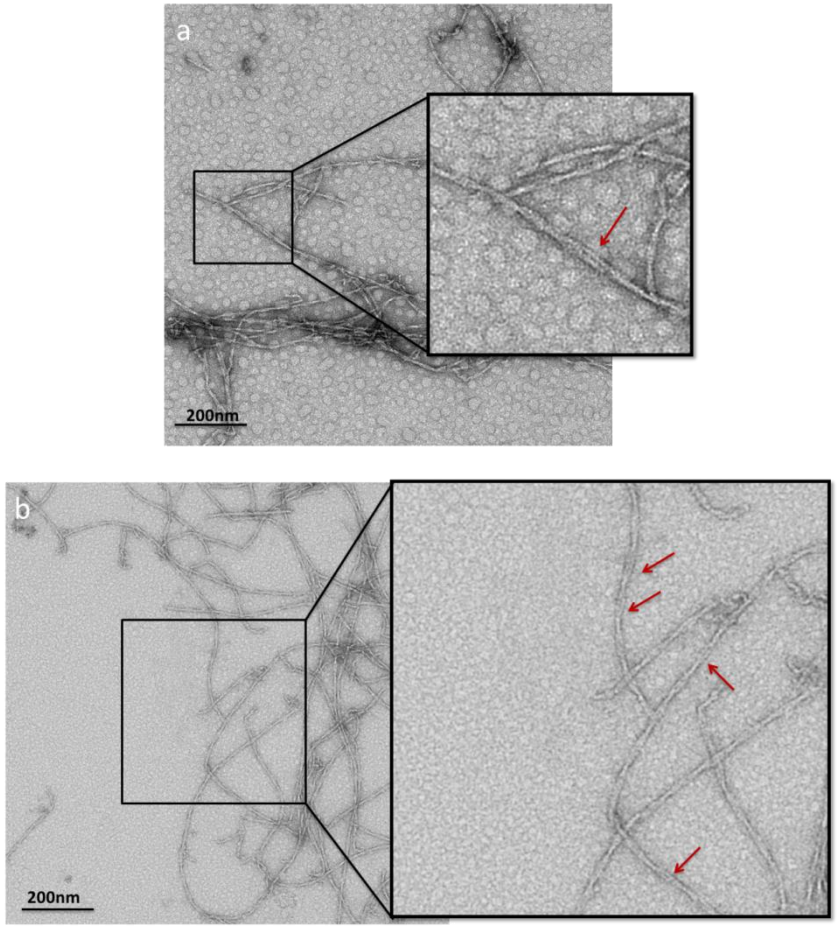

Fig. 12. Contrasted TEM images of L-rich APO fibers demonstrating that fibers are formed by two stranded-fibers.

H APO and L APO fibers were additionally analyzed by electron tomography. Figure 13a represent XY and XZ planes extracted from the 3D reconstructed volume and the corresponding 3D reconstruction of a single

H APO fiber. The intensity profile shows that the gap width is around 7 nm and each strand width coincides with a value of 3.4-4 nm (Figure 13b). Periodicity values between 80-100 nm were measured along the fibers. Again, these values are in concordance with those previously presented for left-handed H APO fibers (see Figure 8).

Similar procedure was performed for L APO fibers. Figure 13c shows the XY planes extracted from the reconstructed volume and the corresponding 3D reconstruction of a single L APO fiber. In this case, XY plane shows different intersection points along the fiber equivalent to the images extracted from L-rich APO fibers. In fact, the mean pitch value around 50nm is in concordance with the extracted value for L-rich APO. The gap width is around 10 nm and each strand width coincides with a value of 4-5 nm (Figure 13b, right). We emphasize that the mean pitch values obtained by 3D reconstruction from ET are in excellent agreement with the periodicity values obtained from AFM statistical analysis.

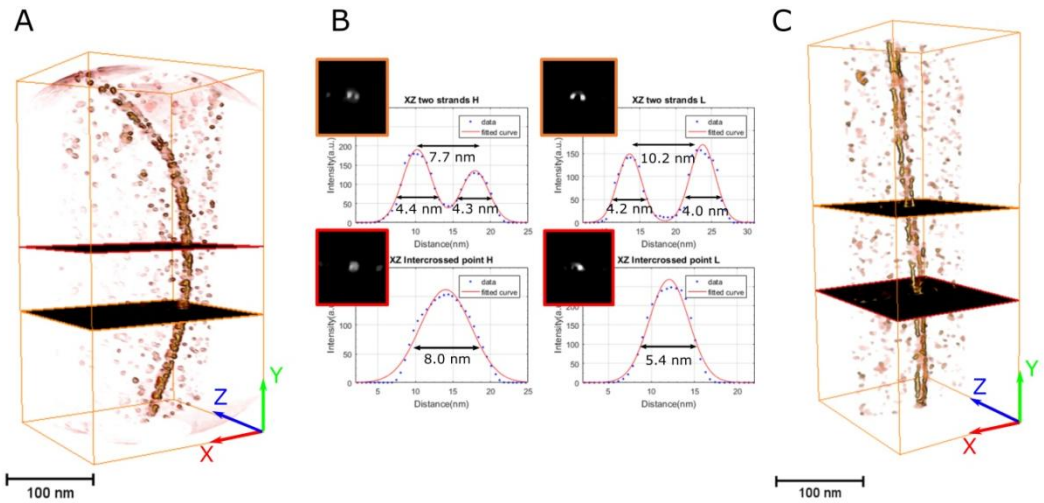

Fig. 13. Electron tomography 3D reconstruction of a single H APO fiber (a) intensity profiles of two strands and an intercrossed point of H APO fiber (b, left) and L APO fiber (b, right), and electron tomography 3D reconstruction of a single L APO fiber (c).

In the case of fibers formed from pure H APO other morphologies as nanotube-like fibers were commonly observed. In this particular case, the fiber is formed by two strands, however, no intersection point was observed (Figure 14).

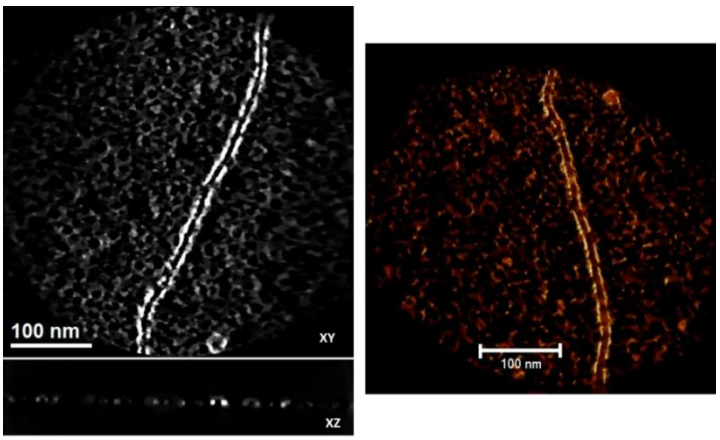

Fig. 14. XY and XZ planes extracted from the reconstructed volume (left) and the corresponding electron tomography 3D reconstruction of nanotube-like polymorph in a single H APO fiber (right).

The hierarchical assembly of paired strands into APO fibers has not been previously described, nor the formation of amyloid-like fibers for L- and H- recombinant human apoferritin protein. Our three dimensional analysis strongly suggests that all APO fibers have a common building block comprising paired strands with a double helical substructure. On the basis of these tomograms, these structural features can now be readily recognized in two-dimensional TEM fiber images. The 3D reconstruction from electron tomography is therefore an excellent and innovative tool for structural characterization of the different iso-apoferritin fibers. Unluckily, the left and right-handed chirality could not be inferred from electron tomography analysis. Both techniques AFM images analysis and high-resolution ET reveal of great value for obtaining complementary

information about the morphology and the supramolecular structure of protein amyloid-like fibers and for probing the helical nanofiber structure.

5. CD and FTIR measurements

Knowing that L and H subunits direct the final chirality and polymorphism in apoferritin fibers, we further investigated possible variations in their secondary structure. In this way, circular dichroism (CD) and Fourier transform infrared spectroscopy (FTIR) measurements were performed for the different iso-apoferritins fibrils samples and for the L-rich APO protein in solution at pH 2 (monomer).

The CD spectra initially obtained for the fibril samples were distort and we therefore had to remove the remaining non-fibrillar material and protein fragments from the fibrils solutions by several centrifugation steps until no protein was detected in the filtrate by UV–vis spectroscopy. Figure 15 shows these different spectra before and after L-rich APO fibers centrifugation.

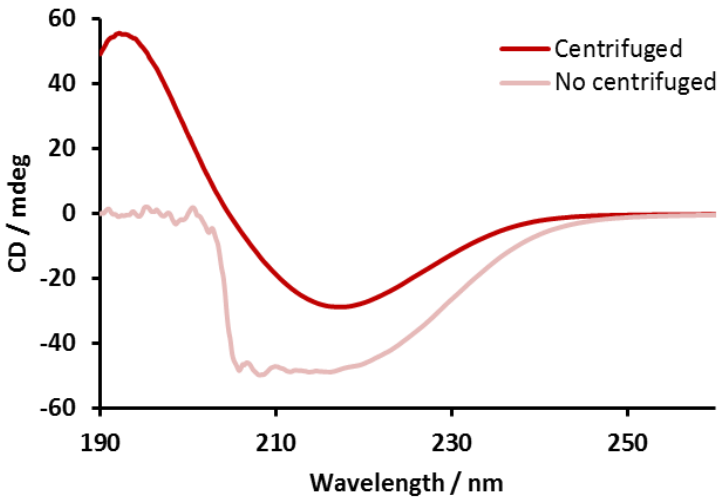

Fig. 15. Far-UV circular dichroism of L-rich APO fibers, before and after being centrifuged.

In this way, CD gave evidence of slight differences between the secondary structure of the right-handed L APO and left-handed H APO

fibers. In general, upon fibrillation process, the apoferritin protein loses α-helix content and gains β-sheet structure, supporting a pathway towards an amyloid fibrillation (Figure 16). In fact, Horse Spleen L-rich APO protein in solution at pH 2 (globular) shows the two typical bands centered at 208 and 222 nm according to an α-helix secondary structure (Figure 16a). Horse Spleen L-rich APO fibers formed after a 9 h heat treatment at pH 2, clearly shows a single minimum at 217 nm, characteristic of well-defined β-sheet structure (Figure 16d). Pure Recombinant Human L APO protein gives rise to a very similar spectrum (β-sheet structure, Figure 16b). Pure Recombinant Human H APO displayed a different curve but the α-helix and β-sheet content for the different iso-apoferritins determined by CDPRO software shows that all fibrillar proteins lose α-helix content and gain β-sheet structure, supporting a pathway towards amyloid fibril formation.

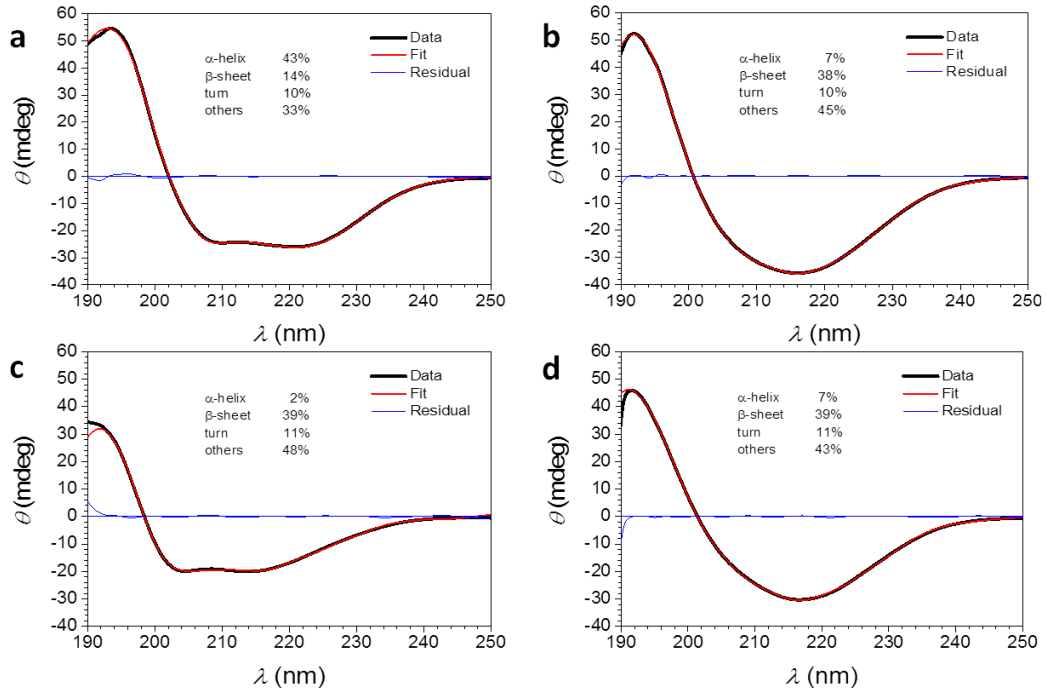

Fig. 16. Far-UV circular dichroism of Horse Spleen L-rich APO globular (a), Pure Recombinant Human L APO fibers (b). Pure Recombinant Human H APO fibers (c) and Horse Spleen L-rich APO fibers (d).

Figure 17 summarizes all iso-apoferritins CD spectra.

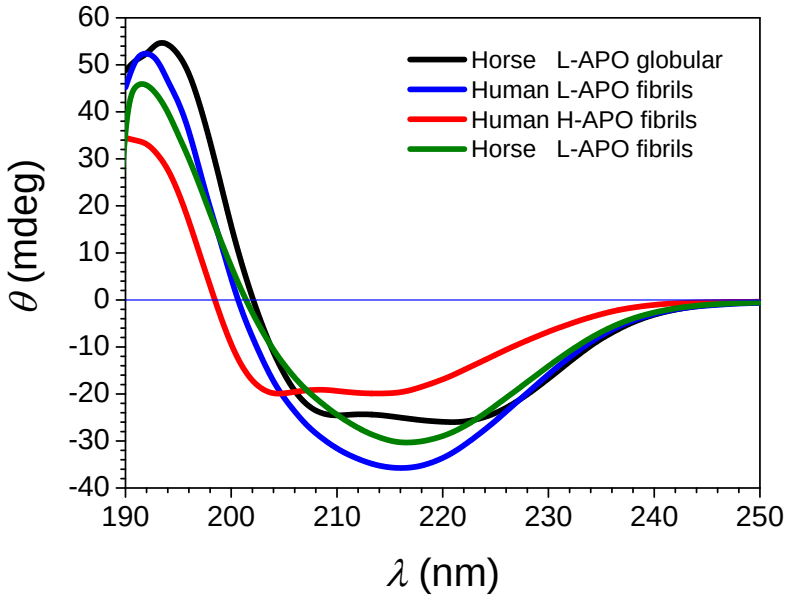

Fig. 17. Far-UV circular dichroism of **Horse Spleen L-rich APO globular**, **Pure Recombinant Human L APO fibers**. **Pure Recombinant Human H APO fibers** and **Horse Spleen L-rich APO fibers** .

FTIR results (Figure 18) further confirm that the two types of fibers have a structure that differ from the initial apoferritin globular conformation and that the cross-β region, characteristic of amyloid structures, become predominant in apoferritin fibers.

The wavenumber range between 1640 and 1670 cm^{-1}, characteristic of α-helical content, is greater, relative to the absorbance at the other wave numbers, in the case of the globular protein. Moreover, the cross-β region, characteristic of amyloid structures, between 1610 and 1630 cm^{-1}, is much more predominant in L-rich APO, L APO and H APO fibers.

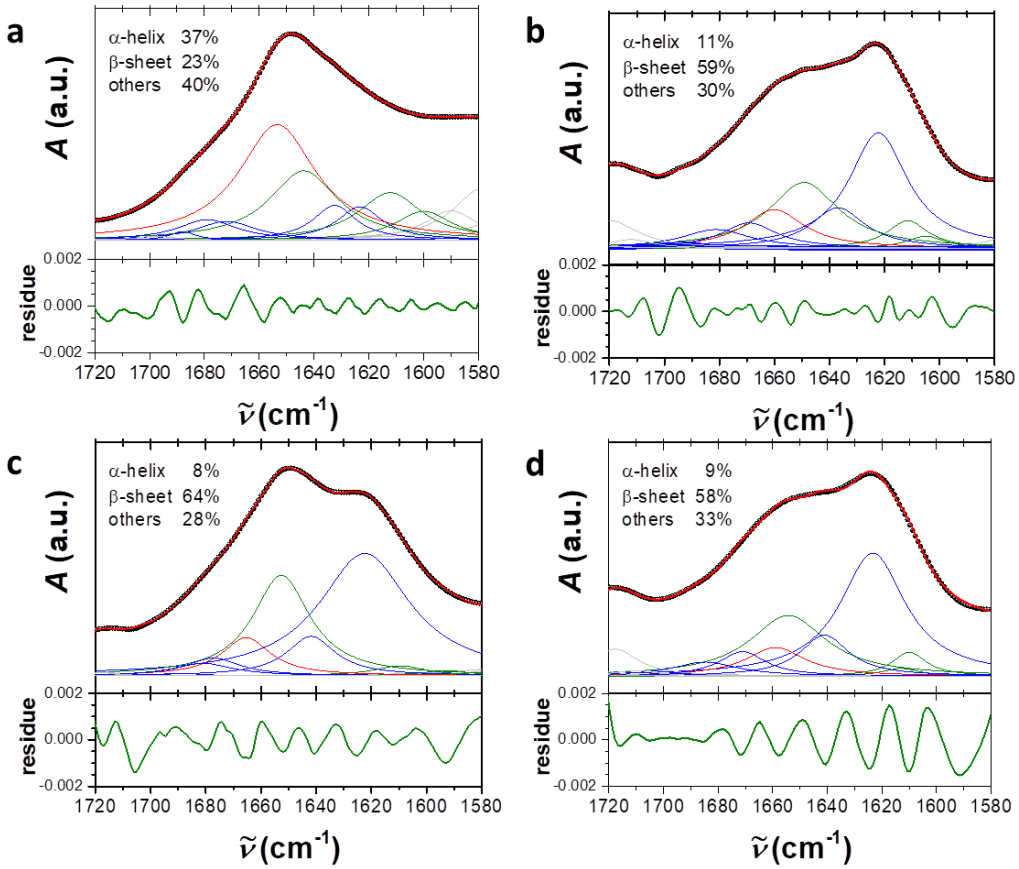

Fig. 18. IR spectra of Horse Spleen L-rich APO monomer (a), Pure Recombinant Human L APO fibers (b). Pure Recombinant Human H APO fibers (c) and Horse Spleen L-rich APO fibers (d). Analysis: IR absorption in the amide I region (1600-1700 cm-1) is sensitive to secondary structure of proteins.

Figure 19 summarizes all iso-apoferritins FTIR spectra.

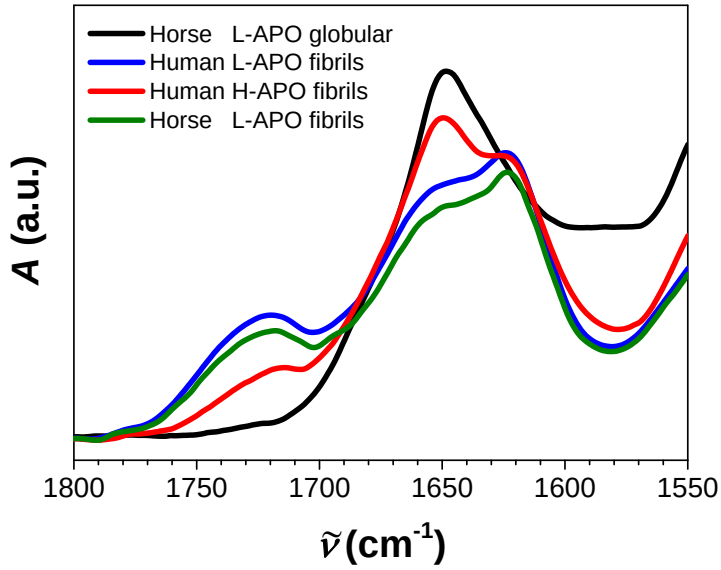

Fig. 19. IR spectra of **Horse Spleen L-rich APO globular**, **Pure Recombinant Human L APO fibers**. **Pure Recombinant Human H APO fibers** and **Horse Spleen L-rich APO fibers** .

6. WAXS measurements

The iso-apoferrtins structures could also be compared by Wide Angle X-ray Scattering (WAXS) (Figure 20). L-rich APO, H APO and L APO fibrils, showing high β-sheet content in CD, also shows the characteristic peak of 4.7 Å d-spacing in the WAXS signal, corresponding to an axial reflection of the inter strand spacing in the cross-β structure typical of amyloids. The second broader peak, around 10 Å, also corresponds to the expected equatorial reflection between 8 and 12 Å, accounting for the spacing between two or several β-sheets stacked in the fibril (Figure 21). In contrast, the L-rich APO globular shows an α-helix type of signal, with no sharp peak but a broad distribution, confirming the CD results.

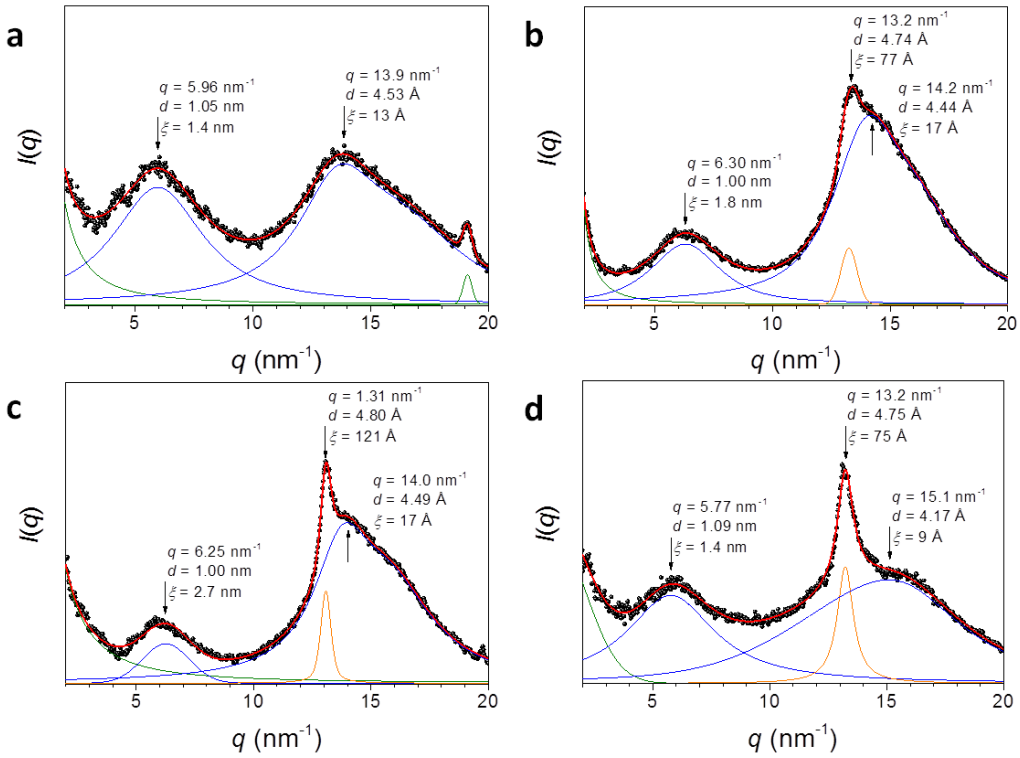

Fig. 20. WAXS log–linear intensity plots of Horse Spleen L-rich APO globular (a), Horse Spleen L-rich APO fibers (b), Pure Recombinant Human H APO fibers (c) and Pure Recombinant Human L APO fibers.

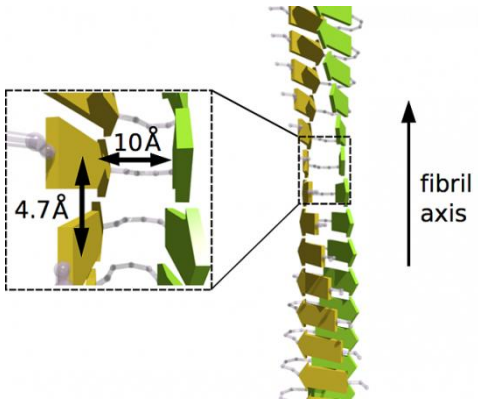

Fig. 21. Scheme showing the inter strand spacing in the cross-β structure (4.7 Å) and the spacing between two or several β-sheets stacked in the fibril (10 Å) typical of amyloids. Image from: http://www.natfak2.unihalle.de/forschung/verbund/sfb trr102/concepedia/amyloids/

Figure 22 summarizes all iso-apoferritins WAXS spectra.

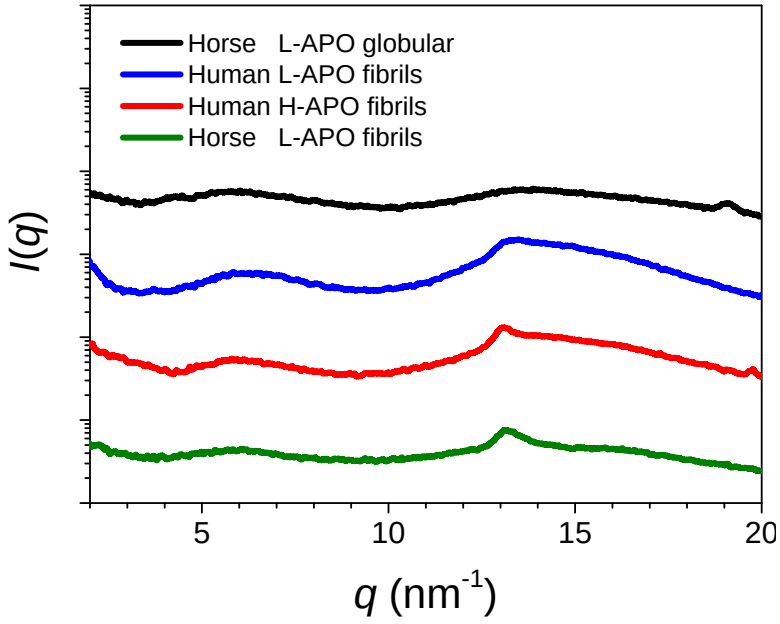

Fig. 22. WAXS log–linear intensity plot of **Horse Spleen L-rich APO globular**, **Pure Recombinant Human L APO fibers**. **Pure Recombinant Human H APO fibers** and **Horse Spleen L-rich APO fibers**.

7. Gel electrophoresis

In chapter 3, it was demonstrated by SDS-PAGE that complete hydrolysis is essential for the formation of large laminated aggregates and that small peptides fragments (<5 kDa) participate in the formation of these L-rich APO fibrils. In the same way, we want to compare these results with those from H APO and L APO fibrils. Subsequently, by comparing the hydrolysis evolution between the three experiments, only minor differences appear. At 24h, the same sizes of fragments (<5kDa) are present in solution for the three iso-apoferritins (Figure 23).

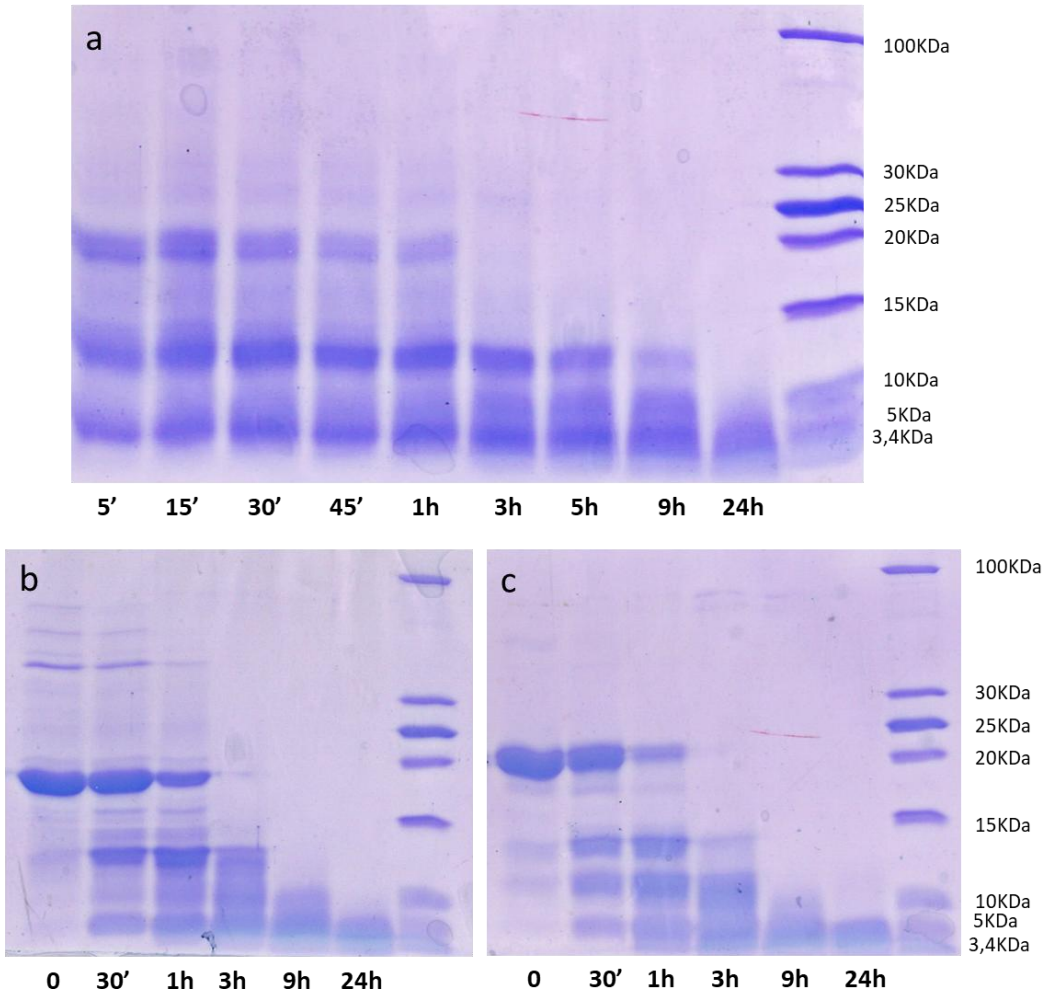

Figure 23. SDS-PAGE electrophoresis of a) L-rich APO, b) L APO and c) H APO.

8. Conclusions

The formation of amyloid-like fibers from L- and H- recombinant human apoferritin protein has not been previously reported, nor their hierarchical assembly into fibers helicates. Our 3D analysis strongly suggests that apoferritin fibers have a common building block comprising paired strands with a double helical substructure. Ferritin a soluble and highly robust protein with its subunits packed into mostly well-defined helices, can convert into an unusual and radically different structure as amyloid fibrils seen in pathological conditions such as Alzheimer's and

Parkinson's diseases. Besides being recognized as a crucial protein related with some neurodegenerative disorders, it is a key component of the iron regulatory system in the brain.

For the first time, it has been demonstrated that native globular protein forms fibers with a right-handed chirality. Usually fibers formed from native proteins present a left-handed helicity, and only when starting from small peptides right-handed chirality has been observed. Whatever the answer to the right-handed chirality of apoferritin amyloid-like fibers is, its existence shows that the supramolecular chirality of aggregated amyloid fibers may be opposite, depending on their starting peptide sequence.

These results open up the possibility of using the control of primary structure to access new forms of protein tertiary and quaternary nanostructures and show how the peptide sequence of such structures can control their final morphology and chirality. Insights into these mechanisms can have significant implications into the growing field of 1D nanostructures. As chiral information is embedded in the helical structure, tuning the chirality could allow dynamic control of nanostructure functions.

9. References

[1] T.P.J. Knowles, R. Mezzenga, *Adv. Mater.,* **2016**, *28,* 6546.

[2] E. Krieg, M.M.C. Bastings, P. Besenius, B. Rybtchinski, *Chem. Rev.,* **2016**, *16*, 2414.

[3] M. Fändrich, M. Fletcher, C.M. Dobson, *Nature,* **2001**, *410*, 165.

[4] P.T. Lansbury, H.A. Lashuel, *Nature,* **2006**, *443*, 774.

[5] S.A. Mostaert, M.J. Higgins, T. Fukuma, F. Rindi, S.P. Jarvis, *J. Biol. Phys.,* **2006**, *32*, 393.

[6] M.R. Chapman, L.S. Robinson, J.S. Pinkner, R. Roth, J. Heuser, M. Hammar, S. Normark, S.J. Hultgren, *Science,* **2002**, *295*, 851.

[7] D.M. Fowler, A.V. Koulov, C. Alory-Jost, M.S. Marks, W.E. Balch, J.W. Kelly, *PLoS Biol.,* **2006**, *4*, 100.

[8] L.R. Volpatti, M. Vendruscolo, C.M. Dobson, T.P.J. Knowles, *ACS Nano,* **2013**, *7*, 10443.

[9] D. Kurouski, R.A. Lombardi, R.K. Dukor, I.K. Lednev, L.A. Nafie, *Chem. Commun. (Camb),* **2010**, *46*, 7154.

[10] W. Dzwolak, A. Loksztejn, A. Galinska-Rakoczy, R. Adachi, Y. Goto, L. Rupnicki, *J. Am. Chem. Soc.,* **2007**, *129*, 7517.

[11] N. Rubin, E. Perugia, M. Goldschmidt, M. Fridkin, L. Addadi, *J. Am. Chem. Soc.,* **2008**, *130*, 4602.

[12] N. Rubin, E. Perugia, S.G. Wolf, E. Klein, F. Mátl, L. Addadi, *J. Am. Chem. Soc.,* **2010**, *132*, 4242.

[13] P. M.Harrison, P. Arosio, *Biochim Biophys Acta,* **1996**, *1275,* 161.

[14] D. Finazzi, P. Arosio, *Arch. Toxicol.,* **2014**, *88,* 1787.

[15] D.M. Lawson, P.J. Artymiuk, S.J. Yewdall, J.M.A. Smith, J.C. Livingstone, A. Treffry, A. Luzzago, S. Levi, P. Arosio, G. Cesareni, C.D. Thomas, W.V. Shaw, P.M. Harrison, *Nature,* **1991**, *349*, 541.

[16] C. Ferreira, B. Bucchini, M.E. Martin, S. Levi, P. Arosio, B. Grandchamp , C. Beaumont, *J. Biol. Chem.,***2000**, *275,* 3021.

[17] A.R. Curtis, C. Fey, C.M. Morris, L.A. Bindoff, P.G. Ince, P.F. Chinnery, A. Coulthard, M.J. Jackson, A.P. Jackson, D.P. McHale, D. Hay, W.A. Barker, A.F. Markham, D. Bates, A. Curtis, J. Burn, *Nat. Genet.,* **2001**, *28,* 350.

[18] J.R. Connor, B.S. Snyder, P. Arosio, D.A. Loeffler, P.A. LeWitt, *J. Neurochem., 65,* 717.

[19] K. H. Ebrahimi, P.L. Hagedoorn, W.R. Hagen, *Chem. Rev.,* **2015***, 115,* 295.

[20] H. Drakesmith, N. Chen, H. Ledermann, G. Screaton, A. Townsend, X.N. Xu, *Proc. Natl. Acad. Sci. U. S. A.,* **2005**, *102,* 11017.

[21] T. Thi Mai, A. Hamaï, A. Hienzsch, T. Cañeque, S. Müller, J. Wicinski, O. Cabaud, C. Leroy, A. David, V. Acevedo, A. Ryo, C. Ginestier, D. Birnbaum, E. Charafe-Jauffret, P. Codogno, M. Mehrpour, R. Rodriguez, *Nat. Chem.,* 2017. doi:10.1038/nchem.2778

[22] I. Usov, J. Adamcik, R. Mezzenga, *ACS Nano,* **2013**, 7, 10465.

[23]A. Uesaka, M. Ueda, A. Makino, T. Imai, J. Sugiyama, S. Kimura, *Langmuir,* **2014**, *30,* 1022.

[24] J. Adamcik, J. Jung, J. Flakowski, P. De los Rios, G. Dietler and R. Mezzenga, *Nat. Nanotechnol*., **2010**, *5*, 423.

[25] M. Kollmer, K. Meinhardt, C. Haupt, F. Liberta, M. Wulff, J. Linder, L. Handl, L. Heinrich, C. Loos, M. Schmidt, T. Syrovets, T. Simmet , P. Westermark, G.T. Westermark, U. Horn, V. Schmidt, P. Walther, M. Fändrich, *Proc. Natl. Acad. Sci.,* **2016**, *113,* 5604.

[26] S. Han, M. Kollmer, D. Markx, S. Claus, P. Walther, M. Fändrich, *Sci. Rep.,* **2017**, *7,* 43577.

[27] E. Vázquez-Fernández, M.R. Vos, P. Afanasyev, L. Cebey, A.M. Sevillano, E. Vidal, I. Rosa, L. Renault, A. Ramos, P.J. Peters, J.J. Fernández, M. van Heel, H.S. Young, J.R. Requena, H. Wille, *PLoS Pathog.,* **2016**, *12,* 1.

[28] M. Lopez-Haro, L. Guétaz, T. Printemps, A. Morin, S. Escribano, P.-H. Jouneau, P. Bayle-Guillemaud, F. Chandezon, G. Gebel, *Nat. Commun.,* **2014**, *5,* 5229.

[29] P. Rueda-Fonseca, E. Robin, E. Bellet-Amalric, M. Lopez-Haro, M. Den Hertog, Y. Genuist, R. André, A. Artioli, S. Tatarenko, D. Ferrand, J. Cibert, *Nano Lett.*, **2016**, *16,* 1637.

[30] R. A. Crowther, D. J. DeRosier, A. Klug, *Proc. R. Soc. Lond. A. Math. Phys. Sci.,* **1970**, *317,* 319.

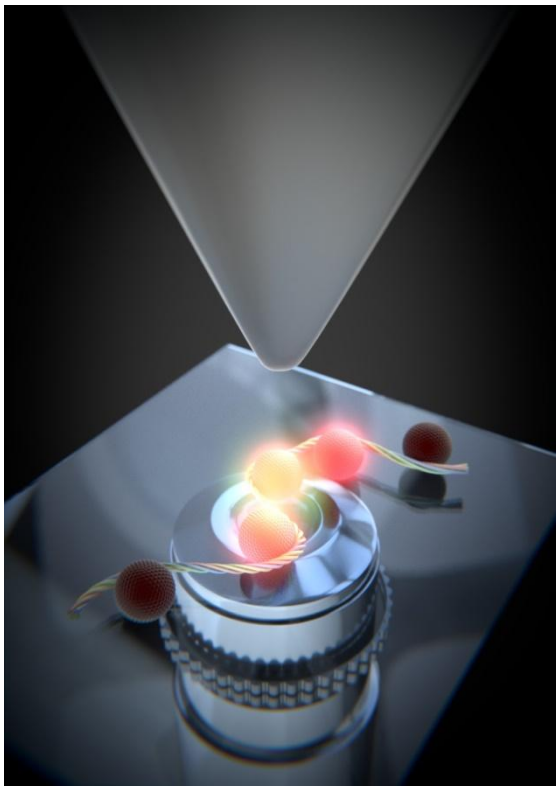

CHAPTER 5. APOFERRITIN FIBERS: A NEW TEMPLATE FOR 1D FLUORESCENT HYBRID NANOSTRUCTURES

1. Introduction

The structuring of zero-dimensional (0D) nanoparticles has great interest in basic and applied research because they provide a direct link between the nanoscale and macroscale worlds.[1,2,3] Therefore, building structures of growing complexity using nano-objects is becoming desired for inorganic nanostructures as the applications of these materials continue to expand.[4,5] One-dimensional (1D) nanoparticle assemblies are thought to improve the efficiencies of various electronic, optoelectronic, and/or magnetic devices.[6,7] Likewise, 1D structures can significantly help in the understanding of numerous biological processes.[8,9] The simplicity of superstructure assemblies, their multifunctionality, and structural versatility represent interesting directions for future research in nanostructures.[10]

As previously reported, biological systems have great flexibility and capacity for self-assembly, hence the interest in them for Nanotechnology. These hybrid nanomaterials find broad applications in Biology and Nanomedicine, but also in Nanotechnology, as templates for the fabrication of metal nanowires and functional polymer nanotubes due to their unique anisotropic properties.[11,12]

In this sense, amyloid-like fibers, either natural or synthetic, and self-assembling peptides are excellent templates for the production of 1D inorganic nanostructures.[13,14,15,16] A strong and important point is that these rigid amyloid fibers have rich and diverse surface functional groups on which other components with desirable functionalities can easily be built with nanoprecision.[17]

β-lactoglobulin (Blg) amyloid protein fibrils act as perfect templates to drive the synthesis of different inorganic materials to form hybrid nanowires.[18,19,20,21,22] For example, titanium dioxide (TiO_2) hybrid nanowires from β-lactoglobulin amyloid protein fibrils have been prepared.

These TiO_2-Blg amyloid fibrils also exhibit complexation with a luminescent water-soluble semiconductive polythiophene (P3HT) (Figure 1). TiO_2 nanowires behave as electron acceptor while P3HT acts as electron donor. In this way, amyloid-TiO_2 hybrid nanowires could serve in heterojunction photovoltaic devices.[20]

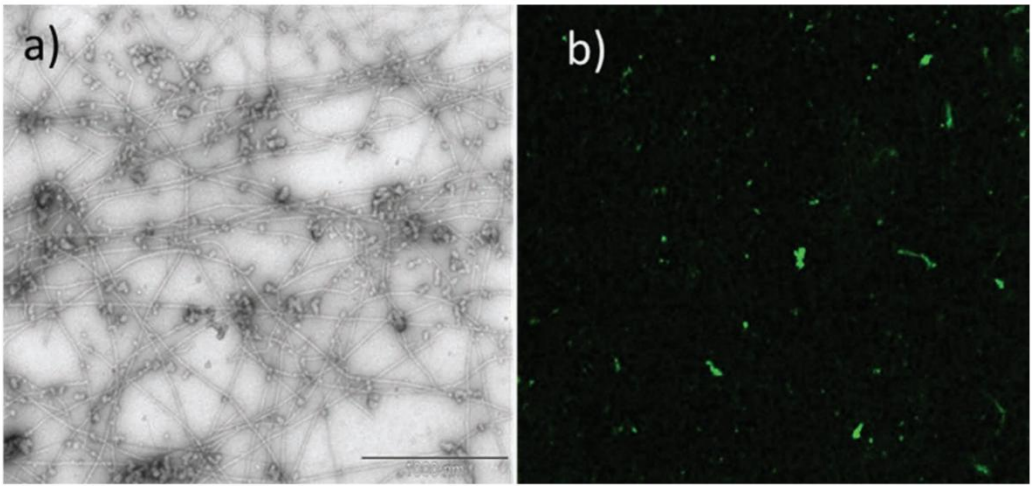

Fig. 1. a) TEM image of the β-lactoglobulin amyloid fibrils incubated with the sulfated polythiophene. b) Confocal laser-scanning microscopy image of the β-lactoglobulin amyloid fibrils incubated with the sulfated polythiophene. Image from: S. Bolisetty, J. Adamcik, J. Heier, R. Mezzenga, *Adv. Funct. Mater.,* **2012**, *22*, 3424.

Our group, among others,[23] has several reports on the preparation of metallic 0D nanoparticles using the protein apoferritin as a template. Besides, we have shown up the capability of this protein to be functionalized using the lysine residues at the external shell, introducing a new physical property.[24] For example, it was prepared a new class of water-soluble, bifunctional (fluorescent and magnetic) ferritin bioconjugate.[25] The magnetoferritin nanoblock can serve as contrast agent in MRI and the other nanoblock, the quantum dot (QD), renders the full nanostructure fluorescent (Scheme 1).

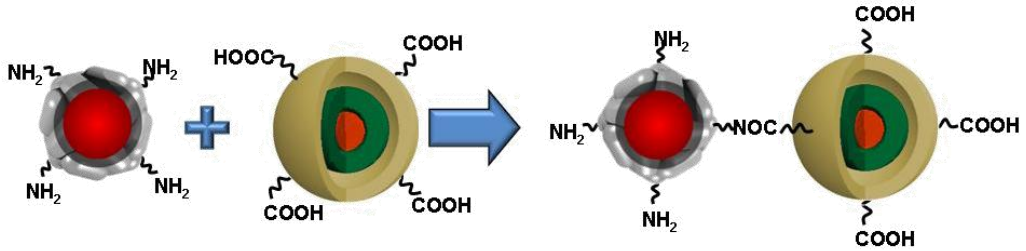

Scheme 1. Coupling between carboxyl-coated QDs and magnetoferritin (MFt) to form the fluorescent, magnetic bioconjugated nanoprobe. The MFt surface NH_2 group reacts with the carboxyl QD to form a covalent amide bond. Image from: B. Fernández, N. Gálvez, R. Cuesta, A.B. Hungría, J.J. Calvino, J.M. Domínguez Vera, *Adv. Funct. Mater*., **2008**, *18*, 3931.

Previously, we have described the formation of APO and Blg amyloid like fibers. The incorporation of fluorescence functionality in these fibers is of considerable and widespread interest, especially in the biomedical field.[26] In addition, these wire-like protein structures are rich in functional groups as previously explained. Therefore, we raised the chemical functionalization of these amyloid fibers with diverse quantum dots (QD), as well as with different Alexa Fluor (AF) dyes, leading to hybrid fluorescent fibers with variable emission wavelengths, from green to near infrared, depending on the QD and AFs coupled (Scheme 2). In a second step, we wanted to simultaneously labeled protein fibers with two Alexa Fluor fluorophores or two different QDs in order to observe if fluorescence resonance energy transfer (FRET) takes place. Thus, adequate functionalization could give rise to fluorescence resonance energy transfer (FRET), commonly used as a sensor in biological research.

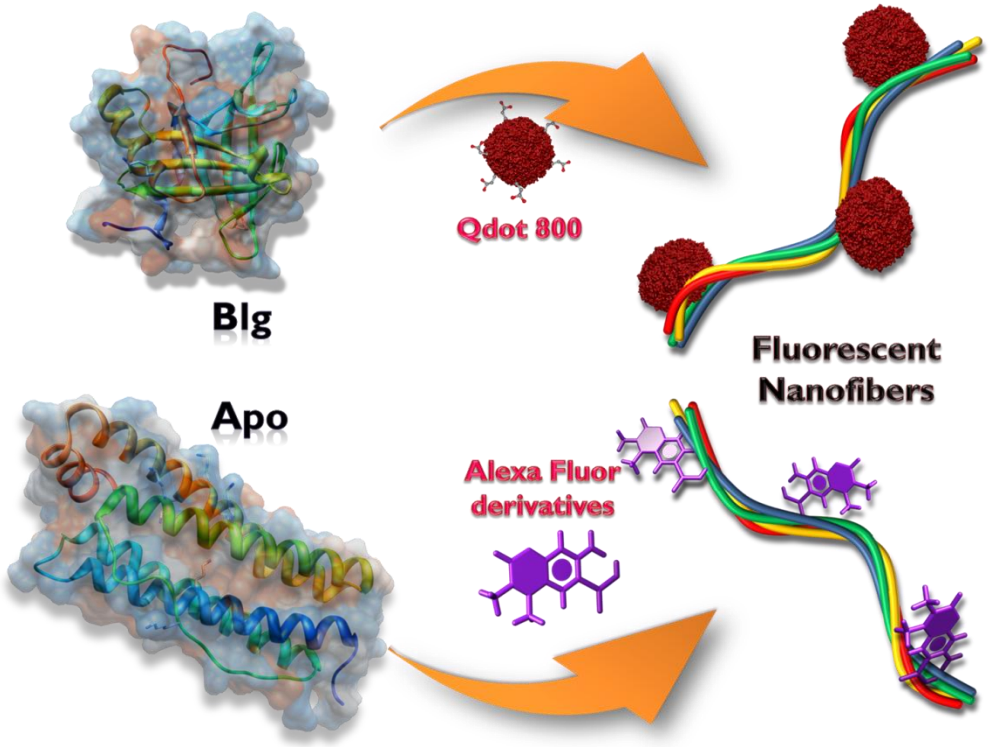

Scheme 2. Schematic illustration of APO and Blg proteins functionalization with diverse AF derivatives and QDs nanoparticles.

Quantum Dots (QDs) are nanocrystals with tunable size-dependent emission, high quantum yields of photoluminescence, broad excitation spectra and narrow emission bandwidths. They can be excited by a single source of light and emit in a wide range of wavelengths, from ultraviolet to NIR (near infrared), depending on their size and composition.[27] Emissions in the NIR region have the advantage of greater tissue penetration. QDs used in this Thesis are commercial composed of a CdSeTe metal core and a ZnS shell, both coated with an organic polymer (PEG type) functionalized with carboxyl groups (Scheme 3). Te is included in order to expand the emission to the NIR region. The aim of using these semiconductor Quantum Dots lies in their growing interest as fluorescent markers in biological applications.[28,29,30]

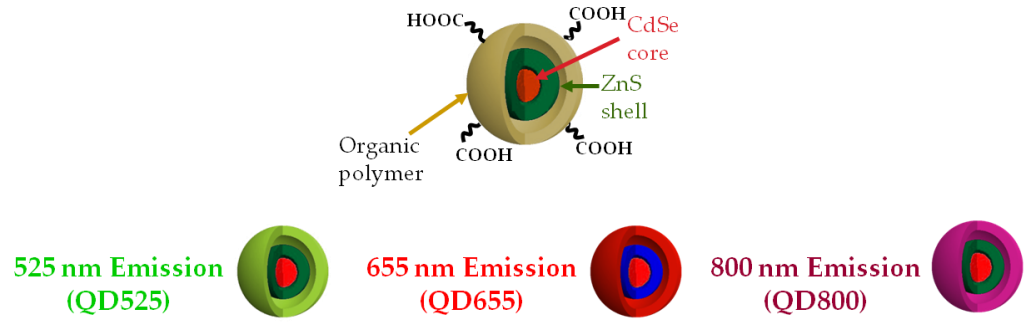

Scheme 3. Quantum Dot structure (up) and three different types of Quantum Dots used in this Thesis (down).

Alexa Fluor dyes are organic fluorophores with fluorescence emissions that include the entire visible spectrum and even the NIR region. AF conjugations exhibit brighter fluorescence and greater photostability than conjugates of other similar fluorophores. These features allow capturing images previously unreachable with conventional fluorophores. In addition, these fluorophores are water soluble, stable in a range of pH 4-10 and quite safe for use in *in vivo* studies as they are non-toxic.

Fluorescence resonance energy transfer (FRET) is a mechanism describing energy transfer between two light-sensitive molecules (chromophores). A donor chromophore, initially in its electronic excited state, may transfer energy to an acceptor chromophore through nonradiative dipole–dipole coupling. The efficiency of this energy transfer depends on the distance between donor and acceptor, making FRET extremely sensitive to small changes in distance (Scheme 4).[31] This is why FRET phenomenon is commonly used as sensor in biomedical research.

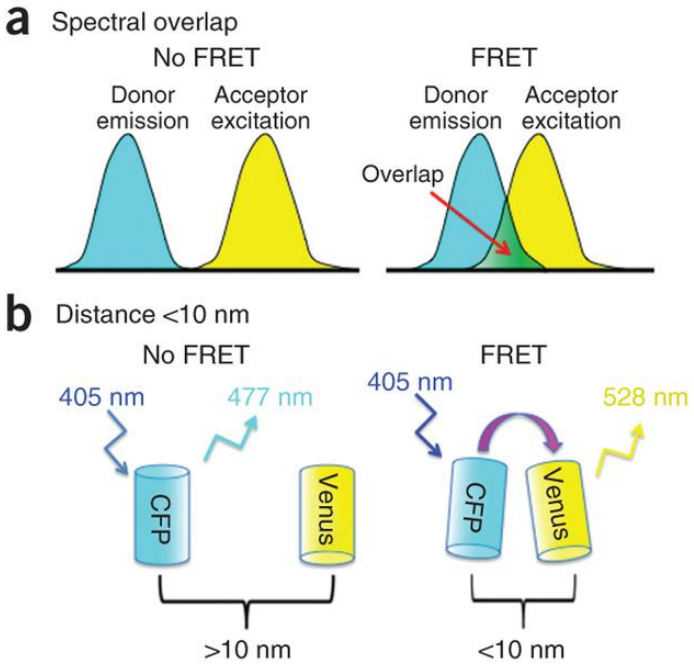

Scheme 4. Schematic diagrams depicting the conditions that must be met for efficient FRET. Image from: J.A. Broussard, B. Rappaz, D.J. Webb, C.M. Brown, *Nature Protocols,* **2013**, *8*, 265.

2. Dye-labelled fibril proteins

It is interesting to highlight here that, as expected, once fibers were formed, the APO protein lost its ability to store Fe, which reflects the dramatic changes occurring at channels and cavity sites in the protein structure with respect to the globular native form. At this point, we wondered if fibers would retain the ability to be functionalized externally exhibited by native apoferritin. Indeed, amyloid fibrils have rich and diverse surface functional groups. However, few reports have been published on the use of these reactive groups as a template for chemical functionalization.[17,32,33] In particular, the native APO protein contains lysine and cysteine residues on the external surface that can be used to covalently couple molecules or nanoparticles as previously explained.[23,24,25] On the

other hand, Blg also contains lysine and cysteine residues to be functionalized.[34,35]

Succinimidyl ester Alexa Fluor derivatives react with amine groups, giving rise to conjugate proteins with high photostability. AF488 and AF647 molecules were readily bound to the APO and Blg nanofibers by the formation of amide bonds. In this way, 1D fluorescent nanofibers were obtained. In a first experiment, APO and Blg fibers were reacted with only AF488 or AF647 in a 1:1 stoichiometry (protein : fluorophore).

Figure 2 shows the fluorescence spectra recorded from APO and Blg fibers tagged with only AF488 or AF647. Both samples displayed the fluorescence bands at 520 nm and 670 nm characteristic of AF488 and AF647 respectively.

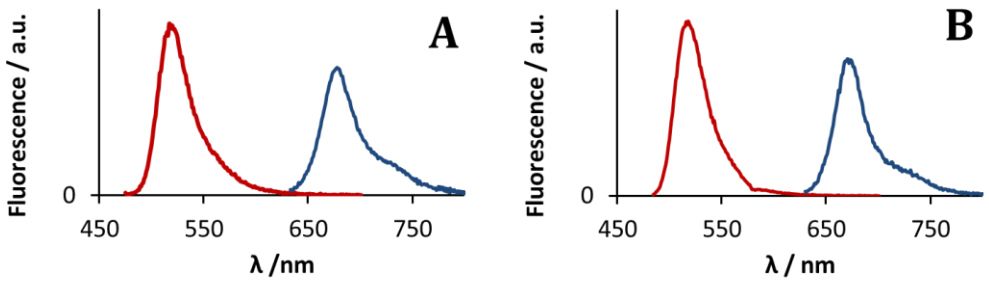

Fig. 2. Fluorescence spectra of (a) APO fibers labeled with only AF488 (red) and APO labeled with only AF647 (blue) and (b) the same for Blg fibers.

To confirm that the functionalization was successful, we imaged the fibers with correlative AFM and standard fluorescence microscopy. Indeed, Figure 3 shows that the pattern in the fluorescence image matches that of the fibers in the AFM image.

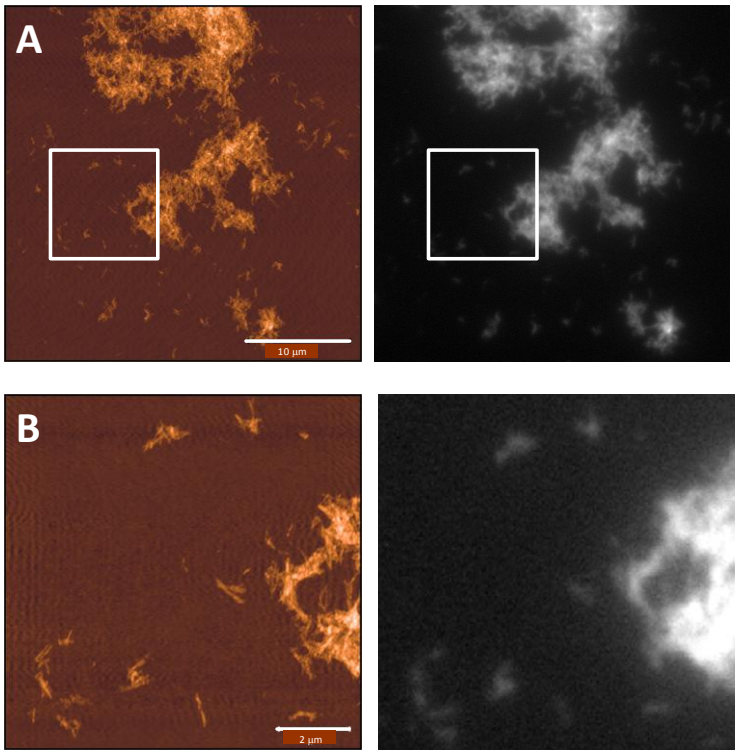

Fig. 3. Correlative AFM (left) and fluorescence imaging (right) of Blg fibers labeled with AF488 that confirms the attachment of the fluorophore to the fiber. B is the zoom of the white squared area in A.

During this study, fibers appear to be homogeneously fluorescent at the spatial resolution provided by standard fluorescence microscopy. With the purpose of obtaining a more in-depth analysis, correlative AFM and localization-based super-resolution fluorescence microscopy was used to gain information about the labeling properties at nanoscale spatial resolution. Figure 4 shows standard fluorescence images, super-resolution images, and AFM images of the same area of Blg-AlexaFluor 488 fibers deposited on glass. At the zoom level of the images, standard fluorescence microscopy hardly gives any information. In contrast, the super-resolution image shows clear features, which correspond very well to those of AFM. The correlative nature of these experiments allows discriminating between "real" localizations in the super-resolution image and spurious ones that

are related, e.g., to nonspecific binding. Importantly, the super-resolution image reveals labeling heterogeneity at the nanoscale, which can be gauged from the comparison with the corresponding AFM image.

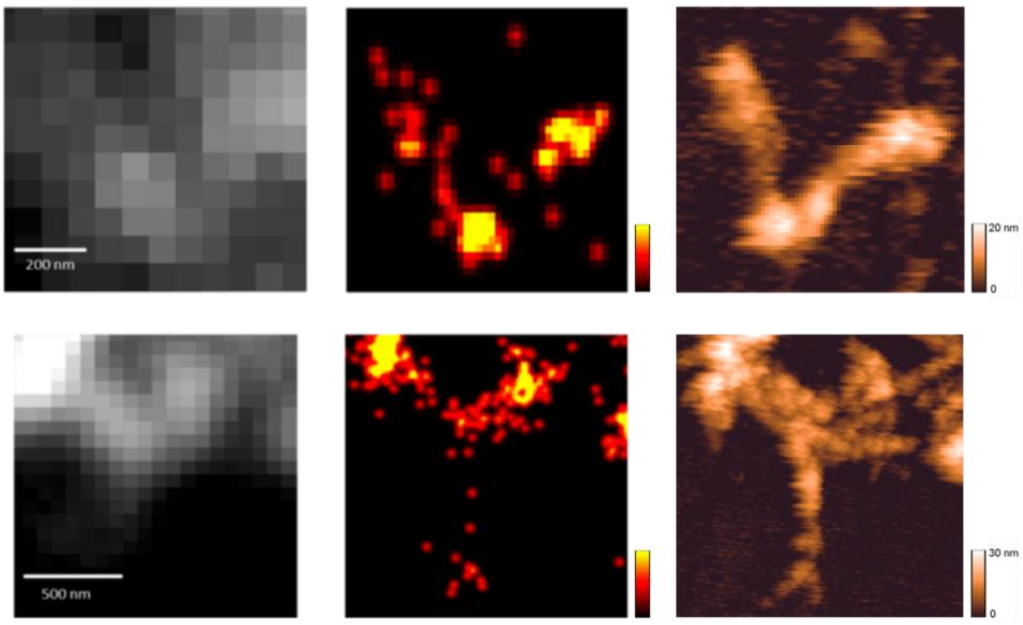

Fig. 4. Standard fluorescence imaging (left), super-resolution imaging (center), and AFM (right) of Blg fibers showing heterogeneous labeling with AlexaFluor488 at the nanoscale. The false color scale in the central panel indicates relative fluorophore localization density. Fibers were immobilized and imaged on glass.

Figure 5 shows the super-resolution image of one single Blg-AlexaFluor 488 nanofiber also revealing labeling heterogeneity.

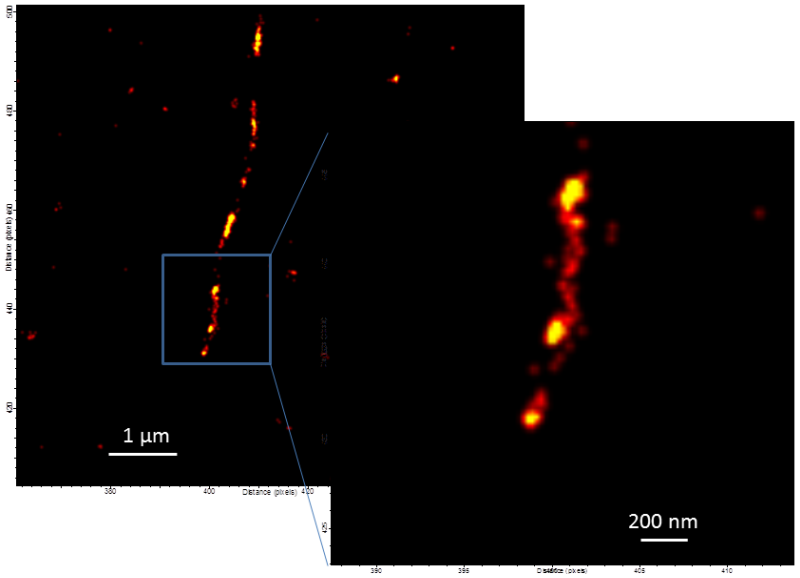

Fig. 5. Super-resolution imaging of a single Blg fiber showing heterogeneous labeling with AlexaFluor488 at the nanoscale.

3. Fluorescence lifetime imaging microscopy with pulsed interleaved excitation (FLIM-PIE) measurements

In a second experiment, APO and Blg fibers were reacted simultaneously with both AF488 and AF647. Figure 6 shows the UV-visible absorption spectra recorded from APO and Blg fibers tagged with both AF488 and AF647 in a 1:1:1 stoichiometry (protein : AF488 : AF647). Both samples displayed the two absorption bands at 488 nm and 647nm characteristic of AF488 and AF647 respectively. The band displayed at 280nm corresponds with the protein band. Simultaneous labeling of protein fibers with both fluorophores (AF488 and AF647) offers the opportunity to achieve FRET, which is strongly dependent on the distance between the AF488 donor and the AF647 acceptor.

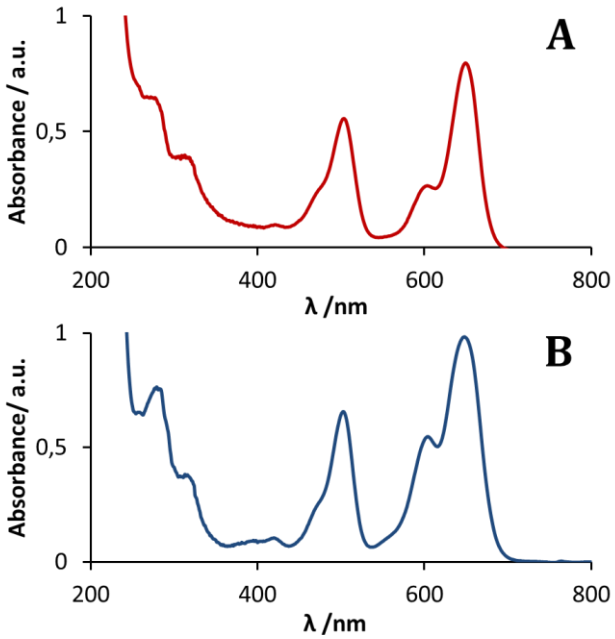

Fig. 6. UV-vis spectra of (a) APO and (b) Blg fibers tagged with both AF488 and AF647.

Consequently, we focused on the FRET from AF488 (donors) to AF647 (acceptors) by observing the fluorescence spectra of both samples. Figure 7 shows the fluorescence spectra recorded from APO and Blg fibers tagged with both AF488 and AF647. Irradiation of these samples at 450 nm produced one emission band at 520 nm (corresponding to AF488) and a second smaller band centered at 670 nm attributable to FRET phenomenon (Scheme 4). The FRET pattern is clearly shown in the magnified spectra on Figure 7 revealing that distances between fluorophores are small enough for having energy transfer. FRET pattern is related to the conformational changes and new arrangements that occur to the globular proteins after the fibrillation process.

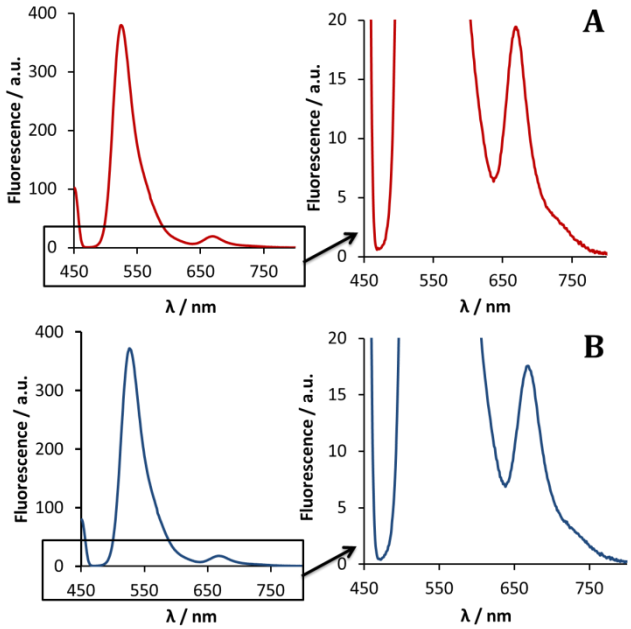

Fig. 7. Fluorescence spectra of (a) APO and (b) Blg fibers tagged with both AF488 and AF647. The images on the right are the magnified spectra of the selected zone.

In order to obtain more information about the arrangement of the fibers and FRET efficiency, we focused on the FRET by observing the donor fluorescence lifetime using Fluorescence Lifetime Imaging Microscopy with pulsed interleaved excitation (FLIM-PIE). The basis for this technique was explained in Chapter 3, but briefly, FLIM imaging allows mapping the lifetime of the donor, τD, which depends on the FRET efficiency, and the PIE excitation scheme provides simultaneous dual-colour excitation for colocalization imaging of the donor and acceptor (see Materials and Methods for details).[41] FLIM-PIE experiments were performed on APO and Blg, both in the native globular form (APO-globular and Blg-globular) and fibers (APO-fibers, Blg-fibers), labeled with both AF488 and AF647 (Figure 8).

In the FLIM analysis of the APO-fibers (Figure 8a and b for representative images, and more images are collected in Figure 9), we

distinguished two different populations: fibrillar structures characterized by high fluorescence intensity due to a high number of emitting dyes, and high FRET efficiency (τD distribution centered at **2.40** ± 0.01 ns, Figure 8b,i); and small aggregates/oligomers with less efficient FRET (τD distribution centered at **3.13** ± 0.02 ns, Fig. 6b,ii), which suggest a less organized conformation of these aggregates. In contrast, APO globular exhibited a τD distribution centered at **3.53** ± 0.01 ns (Figure 8b,iii), indicating a low-FRET. These results are roughly similar to those previously shown in chapter 3 for APO fibers, where different protein aggregates were observed. It is important to highlight that in this case fibrils were functionalized with the fluorophores, whereas in chapter 3 the functionalization was performed on globular APO proteins before the fibrillation process.

Similar results were obtained for Blg (Figure 8c and d). Blg-fibers exhibited highly fluorescent fibrillar structures, characterized by a τD centered at **3.06** ± 0.01 ns, coexisting with small aggregates/oligomers (τD centered at **3.12** ± 0.01 ns). These small aggregates are different from Blg-globular, which exhibited a τD distribution centered at **3.46** ± 0.01 ns. These results demonstrate that in both APO and Blg fibers two different types of structures are formed, which display a more efficient energy transfer and, hence, are more compact than the globular species. However, this is the first time that fluorescent AF-functionalized Blg fibers are reported.

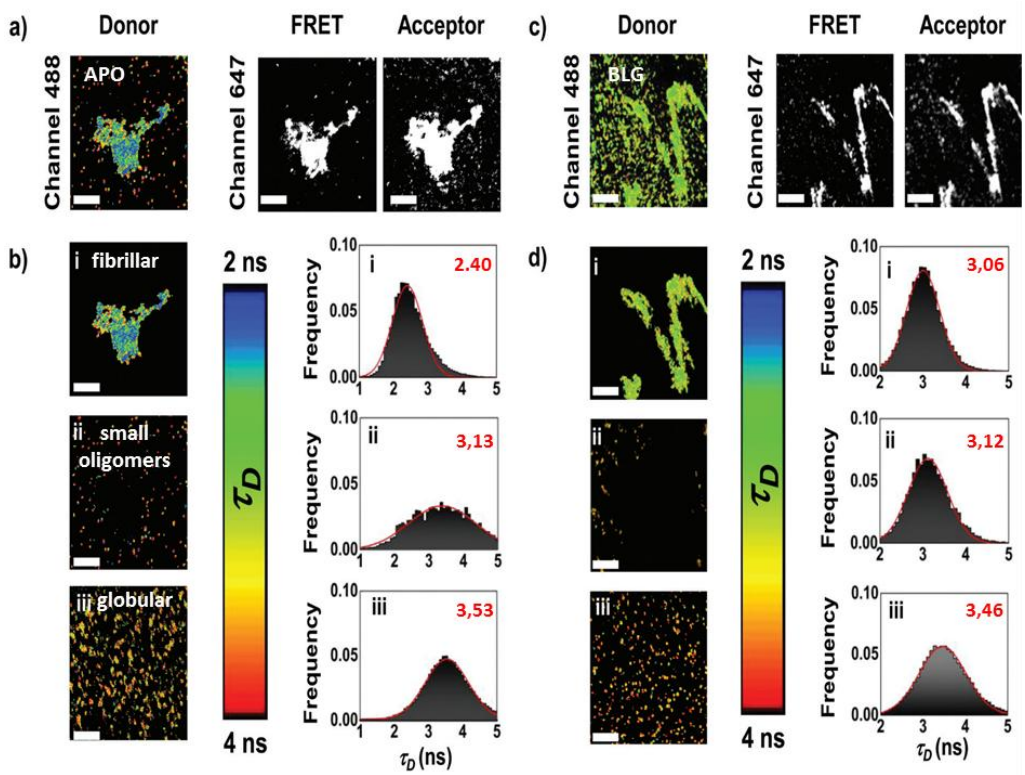

Fig. 8. FLIM-PIE experiments of APO and Blg, in fibers and globular forms tagged with both AF488 and AF647. Donor FLIM image, FRET and directly excited acceptor fluorescence images of APO-fibers (a) and Blg-fibers (c). The donor FLIM images and τD distributions of APO (b) and Blg (d) in fibrillar structures (i) and small oligomers (ii) are shown and compared with the globular forms (iii). The distributions were normalized by using events from 5 different images. White scale bars: 3.3 μm.

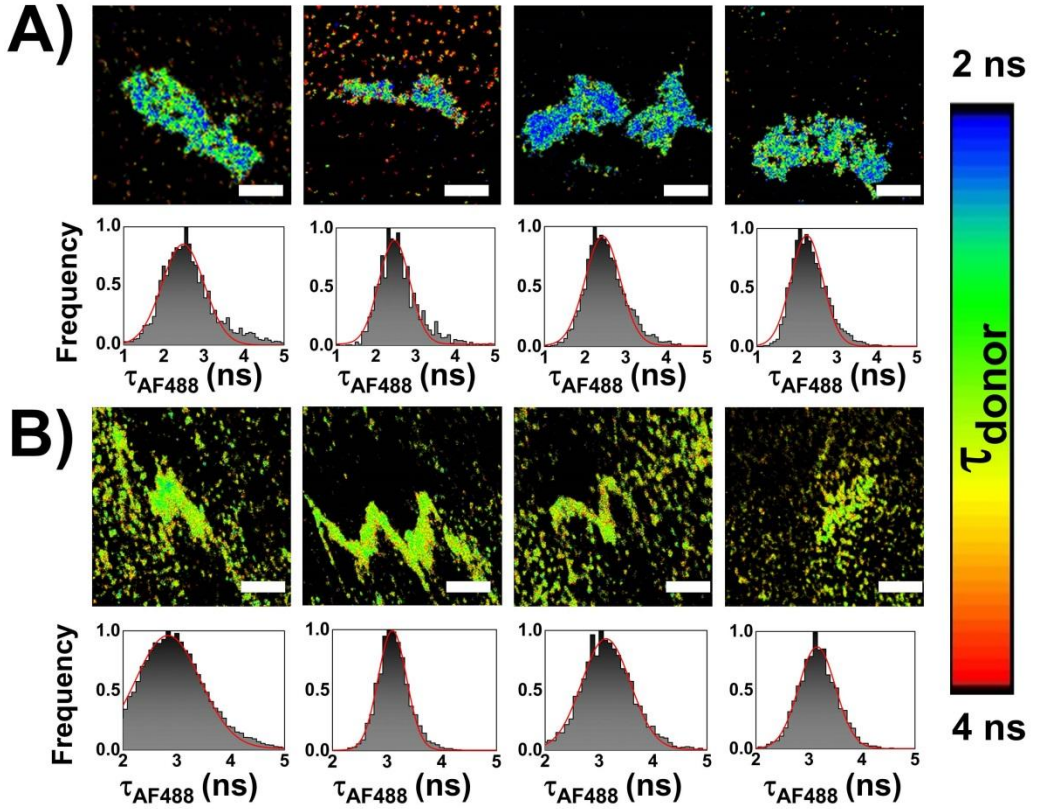

Fig. 9. Donor FLIM images. A: APO-fibers and the corresponding donor lifetime distributions of the smaller oligomers. B: Blg-fibers and the corresponding donor lifetime distributions of the smaller aggregates. The images are represented in a pseudo-color scale from 2 to 4 ns. The scale bars represent 3.3 μm.

4. Fluorescent 1D hybrid QD-fibers

Three types of CdSe nanoparticles (NPs) were covalently coupled to APO and Blg fibers for obtaining fluorescent 1D nanostructures. The surface of the QD, covered with free carboxyl (COOH) residues, enables covalent coupling to the QD probes. The conjugation process of fluorescent QDs (525, 655 or 800) emitting at 525, 655 or 800 nm, to 1D fibers of both proteins has been achieved via covalent crosslinking chemistry (Scheme 5).

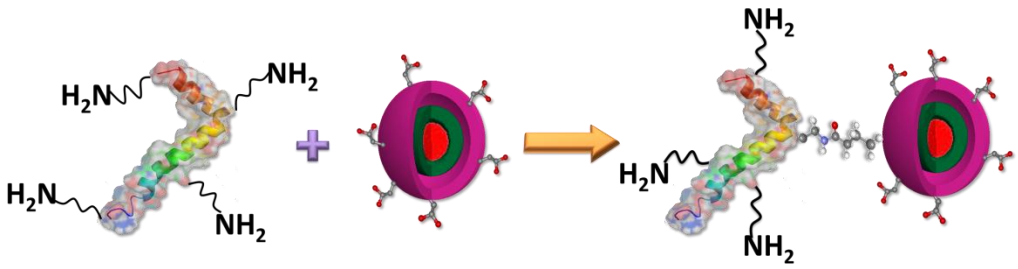

Scheme 5. Coupling between a carboxyl-coated QD and a fiber to form the fluorescent bioconjugated nanoprobe. The protein surface NH_2 group reacts with the carboxyl QD to form a covalent amide bond.

Fluorescence emission spectra of APO-QD and Blg-QD fibers (Figure 10) showed no significant changes in the emission and bandwidths of QDs after the coupling process to fibers.

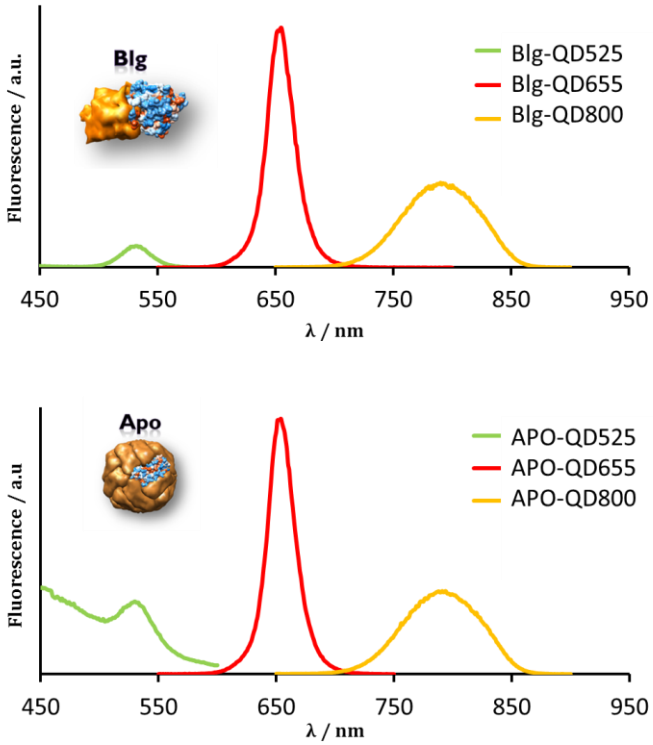

Fig. 10. Fluorescence spectra of up: Blg-QD525, Blg-QD655 and Blg-QD800, and bottom: APO-QD525, APO-QD655 and APO-QD800 hybrid fibers under excitation at 350 nm.

The HR-TEM contrasted images of the APO-QD and Blg-QD hybrid nanofibers (Figure 11) showed that the crosslinking step did not result in later fiber aggregation and that the functionalization of fibers with QDs was clearly successful. The semiconductor NPs arrange along the protein nanofibers alternately on either side of the fiber. The organic PEG shell (of about 2 nm) surrounding the QDs could be perfectly distinguished. For the Blg-QD hybrid structures some free QDs in the medium were observed. In the case of APO-QD fibers the functionalization reaction was practically complete and no free QDs were observed in the medium.

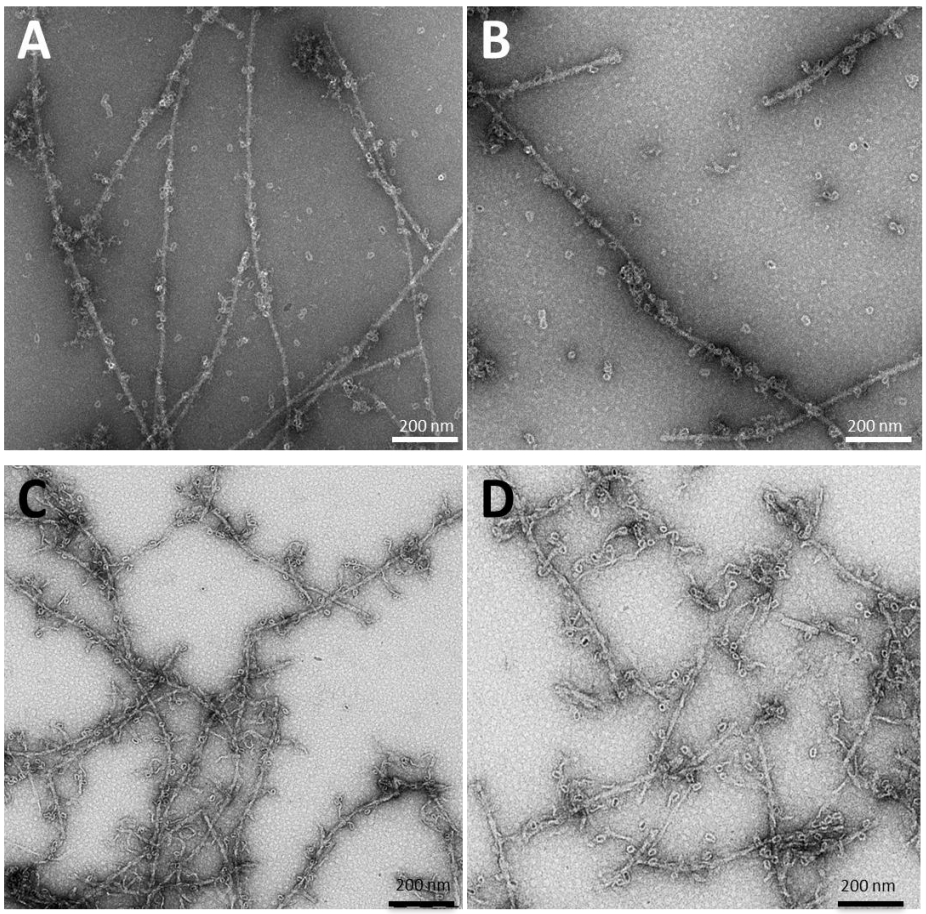

Fig. 11. HR-TEM images of (a) Blg-QD655, (b) Blg-QD800, (c) APO-QD655 and (d) APO-QD800 1D fluorescent hybrid fibers.

The high-angle annular dark-field scanning transmission electron microscopy (HAADF-STEM) images and the energy dispersive X-ray (EDX) analysis of the APO-QDs and Blg-QDs are shown in Figure 12 and Figure 13. The EDX mapping showing colocalization of S, Se and Cd on a single fiber confirms first the presence of the QDs associated with the fibers, and second the successful functionalization.

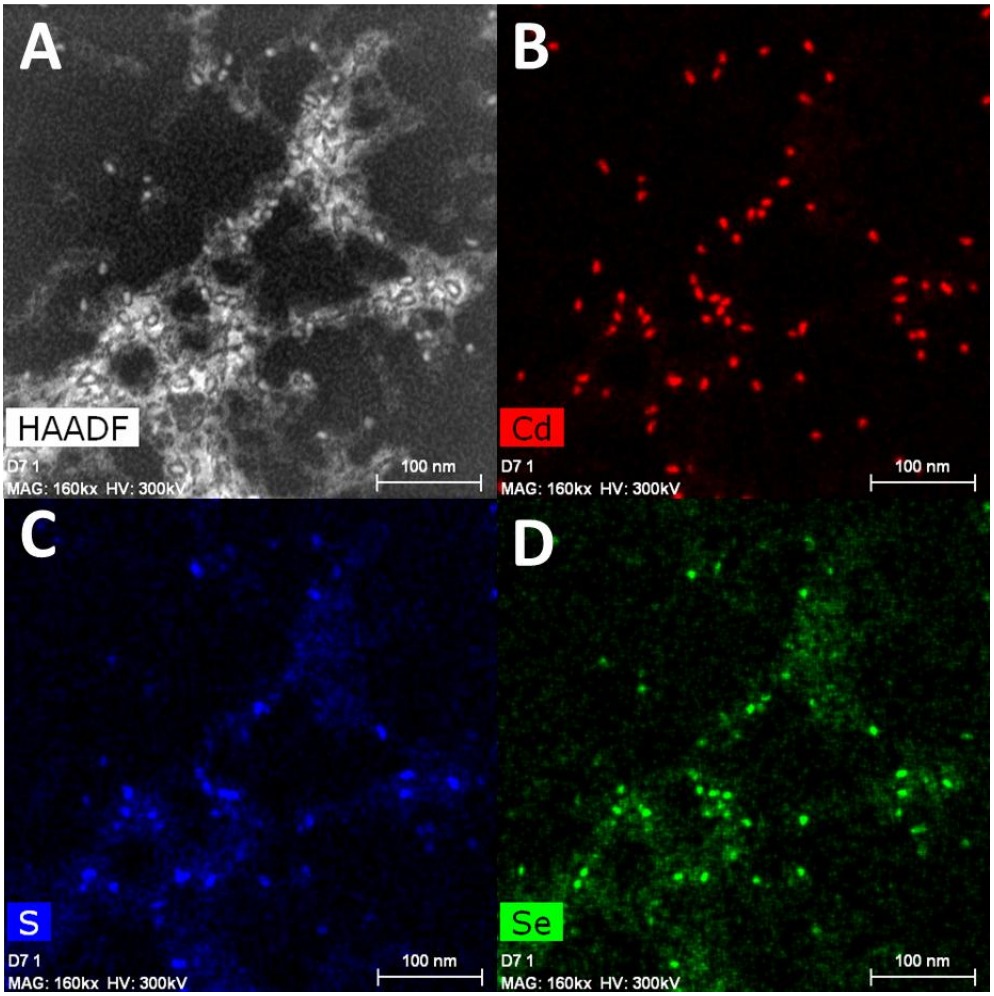

Fig. 12. (a) HAADF-STEM image of QD800 bound to APO protein fibers. (b), (c) and (d) are the corresponding elemental mapping of Cd, S and Se.

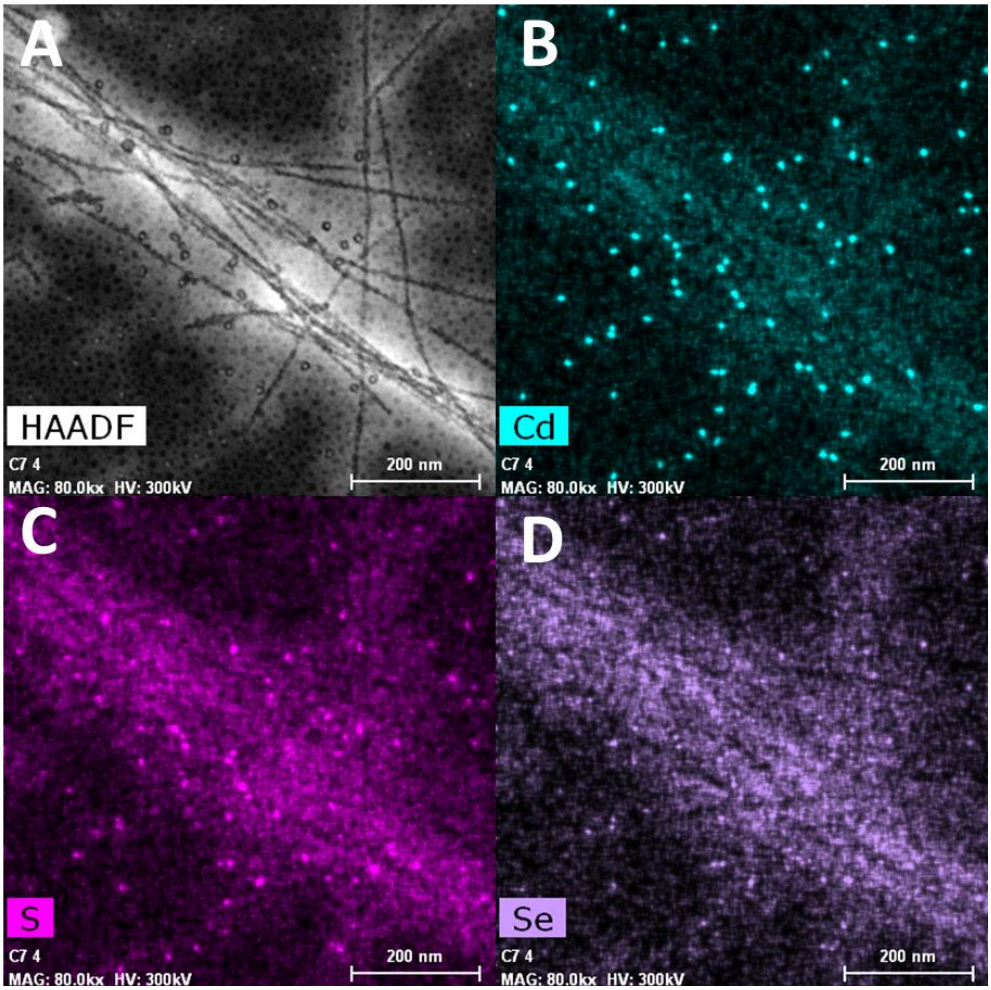

Fig. 13. (a) HAADF-STEM image of QD800 bound to Blg protein fibers. (b), (c) and (d) are the corresponding elemental mapping of Cd, S and Se.

Blg fibers functionalized with carboxyl-coated CdSe quantum dots (QD655) were also imaged with the correlative AFM and localization-based super-resolution fluorescence microscope. Figure 14A shows an AFM image in which the quantum dots are clearly observed attached to the fiber. The labeling density is not homogeneous along the fiber, with some sections where the QDs seem to overlap, while others are not functionalized, consistent with the previous observations using high-resolution transmission electron microscopy (HRTEM). The height of the QDs is about

8 nm and that of the fiber is slightly above 3 nm. The latter value is consistent with a single or double Blg fibril as opposed to a twisted multistranded fibril.[36]

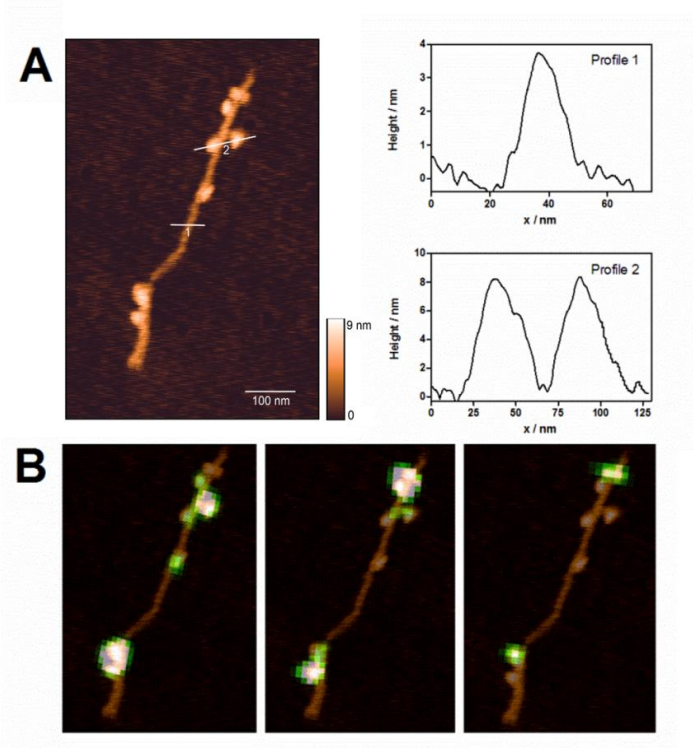

Fig. 14. A) AFM image (left) and topography (right) of a Blg fiber functionalized with QD655. B) Overlay of AFM image and super-resolution images reconstructed from three different data sets of the same fiber in (A). Each data set is built up from about 800 frames of 100 ms per frame.

Fluorescence imaging of the same sample area revealed rich blinking dynamics of the QDs. These fluorescence fluctuations allow separating in time the emission of each QD and to use various superresolution imaging schemes to reconstruct QDs distribution with a spatial resolution below the diffraction limit of light,[37,38,39,40,41,42] although their very different brightness due to their power-law fluorescence on–off distribution deteriorates the quality of the super-resolution images. Figure 14B and Figure 15 show super-resolution images corresponding to three different movies collected

from the same area overlaid with AFM. Our data show QDs separated by subdiffraction distances, and that most, if not all, of the QDs in this particular sample emit at some point during the acquisition time. While data in Figure 14B alone do not allow us to extract reliable statistics, we note that previous work has estimated a significant dark fraction of QDs.[43,44] However, more recent measurements in which the observation times for individual QDs were much longer (in the order of minutes, similar to the total integration time of our three data sets) showed only a small nonemitting fraction (about 15%).[45] We have indeed observed a small fraction of dark QDs in other samples (see below).

In addition to the super-resolution reconstructed image and topography, additional information about blinking dynamics on a fast timescale (100 ms in this case) can be overlaid by color coding the appearance of localization events (Figure 15).[46]

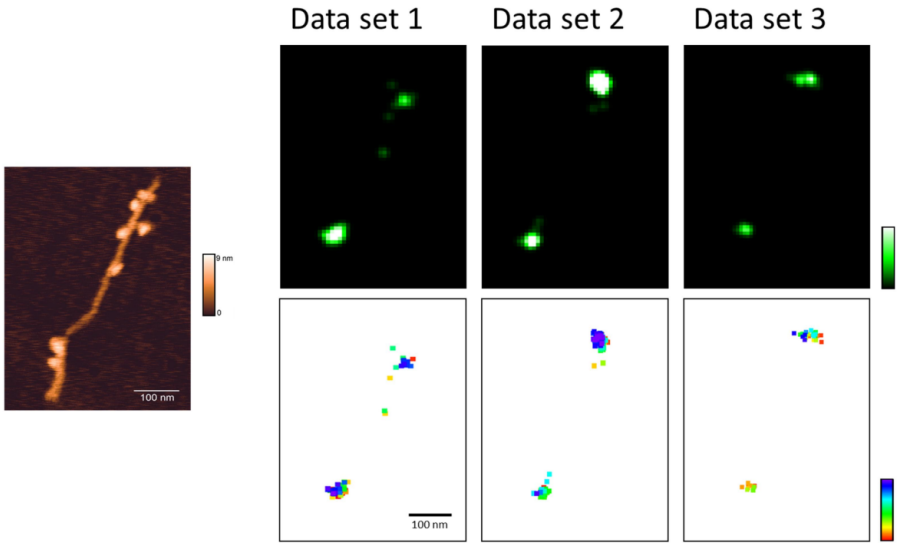

Fig. 15. AFM image (left) and super-resolution images (top right) reconstructed from three different data sets of a Blg fiber labeled with QD655 (same as Figure 14B). The false colour scale in the super-resolution image indicates relative localization density. Bottom right: raw localization data for each data set. The color code indicates frame number (100 ms acquisition time per frame).

In a next step, a more complex sample in which Blg was functionalized with both QD655 and QD525 was studied. This sample was first characterized by HR-TEM (Figure 16), which shows first, the successful attachment of both types of QDs by carboxyl activation with a carbodiimide (see Materials and Methods), and second that this reaction does not result in unwanted fiber crosslinking. Both types of QDs arrange at either side of the fiber, and labeling density along the protein nanofibers is heterogeneous. The organic PEG shell (of about 2 nm) surrounding the QDs can be clearly distinguished in the contrasted image (Figure 16B). The STEM bright-field image (Figure 16C) and the high-angle annular dark-field (HAADF) STEM mode (Figure 16D), which is highly sensitive to variations in the atomic number of the atoms in a sample, allow to distinguish perfectly between the rod-like QD655 (20 ± 2 nm long axis) and the spherical QD525 (5 ± 1.5 nm, mean diameter). The images show that there are roughly double amount of QD525 than QD655, consistent with the expected stoichiometry (see Materials and Methods). The pristine QDs are also shown without fibers in Figure 17.

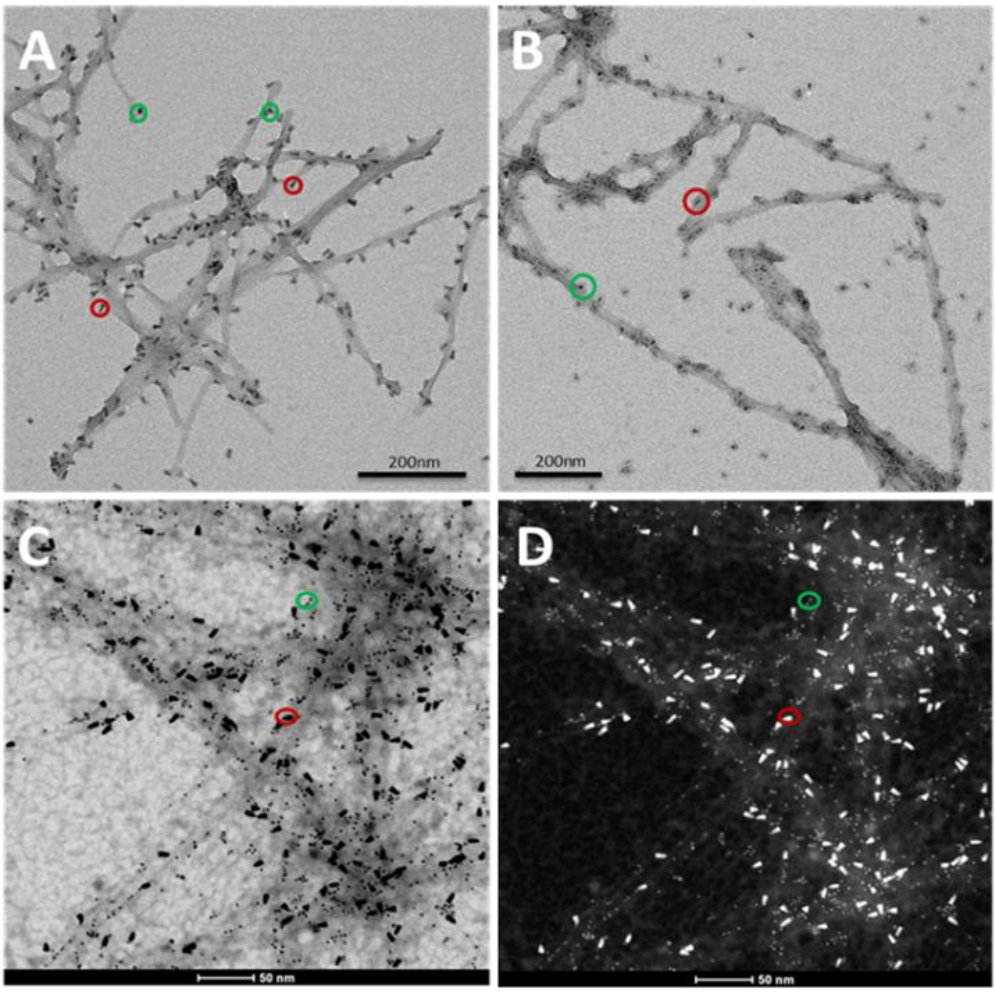

Fig. 16. A) HR-TEM image and B) contrasted HR-TEM image of Blg fibers functionalized with two types of QDs: QD655 and QD525. C) The STEM bright-field image nanofibers and D) the high-angle annular dark-field (HAADF) STEM image of Blg-QDs nanofibers. QD525 and QD655 are marked in green and red circles, respectively.

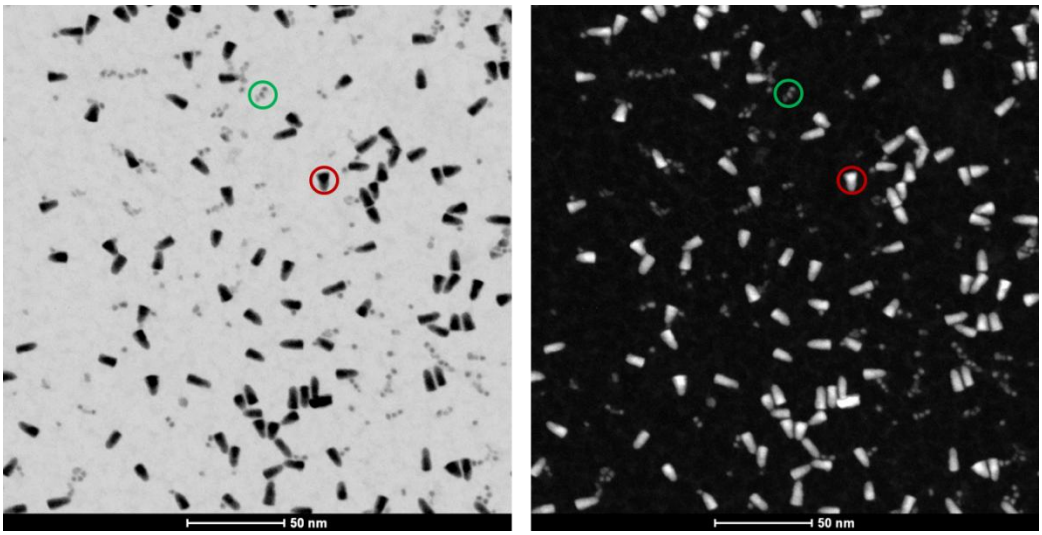

Fig. 17. STEM bright-field image of spherical QD525 (green) and rod-like QD655 (red) and the corresponding high-angle annular dark-field (HAADF) STEM image.

The multicolor fluorescent sample was then imaged with the correlative AFM/super-resolution microscope. First, the topography image reveals relevant structural information about the protein fibers (Figure 18A). The height of Blg fibers can be directly related to the number of twisted filaments that compose the fiber,[36] i.e., heights of about 4, 6, and 8 nm correspond to two, three, and four filaments per fiber. Blg filament twisting induces periodic fluctuations in height along the fiber contour length, which we can also observe in one section with a period of 75 nm, consistent with a fiber composed by three filaments. To obtain information about the properties of the attached QDs, a super-resolution reconstructed image in two colors can be overlaid with the AFM image (Figure 18B) and clearly allows the identification of QDs emitting in their respective colors as well as those nonemitting, which would not be possible with the individual techniques. This hybrid nanoscopy technique has great potential to study multifunctional hybrid materials,[47,48] especially since nanocrystals are characterized by the presence of a significant dark fraction population.

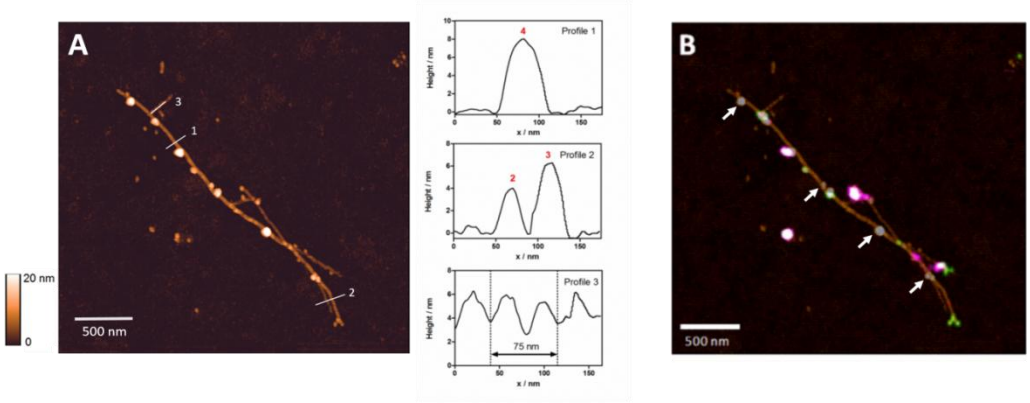

Fig. 18. A) AFM image and topographic profiles of Blg fibers labeled with QD525 and QD655. The red numbers in Profiles 1 and 2 correspond to the number of filaments that compose the fiber as expected from the height values. The periodicity observed in Profile 3 is consistent with a fiber composed by three filaments. B) Correlative AFM and two-color super-resolution image. The arrows highlight examples of nonemitting QDs.

6. Conclusions

1D fluorescent nanofibers have been prepared either using apoferritin or β-lactoglobulin proteins as templates. We showed that apoferritin fibers maintain their ability to be functionalized. Thus, 1D fluorescent fibers with fluorescence emission ranging from green to near-infrared were prepared by coupling dyes or QDs to APO and Blg proteins. FLIM-PIE studies on FRET efficiency within the tagged APO and Blg fibers demonstrate different arrangements of the proteins in mature fibers than in small oligomers. The arrangement of multiple dye molecules into fiber assemblies exhibits a more efficient energy transfer as compared with their counterpart globular proteins. Moreover, the choice of different donors and acceptors may allow wavelength tunability through intrafibrillar energy transfer. Therefore, the results demonstrate the chemically versatile nature of this 1D template and its high potential for manufacturing hybrid and functional nanomaterials, specifically fluorescent nanofibers.

Besides, we have shown that hybrid nanoscopy combining AFM and super-resolution imaging provides valuable complementary information about the structure and properties of luminescent hybrid nanomaterials. While the topography image allowed determining the structure of the fiber, the super-resolution image (in one or two colors) allowed the identification of emissive and nonemissive QDs. This combined insight would not be possible with the individual techniques. The novel insight gained with these techniques can drive the design of improved luminescent nanomaterials for bioimaging, biosensing, and many other different applications.

The well-established knowledge about the apoferritin structure, the availability of numerous methods for its functionalization and the simplicity of fiber synthesis, makes the APO protein a highly promising template for preparing 1D nanomaterials. The ability to control both, the type and number of fluorophores on a fiber template as opposed to being embedded irregularly in a matrix could be advantageous. This would allow rational manipulation of the energy transfer efficiency by varying the type and number of acceptor and donor fluorophores.

Protein fibrils resulting from the assembly of proteins or peptides into long, highly ordered fibrillar structures are emerging as one of the fastest growing scientific areas, because of their functional versatility and broad applications in Biology (as an example, fluorescent amyloid-like fibers are proposed for imaging neurodegenerative diseases) and in Nanotechnology (as templates for the fabrication of metal nanowires and functional polymer nanotubes). In that sense they can find similar applications as fluorescent organic polymers or inorganic nanowires.

7. References

[1] Z. Tang, N.A. Kotov, *Adv. Mater*., **2005**, *17*, 951.

[2] M.R. Buck, R.E. Schaak, *Angew. Chem., Int. Ed*., **2013**, *52*, 2.

[3] M.B. Dickerson, K.H. Sandhage, R.R. Naik*, Chem. Rev.,* **2008**, *108*, 4935.

[4] R.K. Joshia, J.J. Schneider, *Chem. Soc. Rev*., **2012**, *41*, 5285.

[5] L. Nicole, L. Rozes, C. Sanchez, *Adv. Mater*., **2010**, *22*, 3208.

[6] S.A. Maier, M.L. Brongersma, P.G. Kik, S. Meltzer, A.A.G. Requicha, H.A. Atwater, *Adv. Mater*., **2001**, *13*, 1501.

[7] S.A. Maier, P.G. Kik, H.A. Atwater, S. Meltzer, E. Harel, B.E. Koel, A.A.G. Requicha, *Nat. Mater*., **2003**, *2*, 229.

[8] M.M. Walker, T.E. Dennis, J.L. Kirschvink, *Curr. Opin. Neurobiol.,* **2002**, *12*, 735.

[9] P. Alivisatos, *Nat. Biotechnol*., **2004**, *22*, 47.

[10] B. Pelaz, S. Jaber, D.J. de Aberasturi, V. Wulf, T. Aida, J.M. de la Fuente, J. Feldmann, H.E. Gaub, L. Josephson, C.R. Kagan, N.A. Kotov, L.M. Liz-Marzán, H. Mattoussi, P. Mulvaney, C.B. Murray, A.L. Rogach, P.S. Weiss, I. Willner, W.J. Parak, *ACS Nano*, **2012**, *6*, 8468.

[11] I. Cherny, E. Gazit, Angew. *Chem., Int. Ed.,* **2008***, 47*, 4062.

[12] T. Scheibel, R. Parthasarathy, G. Sawicki, X.M. Lin, H. Jaeger, S.L. Lindquist, *Proc. Natl. Acad. Sci. U. S. A.,* **2003***, 100*, 4527.

[13] X. Zan, S. Feng, E. Balizan, Y. Lin, Q. Wang, *ACS Nano,* **2013***, 7*, 8385.

[14] A.K. Nair, A. Gautieri, S.W. Chang, M.J. Buehler*, Nat. Commun.,* **2013***, 4,* 1724.

[15] A. Seidel, O. Liivak, S. Calve, J. Adaska, G. Ji, Z. Yang, D. Grubb, D.B. Zax, L.W. Jelinski, *Macromolecules,* **2000***, 33*, 775.

[16] S. Keten, Z. Xu, B. Ihle and M. J. Buehler, *Nat. Mater.,* **2010***, 9*, 359.

[17] T. Nicolai, D. Durand, *Curr. Opin. Colloid Interface Sci.,* **2013***, 18*, 249.

[18] C. Li, J. Adamcik, R. Mezzenga, *Nat. Nanotechnol.,* **2012***, 7*, 421.

[19] S. Bolisetty, J.J. Vallooran, J. Adamcik, S. Handschin, F. Gramm, R. Mezzenga, *J. Colloid Interface Sci.,* **2011***, 361*, 90.

[20] S. Bolisetty, J. Adamcik, J. Heier, R. Mezzenga, *Adv. Funct. Mater.,* **2012***, 22*, 3424.

[21] S. Bolisetty, J.J. Vallooran, J. Adamcik, R. Mezzenga, *ACS Nano,* **2013***, 7*, 6146.

[22] J.M. Jung, G. Savin, M. Pouzot, C. Schmitt, R. Mezzenga, *Biomacromolecules,* **2008,** *9*, 2477.

[23] G. Jutz, P. van Rijn, B. Santos Miranda, A. Böker, *Chem. Rev.,* **2015***, 115*, 1653.

[24] B. Fernandez, N. Galvez, P. Sanchez, R. Cuesta, R. Bermejo, J.M. Domınguez-Vera, *J. Biol. Inorg. Chem.,* **2008***, 13*, 349.

[25] B. Fernandez, N. Galvez, R. Cuesta, A.B. Hungrıa, J.J. Calvino, J.M. Domınguez-Vera, *Adv. Funct. Mater.,* **2008***, 18*, 3931.

[26] H. Skaat, S. Margel, *Biochem. Biophys. Res. Commun.* **2009**, *386*, 645.

[27] S. J. Lim, M.U. Zahid, P. Le, L. Ma, D.Entenberg, A. S. Harney, J. Condeelis, A. M. Smith, *Nat. Commun.,* **2015***, 6*, 8210.

[28] I. L. Medinitz, H. T. Uyeda, E. R. Goldman, H. Mattoussi, *Nat. Mater.,* **2005***, 4,* 435.

[29] X.Michalet, F. F. Pinaud, L. A. Bentolila, J. M. Tsay, S. Doose, J. J. Li, G. Sundaresan, A. M. Wu, S. S. Gambhir, S. Weiss, *Science,* **2005***, 307*, 538.

[30] S. Nie, Y. Xing, G. J. Kim, J. W. Simons, *Annu. Rev. Biomed. Eng.,* **2007***, 9*, 257.

[31] J.A. Broussard, B. Rappaz, D.J. Webb, C.M. Brown, *Nature Protocols,* **2013**, *8*, 265.

[32] G. Fichman, L. Adler-Abramovich, S. Manohar, I. Mironi-Harpaz, T. Guterman, T. Seliktar, P. Messersmith and E. Gazit, *ACS Nano,* **2014***, 8,* 7220–7228.

[33] D. J. Toft, T. J. Moyer, S. M. Standley, Y. Ruff, A. Ugolkov, S. I. Stupp and V. L. Cryns, *ACS Nano***, 2012***, 6*, 7956.

[34] G.B. Jamesona, J.J. Adamsa, L.K. Creamer, *Int. Dairy J.,* **2002**, *12,* 319.

[35] A.C. Dave, S.M. Loveday, S.G. Anema, G.B. Jameson, H. Singh, *J. Agric. Food Chem.* **2014***, 62,* 3269.

[36] J. Adamcik, J.M. Jung, J. Flakowski, P. De Los Rios, G. Dietler, R. Mezzenga, *Nat. Nanotechnol.,* **2010**, *5*, 423.

[37] J. Xu, K.F. Tehrani, P. Kner, *ACS Nano,* **2015***, 9*, 2917.

[38] K. Lidke, B. Rieger, T. Jovin, R. Heintzmann, *Opt. Express,* **2005***, 13*, 7052.

[39] F.C. Chien, C.W. Kuo, P. Chen, *Analyst,* **2011***, 136*, 1608

[40] T. Dertinger, R. Colyer, G. Iyer, S. Weiss, J. Enderlein, *Proc. Natl. Acad. Sci., USA,* **2009***, 106*, 22287.

[41] T.M. Watanabe, S. Fukui, T. Jin, F. Fujii, T. Yanagida, *Biophys. J.,* **2010***, 99*, L50.

[42] Y. Wang, G. Fruhwirth, E. Cai, T. Ng, P. R. Selvin, *Nano Lett.,* **2013***, 13*, 5233.

[43] Y. Ebenstein, T. Mokari, U. Banin, *Appl. Phys. Lett.* **2002***, 80*, 4033.

[44] T. Pons, I.L. Medintz, D. Farrell, X. Wang, A.F. Grimes, D.S. English, L. Berti, H. Mattoussi, *Small,* **2011***, 7*, 2101.

[45] N.J. Orfield, J.R. McBride, J.D. Keene, L.M. Davis, S.J. Rosenthal, *ACS Nano,* **2015**, *9*, 831.

[46] P. Dedecker, S. Duwe, R.K. Neely, J. Zhang, *J. Biomed. Opt.,* **2012**, *17*, 126008.

[47] L. Sasso, S. Suei, L. Domigan, J. Healy, V. Nock, M.A. Williams, J.A. Gerrard, *Nanoscale,* **2014**, *6*, 1629.

[48] S. Chae, S. Lee, K. Kim, S.W. Jang, B.H. Sohn, *Chem. Commun.,* **2016**, *52*, 6475.

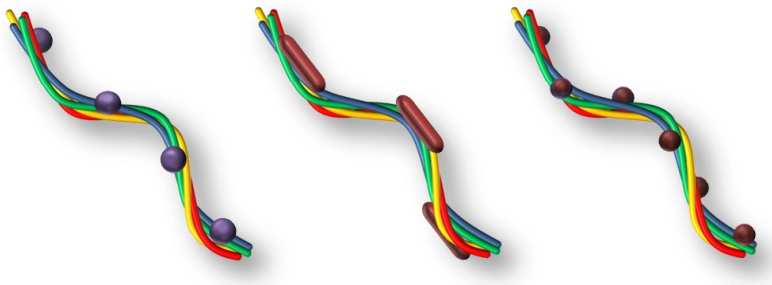

CHAPTER 6. 1D HYBRID METALLIC PROTEIN NANOFIBERS

1. Introduction

Proteins, lipids and macromolecular structures are the main components for biomineralization in nature.[1] They are responsible for the growth, nucleation and morphology of the inorganic phase formed and they also control its mechanical properties.[2] The use of macromolecules to direct the growth and nucleation of biominerals has been employed in various methods for materials chemistry, especially for the synthesis of nanowires, nanoparticles and semiconductors.[3]

Consequently, self-assembled proteins and peptides can be used to guide the hierarchical organization of inorganic matter forming bioinorganic materials. This method has had considerable attention since it is a biomimetic process of mineralization and it can help as well in the advancement of new inorganic materials.[4]

Amyloids are insoluble aggregates formed in vivo from misfolded proteins and are mainly known for their implication in severe neurodegenerative diseases.[5,6] On the other hand, amyloid fibrils are ordered self-assembled nanostructures, which show potential in the synthesis of inorganic nanostructures. In particular, amyloid fibrils, either natural or synthetic, and self-assembling peptides show enormous potential as templates for the fabrication of 1D inorganic nanowires structures.[7,8,9,10,11,12] By mimicking the amyloid fibrillation process in vitro, nanofilaments of remarkable mechanical strength can be formed, which can serve as a platform for nanotechnological materials, combining physical properties with biological compatibility.[13,14]

Basically, amyloid fibrils are composed of highly ordered filaments characterized by β strands that run perpendicular to the fiber axis and are arranged in hydrogen-bonded cross β-strands, which confers to these fibrils exceptional mechanical properties, as mentioned previously, that

along with their unusually high aspect ratio, could be exploited as scaffolds for lightweight functional materials.[15]

Besides their mechanical and biological functionality, amyloid fibrils are also unique in terms of their surface chemistry, where several available chemical groups provide further functionality to the fibrils and can act, for example, as natural reduction sites for the synthesis of inorganic nanoparticles.[16] Taken together, these features suggest that the mechanical properties of amyloid fibrils, their high aspect ratio and their multivalent surface chemistry can be synergistically exploited to design functional hybrid materials of uncommon low densities and functions.[17]

In chapter 3, we have described the formation of apoferritin (APO) and β-lactoglobulin (Blg) amyloid like fibers.[18] In this chapter our aim is to use APO and Blg fibril proteins as platforms for the systematic incorporation of different inorganic metallic nanoparticles by a facile method and in an aqueous medium. Lately, another objective is to use apoferritin amyloid-like fibrils as templates for the synthesis of metal nanoparticles, in similarity with β-lactoglobulin. The apoferritin structure is rich in metal-binding residues, resulting in this protein having a high affinity for a wide range of metals.[19] This together with the need for developing synthetic methods to reliably produce metal-coated fibrils make apoferritin fibers a new promising template for obtaining hybrid functional biomaterials. Both chemical methods proposed here are a mandatory first step towards the exploitation of these fibrils as nanowires with several applications.

2. Decorating APO and Blg fibrils with different nanoparticles.

APO and Blg fibrils were formed as previously explained. In a first step, gold nanospheres,[20] gold nanorods[21] and maghemite nanoparticles[22] were synthesized accordingly to protocols described in literature (see

Materials and Methods) and were patterned using amyloid-like fibrils as prepared (Scheme 1).

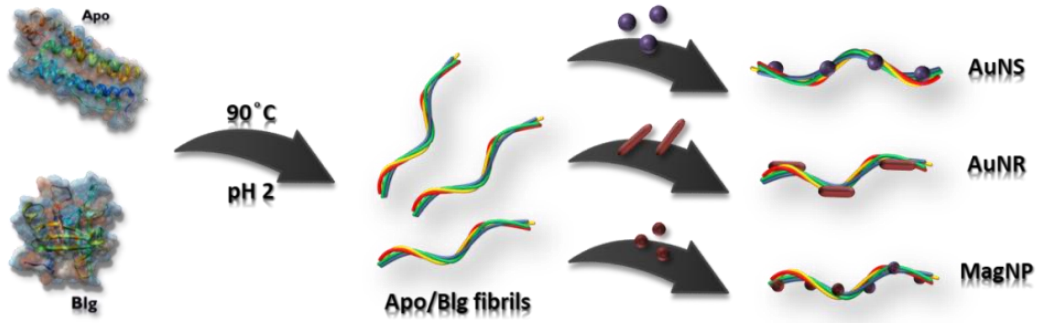

Scheme 1. Schematic illustration of APO and Blg fibrils assemblies with different metal nanoparticles: gold nanospheres (AuNS), gold nanorods (AuNR) and magnetic maghemite nanoparticles (MagNP).

2.1. Decorating APO and Blg fibrils with gold nanoparticles.

Gold nanoparticles (AuNPs) exhibit a strong localized surface plasmon resonance (LSPR) that results from the collective coherent oscillation of conduction band electrons across the NP upon interaction with light at a specific resonant wavelength.[23] The anisotropy of some morphologies, such as nanowires, generates two Surface Plasmon Resonance (SPR) absorption bands corresponding to the transverse and longitudinal axes, the latter usually at low energies, in the infrared region.[24,25] This makes possible that, by means of irradiation of laser light of an adequate wavelength, the gold NP absorbs energy and generates local heating useful for the treatment of cancer by hyperthermia.[26] Moreover, the optical properties of AuNPs are useful in many other bioapplications.[27,28] For instance, the sensitivity of the LSPR to the surrounding dielectric medium has been exploited by using shifts in the LSPR band as an analytical signal.[29] Alternatively, they can also be used in contrast imaging techniques and as drug delivery carriers.[30] Recently, significant effort has been

directed toward assembling nanoparticles into sophisticated structures amenable to practical uses. Examples of some typical methods include molecular templating strategies as the use of amyloid fibers.[31,32]

2.1.1. Assembly of gold spherical nanoparticles.

Au spherical nanoparticles with an average size distribution of 12 ± 2nm were deposited onto APO and Blg fibrils (see Materials and Methods). Figure 1 shows different magnification TEM contrasted images of the AuNSs-APO and AuNSs-Blg fibrils. We can observe that gold nanoparticles are randomly distributed along the fibers and that the assembly step did not result in fiber aggregation. The incorporation of AuNSs onto the fibers was clearly successful and no free AuNSs were observed in the medium. Besides, the presence of the fiber templates prevents irreversible aggregation of the metal nanoparticles and their subsequent precipitation, as it occurred in fibers-free medium.

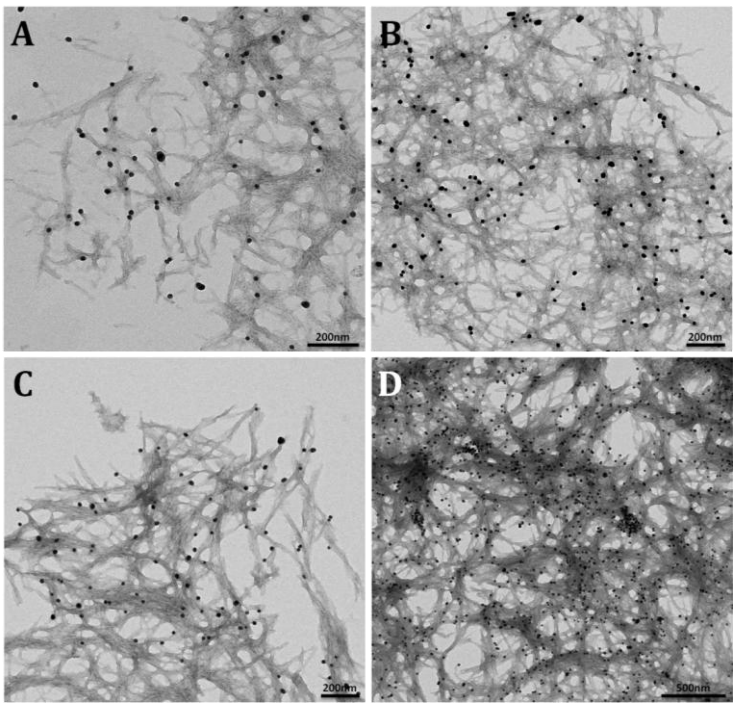

Fig. 1. TEM contrasted images of: (a) and (b) AuNSs-APO fibrils and (c) and (d) AuNSs-Blg fibrils.

Energy dispersive spectroscopy (EDS) confirmed as well the presence of gold nanoparticles. (Figure 2). Samples contained Cu signal peaks coming from the TEM grid.

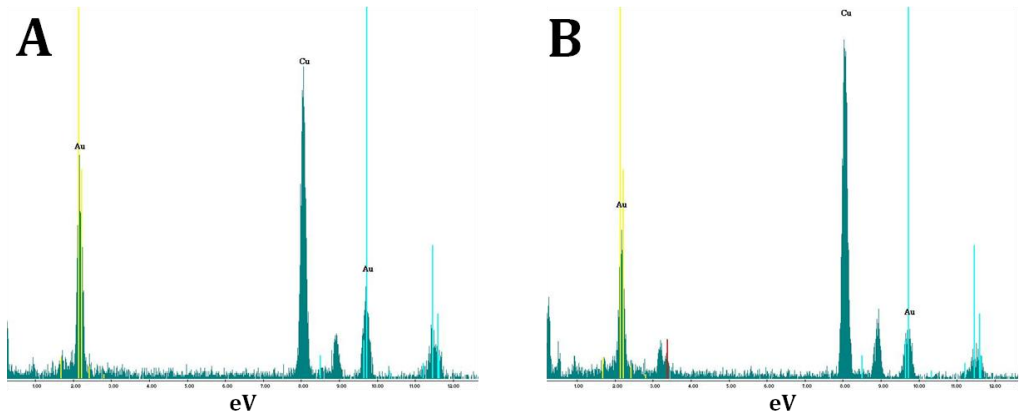

Fig. 2. EDS spectra from (a) AuNSs-APO fibrils and (b) AuNSs-Blg fibrils.

The UV-visible absorption spectra recorded from APO-AuNSs and Blg-AuNSs fibrils displayed the typical SPR absorption band for 12nm gold nanoparticles centered at 530 nm (Figure 3). Both sample solutions were characterized by a pink/purple color (Figure 3, inset).

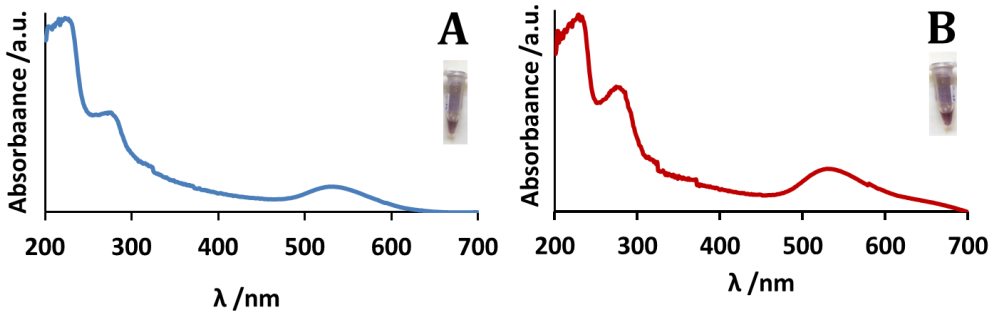

Fig. 3. UV-vis spectra of (a) AuNSs-APO and (b) AuNSs-Blg fibrils. The insert shows the samples of AuNSs-APO and AuNSs-Blg fibrils.

2.1.2. Assembly of gold nanorods.

Au nanorods (AuNRs) displayed an average width of 13 ± 1nm and a length distribution of 42 ± 2nm. Deposition of Au nanorods onto APO and Blg fibrils was conducted by the same procedure as with gold nanospheres (see Materials and Methods). Figure 4 shows the bright-field and the high-angle annular dark-field (HAADF) scanning transmission electron microscopy (STEM) images, as well as the corresponding elemental mapping of Au in the AuNRs-APO and AuNRs-Blg fibrils. The EDX mapping showing colocalization of Au on fibers confirmed the presence of the NRs associated with the fibers. It is confirmed therefore by TEM imaging that the AuNRs were completely incorporated to the fibrils and that the medium was clean.

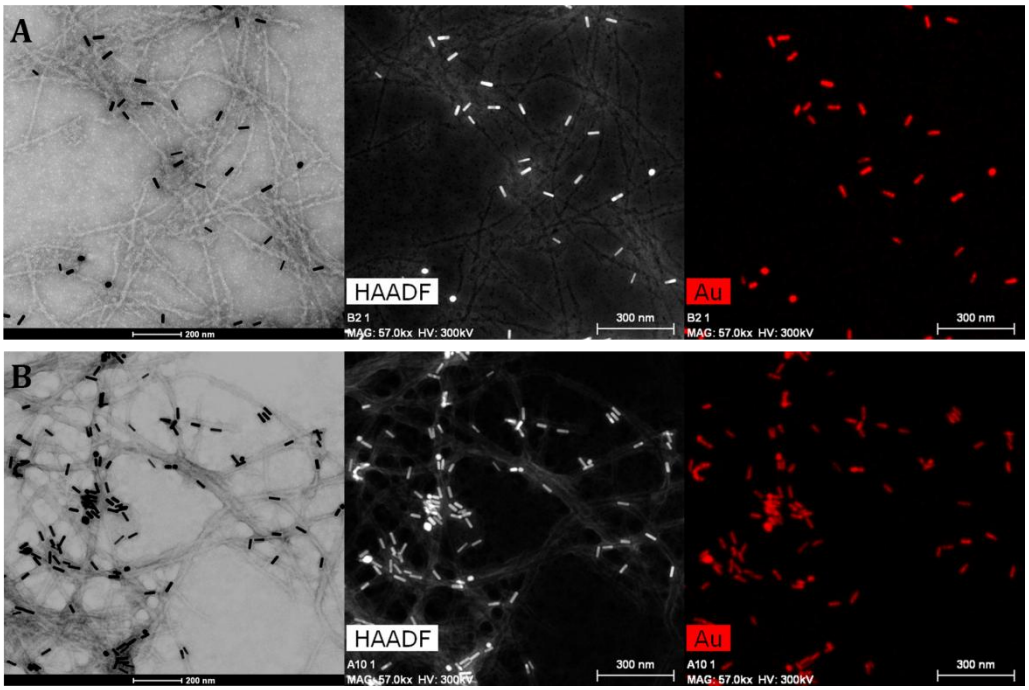

Fig. 4. Bright-field, high-angle annular dark-field (HAADF) STEM images and the corresponding EDX elemental mapping of Au in the AuNRs-APO (a) and AuNRs-Blg (b) fibrils.

As previously commented, the LSPR is very sensitive to NP anisotropy. Rod-shaped AuNPs or "nanorods" are characterized by two LSPR bands: a transverse oscillation with a visible resonance that corresponds to that of a sphere with analogous dimensionality and a longitudinal oscillation, which exhibits a NIR resonance and shifts to longer wavelengths and stronger intensities as the aspect ratio increases. The UV-visible absorption spectra recorded from AuNRs-APO and AuNRs-Blg fibers displayed two absorption bands centered at 530 nm and 750nm (Figure 5). Consequently, it can be concluded from TEM and UV-vis measurements that the AuNRs are randomly distributed among the fibers and that no much nanoparticle aggregation occurs thanks to the fibers.

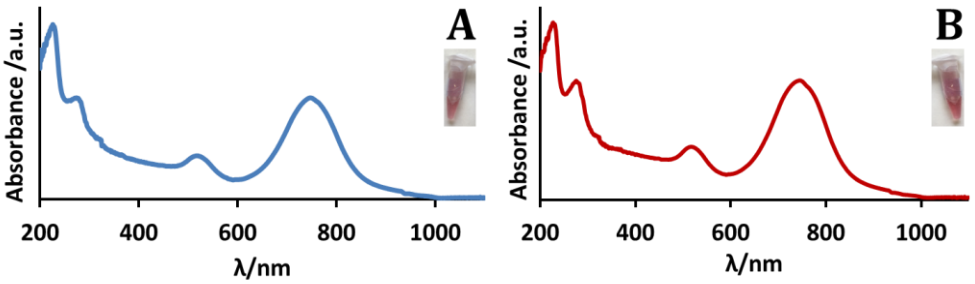

Fig. 5. UV-vis spectra of (a) AuNRs-APO and (b) AuNRs-Blg fibrils. The inserts show pink/purple color for the samples of AuNRs-APO and AuNRs-Blg fibrils.

2.2. Decorating APO and Blg fibrils with iron oxide nanoparticles.

Magnetic nanoparticles are bringing in considerable research efforts due to their potential industrial applications in ultrahigh-density magnetic storage devices,[33,34] as well as their potential biomedical applications as contrast agents in Magnetic Resonance Imaging, drug delivery, hyperthermia treatment[35] or cancer cells removal.[36,37] In particular, magnetic hybrids offer the possibility to achieve high spatial order and alignment, which is a highly desirable feature in several applications.[38]

In a first step, magnetite nanoparticles were prepared by the coprecipitation of iron salts in solution following the Massart's method (see Materials and Methods). As compared to non-polar organometallic routes, aqueous syntheses are more reproducible, cheaper, non-toxic and the prepared samples have high aqueous stability and biological compatibility. We synthesized magnetite nanoparticles of 8 nm ± 2 nm on average size. Oxidation of magnetite in acidic conditions resulted in a colloid of maghemite (γ-Fe_2O_3) nanoparticles (Mag), which are chemically stable at pH 2.[39]

In a second step, the Mag-Fibrils assemblies were formed by electrostatic interactions between the positively charged maghemite nanoparticles at pH 2 and the negatively charged APO and Blg protein fibrils. Figure 6 shows how the inclusion of Mag in the fiber template was completed, in a sense that no free-particles were observed in the medium. In the case of APO-Mag fibers the NPs arranged disjointedly on the fibers. However, for Blg-Mag sample NPs arranged along the protein nanofibers alternately on either side of the fiber.

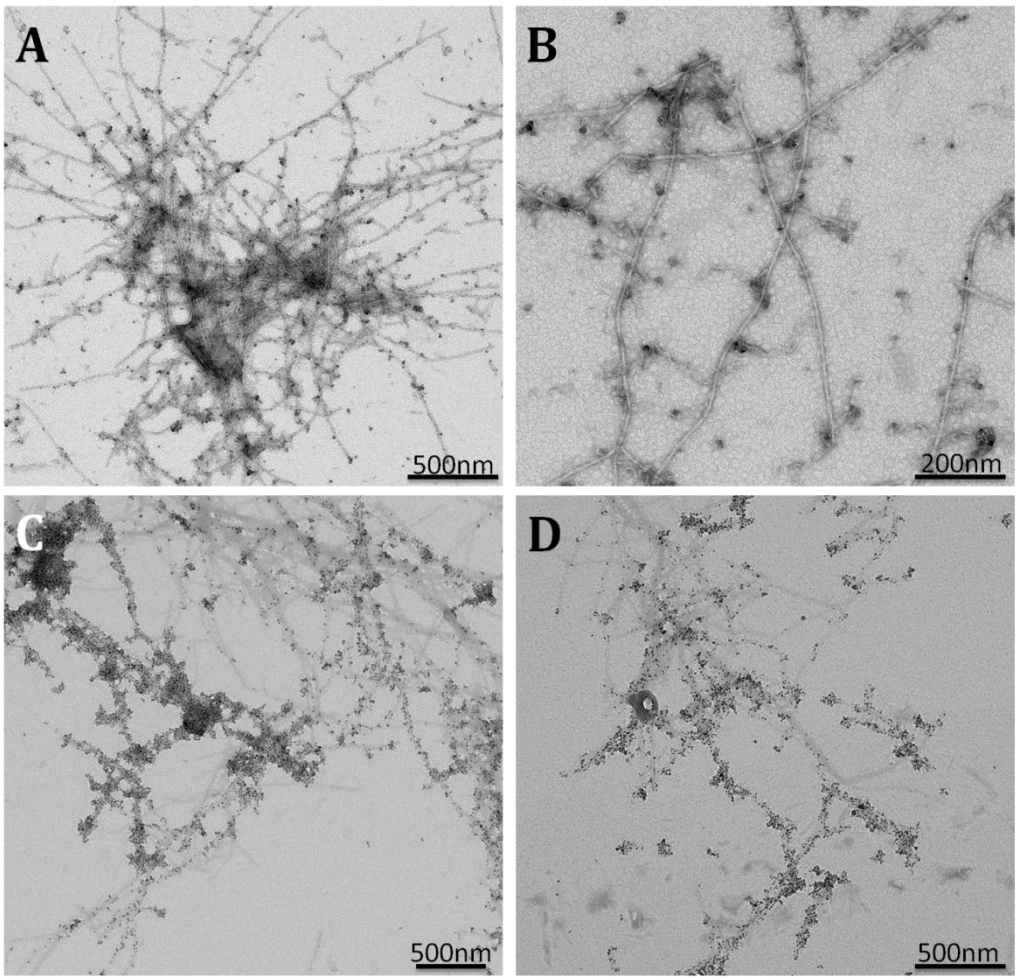

Fig. 6. TEM images of: (a) and (b) APO-Mag fibrils and (c) and (d) Blg-Mag fibrils.

Figure 7 shows the characterization of Mag-protein fibers using the high-angle annular dark-field (HAADF) scanning transmission electron microscopy (STEM) and the corresponding elemental mapping of Fe in the APO-Mag and Blg-Mag fibrils. The EDX mapping proved that the NPs were effectively linked to the fibers.

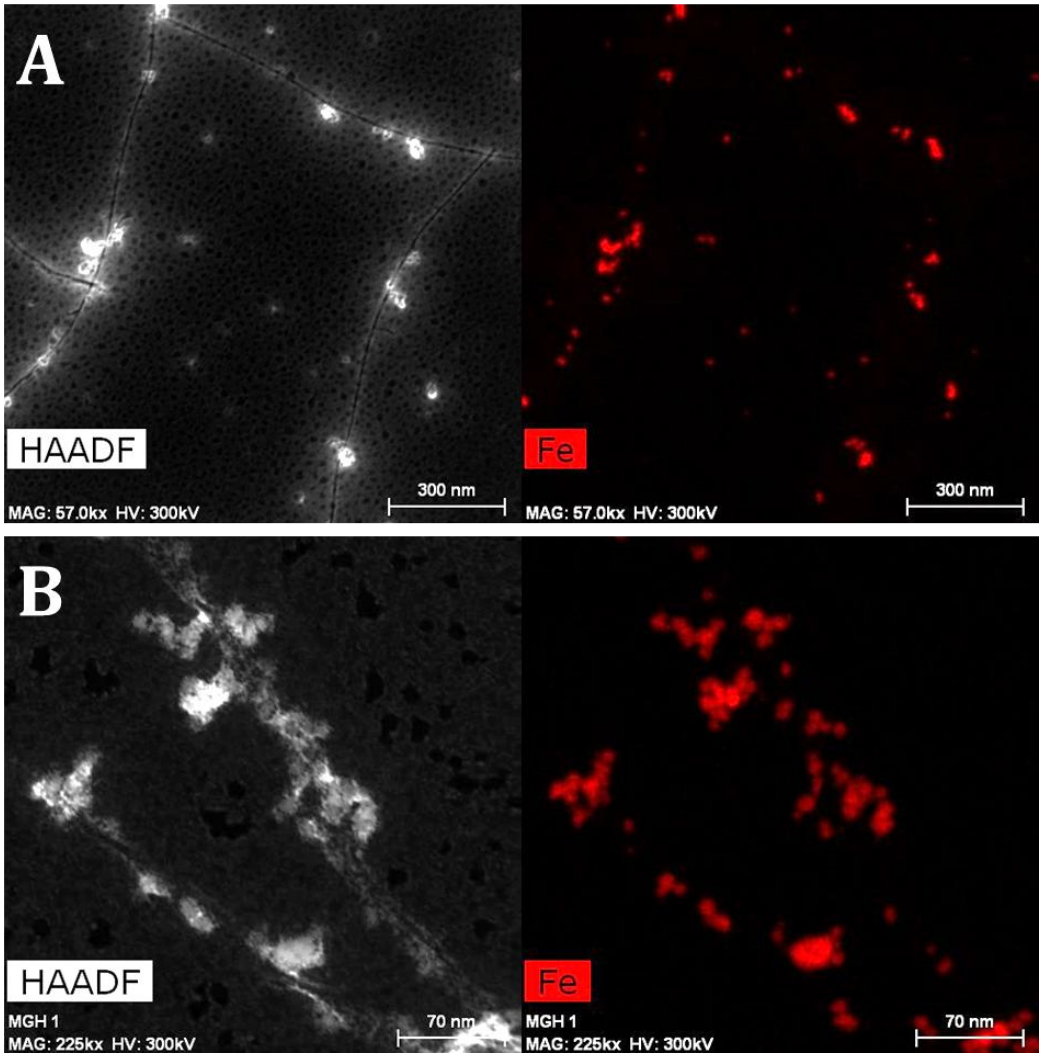

Fig. 7. HAADF-STEM images (left) and the corresponding elemental mapping of Fe (right) in the APO-Mag (a) and Blg-Mag (b) fibrils.

We examined the APO-Mag and Blg-Mag fibrils magnetic properties by the SQUID technique (Figure 8). Zero field cooled-field cooled (ZFC-FC) magnetization curves were performed as a function of temperature (2-300 K) at a field of H = 50 Oe (Figure 8A and 8B). The obtained blocking temperatures (TB) were 125 and 100 K for APO-Mag and Blg-Mag fibrils, respectively. Above TB, ZFC and FC curves superimpose perfectly, so we can rule out the presence of much aggregation. The obtained TB values

were slightly higher than that of isolated γ-Fe_2O_3 nanoparticles of the same size (90K).[40] This increase in TB is caused by the dipole-dipole interactions among nanoparticles.

Figures 8C and 8D show the hysteresis loops recorded at 2 K and 293K for APO-Mag and Blg-Mag fibrils. The magnetization (M) curves measured versus applied fields (H) reflect the particle anisotropy. The coercivity value (Hc) was 250 Oe for both APO-Mag and Blg-Mag fibrils. Again, this value is higher in comparison to the pristine nanoparticles (Hc=175 Oe) due to the dipole-dipole interactions and the 1D organization. Magnetization recorded at 293 K showed a coercivity value of 30 Oe and 40 Oe for APO-Mag and Blg-Mag fibrils, respectively.

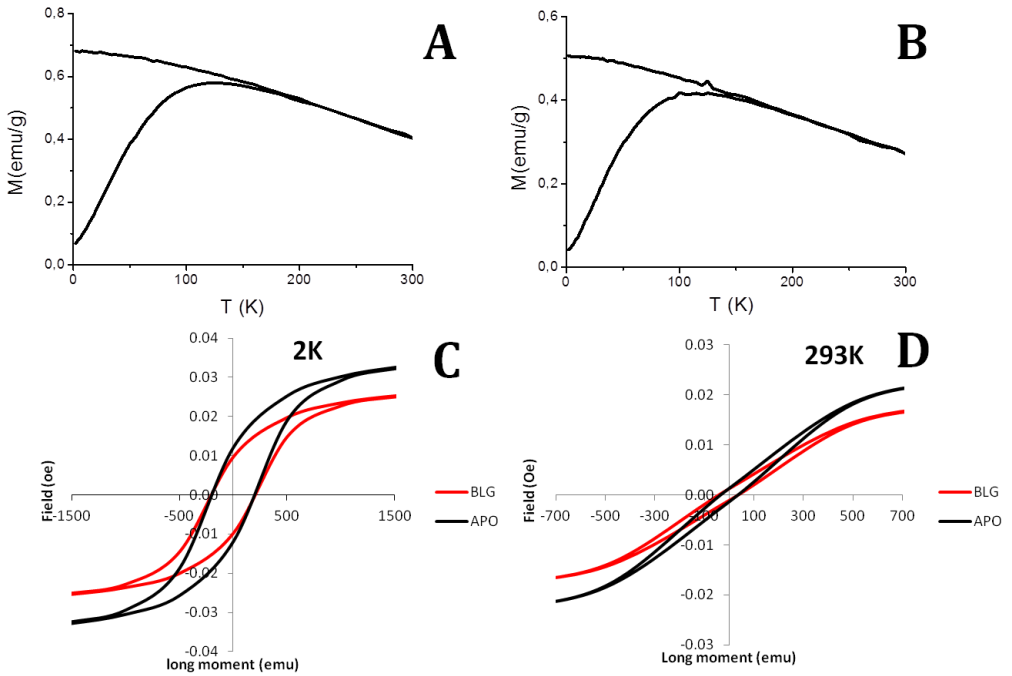

Fig. 8. Zero field cooled-field cooled curves registered at a field (H) of 50 Oe for APO-Mag (a) and Blg-Mag (b) fibrils. Hysteresis loops of APO-Mag and Blg-Mag samples at 2 K(c) and 293 K (d).

3. Metal-binding APO fibers as templates for the preparation of hybrid nanostructures

The amyloid-like protein fibrils can be used for templating metallic nanowires, which are currently in high demand for the construction of conductive circuits in nanoscale electronics and as the active components in electrochemical devices. Apart from their regularity and easy reproduction, the biological templates may have another key advantage as they can grow directly at the required surfaces, thus guiding the assembly of the inorganic nanostructures straight into the nanodevices and eliminating the stage of their positioning and micro-manipulations. We exploited self-assembled amyloid fibers from APO as biotemplates to synthesize noble metal nanoparticle chains.[41,42] The apoferritin amyloid fibrils in the presence and absence of gold, silver or palladium salts were subjected to traditional metal reducing agents such as $NaBH_4$. The approach is based on the binding of some metal ions to the surface of the fibers and on the capacity of these bonded metal ions to react with an appropriate reducing agent to give rise to the nucleation of a metallic nanoparticle (Scheme 2). This method, therefore, could afford a wide range of zero-valent nanoparticle-fibers hybrid materials.

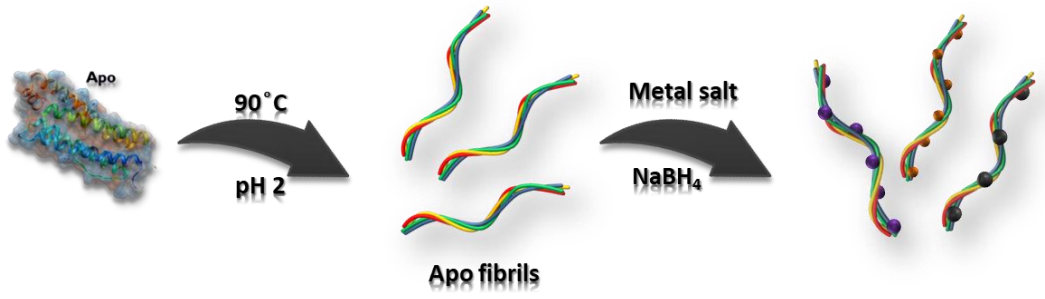

Scheme 2. Schematic illustration of APO fibrils used as templates for producing 1D metallic nanoparticles.

3.1. Fabrication of gold nanoparticle nanowires

Figure 9 shows STEM micrographs of APO fibrils after incubation with $HAuCl_4$ and subsequent reduction with $NaBH_4$ and the corresponding elemental mapping of Au. The AuNPs formed are simultaneously assembled to both sides of the fibers (7 ± 2nm). In this way, continuous Au nanowires were successfully prepared.

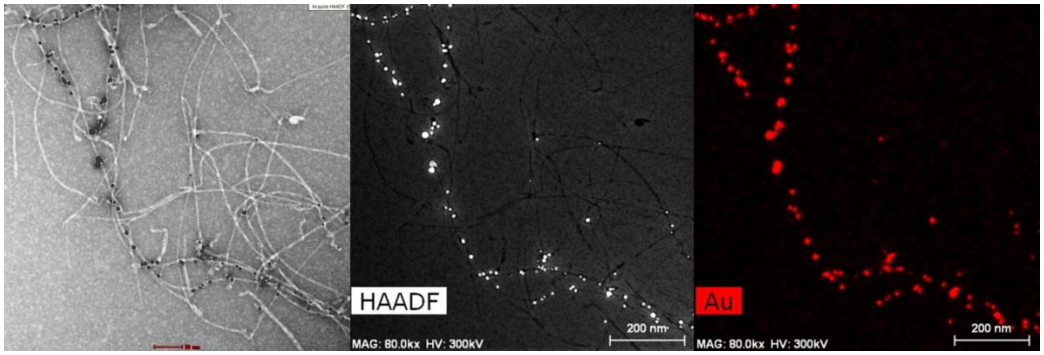

Fig. 9. Bright-field (left), high-angle annular dark-field (HAADF) STEM images (center) and the corresponding elemental mapping of Au (right) for of AuNPs-APO fibers.

The identity of metal particles bounded on the fibrils was confirmed by UV-vis (Figure 10). Again, AuNPs-APO fibers displayed only a single absorption band attributed to the collective dipole oscillation at 530 nm. Therefore, the AuNPs were spherical-like nanoparticles.

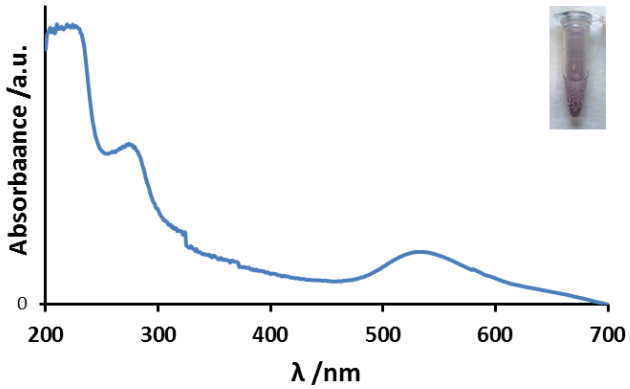

Fig. 10. UV-vis spectrum of AuNPs-APO fibrils. The insert shows the samples of AuNPs-APO fibrils.

3.2. Fabrication of silver nanoparticle nanowires

Figure 11 shows TEM micrographs of APO after incubation with $AgNO_3$ and reduction with $NaBH_4$. Addition of the reductant to the transparent solutions of Ag-fibrils produced brownish solutions. The protein fibers prevented bulk aggregation of the metal particles and resulted in a stable colloidal solution. AgNPs were totally incorporated to the fibrils and they arranged randomly on them. However, the NPs presented a size varying from 20 to 70nm. Energy dispersive spectroscopy (EDS) confirmed as well the presence of silver nanoparticles (Figure 12).

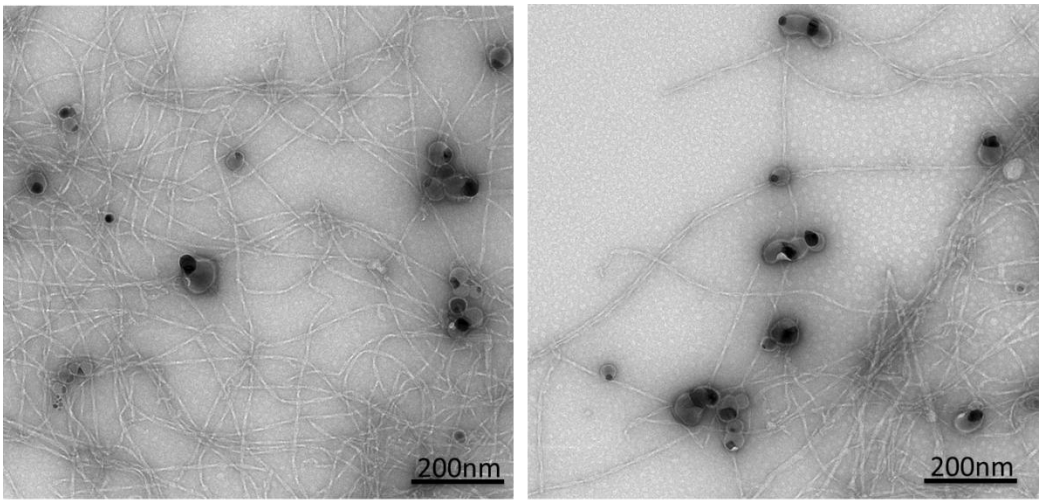

Fig. 11. TEM images of AgNPs-APO fibrils.

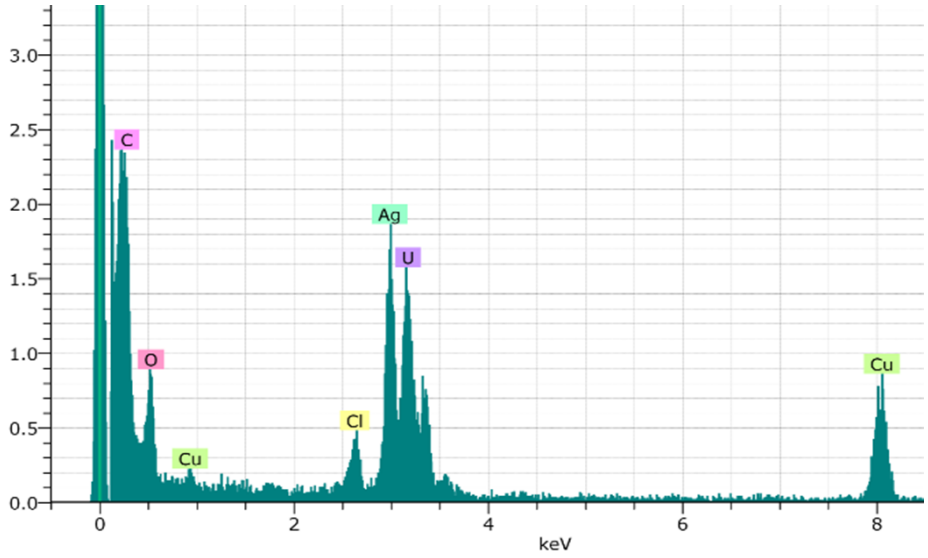

Fig. 12. EDS spectra from AgNPs-APO fibrils.

Analogous to their Au counterparts, AgNPs exhibit a strong LSPR; however, the resonance is stronger, narrower, and shifted to shorter wavelengths than that of AuNPs (ca. 400–525 nm for dimensions ca. 10–100 nm). Moreover, AgNPs also have interesting and potent antimicrobial properties.[43] The UV-visible absorption spectra recorded from AgNPs-APO fibrils displayed an absorption band at 410 nm (Figure 13). For that reason, the corresponding AgNPs prepared were spherical.

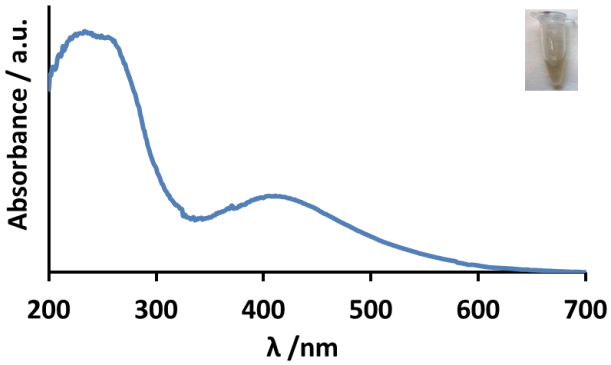

Fig. 13. UV-vis spectra of AgNPs-APO fibrils. The insert shows the corresponding brownish sample of AgNPs-APO fibrils.

3.3. Fabrication of palladium nanoparticle nanowires

Similar procedures were followed to prepare Pd-NPs onto APO fibrils, which were characterized by transmission electron microscopy as shown in Figure 14. TEM images revealed the presence of very small Pd-NPs (5 ± 2 nm) with the NPs arranged alternately on the fibers. Additionally, the medium was clean again. EDS confirmed the presence of palladium (Figure 15).

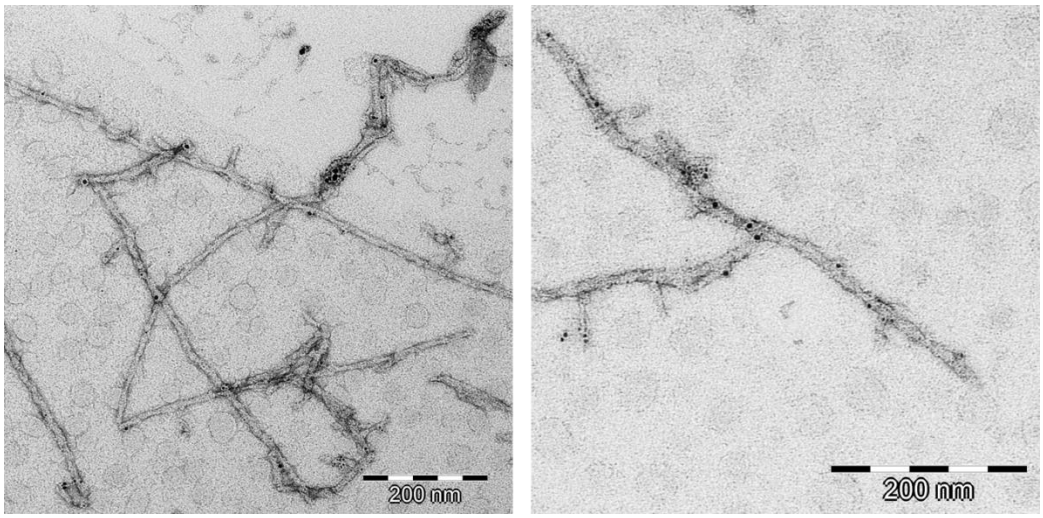

Fig. 15. TEM images of APO-PdNPs fibrils.

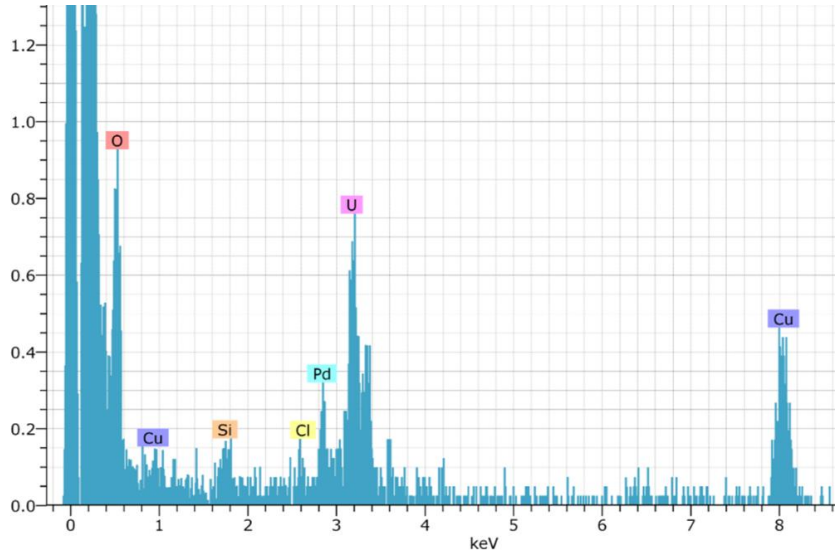

Fig. 16. EDS spectra from PdNPs-APO fibrils.

Although the major interest in PdNPs is mainly centered in catalysis, it is necessary to highlight that they can also have interesting optical properties, just as Ag and Au can have catalytic properties in addition to their optical properties. PdNPs are used in several important applications including petroleum cracking, hydrogenation and dehydrogenation and catalytic converters. Therefore, these hybrid APO-PdNPs fibers could find similar remarkable applications.

4. Conclusions

1D hybrid metallic nanofibers have been prepared either using apoferritin or β-lactoglobulin proteins as templates. We showed for the first time that apoferritin fibers have the ability to assembly different metallic nanoparticles, as well as the β-lactoglobulin. The synthesis procedure involves electrostatic complexation of proteins and nanoparticles. Thus, 1D metallic nanofibers with different optical properties were prepared by coupling different AuNPs to APO and Blg proteins. Optical Au nanoparticles showed the characteristic LSPR band. Therefore, these hybrid nanomaterials could find very appealing applications as sensors and as imaging contrast agents. Moreover, the fast thermalization of absorbed light energy, combined with the NIR resonance of Au nanorods and nanoshells, could be very useful for hyperthermia.

Magnetic-responsive biohybrids of γ-Fe_2O_3 nanoparticles and APO and Blg fibrils have also been synthesized. Their magnetic properties were measured by SQUID. Due to its noninvasive nature and the biocompatibility of the nanoparticle hybrid fibrils, these hybrid nanomaterials may find useful applications in several areas of Bionanotechnology.

These findings have been validated as well with synthetic gold, silver and palladium nanoparticles produced by chemical reduction in the presence of the amyloid fibrils, where the different metals are meant to

illustrate the generality of the approach. In this work, we report for the first time how amyloid APO protein fibrils can serve as nanoreactors for the preparation of metallic NPs. The fibrils coated by gold, silver and palladium nanoparticles, can be fabricated by simply reducing the corresponding metal salt precursors using $NaBH_4$. Optical Ag and Au nanoparticles showed characteristic surface plasmon resonance whereas Pd nanoparticles could find appealing applications in catalysis. Moreover, Ag nanoparticles have antimicrobial properties.

In summary, noble metal nanoparticles, with their unique electrical, optical and magnetic performance and various potential applications, have become one of the popular fields in nanoscience because of their interesting shape-dependent and size-dependent physical and chemical properties. On the other hand, protein fibrils resulting from the assembly of proteins or peptides into long, highly ordered fibrillar structures are emerging as one of the fastest growing scientific areas, because of their functional versatility and broad applications in Biology (amyloid-like fibers are associated with numerous neurodegenerative diseases) and in Nanotechnology.

The well-established knowledge about the apoferritin structure, the availability of numerous methods for its functionalization and the simplicity of fiber synthesis, makes the APO protein a highly promising template for preparing 1D nanomaterials. Therefore, the results demonstrate the versatile nature of this 1D templates and their high potential for manufacturing hybrid and functional nanomaterials.

5. References

[1] F. Nudelman, N.A.J.M. Sommerdijk, *Angew. Chem. Int. Ed. Engl.* **2012**, *51*), 6582.

[2] L.C. Palmer, C.J. Newcomb, S.R. Kaltz, E.D. Spoerke, S.I. Stupp, *Chem. Rev.* **2008**, *108*, 4754.

[3] R. de la Rica, H. Matsui, *Chem. Soc. Rev.* **2010**, *39*, 3499.

[4] M.B. Dickerson, K.H. Sandhage, R.R. Naik, *Chem. Rev.* **2008**, *108*, 4935.

[5] D.J. Selkoe, *Nature* **2003**, *426*, 900.

[6] C.M. Dobson, *Nature* **2003**, *426*, 884.

[7] F. Leroux, M. Gysemans, S. Bals, K.J. Batenburg, J. Snauwaert, T. Verbiest, C. Van Haesendonck, G. Van Tendeloo, *Adv. Mater.* **2010**, *22*, 2193

[8] L. Zhang, N. Li, F. Gao, L. Hou, Z. Xu, ja302959e, Insulin Amyloid Fibrils-- An Excellent Platform for Controlled Synthesis of Ultrathin Superlong Platinum Nanowires with High Electrocatalytic Activity.pdf. **2012**, 11326–11329.

[9] Z.S. Al-Garawi, J.R. Thorpe, L.C. Serpell, *Angew. Chemie Int. Ed.* **2015**, n/a-n/a DOI: 10.1002/anie.201508415.

[10] S. Bolisetty, J. Adamcik, J. Heier, R. Mezzenga, *Adv. Funct. Mater.* **2012**, *22*, 3424.

[11] C. Li, S. Bolisetty, K. Chaitanya, J. Adamcik, R. Mezzenga, *Adv. Mater.* **2013**, *25*, 1010.

[12] Y. Shen, L. Posavec, S. Bolisetty, F.M. Hilty, G. Nyström, J. Kohlbrecher, M. Hilbe, A. Rossi, J. Baumgartner, M.B. Zimmermann, R. Mezzenga, *Nat. Nanotechnol.* **2017**, *12*, 642.

[13] C. Li, S. Bolisetty, R. Mezzenga, *Adv. Mater.* **2013**, *25*, 3694.

[14] C. Li, J. Adamcik, R. Mezzenga, *Nat. Nanotechnol.* **2012**, *7*, 421.

[15] T.P.J. Knowles, M.J. Buehler, *Nat. Nanotechnol.* **2011**, *6*, 469.

[16] J. Zhou, A. Saha, J. Adamcik, H. Hu, Q. Kong, C. Li, R. Mezzenga, *Adv. Mater.* **2015**, *27*, 1945.

[17] S. Kim, J.H. Kim, J.S. Lee, C.B. Park, *Small* **2015**, *11*, 3623.

[18] R. Jurado, F. Castello, P. Bondia, S. Casado, C. Flors, R. Cuesta, J.M. Domínguez-Vera, A. Orte, N.Gálvez, *Nanoscale*, **2016**, *8*, 9648.

[19] N. Gálvez, B. Fernandez, E. Valero, P. Sánchez, R. Cuesta, J.M. Domínguez-Vera, *Comptes Rendus Chim.* **2008**, *11*, 1207.

[20] A.D. McFarland, C.L. Haynes, C.A. Mirkin, R.P. Van Duyne, H.A. Godwin, *J. Chem. Educ.,* **2004**, *81*, 544.

[21] B. Nikoobakht, M.A. El-Sayed, *Chem. Mater.,* **2003**, *15*, 1957.

[22] M. Martín, F. Carmona, R. Cuesta, D. Rondón, N. Gálvez, J.M. Domínguez-Vera, *Adv. Funct. Mater.* **2014**, *24*, 3489.

[23] K. Saha, S.S. Agasti, C. Kim, X. Li, V.M. Rotello, *Chem. Rev.* **2012**, *112*, 2739.

[24] R.A. Alvarez-Puebla, A. Agarwal, P. Manna, B.P. Khanal, P. Aldeanueva-Potel, E. Carbo-Argibay, N. Pazos-Perez, L. Vigderman, E.R. Zubarev, N.A. Kotov, L.M. Liz-Marzan, *Proc. Natl. Acad. Sci.* **2011**, *108*, 8157.

[25] J. Reguera, J. Langer, D. Jiménez de Aberasturi, L.M. Liz-Marzán, *Chem. Soc. Rev.* **2017**, *46*, 3866.

[26] L.C. Kennedy, L.R. Bickford, N.A. Lewinski, A.J. Coughlin, Y. Hu, E.S. Day, J.L. West, R.A. Drezek, *Small* **2011**, *7*, 169.

[27] L. Dykman, N. Khlebtsov, *Chem. Soc. Rev.* **2012**, *41*, 2256.

[28] G. Nyström, M.P. Fernández-Ronco, S. Bolisetty, M. Mazzotti, R. Mezzenga, *Adv. Mater.* **2016**, *28*, 472.

[29] W.Zhao, M. A. Brook, Y. Li, *ChemBioChem* **2008***, 9,* 2363.

[30] C. J. Murphy, A. M. Gole, J. W. Stone, P. N. Sisco, A. M. Alkilany, E. C. Goldsmith, S. C. Baxter, *Acc. Chem. Res.* **2008***, 41*, 1721.

[31] O. Deschaume, B. De Roo, M.J.V. Bael, J. Locquet, C.V. Haesendonck, C. Bartic, *Chem. Mater.* **2014**, *26*, 5383.

[32] C.L. Chen, P. Zhang, N.L. Rosi, *J. Am. Chem. Soc.* **2008**, *130*, 13555.

[33] J. Hoinville, A. Bewick, D. Gleeson, R. Jones, O. Kasyutich, E. Mayes, A. Nartowski, B. Warne, J. Wiggins, K. Wong, *J. Appl. Phys.* **2003**, *93*, 7187.

[34] S. Sun, C. B. Murray, D. Weller, L. Folks, A. Moser, *Science*, **2000**, *287*, 1989.

[35] J. Cheon, J.H. Lee, *Acc. Chem. Res.* **2008**, *41*, 1630.

[36] H. Skaat, S. Margel, *Biochem. Biophys. Res. Commun.* **2009**, *386*, 645.

[37] K.E. Scarberry, E.B. Dickerson, J.F. Mcdonald, Z.J. Zhang, *J. Am. Chem. Soc.*, **2008**, *130*, 10258.

[38] S. Bolisetty, J.J. Vallooran, J. Adamcik, R. Mezzenga, *ACS Nano,* **2013**, *7*, 6146.

[39] E. Valero, S. Tambalo, P. Marzola, M. Ortega-Muñoz, F.J. López-Jaramillo, F. Santoyo-González, J. De Dios López, J.J. Delgado, J.J. Calvino, R. Cuesta, J.M. Domínguez-Vera, N. Gálvez, *J. Am. Chem. Soc.* **2011**, *133*, 4889.

[40] Y. W. Jun, J. W. Seo, J. Cheon, *Acc. chem. Res.* **2008**, *41*, 179.

[41] G. Guo, T.H.A. Truong, H. Tan, H. Ang, W. Zhang, C. Xu, X. Rui, Z. Hu, E. Fong, Q. Yan, *Chem. - An Asian J.* **2014**, *9*, 2555.

[42] M. Malisauskas, R. Meskys, L.A. Morozova-Roche, *Biotechnol. Prog.* **2008**, *24*, 1166.

[43] C. Marambio-Jones, E.M.V. Hoek, *J. Nanopart. Res.* **2010**, *12,* 1531.

CONCLUSIONS

The study developed in this Thesis illustrates the potential of using proteins for the creation of hybrid bioinorganic nanostructures with fascinating properties and applications in the biomedical field. Specifically, from the results obtained in this Thesis we can conclude:

1. Apoferritin protein, an iron storing protein extensively used by our group, has been used for loading **maghemite nanoparticles** (with magnetic properties) and **doxorubicin (DOX)** (antitumoral antibiotic) simultaneously using co-encapsulation or surface-binding methods. The DOX co-encapsulation resulted to be a better method for sustained drug release over time. The resulting magnetic hybrid display good MRI contrast properties, as reported by our group previously. This system can provide sustained DOX release during 25 days. This dual DOX-Apomag nanocarrier may prove useful in the field of "**theranostic nanomedicines**", combining diagnostic and therapeutic components in a single nanoparticle.

2. 1D nanofibers have been prepared either using apoferritin or β-lactoglobulin proteins. This is the first time that a wire-like, micrometer-sized structure with persistence length formed by the heat treatment of apoferritin is described. Controlling the experimental conditions (temperature, pH, incubation time, protein concentration and stirring) the morphology and diameter size can be varied. An incubation time of 9 h, pH of 2, 90 °C, a protein concentration between 0.05-0.2wt% and stirring of 90rpm are the **optimal synthetic conditions** for the formation of wire-like nanofibers.

In a second step, we have been able to demonstrate by combining different techniques that the formation of apoferritin amyloid-like fibers starts from short oligomers aggregates. Protein unfolding and complete hydrolysis are essential for the formation of large laminated aggregates and

small peptides fragments (<5 kDa) participate in the formation of these fibrils. We have been able to resolve and identify **different individual stages of the fibrillation** process using the novel technique FLIM-PIE.

Moreover, we have demonstrated that most of the fibers resulted to be **right-handed**. This is the first time that a native globular protein forms this kind of fibers. Until now, only fibrils prepared starting from short peptides have been reported to form right-handed fibrils.

All these results open a new perspective in the understanding of apoferritin fibrillation. Moreover, these highly ordered fibrillar structures are emerging as one of the fastest growing scientific areas, because of their functional versatility and broad applications in Biology (amyloid-like fibers are associated with numerous neurodegenerative diseases) and in Nanotechnology (as templates for the fabrication of metal nanowires and functional polymer nanotubes).

3. We have demonstrated how H or L apoferritins subunits, with a peptide sequence coincidence of only 54-57% can direct the final chirality of apoferritin fibers. We have compared the apoferritin fibers formed in two different cases: starting from pure Human Apoferritin H (H APO) and from pure Human Apoferritin L (L APO). The observed chirality was nearly a 100% of **right-handeness for L APO** and nearly a **100% of left-handeness for H APO.**

Moreover, we have been able to study their structure by combining different techniques such as TEM or AFM. Electron tomography provided novel appealing results such as APO fibers have a common building block comprising **paired strands with a double helical substructure**. On the other hand, additional measurements provided information about the secondary structure of the different iso-apoferritins.

These results open up the possibility of using the control of chirality to access new forms of protein and peptide nanostructures and show how the peptide sequence of such structures can control their final morphology. Insights into these mechanisms can have significant implications into the growing field of 1D nanostructures.

4. We have prepared **1D fluorescent nanofibers** either using apoferritin or β-lactoglobulin proteins as templates and we have showed that apoferritin fibers maintain their ability to be functionalized. Thus, we have been able to prepare 1D fluorescent fibers with fluorescence emission ranging from green to near-infrared by coupling **dyes** or **QDs** to APO and Blg proteins. **FLIM-PIE** studies on FRET efficiency within the tagged APO and Blg fibers demonstrated a more efficient energy transfer of the mature fibers as compared with their counterpart globular proteins.

Moreover, valuable complementary information about the effective functionalization at nanoscale and properties of luminescent hybrid nanomaterials was provided by **hybrid nanoscopy** combining AFM and super-resolution imaging. While the topography image allowed determining the fiber structure, the super-resolution image (in one or two colors) allowed the identification of emissive and nonemissive QDs.

Therefore, these results demonstrate the chemically versatile nature of this 1D template and its high potential for manufacturing hybrid and functional nanomaterials, specifically fluorescent nanofibers. Additionally, the well-established knowledge about the apoferritin structure, the availability of numerous methods for its functionalization and the simplicity of fiber synthesis, makes the APO protein a **highly promising template** for preparing 1D nanomaterials.

5. In a last step, we have prepared **1D hybrid metallic nanofibers** either using apoferritin or β-lactoglobulin proteins as templates. We have shown for the first time that apoferritin fibers have the ability to assembly different metallic nanoparticles, as well as the β-lactoglobulin. Thus, 1D metallic nanofibers with different optical and magnetic properties were prepared by coupling different **AuNPs** and **maghemite** NPs to APO and Blg fibers. These hybrid nanomaterials could find very appealing applications as sensors or as imaging contrast agents and they could be very useful for hyperthermia as well.

These findings have been validated as well with synthetic **gold, silver and palladium** nanoparticles produced by chemical reduction in the presence of the amyloid fibrils. Therefore, we have reported for the first time how amyloid APO protein fibrils can serve as nanoreactors for the preparation of metallic NPs with several applications in Nanomedicine and Nanotechnology.

In summary, these results demonstrate the versatile nature of these 1D templates and their high potential for manufacturing hybrid and functional nanomaterials.

MATERIALS AND METHODS

1. Materials and methods from Chapter 2

1.1. Preparation of the maghemite colloid

Magnetite was synthesized with slight modifications to Massart's method[1] by coprecipitation of Fe^{2+} and Fe^{3+} salts in 1:2 stoichiometric ratio. Briefly, magnetite nanoparticles were prepared by coprecipitation of Fe^{2+} [$(NH_4)_2Fe(SO_4)_2$] and Fe^{3+} [$Fe(NO_3)_3$] salts in stoichiometry of 0.5. By adjusting both pH (11.0 for 6nm nanoparticles) and ionic strength (1 M $NaNO_3$), the size of the resulting magnetite nanoparticles can be controlled.[2] All solutions were carefully deaerated with argon before reaction. After oxidation of magnetite to maghemite[3] with 1 M $HClO_4$ we obtained a sol (stable colloid solution) of 6 nm maghemite nanoparticles at pH 2 with an iron concentration of 0.1 M.

1.2. Co-encapsulation of maghemite and doxorubicin in apoferritin protein

Doxorubicin hydrochloride (DOX) and Horse Spleen Apoferritin protein (lot. 048 K7004, 50 mg/mL) were purchased from Sigma-Aldrich. This apoferritin protein has usually a 90%L/10%H (L= light chain, H= heavy chain) subunit ratio. An acidic colloid of 6 nm maghemite nanoparticles (200 μL, 0.1 M) and a solution of DOX (30 μL, 5 mg/L) were incubated with disassembled apoferritin (1mg/mL, 2mL) at pH 2 (pH was decreased with 0.1 M HCl) for 30 min and then the protein was reassembled by increasing the pH to 7.4 with 0.1 M NaOH, thereby simultaneously entrapping the magnetic nanoparticles and DOX inside the protein cavity. At pH 2 the apoferritin is dissociated into its 24 polypeptide subunits, whereas an increase to pH 7.4 results in re-assembly of the subunits in an almost intact manner.[4,5]

The resulting clear reddish solution (DOX-Apomag 7.4) was purified to remove unfolded subunits by exhaustive dialysis against TRIS buffer (pH 7.4, NaCl 150 mM) until complete removal of unbound drug (Spectra/Por Float-A-Lyzer with a Molecular Weight Cut-Off (MWCO) of 12,000 Da, SpectrumLabs), then chromatographed on Sephadex G-25 column to isolate the protein-containing fractions.

For simulating the acidic extracellular pH of tumor tissues, the co-encapsulation experiments were carried out also at pH 5.2 (DOX-Apomag 5.2) following the same protocol described for co-encapsulation at pH 7.4.

1.3. Doxorubicin surface binding (sb) after previous maghemite encapsulation

First, maghemite nanoparticles were encapsulated inside the apoferritin protein following our previous method. Then the clear reddish solution was dialyzed to remove unfolded subunits. In a third step, the Apomag was incubated with a solution of DOX (30 μL, 5 mg/L) for 24 h. The final sample (DOX-Apomag sb) was purified by dialysis and chromatography as described in the co-encapsulation protocol.

1.4. Kinetics studies of drug release

Drug release experiments were performed by the dialysis method (MWCO 3.5-5 kDa).[6] 2 mL of DOX-Apomag samples were placed in separated dialysis tubes (Float-A-Lyzer MWCO: 3.5–5 kDa) and dialysis against 25mL of TRIS–HCl (pH7.4,NaCl 150mM) or sodium acetate buffer (pH 5.2, NaCl 150 mM) was performed at room temperature (RT) (Figure 1). We simulated in this way “sink” conditions, initially replacing the dialysate every hour in the first day and then replacing the dialysate buffer regularly from the second day onwards. At fixed time intervals, 1 mL of

solution was withdrawn from dialysis bag and an UV–VIS spectrum was recorded (Varian Cary-100 spectrophotometer) to quantify the released DOX. After each measurement the solution was reincorporated to the dialysis bag and fresh medium was replaced. DOX can be easily followed by UV–vis spectroscopy because of its intense band at 481 nm. This experiment was repeated 5 times and the average values calculated.

Fig. 1. Float-A-Lyzer dyalisis device.

For the kinetics experiments carried out at 50 °C (co-encapsulation, pH 7.4, DOX-Apomag 7.4 50 °C) the temperature was maintained during the drug release process using an incubator (Precision incubator Model INB 300).

1.5. Samples for transmission electronic microscopy

TEM samples were prepared by placing a drop onto a carbon-coated Cu grid. TEM images of samples were negatively stained with uranyl acetate to visualize the protein shell. Electron micrographs were taken with a Phillips CM-20 HR analytical electron microscope operating at 200 keV.

1.6. Dynamic light scattering

Values of average hydrodynamic diameter in dilute dispersions were obtained by dynamic light scattering measurements using a 4700C System from Malvern Instruments and a 3D-DLS from LS Instruments, respectively. In both cases, a helium–neon laser operating at 632.8 nm wavelength and about 20 mW was used. The experiments were performed at 25°C and scattering angle of 90° (q = 0.018 nm−1). The CONTIN analysis of the intensity autocorrelation function reveals the existence of two population sizes, the first one centered on ~30 nm and the second one at ~200 nm.

1.7. Zeta potential measurements

Zeta potential of samples was measured by a Zetasizer Nano-ZS (Malvern) at 25 °C.

1.8 Gel electrophoresis

One-dimensional (1D) PAGE was used to analyze the samples. After preparing the appropriate gel, 10 to 20 µl samples of 1 mg protein/ml solutions diluted with appropriate sample buffer (20% stacking gel buffer, 0.009% bromophenol blue, and 8% glycerol) were injected into sample wells and separated at 200 V (2h). The gel was collected and was stained for 30min in Coomassie blue dye solution (0.1% Coomassie blue R-250, 40% methanol, 10% acetic acid in water) in a closed container with continuous agitation. This was followed by several destaining steps with a destaining solution (40% methanol, 10% acetic acid) with continuous agitation.

1.9. Cell toxicity test

MCF7 human breast cancer cells and MCF10-A normal breast cells were provided by Scientific Implementation Center, University of Granada, Spain. Breast cancer cell lines were grown adherently and maintained in Eagle's minimal essential medium containing 10% fetal bovine serum, and 1% antibiotic solution at 37 °C in 5% CO_2. MCF10-A line cells were grown adherently and maintained in Mammary Epithelial Cell Growth Medium (without fetal bovine serum), 1% antibiotic solution, and 100 ng·mL^{-1} of choleric toxin, which has an enhanced mitogenic effect on epithelial cells. All experiments were performed in 96-well plates. Cells were seeded onto the plates at a density of 1 × 104 cells per well and incubated for 48 h prior to the experiments. Samples containing different concentrations of DOX were added (75 µL/well) and each concentration was tested in triplicate. Subsequently, MTS (20 µL/well of CellTiter 96® AQ_{ueous} Promega) was introduced and incubated with the cells for an additional 72 h. The optical density at 490 nm was determined on a microtiter plate reader (NanoQuant, Infinite M200 Pro). Each experiment was repeated three times.

2. Materials and methods from Chapter 3

2.1. Preparation of the apoferritin (APO) and β-lactoglobulin (Blg) stock solution proteins

Horse Spleen apoferritin and Biopure bovine β-lactoglobulin proteins were purchased from Sigma-Aldrich. Apoferritin and β-lactoglobulin protein solutions (2mL, 0.4 wt %) were purified by centrifugation (13552rcf, 15min) and the supernatant was filtered through a 0.22 µm Millipore filter.

2.2. Influence of temperature, pH and incubation time on fiber formation

Purified protein solutions (0.2 wt %) were adjusted to the appropriate pH (2 or 5, diluted HCl dissolved in Milli-Q water) before heat treatment (50°C or 90°C, glass tubes hermetically sealed) over incubation time periods of 5 min, 10 min, 20 min, 30 min, 40 min, 50 min, 1 h, 3 h, 9h, 12 h, 24 h, 48 h or 120 h. After heat treatment, glass tubes were cooled in an ice bath to quench the aggregation process. Samples were collected for TEM and AFM analysis.

2.3. Influence of protein concentration and stirring on fiber formation

Purified protein solutions (0.05, 0.1, 0.2, 0.4 wt %) were adjusted to pH 2 (diluted HCl dissolved in Milli-Q water) before heat treatment (90°C, glass tubes hermetically sealed) over incubation time period of 9h. For the influence of stirring, one sample was heated at 220rpm and another one at 90rpm. After heat treatment, glass tubes were cooled in an ice bath to quench the aggregation process. Samples were collected for TEM and AFM analysis.

2.4. APO aggregation kinetics

Protein solutions were adjusted to the appropriate pH 2 (diluted HCl dissolved in Milli-Q water) before heat treatment (90°C, glass tubes hermetically sealed). Ten aliquots of the samples were collected at times of 0, 5 min, 15 min, 30 min, 45 min, 1 h, 3 h, 5 h, 9 h and 24 h from the heating onset and quenched immediately in a water–ice bath to arrest at that specific time the conversion of monomers into fibrils. These aliquots were then labelled for the characteristic heating time, stored at 4°C and used without further manipulation for structural analysis.

2.5. Samples for transmission electronic microscopy

Samples were prepared by placing a drop onto a carbon-coated Cu grid. Electron micrographs were taken with a LIBRA 120 PLUS microscope operating at 120 keV.

2.6. Samples for Scanning Electron Microscopy

Samples were prepared following the same procedure as for Transmission Electron Microscopy. A solution of osmium tetroxide was used as fixative as well as enhancer of contrast of the samples. Grids were observed with a LEO 1430 VP Scanning Electron Microscope.

2.7. Samples for atomic force microscopy

Tapping mode AFM was carried out on a Nanoscope V Multimode Scanning Force Microscope (Veeco). The different time-quenched collected aliquots were deposited onto freshly cleaved mica, incubated for 2 min, rinsed with Milli-Q water and dried by nitrogen. For all experiments, MPP-11100-10 tips for tapping mode in soft tapping conditions were used (Veeco, USA) at a vibrating frequency of 300 KHz. Images were simply flattened using the Nanoscope 8.1 software, and no further image processing was carried out. The images acquired were used for the statistical analysis.

2.8. Dynamic light scattering

The intermediates of apoferritin fibrils formed at different times were studied also by light scattering using a LS Instruments machine equipped with He–Ne Laser emitting a polarized light beam of wavelength of 632.8 nm. The dynamic light scattering measurements were performed at a fixed angle of 90° by averaging 3 runs of 600 s each. In dynamic light scattering, the time correlation function (TCF) of the scattered intensity is analyzed by the CONTIN method.

2.9. Gel electrophoresis

For each sample, 12 µL of aliquots at 2 mg/mL was mixed with 3 µL of dithiothreitol (DTT) and 15 µL of XT sample buffer 4X (Bio Rad Laboratories). The solutions were then heated 10 min at 90 °C. The 30 µL solutions and the molecular weight (Mw) markers (PageRuler™ Unstained Protein Ladder) were then loaded on Criterion 10-20% stain-free precast gel (Bio Rad Laboratories) and separated at 100 V (5min) and 300 V (20min). The gel was collected and the image was recorded with Biorad Stain-free technology using a ChemiDoc™ Touch Imaging System. To compare the L-rich APO and the dye-labelled L-rich APO aggregation process a concentration of 0.05% wt of protein was used for all aliquots.

2.10. ThT analysis

Formation of amyloid aggregates was detected as enhancement of the ThT fluorescence intensity. Fluorescence of the samples was recorded after the addition of 25 µL of 0.1 wt % APO aliquots in 25 µL of 56 µM ThT solution in pH 2 Milli-Q water. The measurements were performed on a Cary Eclipse fluorescence spectrophotometer in quartz cuvettes. For each sample, the emission spectra were recorded at 482nm after excitation at 412nm. The slits were adjusted to 20 and 20 nm for the excitation and emission respectively.

2.11. CD measurements

Previously, samples were centrifuged 3 times using Amicon Ultra-4 centrifugal filter devices with a molecular weight cut-off (MWCO) of 50000 Da and the supernatant was recovered. Circular dichroism (CD) spectra of APO were recorded using a Jasco J-815 spectropolarimeter equipped with a peltier-controlled cell holder. Spectra at 20 ˚C were collected using a precision quartz cell of 2 mm path-length from 190-260 nm with a bandwidth of 1 nm and a scan speed of 50nm/min. All spectra were recorded by diluting the incubated 0.2 wt % 10 times in pH 2 deionized

water. Spectra were background subtracted, averaged over 5 scans, and smoothed by Spectra Manager software.

2.12. Preparation of the dye-labelled L-rich APO fibril proteins

Atto succinimidyl ester derivatives (Atto488, Atto647N) were purchased from Atto-Tec GmbH. Solution of globular Horse Spleen apoferritin protein (2 mL) was prepared in aqueous solution pH 8.0 and incubated for 1h with the corresponding fluorophore succinimidyl ester derivatives specifically, Atto88 (tag1), Atto647(tag2). The resulting solutions were then exhaustively dialyzed for 2 days against several changes of distilled water. The samples were collected and mixed in a 1:1:1 (protein:tag1:tag2) stoichiometry. Subsequently, samples were adjusted to the appropriate pH 2 (diluted HCl dissolved in Milli-Q water) before heat treatment (90°C, glass tubes hermetically sealed) at different times (1h, 3h and 9 h) and quenched immediately in a water–ice bath. An aliquot of the sample heated for 9h was centrifuged 3 times using Amicon Ultra-4 centrifugal filter devices with a molecular weight cut-off (MWCO) of 50000 Da and the supernatant was recovered. All samples were characterized by fluorescence spectroscopy (Varian Cary Eclipse Fluorescence Spectrophotometer). The Förster distance, R_0, for this pair of fluorophores is 51 Å, which allowed us to detect the formation of aggregates at the single-molecule level based on the FRET efficiency, E, when the labelled monomers interacted with each other.

2.13. Fluorescence lifetime imaging microscopy with pulsed interleaved excitation (FLIM-PIE) measurements

FLIM-PIE experiments of dye-labelled APO fibrils were performed with a MicroTime 200 time-resolved fluorescence microscope (Pico-Quant GmbH, Germany). We employed a dual-color pulsed interleaved excitation (PIE) scheme, with two spatially overlapped pulsed lasers, at 470 (LDH-P-C-470, PicoQuant) and 635 nm (LDH-P-635, PicoQuant). These settings

permit the simultaneous collection in a single step of the donor FLIM image, the FRET image, and the directly excited acceptor fluorescence intensity image.

3. Materials and methods from Chapter 4

3.1. Preparation of the apoferritin (L-rich APO) fibrils and human APO L and H fibers

Horse spleen apoferritin protein was purchased from Sigma-Aldrich and human apoferritin L and H were purchased from MoLiRom. Purified protein solutions (0.1 wt%) were adjusted to pH 2 (diluted HCl dissolved in Milli-Q water) before heat treatment (90°C, glass tubes hermetically sealed) over incubation time period of 9h and under magnetic agitation (90rpm). After heat treatment, glass tubes were cooled in an ice bath to quench the aggregation process. Samples were collected for TEM and AFM analysis.

3.2. Samples for atomic force microscopy

Tapping mode AFM was carried out on a Nanoscope V Multimode Scanning Force Microscope (Veeco). The different time-quenched collected aliquots were deposited onto freshly cleaved mica, incubated for 2 min, rinsed with Milli-Q water and dried by nitrogen. For all experiments, MPP-11100-10 tips for tapping mode in soft tapping conditions were used (Veeco, USA) at a vibrating frequency of 300 KHz. Images were simply flattened using the Nanoscope 8.1 software, and no further image processing was carried out. The images acquired were used for the statistical analysis.

3.3. Samples for transmission electronic microscopy

Samples were prepared by placing a drop onto a carbon-coated Cu grid. Electron micrographs were taken with a LIBRA 120 PLUS microscope operating at 120 keV.

3.4. Electron tomography

Electron tomography analysis was performed in the high angle annular dark field scanning transmission electron microscopy (HAADF-STEM) mode on a FEI TITAN 80–300 LB electron microscope equipped with a probe Cs-corrector, operating at 200 kV and using a Fischione 2020 ultrahigh-tilt tomography holder. Before recording a series of images, the aberrations of the condenser lenses were corrected up to second-order using the Zemlin tableau. A convergence angle of 10 mrad was used in order to improve the depth of focus. The data collections were performed by tilting the specimen around a single axis perpendicular to the electron beam in a range of −70° to +70° every 5°. The registered tilt series were aligned using the FEI Inspect 3D software and reconstructed using software written in MATLAB. In particular, 50 iterations were used using SIRT algorithm. The reconstructed volumes were thereafter processed using the Avizo 7.0 Fire edition and Fiji software.

3.5. CD measurements

Previously, samples were centrifuged 3 times using Amicon Ultra-4 centrifugal filter devices with a molecular weight cut-off (MWCO) of 50000 Da and the supernatant was recovered. Circular dichroism (CD) spectra of L-rich APO, APO H and APO L were recorded using a Jasco J-815 spectropolarimeter equipped with a peltier-controlled cell holder. Spectra at 20˚C were collected using a precision quartz cell of 2 mm path-length from 190-260 nm with a bandwidth of 1 nm and a scan speed of 50nm/min. All spectra were recorded by diluting the incubated 0.1 wt % 10 times in pH 2 deionized water. Spectra were background subtracted, averaged over 5 scans, and smoothed by Spectra Manager software.

3.6. Attenuated Total Reflectance Fourier Transform Infrared Spectroscopy (ATR-FTIR)

FTIR spectra were obtained with a Bruker Tensor 27 FTIR Spectrometer. Samples powders were scanned over the range of 4000 to

400 cm^{-1} with a resolution of 4 cm^{-1} at room temperature and averaged over 16 scans. Spectra were background subtracted and smoothed by OPUS Data Collection Program.

3.7. Wide Angle X-ray Scattering (WAXS) measurements

X-ray scattering experiments were performed on a MicroMax-002+ microfocused beam with a sealed tube Cu Kα (λ = 1.542 Å) source, collimated by three pinhole (0.4, 0.3, and 0.8 mm) collimators, the applied voltage and filament current being 45 kV and 0.88 mA, respectively. The data were collected with the help of a Fuji Film BAS-MS 2025 imaging plate system: 15.2 × 15.2 cm, 50 μm resolution. Protein powders were used and held between mica plates.

3.8. Gel electrophoresis

For each sample, 12 μL of aliquots was mixed with 3 μL of dithiothreitol (DTT) and 15 μL of XT sample buffer 4X (Bio Rad Laboratories). The solutions were then heated 10 min at 90 °C in an oil bath. The 30 μL solutions and the molecular weight (Mw) markers (PageRuler™ Unstained Protein Ladder) were then loaded on 19% stacking gel buffer and separated at 100 V (10min) and 200 V (40min). The gel was collected and was stained for 30min in Coomassie blue dye solution (0.1% Coomassie blue R-250, 40% methanol, 10% acetic acid in water) in a closed container with continuous agitation. This was followed by several destaining steps with a destaining solution (40% methanol, 10% acetic acid) with continuous agitation. To compare the L-rich APO, APO L and APO H aggregation process a concentration of 0.1% wt of protein was used for all aliquots.

4. Materials and methods from Chapter 5

4.1. Preparation of the dye-labelled fibril proteins

In a first step amyloid-like protein fibers were formed after the heat treatment of protein solutions at 90 °C and pH 2. Later, the so-obtained fibril proteins were purified by ultrafiltration using VIVASPIN 6 with a molecular weight cut-off (MWCO) of 100000Da. Alexa Fluor succinimidyl ester derivatives (AF488, AF647) were purchased from Life Technologies. Solutions of protein fibers (2 mL) were prepared in aqueous solution pH 8.0 and incubated for 24 h with the corresponding fluorophore succinimidyl ester derivatives specifically, AF488 (tag1), AF647(tag2) or a mixture of both to obtain FRET samples in a 1:1:1 (protein:tag1:tag2) stoichiometry. The resulting solutions were then exhaustively dialyzed for 3 days against several changes of distilled water.

4.2. Synthesis of fluorescent 1D hybrid QD-fibers

Amyloid-like protein fibers were prepared as described previously. Carboxyl-coated quantum dots (QD525, QD655, QD800) were purchased from Life Technologies. 1-Ethyl-3-[3-dimethylaminopropyl] carbodiimide hydrochloride (EDC) was purchased from Sigma-Aldrich. 10 µL of a stock solution (10mg/mL) of EDC in milli-Q water was mixed with a carboxyl-QD stock solution (20 µL, 8 µM) for 30 min at room temperature. A 2 mL APO and Blg protein fiber solution at pH 8.0 was added to this mixture and incubated for 24 h. For the dual QD sample a 10 µL of a stock solution (10 mg/mL) of EDC in milli-Q water was mixed with a carboxyl-QD mixture stock solution (6 µL QD525, 8 µM and 3 µL QD655, 8 µM; with a ratio QD525:QD655= 2:1) for 30 min at room temperature. A 500 µL Blg protein fiber solution at pH 8.0 was added to this mixture and incubated for 24 h. Fluorescence emission and excitation spectra were recorded on a Cary Eclipse spectrofluorometer.

4.3. Fluorescence lifetime imaging microscopy with pulsed interleaved excitation (FLIM-PIE) measurements

FLIM-PIE experiments of APO and Blg were performed with a MicroTime 200 time-resolved fluorescence microscope (Pico-Quant GmbH, Germany). We employed a dual-color pulsed interleaved excitation (PIE) scheme, with two spatially overlapped pulsed lasers, at 470 (LDH-P-C-470, PicoQuant) and 635 nm (LDH-P-635, PicoQuant). These settings permit the simultaneous collection in a single step of the donor FLIM image, the FRET image, and the directly excited acceptor fluorescence intensity image. For more experimental details, see below.

4.4. Correlative AFM and Super-Resolution Fluorescence Imaging

Functionalized fibrils solutions were incubated on glass coverslips during 15 min, washed three times with ultrapure water, and dried with nitrogen. Glass coverslips were previously cleaned by sonication cycles of 15min in spectroscopic grade acetone, alkaline detergent (Hellmanex), and ultrapure water.

The correlative microscope is based on a commercially available platform that integrates AFM (Nanowizard II, JPK Instruments) on a standard inverted optical microscope (Nikon Eclipse Ti), which has been adapted for super-resolution imaging.[7] Samples were excited with 488 and 638 nm lasers (0.5–1 kW cm^{-2}, Luxx Omicron and Toptica iBeam Smart, respectively) and imaged onto an EMCCD camera (iXon Ultra 897, Andor Technology) through a 60× NA 1.49 oil immersion objective (Nikon). AFM and super-resolution imaging are performed sequentially. AFM images were collected in dynamic mode using HQ:NSC35/Cr-AuBS cantilevers (MikroMasch) of typical 8.9 N m^{-1} force constant and 205 KHz resonance frequency under dry conditions. During AFM scanning, the objective was slightly retracted to reduce coupled vibrations. It was noted that the experiments were not performed in an acoustic enclosure.

For super-resolution imaging of Blg-AlexaFluor 488 fibers, fluorophore blinking was induced with a "switching buffer" containing phosphate-buffered saline (pH 7.4, Sigma) with an oxygen scavenger [0.5 mg mL^{-1} glucose oxidase (Sigma), 40 μg mL^{-1} catalase (Sigma), and 10 % w/v glucose (Fischer Scientific)], which was gently added after AFM imaging. It is worth noting that the switching buffer did not contain a thiol compound (typically added to improve fluorophore blinking) since thiols induce breakage of Blg fibers (Figure 2) and are not required to induce blinking of AlexaFluor 488.[8] For Blg fibers functionalized with QDs, switching buffer was not required due to intrinsic blinking, and super-resolution imaging was performed under dry conditions. Between 1000 and 4000 frames were typically collected on an Andor iXon EMCCD camera with 100 ms integration time per frame.

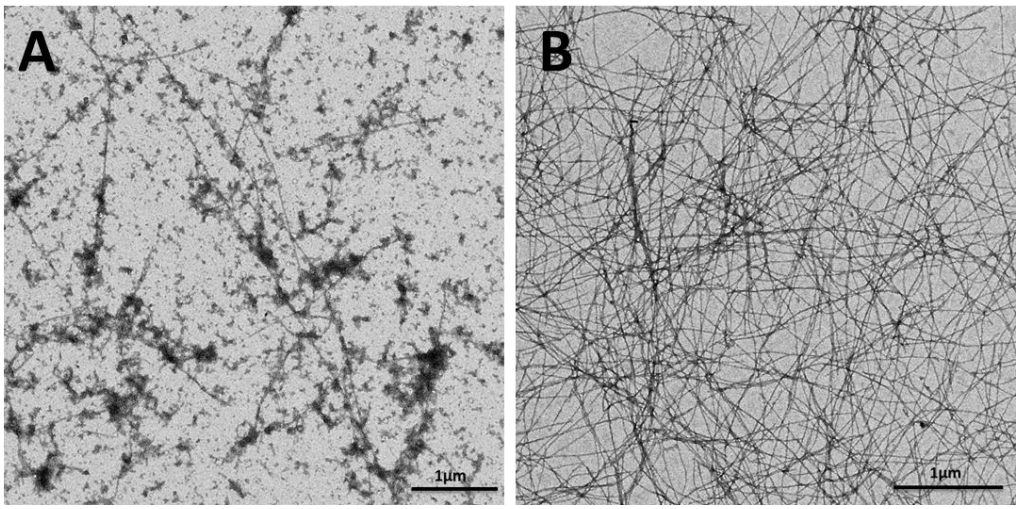

Fig. 2. a) Blg fibers broken due to 2-mercaptoethanol presence. b) Blg fibers.

Noise reduction in AFM images was performed with Gwyddion[9] by applying a fast Fourier transform filter after a linear background subtraction. The movies collected for single-molecule localization microscopy were analyzed with Localizer,[10] which allows identification and localization of single fluorophores, and image reconstruction of the localized coordinates. Coarse image alignment in the correlative

experiments was performed by selecting characteristic sample features. Improved nanoscale precision alignment was achieved in images of QD labeled fibers by using the QDs as fiduciary markers for determining a correction matrix with a transform plugin in Fiji,[11] which compensates the distortion arising from both imaging techniques.

4.5. Samples for transmission electronic microscopy

Samples were prepared by placing a drop onto a carbon-coated Cu grid. Electron micrographs were taken with a LIBRA 120 PLUS microscope operating at 120 keV. HR-STEM, HAADF-STEM and EDX maps were obtained with a FEI TITAN G2 microscope.

5. Materials and methods from Chapter 6

5.1. Metal nanoparticle synthesis

5.1.1. Gold spherical nanoparticles (AuNSs) synthesis

The chloroauric acid was purchased from Sigma Aldrich and used without any further purification. 5 mL of a 1.0 mM $HAuCl_4$ solution in water was stirred and heated to boiling on a hot plate. After the solution began to boil, 500 μL of a 38.8 mM $Na_3C_6H_5O_7$ solution in water was added. The mixture was boiled and stirred continuously for about 10 min until it was a deep red color. The solution was cooled to room temperature. The AuNSs were characterized by UV-vis spectroscopy (Varian Cary-100 spectrophotometer) and transmission electron microscopy (TEM) (Figure 3).

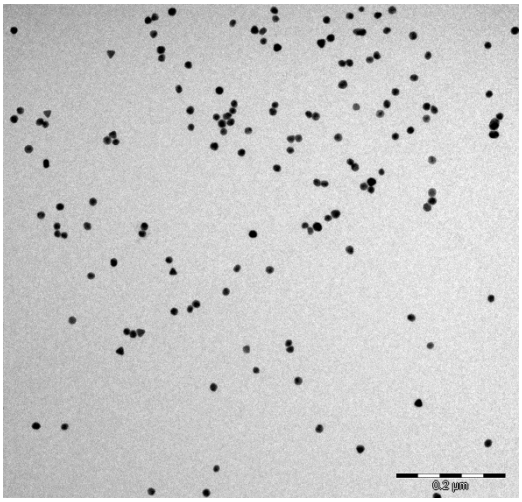

Fig. 3. Gold spherical nanoparticles TEM image.

5.1.2. Gold nanorods (AuNRs) synthesis

Seed synthesis. To prepare AuNRs, a seed-mediated growth method was carried out. Gold seed was prepared as described elsewhere. A solution of 10mM $NaBH_4$ was freshly prepared. To an $HAuCl_4$ solution (1mL, 1mM) in 0.2M CTAB was added 600µL of the $NaBH_4$ solution under rapid stirring. When seeds were formed, the solution color changed from yellow to slightly brown.

NRs synthesis. Silver nitrate (100µL, 8mM) solution was added to an $HAuCl_4$ solution (5mL,1mM) in 0.2M CTAB, followed by addition of ascorbic acid solution (70µL, 78.8mM), and the resulting mixture was stirred until it became clear. Next, 24µL of seed solution was added, and the growth solution was mixed thoroughly at 30°C for seven days.

NRs purification. The so-obtained nanorods were purified by centrifugation at 13000 rpm and redispersed in water.

NRs characterization. The NRs were characterized by UV-vis spectroscopy and transmission electron microscopy (TEM) (Figure 4).

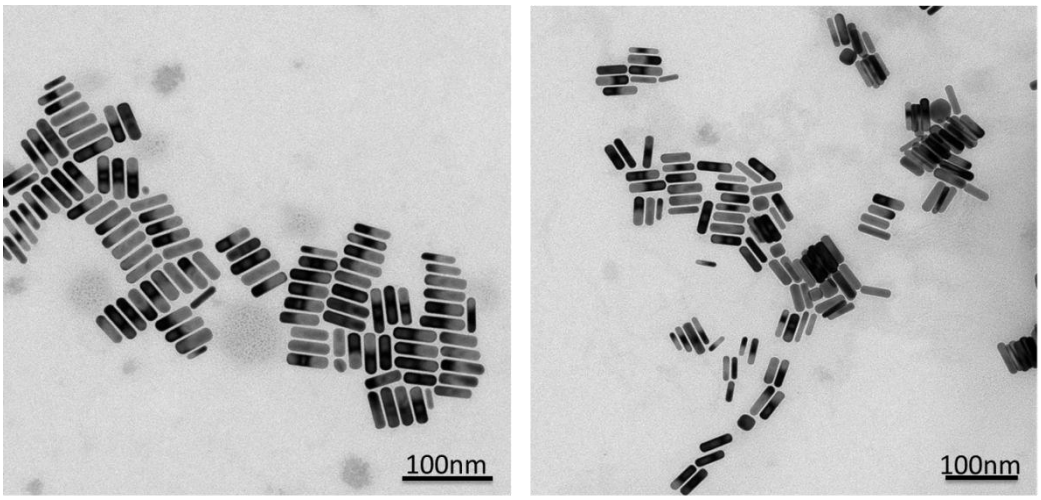

Fig. 4. Gold nanorods TEM images.

5.1.3. Maghemite (mag) synthesis

Maghemite nanoparticles were synthesized by the method previously explained (see *1.1. Preparation of the maghemite colloid).* We obtained a sol (stable colloid solution) of 8 ± 2nm maghemite nanoparticles at pH 2 with an iron concentration of 0.1 M.

5.2. Assemblies of metal nanoparticles and APO and Blg fibrils

Preparation of Apo and Blg fibrils was described previously. Briefly, amyloid-like protein fibers were formed after heat treatment of protein purified solutions at 90 °C and pH 2 for 9 h. A 500μL AuNSs or AuNRs solution was added to a 1ml Apo or Blg fibril solution at pH 8 and incubated for 24 h. An acidic colloid of 8 nm maghemite nanoparticles (200 μL, 1 mM) was added to a 1ml Apo or Blg fibril solution at pH 8 and incubated for 24 h. Maghemite nanoparticles were previously sonicated to prevent particle aggregation.

5.3. Magnetic Measurements.

Magnetic measurements were performed on lyophilized samples using a magnetometer (Quantum Design MPMS-XL-5) equipped with a SQUID sensor.

5.4. Fabrication of metal nanoparticle nanowires

The gold, silver, and palladium nanoparticles were prepared by initial mixing of a 0.1 wt % concentration solution of the APO fibrils (500µl) with 0.004 M $HAuCl_4$, $AgNO_3$, and $PdCl_2$ salts, respectively. After 15 min of incubation at room temperature (23 °C), 6 µL of reducing agent ($NaBH_4$ 0.01M) was added for 1 h.

5*.5. Samples for transmission electronic microscopy*

Samples were prepared by placing a drop onto a carbon-coated Cu grid. Electron micrographs were taken with a LIBRA 120 PLUS microscope operating at 120 keV. HR-STEM, HAADF-STEM and EDX maps were obtained with a FEI TITAN G2 microscope.

6. Techniques

6.1. Fluorescence Lifetime Imaging Microscopy with Pulsed Interleaved Excitation (FLIM-PIE)

For FLIM-PIE imaging collection, the APO fiber samples at concentration of 49 µM were diluted with Milli-Q water 300-fold to a final concentration of 163 nM; the APO globular samples, at 40 µM of protein concentration, were diluted 200-fold to a final concentration of 200 nM; the Blg-fibers at concentration of 67 µM were diluted 900-fold to a final concentration of 74 nM; and the Blg-globular samples at the concentration of 52 µM were diluted 2700-fold to a final concentration of 19 nM. After dilution, 40 µL of sample were deposited on a microscope cover slide

(Thermo-Scientific, Menzel-Gläser, Brawnschweig, Germany) previously washed 5x with milli-Q water.

FLIM-PIE experiments were performed with a MicroTime 200 time-resolved fluorescence microscope (PicoQuant GmbH, Germany). We employed a dual-color pulsed interleaved excitation (PIE) scheme, with two spatially overlapped pulsed lasers, at 470 (LDH-P-C-470, PicoQuant) and 635 nm (LDH-P-635, PicoQuant). The total excitation pulse frequency was 20 MHz, with the 635-nm laser delayed 30 ns (Ortec delay box) with respect the 470-nm laser pulse. By applying specific time windows (Figure 5), these settings permit one-step reconstruction of the donor dye FLIM image, FRET fluorescence image, and directly excited acceptor FLIM image which make FLIM-PIE an extremely suited tool for quantitatively measuring FRET between the two different dyes. The excitation power of each laser at the microscope entrance was adapted at the emission properties of the proteins analyzed. For the FLIM measurements of the 5 APO-fibers, the excitation power was 448 nW for the 470-nm and 24 nW for the 635-nm laser. For the APO-globular, the power was 980 nW for the 470-nm and 178 nW for the 635-nm laser. For the Blg-fiber the excitation power was 372 nW and 23 nW for the 470-nm and the 635-nm laser, respectively. Finally, for the Blg-globular experiments, the laser power was 1.88 μW and 51.5 nW for the 470-nm and the 635- nm laser, respectively.

The excitation beams were focused just above the glass surface, and the fluorescence emission was collected through a high numerical aperture oil-immersion objective (Plan Achromat 100x/1.40, Olympus), and then imaged onto a 75-μm pinhole (Melles Griot). The transmitted signal was then separated by a 600 dcxr dichroic beam splitter (AHF/Chroma), filtered into the donor (520/35 Omega Filters) and acceptor (685/70 Omega Filters) channels, and directed to two avalanche photodiodes (APD) (SPCMAQR-14, Perkin-Elmer Optoelectronics). FLIM images were collected

with a time resolution of 116 ps per channel, an image size of 15 μM x 15 μM, a pixel resolution of 512 × 512 and a collection time of 0.60 ms per pixel.

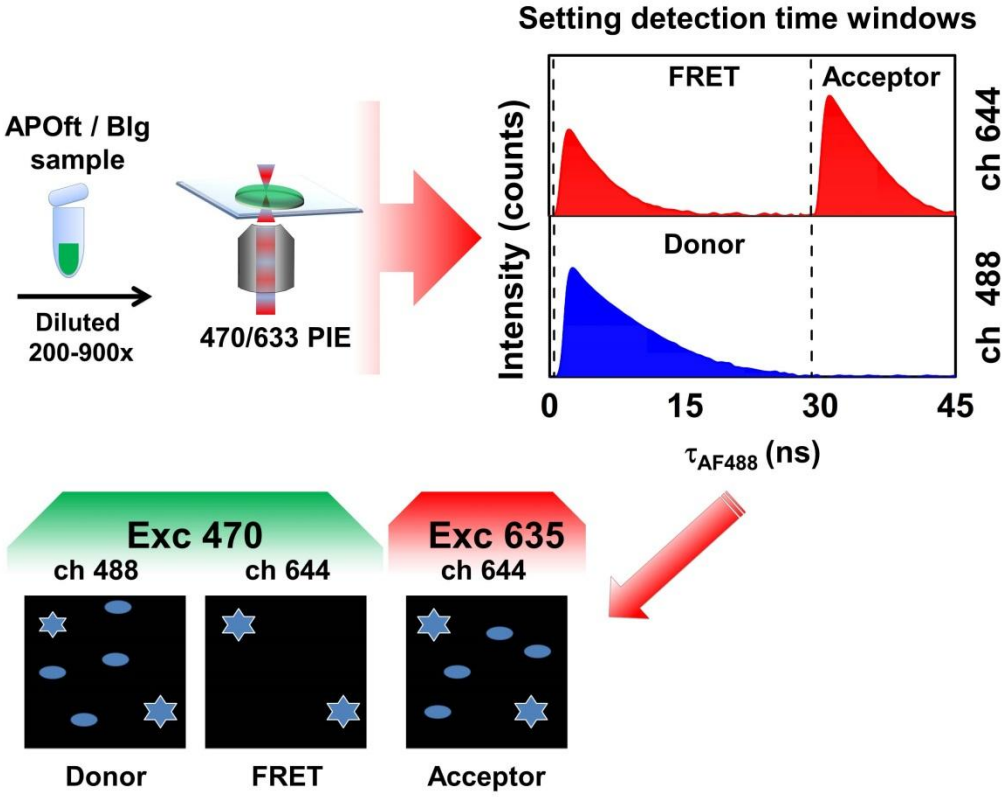

Fig. 5. FLIM-PIE scheme experiment.

6.2. Transmission Electron Microscopy (TEM)

Transmission electron microscopy (TEM) is a microscopy technique in which a beam of electrons is transmitted through an ultra-thin specimen, interacting with the specimen as it passes through it (Figure 6). Then an image is formed, magnified and focused onto an imaging device, such as a fluorescent screen on a layer of photographic film, or detected by a sensor such as a charge-coupled device (CCD) camera. The difference with scanning electron microscopy (SEM) is the energy of the incident electrons

(20-30kV for SEM in comparison to 200-300kV for TEM). These electrons can now penetrate in the sample and give information of the morphology, size or crystalline structure. Electrons are emitted from a field emission gun and focused by means of magnetic lenses, whose magnetic fields deviate the trajectories. A final lens sets the sample either on the image or on the focal plane. In the first case a magnified image of the sample is obtained at the CCD camera. On the contrary, when the sample is focused on the focal plane an image of the reciprocal space is taken, then electron diffraction can be performed.

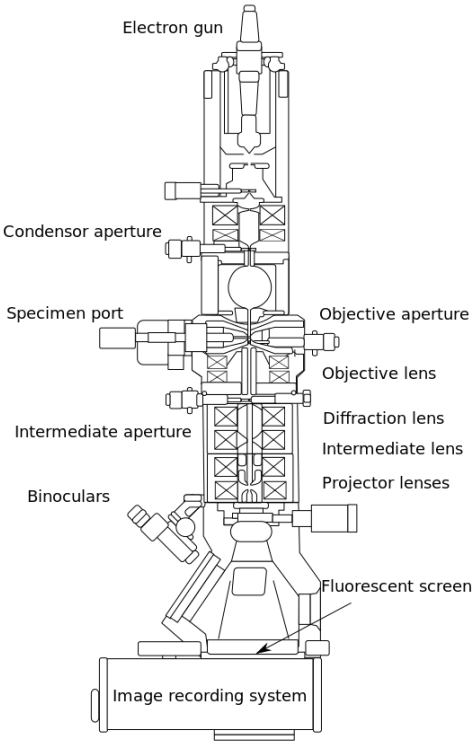

Fig. 6. Layout of optical components in a basic TEM.

6.2.1. High-resolution transmission electron microscopy (HRTEM)

High-resolution transmission electron microscopy (HRTEM) is an imaging mode of the transmission electron microscope (TEM) that allows for direct imaging of the atomic structure of the sample. HRTEM is a

powerful tool to study properties of materials on the atomic scale, such as semiconductors, metals, nanoparticles and sp^2-bonded carbon (graphene, carbon nanotubes). At present, the highest point resolution realized in phase contrast TEM is around 0.5Å (0.050 nm). At these small scales, individual atoms of a crystal and its defects can be resolved.

6.2.2. Scanning transmission electron microscope (STEM)-high-angle annular dark-field imaging (HAADF)

A scanning transmission electron microscope (STEM) is a type of transmission electron microscope (TEM). Images are formed by electrons passing through a sufficiently thin specimen. In STEM the electron beam is focused to a fine spot which is then scanned over the sample in a raster. The rastering of the beam across the sample makes STEM suitable for analytical techniques such as Z-contrast annular dark-field imaging, and spectroscopic mapping by energy dispersive X-ray (EDX) spectroscopy, or electron energy loss spectroscopy (EELS). These signals can be obtained simultaneously, allowing direct correlation of images and spectroscopic data.

In annular dark-field mode, images are formed by fore-scattered electrons incident on an annular detector, which lies outside of the path of the directly transmitted beam. By using a high-angle ADF detector, it is possible to form atomic resolution images where the contrast of an atomic column is directly related to the atomic number (Z-contrast image). Directly interpretable Z-contrast imaging makes STEM imaging with a high-angle detector an appealing technique in contrast to conventional high resolution electron microscopy, in which phase-contrast effects mean that atomic resolution images must be compared to simulations to aid interpretation.

6.2.3. Energy-dispersive X-ray spectroscopy (EDX)

Energy-dispersive X-ray spectroscopy (EDX) is an analytical technique used for the elemental analysis or chemical characterization of a sample. It relies on an interaction of some source of X-ray excitation and a sample. Its characterization capabilities are due in large part to the fundamental principle that each element has a unique atomic structure allowing a unique set of peaks on its electromagnetic emission spectrum.

To stimulate the emission of characteristic X-rays from a specimen, a high-energy beam of charged particles such as electrons, or a beam of X-rays, is focused into the sample being studied. At rest, an atom within the sample contains ground state (or unexcited) electrons in discrete energy levels or electron shells bound to the nucleus. The incident beam may excite an electron in an inner shell, ejecting it from the shell while creating an electron hole where the electron was. An electron from an outer, higher-energy shell then fills the hole, and the difference in energy between the higher-energy shell and the lower energy shell may be released in the form of an X-ray. The number and energy of the X-rays emitted from a specimen can be measured by an energy-dispersive spectrometer. As the energies of the X-rays are characteristic of the difference in energy between the two shells and of the atomic structure of the emitting element, EDS allows the elemental composition of the specimen to be measured.

6.3. Atomic force microscopy (AFM)

Atomic-force microscopy (AFM) is a type of scanning probe microscopy (SPM), with demonstrated resolution on the order of fractions of a nanometer, more than 1000 times better than the optical diffraction limit. The information is gathered by "feeling" or "touching" the surface with a mechanical probe. Piezoelectric elements that facilitate tiny but accurate and precise movements on (electronic) command enable very

precise scanning. For imaging, the reaction of the probe to the forces that the sample imposes on it can be used to form an image of the three-dimensional shape (topography) of a sample surface at a high resolution. This is achieved by raster scanning the position of the sample with respect to the tip and recording the height of the probe that corresponds to a constant probe-sample interaction. The surface topography is commonly displayed as a pseudocolor plot.

Figure 7 shows an AFM typically consisting of the following features: the small spring-like cantilever is carried by the support. Optionally, a piezoelectric element oscillates the cantilever. The sharp tip is fixed to the free end of the cantilever. The detector records the deflection and motion of the cantilever. The sample is mounted on the sample stage. An xyz drive permits to displace the sample and the sample stage in x, y, and z directions with respect to the tip apex.

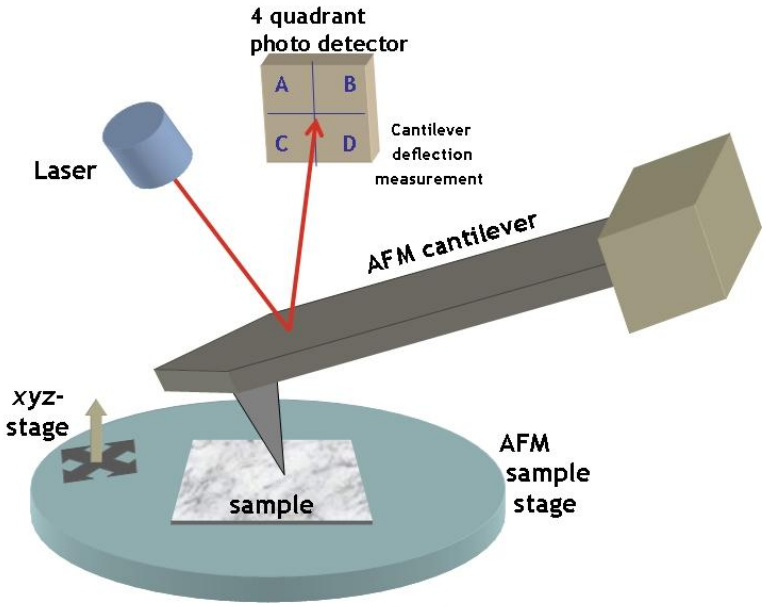

Fig. 7. Atomic force microscope configuration.

AFM operation is usually described as one of three modes, according to the nature of the tip motion: contact mode, also called static mode (as

opposed to the other two modes, which are called dynamic modes); tapping mode, also called intermittent contact, AC mode, or vibrating mode; and non-contact mode. These modes are represented in Figure 8.

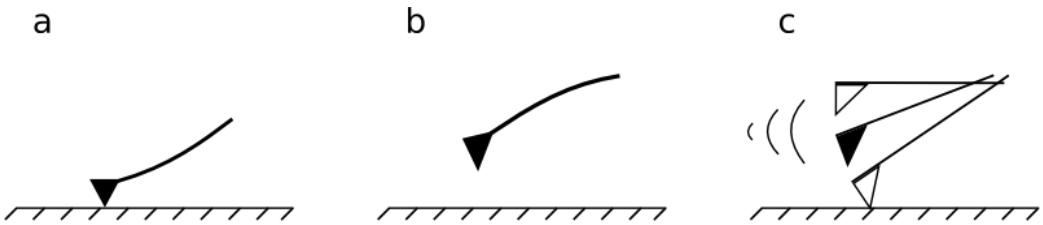

Fig. 8. AFM modes: contact mode (a), non-contact mode (b) and tapping/intermittent mode.

6.4. Electron tomography (ET)

Electron tomography is a tomography technique that provides a way to determine 3D cellular architecture at resolutions that could reach 50Å or better, potentially high enough to identify individual macromolecules such as proteins within 3D density maps. Electron tomography is an extension of traditional transmission electron microscopy and uses a transmission electron microscope to collect the data. Electron microscopes typically record projection images, meaning that those images contain information from all regions of the specimen through which the beam is transmitted. Thus, each image contains information from all heights of the specimen collapsed onto a single plane. However, by recording a series of images in which the orientation of the specimen is varied relative to the incident beam and spans a full angular range, a series containing all of the information required to describe the 3D structure of the imaged object results (Figure 9). [12]

Because all of these images are projection images, it is not possible to reconstruct the structure of the object by simply combining the tilted views within such a series. One approach to overcoming this difficulty

involves use of a “back-projection” algorithm. In using this algorithm, the density for each projection image is first smeared back evenly along the direction of the electron beam into an imaginary box whose height is approximately equal to the thickness of the specimen. When this procedure is repeated over a full series of tilted images and these serial back projection profiles are combined, the spatial distribution of density in the superimposed reconstruction is proportional to the original density of the object.

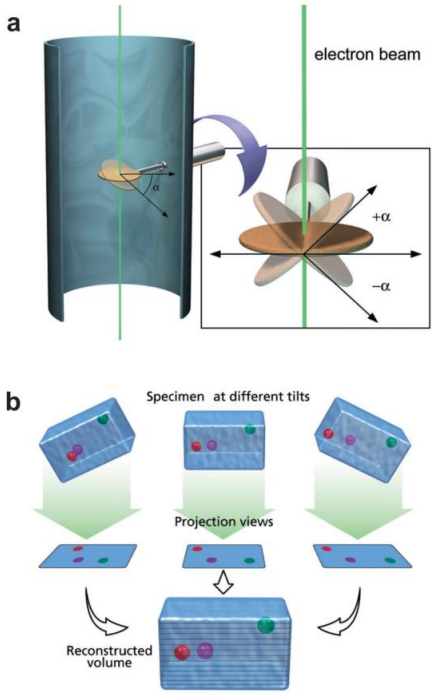

Fig. 9. Illustration of the principle of 3D tomographic reconstruction using back-projection algorithms. (a) The specimen is tilted to varying angles (+α,-α) along an axis perpendicular to the electron beam and a series of corresponding projection images are recorded. (b) Schematic demonstration of a set of 2D projection views generated by tilting a three-dimensional object to different angles. To reconstruct the 3D volume, the projection images are smeared out to the reconstruction volume along their viewing directions to form back-projection profiles. The final volume is then calculated by summation of all the back-projection profiles and represented as a series of stacked thin slices.

There is considerable excitement about the prospect of applying ET methods, especially for the analysis of large cellular structures and dynamic macromolecular assemblies that are not easily studied by methods such as X-ray crystallography and NMR spectroscopy.

6.5. Dynamic light scattering (DLS)

Dynamic light scattering (DLS) is a technique in physics that can be used to determine the size distribution profile of small particles in suspension or polymers in solution. In the scope of DLS, temporal fluctuations are usually analyzed by means of the intensity or photon auto-correlation function (also known as photon correlation spectroscopy or quasi-elastic light scattering). In the time domain analysis, the autocorrelation function (ACF) usually decays starting from zero delay time, and faster dynamics due to smaller particles lead to faster decorrelation of scattered intensity trace. It has been shown that the intensity ACF is the Fourier transformation of the power spectrum, and therefore the DLS measurements can be equally well performed in the spectral domain. DLS can also be used to probe the behavior of complex fluids such as concentrated polymer solutions.

A monochromatic light source, usually a laser, is shot through a polarizer and into a sample. The scattered light then goes through a second polarizer where it is collected by a photomultiplier and the resulting image is projected onto a screen. This is known as a speckle pattern. All of the molecules in the solution are being hit with the light and all of the molecules diffract the light in all directions. The diffracted light from all of the molecules can either interfere constructively (light regions) or destructively (dark regions). This process is repeated at short time intervals and the resulting set of speckle patterns are analyzed by an autocorrelator that compares the intensity of light at each spot over time.

The polarizers can be set up in two geometrical configurations. One is a vertical/vertical (VV) geometry, where the second polarizer allows light through that is in the same direction as the primary polarizer. In vertical/horizontal (VH) geometry the second polarizer allows light not in same direction as the incident light.

6.6. Polyacrylamide gel electrophoresis (PAGE)

Gel electrophoresis is a method for separation and analysis of macromolecules and their fragments, based on their size and charge (Figure 10). Molecules are separated by applying an electric field to move the negatively charged molecules through a matrix of agarose or other substances. Shorter molecules move faster and migrate farther than longer ones because shorter molecules migrate more easily through the pores of the gel. This phenomenon is called sieving. Gel electrophoresis uses a gel as an anticonvective medium and/or sieving medium during electrophoresis.

Polyacrylamide gel electrophoresis (PAGE) is used for separating proteins ranging in size from 5 to 2,000 kDa due to the uniform pore size provided by the polyacrylamide gel. Pore size is controlled by modulating the concentrations of acrylamide and bis-acrylamide powder used in creating a gel.

Typically resolving gels are made in 6%, 8%, 10%, 12% or 15%. Stacking gel (5%) is poured on top of the resolving gel and a gel comb (which forms the wells and defines the lanes where proteins, sample buffer and ladders will be placed) is inserted. The percentage chosen depends on the size of the protein that one wishes to identify or probe in the sample. The smaller the known weight, the higher the percentage that should be used. Changes on the buffer system of the gel can help to further resolve proteins of very small sizes.

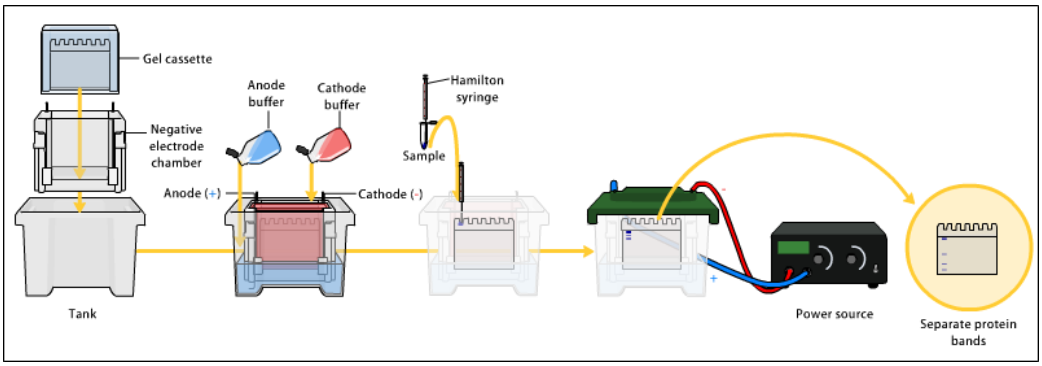

Fig. 10. Gel electrophoresis method.

6.7. Circular dichroism (CD)

Circular dichroism (CD) is an excellent tool for rapid determination of the secondary structure and folding properties of proteins that have been obtained using recombinant techniques or purified from tissues. Circular dichroism is defined as the unequal absorption of left-handed and right-handed circularly polarized light (Figure 11). A beam of light has time dependent electric and magnetic fields associated with it. If the light is polarized by passing through suitable prisms or filters its electric field, E, will oscillate sinusoidally in a single plane. When viewed from the front, the sinusoidal wave can be visualized as the resultant of two vectors of equal length, which trace out circles, one which rotates clockwise (E_R) and the other which rotates counterclockwise (E_L). The two circularly polarized waves have physical existence. The waves are 90 degrees out of phase with each other and can be separated using a variety of prisms or electronic devices which utilize Pockel's effect. When asymmetric molecules interact with light, they may absorb right and left handed circularly polarized light to different extents (hence the term circular dichroism) and also have different indices of refraction for the two waves. The result is that the plane of the light wave is rotated and that the addition of the E_R and E_L vectors results in a vector that traces out an ellipse and the light is said to be

elliptically polarized. CD is reported either in units of ΔE, the difference in absorbance of E_R and E_L by an asymmetric molecule, or in degrees ellipticity, which is defined as the angle whose tangent is the ratio of the minor to the major axis of the ellipse. [θ], the molar ellipticity in deg. · cm^2/dmol = 3298ΔE.[13]

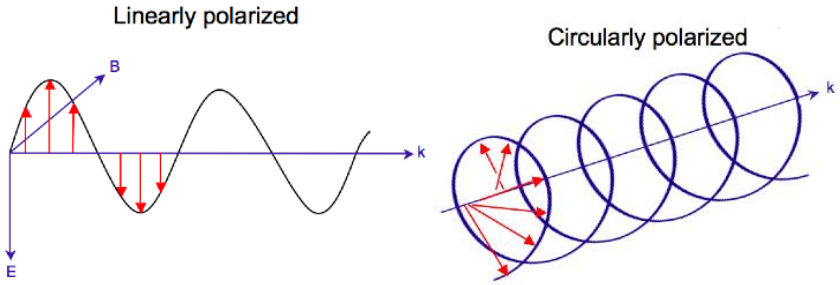

Fig. 11. Physical principles of circular dichroism.

CD is an excellent method of determining the secondary structure of proteins. When the chromophores of the amides of the polypeptide backbone of proteins are aligned in arrays, their optical transitions are shifted or split into multiple transitions due to "exciton" interactions. The result is that different structural elements have characteristic CD spectra. For example, α-helical proteins have negative bands at 222 nm and 208 nm and a positive band at 193 nm. Proteins with well-defined antiparallel β-pleated sheets (β-helices) have negative bands at 218 nm and positive bands at 195 nm, while disordered proteins have very low ellipticity above 210 nm and negative bands near 195 nm. Because the spectra of proteins are so dependent on their conformation, CD can be used to estimate the structure of unknown proteins and monitor conformational changes due to temperature, mutations, heat, denaturants or binding interactions. While CD does not give the secondary structure of specific residues, as do X-ray crystallographic and NMR structural determinations, the method has the advantage that data can be collected and analyzed in a few hours on

solutions of samples containing 20 μg or less of protein in aqueous buffers under physiological conditions.

CD spectra are collected in high transparency quartz cuvettes (cells). Both rectangular and cylindrical cells are available, with path lengths ranging from 0.01 to 1 cm.

6.8. Wide-angle X-ray scattering (WAXS)

Wide-angle X-ray scattering (WAXS) is an X-ray-diffraction[14] technique for determining structure by directing a beam of X-rays at the sample and detecting the positions and intensities of the diffracted X-rays as a pattern of spots on a photographic plate (Figure 12). The incident X-ray beam strikes the sample at a wide angle (>10 deg.).

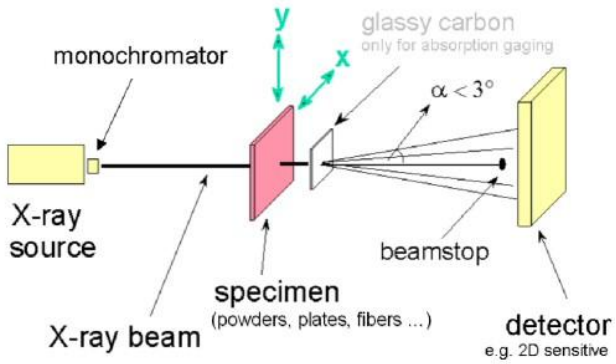

Fig. 12. Wide-angle X-ray scattering (WAXS) method.

Wide-angle X-ray scattering is the same technique as small-angle X-ray scattering (SAXS) only the distance from sample to the detector is shorter and thus diffraction maxima at larger angles are observed.

The technique is a time-honored but a somewhat out-of-favor technique for the determination of degree of crystallinity of polymer samples. The diffraction pattern generated allows determining the chemical composition or phase composition of the film, the texture of the film (preferred alignment of crystallites), the crystallite size and presence of film stress. According to this method the sample is scanned in a wide-angle

X-ray goniometer, and the scattering intensity is plotted as a function of the 2θ angle.

X-ray diffraction is a non-destructive method of characterization of solid materials. When X-rays are directed in solids they will scatter in predictable patterns based upon the internal structure of the solid. A crystalline solid consists of regularly spaced atoms (electrons) that can be described by imaginary planes. The distance between these planes is called the d-spacing. The intensity of the d-space pattern is directly proportional to the number of electrons (atoms) that are found in the imaginary planes. Every crystalline solid will have a unique pattern of d-spacings (known as the powder pattern), which is a "finger print" for that solid. In fact solids with the same chemical composition but different phases can be identified by their pattern of d-spacings.

WAXS data are sensitive to small structural changes in proteins. It holds great potential for the testing of structural models of proteins, identification of proteins that may exhibit novel folds, characterization of unfolded or natively disordered proteins and detection of structural changes associated with protein function.[15]

6.9. Fourier-transform infrared spectroscopy (FTIR)

Fourier-transform infrared spectroscopy (FTIR) is a technique used to obtain an infrared spectrum of absorption or emission of a solid, liquid or gas. An FTIR spectrometer simultaneously collects high-spectral-resolution data over a wide spectral range. This confers a significant advantage over a dispersive spectrometer, which measures intensity over a narrow range of wavelengths at a time.[16]

Fourier transform infrared spectroscopy is preferred over dispersive or filter methods of infrared spectral analysis for several reasons: it is a non-destructive technique, it provides a precise measurement method which requires no external calibration, it can increase speed, collecting a

scan every second, it can increase sensitivity – one second scans can be co-added together to ratio out random noise, it has greater optical throughput, it is mechanically simple with only one moving part.

Because the analyst requires a frequency spectrum (a plot of the intensity at each individual frequency) in order to make an identification, the measured interferogram signal cannot be interpreted directly. A means of "decoding" the individual frequencies is required. This can be accomplished via a well-known mathematical technique called the Fourier transformation. This transformation is performed by the computer which then presents the user with the desired spectral information for analysis (Figure 13).

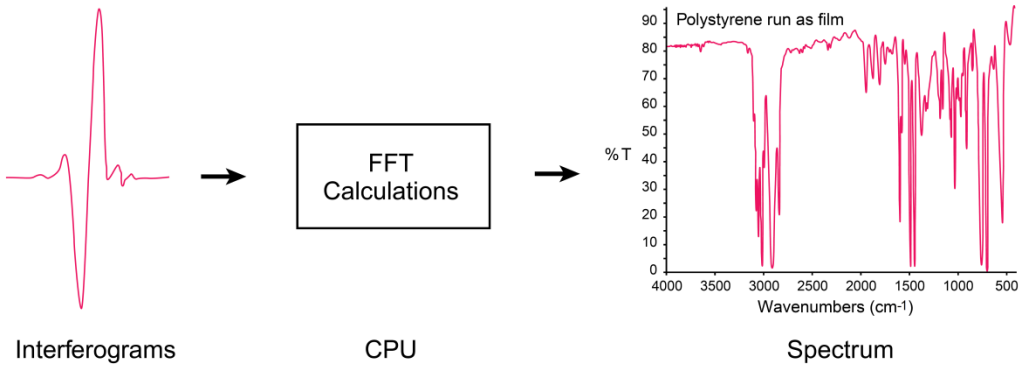

Fig. 13. Fourier-transform infrared spectroscopy (FTIR) method.

The IR spectral data of polymers are usually interpreted in terms of the vibrations of a structural repeat. The repeat units in proteins give rise to nine characteristic IR absorption bands (amides A, B and I–VII). The amide I bands provide information on C=O bonding, while the amide II bands provide information on N-H bonding. This gives valuable insights regarding the secondary structure, as both of these forms of bonding are influenced by the protein's secondary structural content. Amide I bands (1,700–1,600 cm^{-1}), especially, are the most prominent and sensitive

vibrational bands of the protein backbone, and they relate to protein secondary structural components.

6.10. Magnetism

Magnetism measurements are provided by a superconducting quantum interference device (SQUID) which is a very sensitive magnetometer used to measure extremely subtle magnetic fields. This magnetometer is used to provide magnetic susceptibility (χM) measurements as a function of temperature and magnetization (M) measurements as a function of the applied field (magnetic hysteresis) of samples over a wide range of temperatures (from 1.9 K to 400 K) and magnetic fields (from 5 T to -5 T). In addition, the high sensitivity of the SQUID magnetometer allows determination of magnetic susceptibility with only a few milligrams of sample.

6.10.1. Zero-field cooled (ZFC) and field-cooled (FC) magnetization curves

These curves provide the experimental value of the blocking temperature (T_B) which corresponds to the "merging point" of the zero-field cooled (ZFC) and field-cooled (FC) magnetization curves. In ZFC measurements, a sample is first cooled to low temperature (e.g., 2–10 K) in the absence of an external field (zero-field). At this point, a small external field is applied, and the temperature is gradually increased while measuring the sample magnetization as a function of temperature. In FC measurements, the process is repeated, but the sample is cooled in the presence of an external field (~50 Oe) and the same external field is applied as the temperature is increased. As shown in Figure 14, the maximum on the ZFC curve is the blocking temperature, T_B.[17]

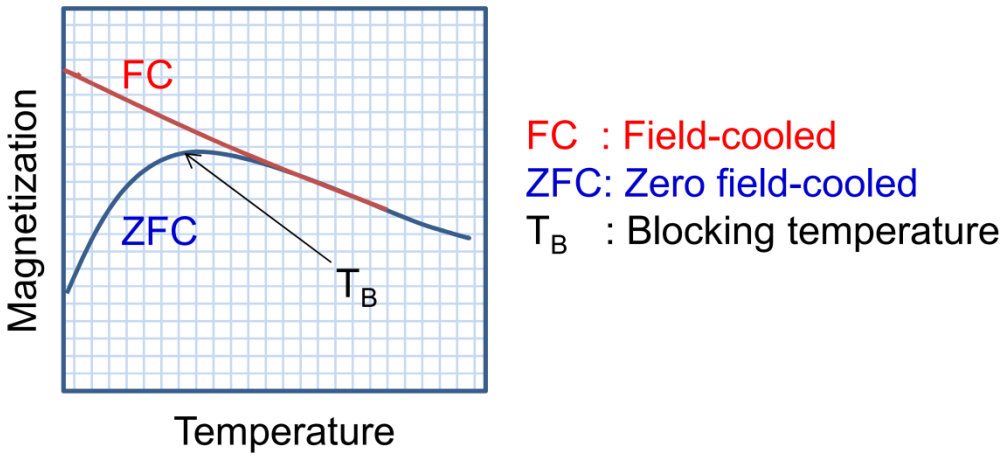

Fig. 14. ZFC-FC example curve.

The T_B indicates the point at which the behavior of the material changes. Above it, the material exhibits superparamagnetic behavior manifested by rapid random magnetization reversals leading to a zero time-average magnetic moment. Below it, the material does not have sufficient thermal energy to overcome the magnetic interactions, so the dipoles are aligned and behaves like a ferromagnetic material.

6.10.2. Hysteresis loops

The hysteresis loop provides the magnetic behavior of a material under the influence of an applied field. The maximum magnetization possible for a material is called the saturation magnetization and it arises when all the magnetic dipoles are aligned in an external magnetic field. Figure 15 shows a typical magnetization curve for ferromagnetic or ferrimagnetic nanoparticles showing the characteristic positions on the curve associated with *saturation magnetization* (Ms, maximum induced magnetization), *remanent magnetization* (Mr, induced magnetization remaining after an applied field is removed), and *coercivity* (H, the intensity of an external coercive field needed to force the magnetization to zero). In the same figure, in contrast to the hysteresis observed in the case of ferromagnetic nanoparticles (red loop), the response of superparamagnetic

nanoparticles to an external field also follows a sigmoidal curve but shows no hysteresis (green line). The response of paramagnetic (blue line) and diamagnetic (black line) nanoparticles is also shown in the schematic. The Ms shown in Figure 15 depends on temperature and is at a maximum at 0 K when the thermal vibrations (and thus randomization of aligned moments) are reduced.

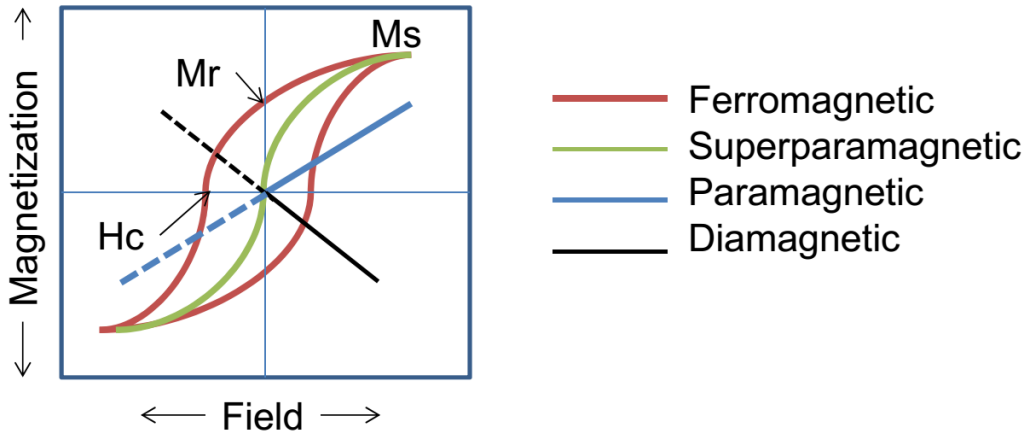

Fig. 15. Different materials hysteresis loops.

[1] N. Gálvez, E. Valero, M. Ceolin, S. Trasobares, M. López-Haro, J.J. Calvino, J.M. Domínguez-Vera, *Inorg. Chem.,* **2010**, *49,* 1705.

[2] E. Valero, S. Fiorini, S. Tambalo, H. Busquier, J. Callejas-Fernández, P. Marzola, N. Gálvez, J.M. Domínguez-Vera, *J. Med. Chem.,* **2014**, *57,* 5686.

[3] E. Valero, S. Tambalo, P. Marzola, M. Ortega-Muñoz, F.J. López-Jaramillo, F.J. Santoyo González, J.J. López-Delgado, J.J. Calvino, R. Cuesta, J.M. Domínguez-Vera, N. Gálvez, *J. Amer. Chem. Soc.,* **2011**, *133,* 4889.

[4] Z. Zhen, W. Tang, H. Chen, X. Lin, T. Todd, G. Wang, T. Cowger, X. Chen, J. Xie, *ACS Nano,* **2013**, *7,* 4830.

[5] X. Lin, J. Xie, G. Niu, F. Zhang, H. Gao, M. Yang, Q. Quan, M.A. Aronova, G. Zhang, S. Lee, et al., *Nano Lett.*, **2011**, *11,* 814.

[6] Q. Zeng, H. Wen, Q. Wen, X. Chen, Y. Wang, W. Xuan, J. Liang, S. Wan, *Biomaterials,* **2013**, *34,* 4632.

[7] A. Monserrate, S. Casado, C. Flors, *Chem. Phys. Chem.,* **2014***, 15*, 647.

[8] G.T. Dempsey, J.C. Vaughan, K.H. Chen, M. Bates, X. Zhuang, *Nat. Methods*, **2011**, *8*, 1027.

[9] D. Necas, P. Klapetek, *Open Phys,.* **2012***, 10*, 181.

[10] P. Dedecker, S. Duwe, R.K. Neely, J. Zhang, *J. Biomed. Opt*., **2012**, *17*, 126008.

[11] J. Schindelin, I. Arganda-Carreras, E. Frise, V. Kaynig, M. Longair, T. Pietzsch, S. Preibisch, C. Rueden, S. Saalfeld, B. Schmid, J. Y. Tinevez, D. J. White, V. Hartenstein, K. Eliceiri, P. Tomancak, A. Cardona, *Nat. Methods,* **2012***, 9*, 676.

[12] S. Subramaniam, P. Zhang, J. Lefman, J. Juliani, M. Kessel, *ASM News*, **2003**, *69*, 240.

[13] N. J. Greenfield, *Nat Protoc.,* **2007**, *1*, 2876.

[14] S.G. Podorov, A. Nazarkin*, Recent Res. Devel. Optics*, **2009**, *7* , ISBN 978-81-308-0370-8

[15] L. Makowski, *J. Struct. Funct. Genomics*, **2010**, *11*, 9.

[16] P. Griffiths, J.A. de Hasseth, J. A. (18 May 2007). Fourier Transform Infrared Spectrometry (2nd ed.). Wiley-Blackwell. ISBN 0-471-19404-2.

[17] A. G. Kolhatkar, A. C. Jamison, D. Litvinov, R. C. Willson, T. R. Lee, *Int. J. Mol. Sci.,* **2013**, *14*, 15977.